Chemical characterization and timing of uranium occurrences in the Nonacho Basin, Northwest Territories, Canada

By
Kerstin Landry

A Thesis Submitted to Saint Mary's University, Halifax, Nova Scotia in Partial Fulfillment of the Requirements for the Degree of Masters of Applied Science

April 2022, Halifax, Nova Scotia

Approved:	Dr. Erin Adlakha Supervisor Department of Geology Saint Mary's University
Approved:	Dr. Jacob Hanley Supervisory Committee Department of Geology Saint Mary's University
Approved:	Dr. Danielle Tokarz Supervisory Committee Department of Chemistry Saint Mary's University
Approved:	Mr. Hendrik Falck Supervisory Committee Department of Industry, Tourism and Investment, Government of the Northwest Territories
Approved:	Dr. Julien Mercadier External Examiner Research Associate French National Centre for Scientific Research

Date: April 28, 2022

Chemical characterization and timing of uranium occurrences in the Nonacho Basin, Northwest Territories, Canada

By Kerstin Landry

Abstract

The intracratonic Paleoproterozoic Nonacho Basin, deposited on the western margin of the Rae craton, Northwest Territories, Canada, contains numerous historic uranium, polymetallic and critical metal (Cu, Pb, Zn, Ni, Au, Th, Pt, Ta and Sn) occurrences near its unconformable contact with crystalline basement rocks. The integration of multiple bulk and microanalytical techniques, including petrography, scanning electron microscopy (SEM), electron probe microanalyzer (EPMA), U-Pb in uraninite geochronology using secondary ion mass spectrometry (SIMS), in addition to Re-Os in molybdenite and Ar-Ar in biotite geochronology, and inductively coupled mass spectrometry (ICP-MS) and optical emission spectroscopy (ICP-OES) has allowed for characterization of uranium occurrences within the Nonacho Basin. Developing constraints on timing, and chemical characterization of two styles of uranium mineralization: primary detrital uraninite (Hope occurrence) and a hydrothermal, remobilized mixture of uranophane±uraninite (MacInnis Lake study area) aids in understanding the metallogenic evolution of the Nonacho Basin and the western Rae craton.

April 2022

Acknowledgements

Firstly, I would like to thank my supervisor, Dr. Erin Adlakha for this opportunity, your endless encouragement, and for always having a box of tissues ready for me during our meetings. I would also like to thank Dr. Jacob Hanley for his support, encouragement and discussions; Edith Martel and Hendrik Falck for an amazing field experience, for showing me the ropes, and blossoming my love for field work. I would also like to acknowledge the Northwest Territories Geological Survey for funding and logistical support throughout my research. Thank you to Xiang Yang for all your assistance on the SEM and for spending countless hours in the SMU basement with me; Yanan Liu for your expertise, patience and assistance while remotely operating the EPMA; Mostafa Fayek and Ryan Sharpe for your assistance with the SIMS and for your knowledge and discussions regarding my research.

I would like to thank the whole SMU geology department for being full of amazing, caring and supportive faculty and students. You are all so special. Thank you so much to my incredible friends Gabe, Priyal and Andree for being such an amazing support system – I am so thankful our paths crossed. Thank you, Logan for your office chats, encouragement, your mineral hunting skills, your homemade bread and your bicycle knowledge. I also want to say thank you to Naomi Welt, who, without, I don't know if I could have succeeded. Thank you for being you; for being fearless, bold and for being the best friend I could have asked for. I am so proud of your accomplishments, and I am so grateful for you.

Lastly, I would like to thank my family: my mom, dad and my long-time partner, Nolan. Thank you for your endless support, encouragement and your unconditional love. I could not have done it without any of you. From the bottom of my heart, thank you.

Table of Contents

List of Figures

In Chapter 2

In Chapter 3

List of Tables

In Chapter 2

In Chapter 3

List of Appendices

Appendix 2:

Appendix 3:

Figure A3-1: Generalized stratigraphic sequence of the Nonacho Group sediments after Aspler (1985) and Aspler and Donaldson (1985)

Figure A3-2: XRF false-colour elemental maps from sample C-02-2

Table A3-1: EPMA data in wt.% for MacInnis Lake uranium minerals from Kult-82, Island, Cole and Welch

Table A3-2: U-Pb ages determined using Bowles (2015) and EPMA data on MacInnis Lake uranium minerals

Table A3-3: Abundance of major oxides in chlorite (wt.%) and their atomic proportions from Type-I chlorite at MacInnis Lake occurrences, used to determine temperature (T in °C)

Table A3-4: Abundance of major oxides in chlorite (wt.%) and their atomic proportions from Type-II chlorite at MacInnis Lake occurrences, used to determine temperature (T in °C)

Table A3-5: Abundance of major oxides in chlorite (wt.%) and their atomic proportions from Type-III and Type-IV chlorite at MacInnis Lake occurrences, used to determine temperature (T in °C)

Figure A3-3: Chlorite classification for each showing and type of chlorite observed

Table A3-6: Whole rock geochemical data in weight % and ppm for the Cole, Welch and Dussault occurrences

Table A3-7: Whole rock geochemical data in weight % and ppm for the Kult-82, Island and Pyramid occurrences

Chapter 1: Introduction

1.0. Structure of Thesis

This is a manuscript-based thesis and therefore, there are repetitions throughout the dissertation, mainly in the Abstracts, Introduction, Methods, and Conclusions sections of the chapters and thesis. This thesis is comprised of four chapters: an introduction (Chapter 1), two manuscript chapters (Chapters 2 and 3), and a conclusion (Chapter 4).

The student is the primary author of Chapter 2, a stand-alone manuscript prepared for submission to Precambrian Research. Co-authors are Erin Adlakha, Jacob Hanley, Hendrik Falck, Mostafa Fayek, and Ryan Sharpe. The student was the main contributor in data acquisition, background research, analyzing results, writing the chapter, formulating figures and tables. In Chapter 2, we determined that the Hope occurrence hosts the oldest detrital uraninite recorded in the Rae craton.

The student is also the primary author of Chapter 3, a stand-alone manuscript prepared for submission to Ore Geology Reviews. Co-authors are Erin Adlakha, Andree Roy-Garand, Anna Terekhova, Jacob Hanley, Hendrik Falck, and Edith Martel. The student was the main contributor in data acquisition, background research, and analyzing results, writing the chapter, formulating figures and tables. In is chapter, we determined that the uranium occurrences in the MacInnis Lake area, although previously extensively prospected, host secondary hydrothermal uraninite and uranophane and show similarities with hematite-group IOCG deposits.

1.1.Objective of Thesis

The Nonacho Basin is located in an underexplored and understudied area of the western Canadian Shield that lies within the highly uraniferous Rae craton. The uranium occurrences throughout the Nonacho Basin are widespread and, although they have undergone exploration for over 70 years, the chemical, geochronological, and genetic constraints are poorly understood.

The primary objectives of this thesis are to describe the mineralogy, paragenesis, mineral chemistry and timing of uranium mineralization from two areas of the Nonacho Basin: the Hope occurrence (Chapter 2) and the MacInnis Lake sub-basin (Chapter 3). This study combines a suite of analytical techniques, including petrography, SEM-EDS and electron microprobe analyses, whole-rock geochemistry, SIMS U-Pb geochronology, and Re-Os and laser Ar-Ar geochronology in order to classify the style and mode of uranium occurrences and further understand the metallogenic evolution of the Rae craton.

1.2.List of Abbreviations

Table 1: List of acronyms and abbreviations used throughout this thesis

Abbreviation	Meaning
BSE	Backscatter electron
EDS	Electron dispersive spectroscopy
EPMA	Electron probe microanalyzer
Ga	Billion years
HREE	Heavy rare earth elements (Eu, Gd, Tb, Dy, Ho, Er, Tm, Yb, Lu)
LREE	Light rare earth elements (La, Ce, Pr, Nd, Pm, Sm)
Ma	Million years
MIAC	Metasomatic iron and alkali calcic
MSWD	Mean squared weighted deviation
ppm	Parts per million
TTZ	Thelon tectonic zone
TMZ	Taltson magmatic zone
SIMS	Secondary ion mass spectrometry
STZ	Snowbird tectonic zone
WDS	Wavelength-dispersive spectroscopy
wt.%	Weight percentage
Ab	Albite
Bt	Biotite
Bn	Bornite
Cal	Calcite
Chl	Chlorite
Ccp	Chalcopyrite
Gn	Galena
Hem	Hematite
Ilm	Ilmenite
Mag	Magnetite
Qz	Quartz
Rt	Rutile
Ser	Sericite
Thr	Thorite
Ttn	Titanite
Uph	Uranophane
Urn	Uraninite
Mol	Molybdenite

Chapter 2: The oldest recorded uranium mineralization in the Rae craton: evidence from mineralogy, uranium trace-element chemistry and U-Pb systematics of the Hope occurrence, Nonacho Basin, Northwest Territories

Kerstin Landry[a,*], Erin Adlakha[a], Jacob Hanley[a], Hendrik Falck[b], Edith Martel[c], Mostafa Fayek[d], Ryan Sharpe[d]

[a]*Department of Geology, Saint Mary's University, 923 Robie St., Halifax, Nova Scotia, B3H 3C3*
[b]*Department of Industry, Tourism and Investment, Government of the Northwest Territories, 5102 50th Avenue, Yellowknife, Northwest Territories, X1A 2L9*
[c]*Northwest Territories Geological Survey, 4601-B 52 Avenue, Yellowknife, Northwest Territories, X1A 1K3*
[d]*Department of Geological Sciences, University of Manitoba, 240 Wallace Bldg., 125 Dysart Rd., Winnipeg, Manitoba, R3T 2N2*

Keywords:
Nonacho Basin
Rae craton
Paleoproterozoic
Uranium

*Corresponding author
E-mail address: Kerstin.Landry@smu.ca

Abstract

Petrography, mineral chemistry, and geochronology of the Hope uranium occurrence in the Nonacho Basin, Northwest Territories, Canada, reveal the oldest known uraninite in the Rae craton and record subsequent alteration and isotopic resetting by magmatic and hydrothermal activity in the area. Mineralization occurs in a sheared and hydrothermally altered quartz-biotite-albite-breccia. Coarse-grained (~500 μm), Th- and REE-rich uraninite is of magmatic origin and occurs as overgrowths on, and as intergrowths with, coarse-grained metamict zircon, with primary uraninite U-Pb ages between ~2780 to 2790 Ma. The uraninite is highly fractured with elevated concentrations of remobilized LREE, Ca and Pb along grain boundaries and fractures. The uraninite is in textural disequilibrium with later hydrothermal albite and quartz, where K-feldspar and galena-rich reaction rims surround uraninite. Geochronological data on uraninite reveal three isotopic resetting and alteration events: i) 2614 ± 11 Ma corresponding to the emplacement of the

Snow Island Suite, (ii) 2531 ± 17 Ma corresponding to widespread magmatism throughout the western Rae, and local granites at Hope and, (iii) 1778 ± 14 Ma recording alteration by hydrothermal fluids, which also produced molybdenite (1794 ± 28 Ma; Re–Os) and chloritized earlier biotite (1834 ± 1.17 Ma; Ar-Ar). This late hydrothermal event is coincident with sinistral strike slip movement of the adjacent King Shear Zone and the extensional collapse of the Trans-Hudson Orogeny proposed for the western Rae at that time.

2.1. Introduction

The Rae craton hosts a variety of uranium occurrences and deposit types (**Figure 2-1**), with the best known unconformity-type uranium deposits in the < 1.7 Ga Athabasca Basin (Jefferson et al. 2007, Alexandre et al. 2012a, 2012b, Adlakha et al. 2017; Johnstone et al. 2020, Hillacre et al. 2021) and the Thelon Basin (Jefferson 2013, Sharpe et al. 2015, Shabaga et al. 2017, 2021, Tschirhart et al. 2017), as well as the Beaverlodge uranium district, where six stages of uranium mineralization are associated with multi-stage deformation events from 2.29 to 1.62 Ga (Dieng et al. 2013, 2015). The fault-bound, 1.93-1.83 Ga Nonacho Basin is less known for uranium deposits than the Athabasca and Thelon, but also overlies the western Rae craton and hosts over 60 uranium, and critical metal polymetallic (Cu, Pb, Zn, Ni, Au, Th, Pt, Ta and Sn) occurrences (**Figure 2-2**; Gandhi and Prasad 1980, Maurice 1984, Gatzweiler et al. 1987, Jefferson et al. 2007; NORMIN 2019). Characterizing the geochemistry and geochronology of uranium mineralization in the Nonacho Basin will provide further insight into the uranium evolution of the Rae craton during its amalgamation.

In this paper, U–Pb dating of uraninite by secondary ion mass spectrometry (SIMS), uraninite mineral chemistry by electron microprobe analyzer (EPMA), along with petrographic analysis are used to constrain the origin and timing of uraninite mineralization at the Hope uranium

occurrence of the Nonacho Basin. Geochronological data on uraninite and accessory biotite and molybdenite reveal several stages of isotopic resetting and alteration by later fluids, coincident with a suite of magmatic and hydrothermal activity in the Rae craton. These data provide evidence for early uranium enrichment and a long-lived system of uranium recycling within the Rae craton

2.2. Geological Setting

2.2.1. Regional Geology

The Hope uranium occurrence is hosted in the Archean basement rocks below the Nonacho Basin, located in the Rae craton of the western Churchill Province. The western Churchill Province is separated into two Meso-Neoarchean cratons; the Rae and the Hearne (**Figure 2-1**). To the east, the Rae is separated from the Hearne by the 1.9 Ga Snowbird Tectonic Zone (STZ; **Figure 2-1**; Berman et al. 2007). To the west, the 2.0 to 1.9 Ga Taltson and Thelon suture zones border the Rae, separating it from the Slave craton, recording the amalgamation of the Slave craton with the Buffalo Head Terrane and the Rae (Hoffman 1988; Berman et al. 2018).

The Rae craton is a large (> 1000 km) structural block that consists of Archean tonalitic to granitic orthogneisses (Pehrsson et al. 2013b, Berman et al. 2013). The orthogneisses have undergone a complex and variable structural and metamorphic reworking during several stages of tectono-metamorphism. These events include: the 2.56-2.60 MacQuoid orogeny (Berman 2010; Pehrsson et al. 2013b) along its southeastern margin and the Chesterfield Block (**Figure 2-1**); 2.5-2.3 Ga Arrowsmith orogeny (Berman et al. 2005, 2010, Hartlaub et al. 2007); the 2.0-1.91 Ga Taltson and Thelon orogenies (Hoffman 1988); and the far-field effects of the 1.9-1.8 Ga Trans-Hudson orogeny (Hoffman 1988, Ashton et al. 2009, Pehrsson et al. 2013a), which completely reworked the interior of the Rae craton (Pehrsson et al. 2013b) and is defined by 1.8 Ga tectono-metamorphic overprints that extend 1800 km across the Canadian Shield (Corrigan et al. 2009).

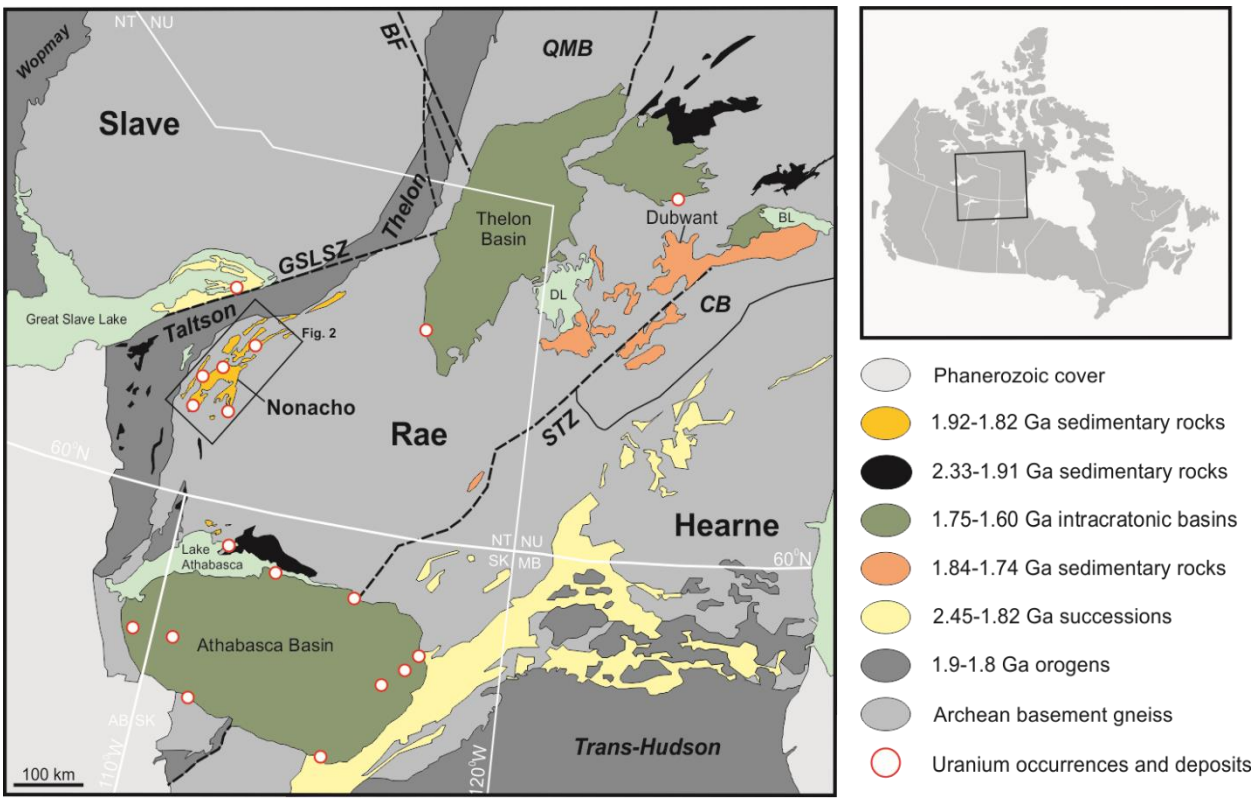

Figure 2-1: Generalized regional map showing the location of the Nonacho Basin relative to major lithotectonic domains and uranium occurrences and deposits throughout the Rae craton. Abbreviations: BF–Bathurst Fault; BL–Baker Lake; CB–Chesterfield Block; DL–Dubwant Lake; GSLSZ–Great Slave Lake Shear Zone; STZ–Snowbird Tectonic Zone; QMB; Queen Maud block. Canadian Provinces and Territories: AB–Alberta; MB–Manitoba; NT–Northwest Territories; NU–Nunavut; SK–Saskatchewan. Dashed lines mark major structures and faults. Figure modified after Ashton et al., (2013) and Neil et al. (2021).

2.2.2. Local Geology

The Nonacho Basin is a Paleoproterozoic northeast striking siliciclastic basin that lies southeast of Great Slave Lake (**Figure 2-2**). The Archean basement rocks consist of variably metamorphosed gneisses and granitoids, which are overlain by the 1.91-1.83 Ga Nonacho Group sediments (Aspler, 1985; Aspler and Donaldson 1985). A variety of uranium and base metal occurrences have been noted in both the basement rocks and the overlying sedimentary sequence (NORMIN 2019; **Figure 2-2**).

The Hope occurrence, located in the northwestern margin of the Nonacho Basin (**Figure 2-2**), is hosted in basement biotite-paragneiss units, adjacent to the King Shear Zone, a 1.78 Ga north-northeast trending sinistral strike-slip shear zone (Canam et el. 2021). In 1971, the Hope occurrence was the subject of an exploration program and radiometric survey by Nissho-Iwai Canada Ltd. They describe basement rocks as light to dark grey, thinly bedded gneissic sandstone trending 062/85, composed of quartz, feldspar and biotite, but silicified and feldspathized (Doi et al. 1971). Gneisses are intruded by a pink to reddish-brown, medium- to coarse-grained, biotite-rich granite. Radiometric surveying outlined a number of anomalies hosted in gneissose sandstone (Doi et al. 1971). The authors identified two styles of mineralization: 1) uraninite in quartz-biotite schist, interbedded with gneissose sandstone; and, 2) uranothorite in brecciated, quartz-filled fault and shear zones, cross-cutting the gneissose sandstone.

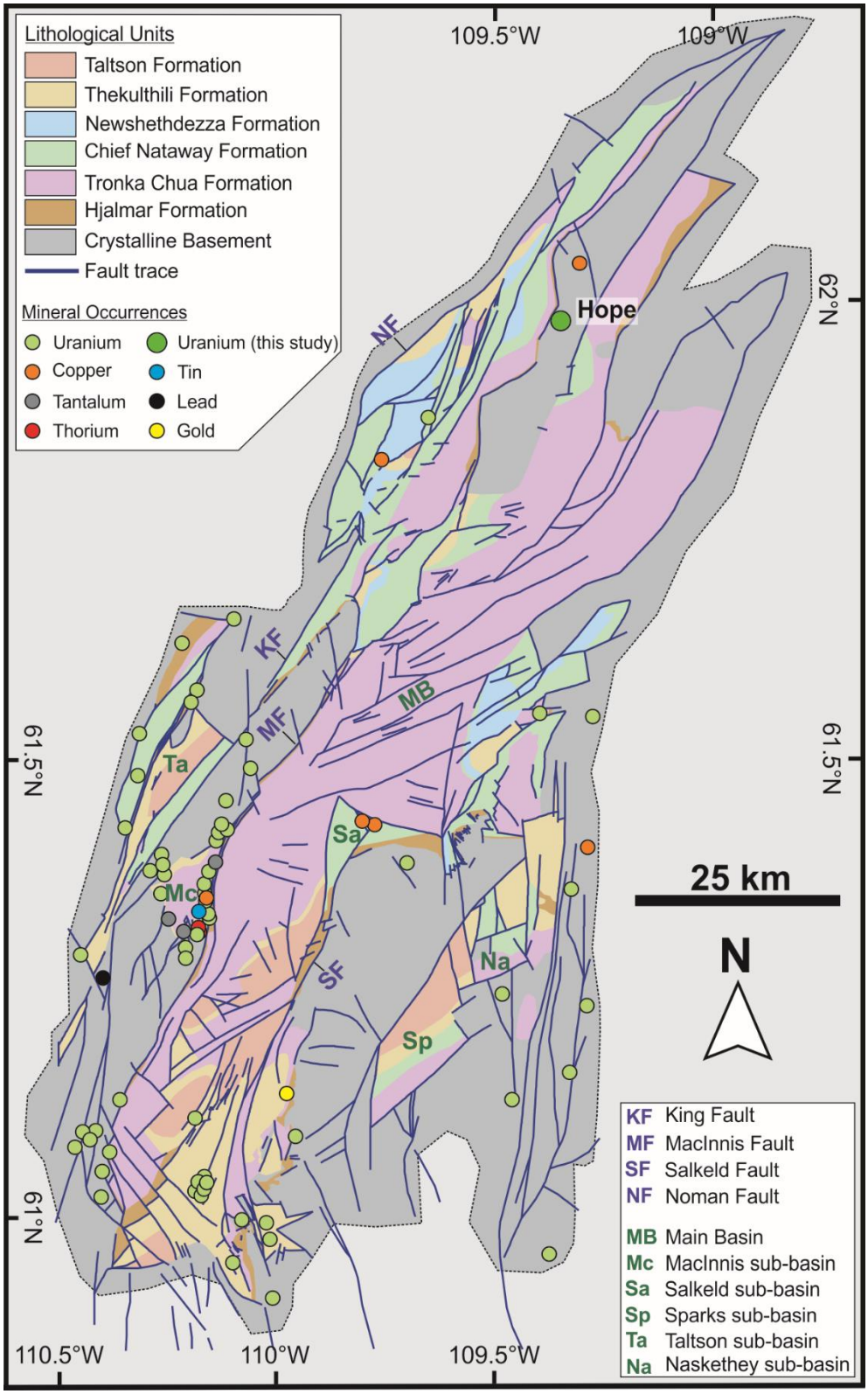

Figure 2-2: Geological sketch of the Nonacho Basin showing the location of uranium and base metal occurrences modified after (Aspler 1985, NORMIN 2019, Ielpi et al. 2021)

2.3. Methods

2.3.1. Rock Collection and Mineral Identification

The Hope uranium occurrence was examined during a field visit in August 2019, where host rocks, structures, alteration and mineralization were documented. Representative samples of host lithology, uranium mineralization (detected by high radioactivity) and associated alteration were collected.

Six polished thin sections were prepared at Precision Petrographics and characterized using a petrographic microscope in both transmitted and reflected light. Petrographic analyses were complimented with a TESCAN MIRA 3 LMU Variable Pressure Schottky Field Emission scanning electron microscope (SEM) at Saint Mary's University to further identify mineralogy and alteration of uraninite, associated sulphides and alteration minerals. The system is equipped with an electron dispersive X-ray (EDS) Oxford INCA 80mm^2 silicon draft detector capable of quantitative analysis and a backscatter electron (BSE) detector for imaging. Measurements were conducted at a working distance of ~17 mm, with a beam current of 40 μA and accelerating voltage of 20 kV. Raw data (counts and keV) were reduced using the INCA software package.

2.3.2. Electron Probe Microanalyzer

Targeted uraninite grains in polished thin sections were cut into chips with a dremel tool and mounted into 1-inch diameter epoxy pucks before analysis with a JEOL JXA8230 5-WDS (wavelength dispersive spectrometer) electron probe X-ray microanalyzer (EPMA) at the University of Toronto. The composition of uraninite was determined using 100 EPMA measurements from two uraninite-bearing samples (H-12 and H-14) and nine analyses from a thorite-sericite breccia (sample H-09) were analyzed with an accelerating voltage of 15 kV, a beam current of 30 nA and a 1 μm focused beam. Counts of characteristic X-rays for each element were

quantified by comparison with analyses of known standards and energy lines: apatite (P*Kα*), barite (Ba*Kα*), $CePO_4$ (Ce*Lα*), Cr-augite (Al*Kα*, Ca*Kα*, Mg*Kα*, Si*Kα*), $DyPO_4$ (Dy*Lα*), $ErPO_4$ (Er*Lα*), $EuPO_4$ (Eu*Lα*), galena (Pb*Mα*, S*Kα*), $GdPO_4$ (Gd*Lα*), hematite (Fe*Kα*), $HoPO_4$ (Ho*Lα*), $LaPO_4$ (La*Lα*), $LuPO_4$ (Lu*Lα*), $NdPO_4$ (Nd*Lα*), $PrPO_4$ (Pr*Lα*), sanidine (K*Kα*), $SnPO_4$ (Sm*Lα*), $TbPO_4$ (Tb*Lα*), $ThSiO_4$ (Th*Mα*), TiO_2 (Ti*Kα*), $TmPO_4$ (Tm*Lα*), tugtupite (Cl*Kα*), UO_2 (U*Mα*), YPO_4 (Y*Lα*), $YbPO_4$ (Yb*Lα*) and $ZrSiO_4$ (Zr*Lα*)

2.3.4. Whole-Rock Geochemistry

Five uraninite-mineralized samples were selected for whole-rock geochemistry. Sample preparation and analysis were performed at Activation Laboratories Inc. in Ancaster, Ontario. Major elements were analyzed using X-ray fluorescence (XRF) on borate metafusion glass pellets. Trace elements were analyzed using Inductively Coupled Plasma Mass Spectrometry (ICP-MS) and Inductively Coupled Plasma Optical Emission Spectrometry (ICP-OES) on samples prepared using a closed vessel multi-acid digestion.

2.3.5. Geochronology

In-situ Secondary Ion Mass Spectrometry (SIMS)

Secondary Ion Mass Spectrometry was completed using the CAMECA 7f ion microprobe at the Manitoba Research Facility, University of Manitoba to measure U and Pb isotope ratios of 79 points in the most homogeneous areas of 9 uraninite grains from samples H-12 and H-14. Targets from polished thin sections were cut into chips from thin sections using a dremel tool, mounted into 1-inch diameter epoxy pucks, which were cleaned with ethanol and polished using 1-μm diamond cleaning compound. Once cleaning was complete, pucks were sputter-coated with a thin layer of gold to produce a conductive surface for the SIMS analyzer.

Measurements were conducted using a 10nA primary ion beam of O^-, accelerated at 12.5 kV with a focused spot size of 15 × 30 μm. The sample accelerating voltage was +7.95 kV, with the electrostatic analyzer in the secondary column at +8.00 kV. The entrance and exit slits were narrowed to obtain mass resolving power of 1300. Ions of $^{204}Pb^+$, $^{206}Pb^+$, $^{207}Pb^+$, $^{208}Pb^+$, $^{235}U^+$ and $^{238}U^+$ were detected using an ETP 133H electron multiplier with an ion-counting system for an overall deadtime of 25s. A typical analysis lasts ~8 minutes, comprising 30 cycles of analysis. Spot-to-spot reproducibility on the uraninite reference material is 2.2% and 2.1% for $^{206}Pb/^{238}U$ and $^{207}Pb/^{235}U$, respectively. Methods outlined in Sharpe and Fayek (2016) were used to determine 2σ and σx.

Ar/Ar of Biotite

$^{40}Ar/^{39}Ar$ analytical work on biotite was performed at the University of Manitoba using a multi-collector Thermo Fisher Scientific ARGUSVI mass spectrometer, linked to a stainless steel Thermo Fisher Scientific extraction/purification line, Photon Machines (55 W) Fusions 10.6 CO_2 laser and Photon Machines (Analyte Excite) 193 nm laser. Argon isotopes were measured using: ^{40}Ar (H1; 1 x 10^{12} Ω resistor), ^{39}Ar (AX; 1 x 10^{13} Ω resistor), ^{38}Ar (L1; 1 x 10^{13} Ω resistor), ^{37}Ar (L2; 1 x 10^{13} Ω resistor) and ^{36}Ar (compact discrete dynode [CDD]). The sensitivity for argon measurements is ~6.3 x 10^{17} moles/fA as determined from measured aliquots of Fish Canyon Sanidine (Dazé et al. 2003, Kuiper et al. 2008).

Re/Os of Molybdenite

A rock sample containing visible molybdenite mineralization was sent to the Crustal Re-Os Geochronology Laboratory at the University of Alberta where molybdenite was separated by metal-free crushing and sieving followed by magnetic and gravity concentration methods,

described in detail by Selby and Creaser (2004). The ^{187}Re and ^{187}Os concentrations in molybdenite were determined by isotope dilution mass spectrometry using used a ThermoScientific Triton mass spectrometer by Faraday collector with a Carius-tube, solvent extraction, anion chromatography and negative thermal ionization mass spectrometry techniques. For this work, a mixed double spike containing known amounts of isotopically enriched ^{185}Re, ^{190}Os, and ^{188}Os analysis was used (Markey et al., 2007). Total procedural blanks for Re and Os are less than < 3 picograms and 1 picograms, respectively, which are insignificant in comparison to the Re and Os concentrations in molybdenite.

2.4. Results

2.4.1. Petrography and Paragenesis

Basement Gneisses and Granitoids

Least altered basement gneisses are fine-grained, light grey and thinly banded, trend north-northeast and are steeply dipping, at 065/76 (**Figure 2-3a**). At the Hope occurrence, the gneiss is pervasively silicified, and locally contain decimetre-scale massive quartz veins following gneissosity (**Figure 2-3b**). The gneiss is also feldspathized, where felsic layers are altered to K-feldspar and quartz (**Figure 2-3c**) and cross-cut by locally radioactive pegmatitic quartz-feldspar ± magnetite veins (**Figure 2-3d, e**) and granitoids (**Figure 2-3f, g**) of unknown origin. Feldspar predominantly occurs along vein margins within pegmatites (**Figure 2-3d, e**)

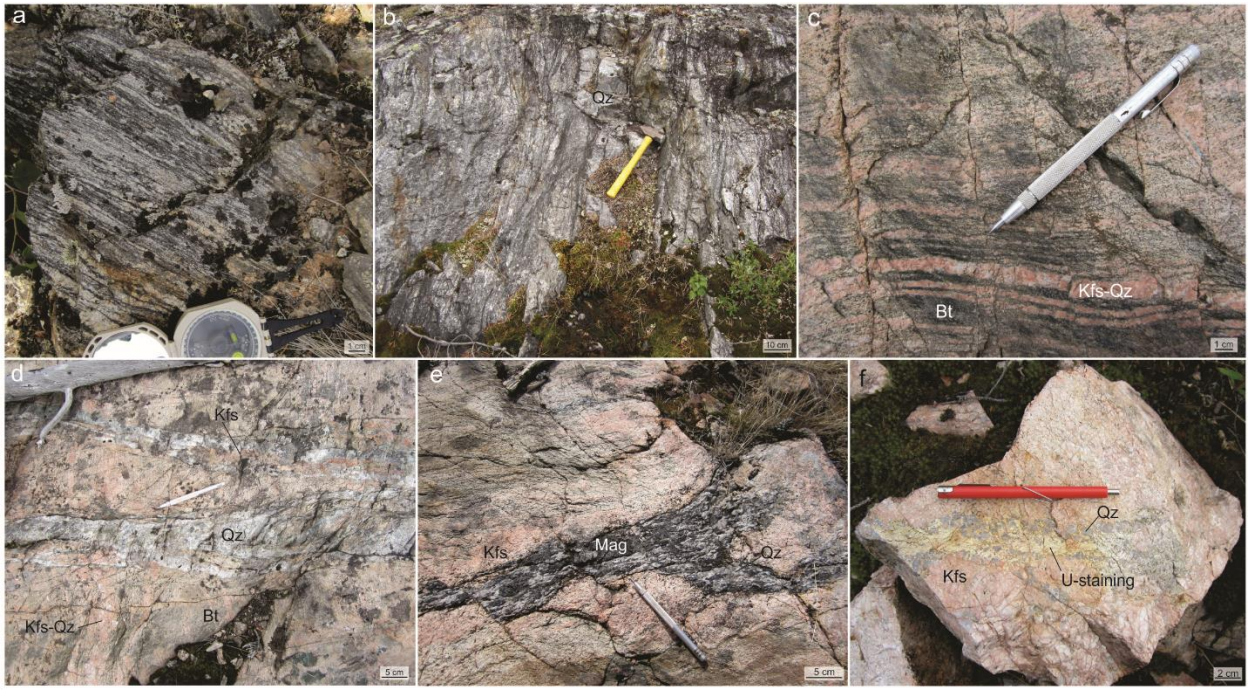

Figure 2-3: Basement gneisses and granitoids at the Hope occurrence. (a) Biotite (Bt) paragneiss of the Hope occurrence; (b) biotite paragneiss with decimetre-scale zone of silicification following gneissosity; (c) feldspathized gneiss with K-feldspar (Kfs) and quartz (Qz) replacing leucosomes; (d) Coarse-grained to pegmatitic quartz and K-feldspar veins cross-cutting gneissosity; (e) pegmatitic quartz and K-feldspar vein with massive magnetite (Mag); (f) coarse-grained granitoid with local yellow uranium-hydroxide staining (U-staining).

Uraninite Mineralized Gneiss

The paragenetic sequence for the uraninite-mineralized breccia of the Hope occurrence is outlined in **Figure 2-4.** The host biotite-paragneiss has undergone variable deformation forming sheared breccia that locally host uraninite mineralization and yellow uranium-hydroxide staining (**Figure 2-5a, b**). The breccia consists of milled albitized (Ab_{95-98}) feldspar clasts (**Figure 2-5c**), containing "islands" of fresh oligoclase (Ab_{73-84}). Albitized oligoclase exhibits a pitted texture which is infilled by sericite (**Figure 2-5d, e**). Massive to foliated biotite and food quartz, which has undergone grain-boundary migration recrystallization, surround albitized clasts and form the breccia matrix (**Figure 2-5d, e, f**).

Uraninite occurs in the biotite-rich matrix as subhedral, highly fractured grains from 200 to 500 μm in size (**Figure 2-5g, h**) spatially associated and/or intergrown with 50 to 100 μm metamict and zoned euhedral zircon grains (**Figure 2-5g, h**). Semi-quantitative SEM-EDS analyses indicate appreciable levels of Ca (2–3 wt.%) and Al (0.8–1.5 wt.%) within relatively darker zones (in BSE-images) of zircon (**Figure 2-5i**). Uraninite displays reaction rims consisting of K-feldspar, calcite and galena where in contact with quartz (**Figure 2-5h**). Titanite with ilmenite cores and coarse-grained molybdenite (up to 2 mm) laths occur along biotite cleavage planes, where biotite is locally chloritized (**Figure 2-5g, j**).

Highly silicified zones are cross-cut by sericite stockwork, which contain minor blebs of apatite, spatially associated with anhedral thorite and pyrite (**Figure 2-6a-c**). Veinlets of K-feldspar and acicular chlorite cross-cut quartz and sericite stockwork (**Figure 2-6d**). Highly fractured, but euhedral pyrite is disseminated throughout quartz and thin (< 15 μm) veinlets of pyrite cross-cut all earlier mineral phases (**Figure 2-6a-d**).

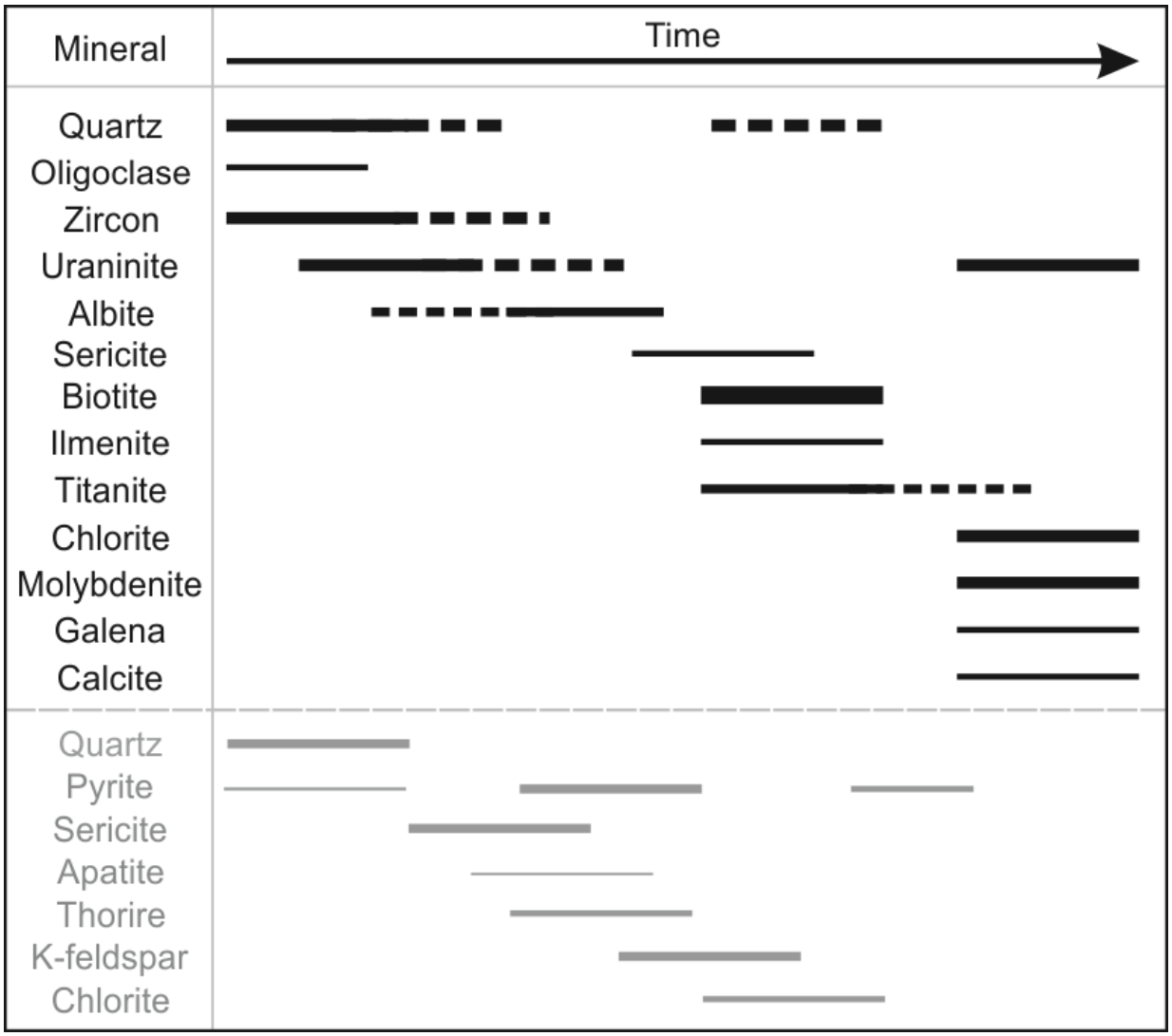

Figure 2-4: Mineral paragenesis of uraninite-mineralized deformation zones (top) and the silicified sericite-pyrite-thorite stockwork (bottom). The timing of the bottom paragenetic sequence relative to uraninite mineralization is unknown. The weight of lines indicates the relative abundance; dashed lines represent uncertainty in the paragenetic sequence.

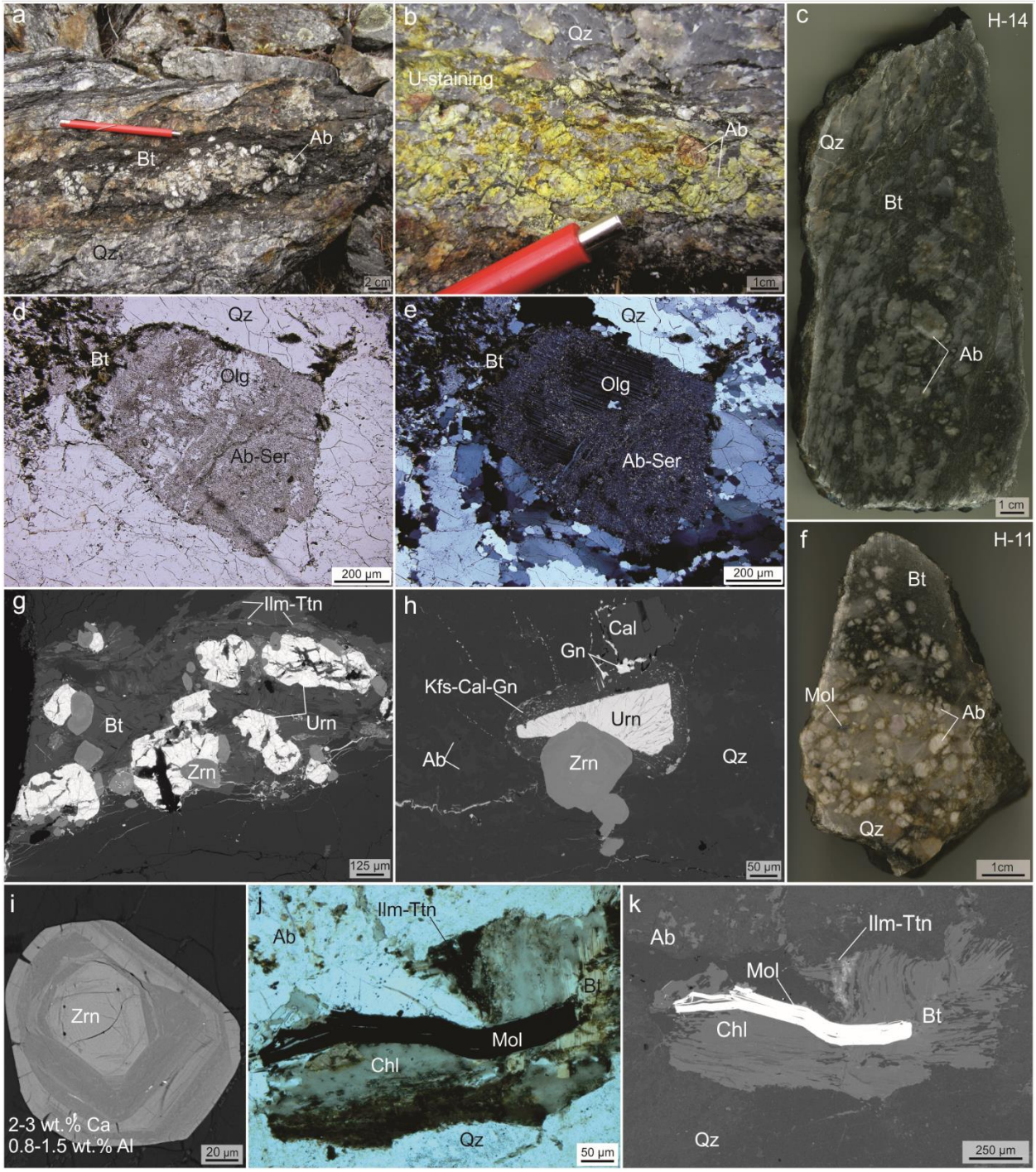

Figure 2-5: Host rocks and uraninite mineralization at the Hope occurrence: (a) uraninite mineralized biotite (Bt) and quartz (Qz) rich deformation zone hosting milled albite (Ab) clasts; (b) yellow uranium-hydroxide staining in quartz-rich zones with milled albite; (c) breccia sample H-14 displaying milled albite clasts within quartz and biotite rich matrix; (d) photomicrograph in plain polarized light (PPL) of a milled albitized clast with islands of fresh oligoclase (Olg) in biotite and quartz; (e) cross-polarized light (XPL) image of (d), showing flood quartz textures and sericite (Ser) infilling pitted albite; (f) breccia sample H-11 with milled albite and minor

molybdenite (Mol) in quartz and biotite; (g) SEM-BSE image of foliated biotite with ilmenite (Ilm) and titanite (Ttn) along biotite cleavage planes and grains of uraninite (Urn) intergrown with zircon (Zrn); (h) SEM-BSE image of uraninite with zircon showing a reaction rim of K-feldspar (Kfs), calcite (Cal) and galena (Gn) separating uraninite from quartz and patchy albite; (i) zoned zircon grain Ca- and Al-rich zoning; (j) plane polarized (PPL) image of molybdenite associated with chlorite (Chl) altered biotite. Ilmenite and titanite are associated with biotite and chlorite; (k) SEM-BSE image of (j) where molybdenite is associated with chlorite altered biotite, surrounded by quartz. Corroded ilmenite cores are surrounded by titanite rims along the cleavage planes of biotite and chlorite.

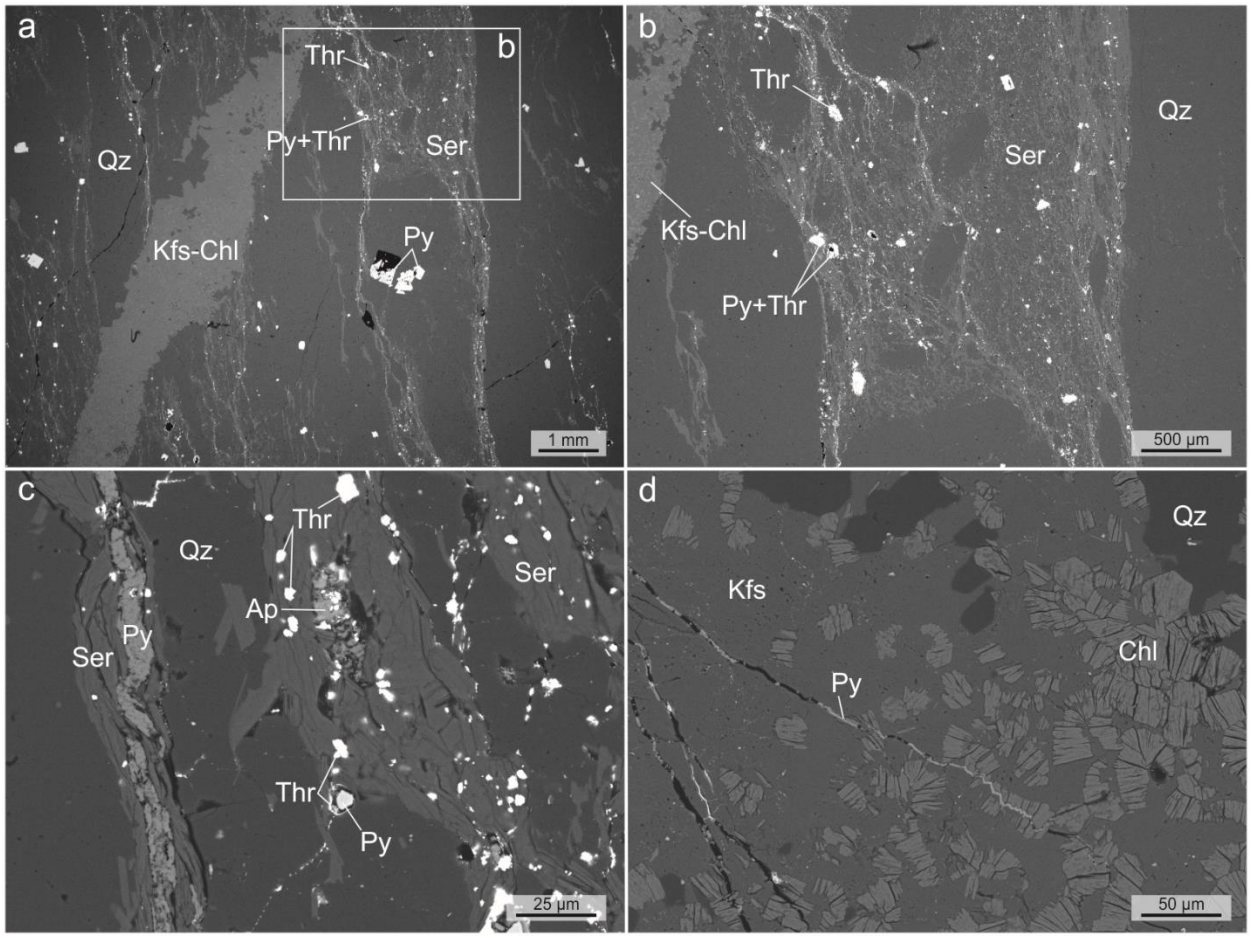

Figure 2-6: SEM-BSE images of thorite-sericite breccia sample (H-09): (a) sericite (Ser) and thorite (Thr), pyrite (Py) stockwork in quartz (Qz), cross-cut by a K-feldspar (Kfs) and chlorite (Chl) vein; (b) enhanced image of box in (a) showing sericite stockwork in quartz hosting thorite and pyrite; (c) Textural relationships between apatite (Ap), pyrite and thorite, where thorite overprints apatite, and locally occurs as rims on pyrite. Pyrite veins and stringers are also present within sericite; (d) Enhanced image of K-feldspar and chlorite vein, locally cross-cut by pyrite stringers.

2.4.2. Mineral Chemistry of Uraninite and Thorite

Electron microprobe analyses were conducted on 100 spots from six uraninite grains from samples H-12 and H-14. In general, the chemical composition of Hope uraninite is variable consisting of 61.4–80.4 wt.% UO_2, 7.2–16.7 wt.% ThO_2, 5.1–22.8 wt.% PbO, 0.3–3.6 wt% CaO, < 1.3 wt.% SiO_2 and < 1.3 wt.% FeO and 1.2–3.2 wt.% ΣREE+Y (**Table 2-**). Qualitative EPMA-WDS elemental mapping of uraninite grains (**Figure 2-7**) show relatively homogeneous U concentrations (**Figure 2-7b**), but depletions along cracks and fractures that are infilled by Pb (**Figure 2-7c**). Primary zonation is preserved in some grains showing high Th (**Figure 2-7d**) and REE (**Figure 2-7e**), using Y as a proxy. The EPMA-WDS elemental mapping also shows Ca-alteration in both uraninite and zircon (**Figure 2-7f**) and K-feldspar, calcite and galena reaction rims (**Figure 2-7c, g, h**) around uraninite, where it is in disequilibrium with surrounding albite and quartz. The chondrite normalized REE patterns of uraninite are 3–4 orders of magnitude higher than chondrite (**Figure 2-8a**), and. using Ce and Y as proxies for LREE and HREE respectively, normalized LREE/HREE ratios range from 0.3–4.7 and concentrations of Eu, Tb and Yb falling beneath the lower limits of detection for the EPMA (**Table 2-**).

Subhedral grains of thorite occur within a sericite-thorite-apatite-pyrite breccia (**Figure 2-6**). Nine spots from thorite in sample H-09 were analyzed using the EPMA. The sample contains 69.5–71.8 wt.% ThO_2, 9.4–11.8 wt.% SiO_2, 5.6–6.7 wt.% P_2O_5, 2.3–3.2 wt.% SO_3, 1.2–1.7 wt.% FeO, 1.1–1.5 wt.% CaO, 0.5–0.7 wt.% UO_2, and 1.7–2.3 wt.% ΣREE (**Table 2-2**). The chondrite normalized REE patterns of thorite are lower, only 1–2 orders of magnitude higher than chondrite (**Figure 2-8a**), with the exception of increased Y, ranging from 0.1–1.4 wt.% Y_2O_3 (**Table 2-2**). Using chondrite normalized Ce and Y concentrations as proxies for LREE and HREE respectively,

the LREE/HREE ratios for thorite are low relative to uraninite mineralized samples, ranging from 0.13–0.16 (**Table 2-2**).

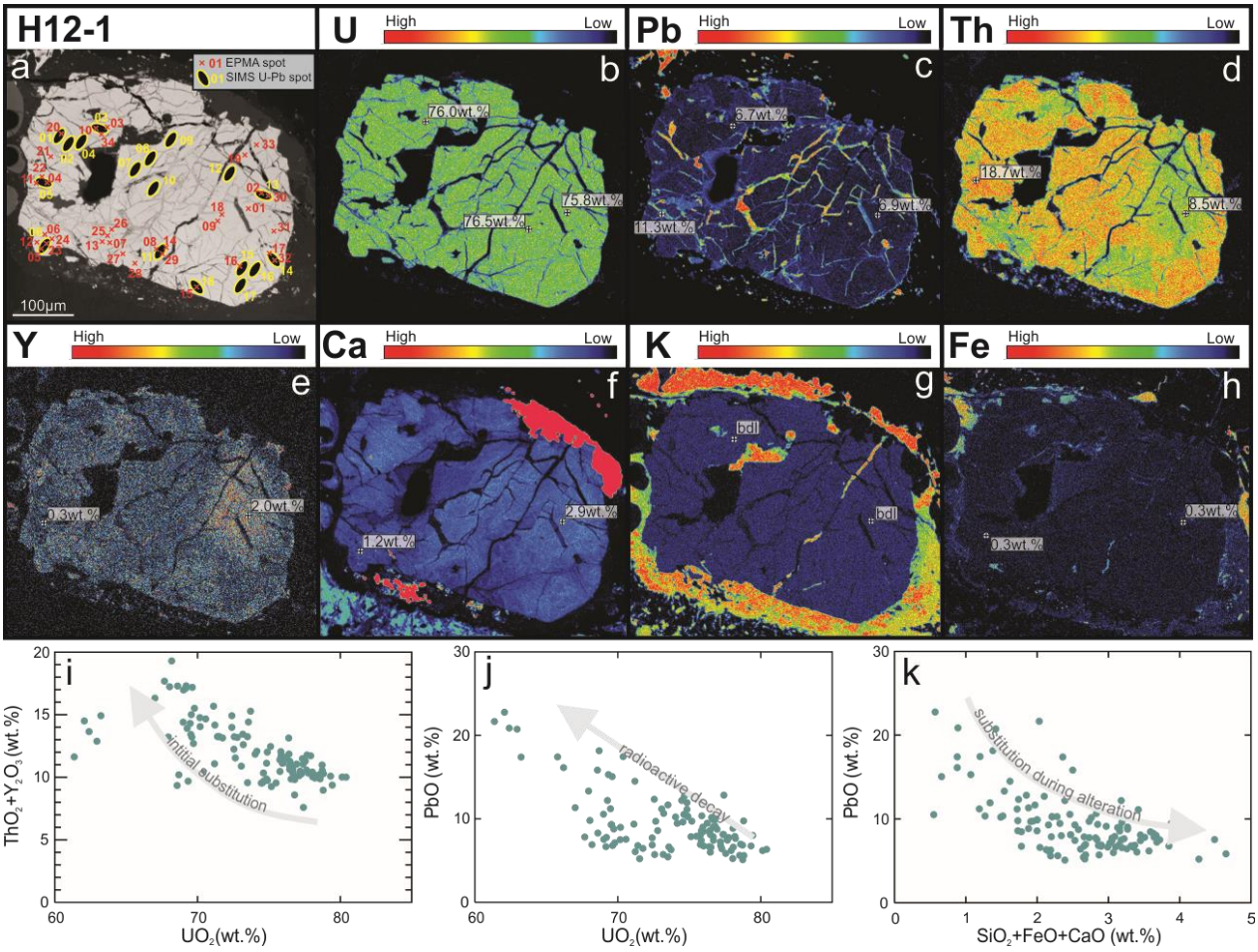

Figure 2-7: EPMA-WDS false colour elemental maps of coarse-grained uraninite from sample H-12-1 (b-h) and biplots using EPMA data from samples H-12 and H-14 (i-k): (i) UO_2 vs. ThO_2 showing initial substitution; (j) UO_2 vs. PbO showing radioactive decay; (k) SiO_2+FeO+CaO vs. PbO showing substitution during alteration. Modified after Alexandre et al. (2015). Scale bars in (b-h) represent relatively high (red) and low (blue) qualitative elemental concentrations. Abbreviations: below detection limit (bdl).

Table 2-1: Representative EPMA data (wt.% oxide) of three grains of uraninite at the Hope occurrence from sample H-12

	H12-1				H12-3				H12-4			
SiO_2	<0.03	<0.03	<0.03	<0.03	<0.03	<0.03	<0.03	<0.03	0.19	<0.03	<0.03	0.47
TiO_2	0.03	<0.06	0.02	0.02	0.00	0.01	<0.06	0.03	<0.06	<0.06	<0.06	0.05
Al_2O_3	<0.03	<0.03	<0.03	<0.03	<0.03	<0.03	<0.03	<0.03	<0.03	<0.03	<0.03	<0.03
MgO	0.02	0.00	0.01	0.02	0.01	<0.02	0.01	0.04	<0.02	<0.02	0.02	0.00
$FeO_{(total)}$	0.30	0.26	0.28	0.32	0.13	0.14	0.05	0.11	0.24	0.30	0.26	0.31
CaO	2.85	2.83	1.21	1.59	2.54	2.47	1.99	2.18	1.54	0.77	0.29	0.60
K_2O	0.00	0.01	0.01	0.01	<0.04	<0.04	0.02	<0.04	0.03	0.00	0.04	0.02
P_2O_5	0.05	0.08	0.09	0.09	0.09	0.10	0.08	0.07	0.08	0.06	0.09	0.11
SO_3	0.83	1.07	0.76	1.55	0.03	0.01	<0.04	<0.04	1.62	2.58	2.25	0.13
Zr_2O_3	0.00	<0.09	0.01	<0.09	<0.09	<0.09	<0.09	<0.09	<0.09	<0.09	<0.09	<0.09
BaO	0.07	0.05	0.03	0.07	<0.10	0.14	0.05	0.03	0.03	0.07	0.05	0.03
La_2O_3	<0.24	0.13	<0.25	<0.23	<0.24	<0.24	0.04	0.06	<0.24	0.07	0.09	<0.24
Ce_2O_3	0.21	0.31	0.29	0.59	0.35	0.42	0.38	0.47	0.18	0.17	0.37	0.20
Pr_2O_3	0.05	0.03	0.01	0.06	0.03	0.06	0.02	0.05	<0.18	0.07	<0.18	0.01
Nd_2O_3	0.49	0.70	0.44	0.66	0.54	0.61	0.49	0.67	0.38	0.44	0.35	0.44
Sm_2O_3	0.28	0.31	0.15	0.27	0.36	0.37	0.29	0.23	0.19	0.20	0.10	0.08
Eu_2O_3	<0.15	<0.15	<0.15	<0.15	<0.15	<0.15	<0.15	<0.15	<0.15	0.01	0.00	<0.15
Gd_2O_3	0.36	0.36	0.25	0.22	0.50	0.38	0.40	0.40	0.24	0.22	0.19	0.23
Tb_2O_3	<0.14	<0.14	<0.14	<0.14	<0.14	<0.14	<0.14	<0.14	<0.14	<0.14	<0.14	<0.14
Dy_2O_3	0.61	0.45	0.17	0.24	0.56	0.56	0.63	0.55	0.17	0.28	0.26	0.12
Ho_2O_3	0.06	0.20	0.08	0.16	0.24	0.28	0.25	0.14	0.11	0.13	0.14	0.04
Y_2O_3	2.00	1.35	0.74	0.59	2.63	2.60	2.42	2.47	0.52	0.63	0.88	0.39
Er_2O_3	0.26	0.00	0.01	0.01	0.22	0.31	0.09	0.25	<0.15	<0.15	<0.15	<0.15
Tm_2O_3	0.10	0.08	0.02	0.07	0.02	0.01	0.08	0.04	0.13	0.03	<0.16	<0.16
Yb_2O_3	0.09	0.01	<0.17	<0.17	0.17	0.16	0.16	0.10	<0.17	<0.17	<0.17	0.05
Lu_2O_3	0.07	<0.18	<0.18	0.10	0.10	0.07	0.10	0.09	<0.18	<0.18	0.04	0.05
PbO	6.92	7.91	10.22	9.70	5.23	6.40	6.61	5.62	11.66	15.29	10.52	18.16
ThO_2	8.46	8.19	11.10	10.95	7.78	7.66	7.76	7.73	9.04	9.05	9.45	9.80
UO_2	75.78	75.50	74.04	72.65	78.04	77.28	78.08	78.52	73.51	69.35	74.62	68.70
Total	99.88	99.84	99.92	99.92	99.56	100.02	100.01	99.83	99.87	99.69	98.99	99.98
ΣREE	2.56	2.57	1.43	2.38	3.08	3.21	2.95	3.04	1.40	1.59	1.55	1.22
$(LREE/HREE)_{CN}$[§]	0.29	0.63	1.09	2.79	0.37	0.45	0.44	0.53	0.98	0.74	1.78	0.52

Notes: Analyses taken from three different grains (labelled 1, 3 and 4) from sample H12. Analyses that fell below their limits of detection are noted as less than (<) ½ of their respective limit of detection on the EPMA. Full data set in **Table A2-1**

[§] Chondrite normalized (CN) Ce and Y used as proxies for LREE and HREE, respectively.

Table 2-2: EPMA data (wt.%) of thorite at the Hope occurrence

	H-09					
SiO_2	11.43	11.76	10.70	11.20	10.39	9.36
TiO_2	0.01	0.04	0.04	<0.06	0.04	<0.06
Al_2O_3	0.13	0.42	0.11	0.12	0.11	0.31
MgO	<0.02	0.03	<0.02	<0.02	<0.02	<0.02
$FeO_{(total)}$	1.65	1.37	1.21	1.27	1.29	1.26
CaO	1.11	1.35	1.23	1.29	1.28	1.50
K_2O	0.04	0.11	0.06	0.06	0.07	0.12
P_2O_5	5.58	6.60	6.71	6.41	6.27	6.10
SO_3	3.00	2.85	2.95	3.19	2.89	2.36
Zr_2O_3	0.61	0.49	0.53	0.52	0.51	0.47
BaO	0.13	0.20	0.04	0.07	0.06	0.02
La_2O_3	0.24	0.10	0.17	0.15	0.26	0.13
Ce_2O_3	0.28	0.42	0.33	0.38	0.37	0.35
Pr_2O_3	<0.16	0.02	0.07	0.11	0.13	0.04
Nd_2O_3	0.19	0.27	0.26	0.33	0.16	0.21
Sm_2O_3	0.14	0.22	0.18	0.20	0.12	0.21
Eu_2O_3	<0.14	0.07	0.06	0.11	0.05	0.02
Gd_2O_3	0.30	0.38	0.32	0.25	0.30	0.31
Tb_2O_3	<0.12	<0.12	<0.12	<0.12	<0.12	<0.12
Dy_2O_3	0.25	0.25	0.24	0.26	0.28	0.32
Ho_2O_3	0.16	0.23	0.10	0.23	0.19	0.20
Y_2O_3	0.93	1.18	1.06	1.01	0.97	1.14
Er_2O_3	0.04	0.07	0.01	<0.13	0.02	0.05
Tm_2O_3	<0.14	0.09	0.02	<0.14	<0.14	0.05
Yb_2O_3	<0.15	0.05	0.08	0.04	0.03	<0.15
Lu_2O_3	0.06	0.10	<0.16	<0.16	0.05	0.08
PbO	0.12	0.10	0.08	0.17	0.15	0.13
ThO_2	69.48	70.45	69.27	71.60	70.95	71.81
UO_2	0.53	0.47	0.72	0.53	0.58	0.72
Total	96.41	99.67	96.52	99.49	97.52	97.27
ΣREE	1.65	2.26	1.83	2.05	1.97	1.98
$(LREE/HREE)_{CN}$[§]	0.13	0.15	0.13	0.16	0.16	0.13

Notes: Analyses that fell below their limits of detection are noted as less than (<) ½ of their respective limit of detection on the EPMA.

[§] Chondrite normalized (CN) Ce and Y used as proxies for LREE and HREE, respectively.

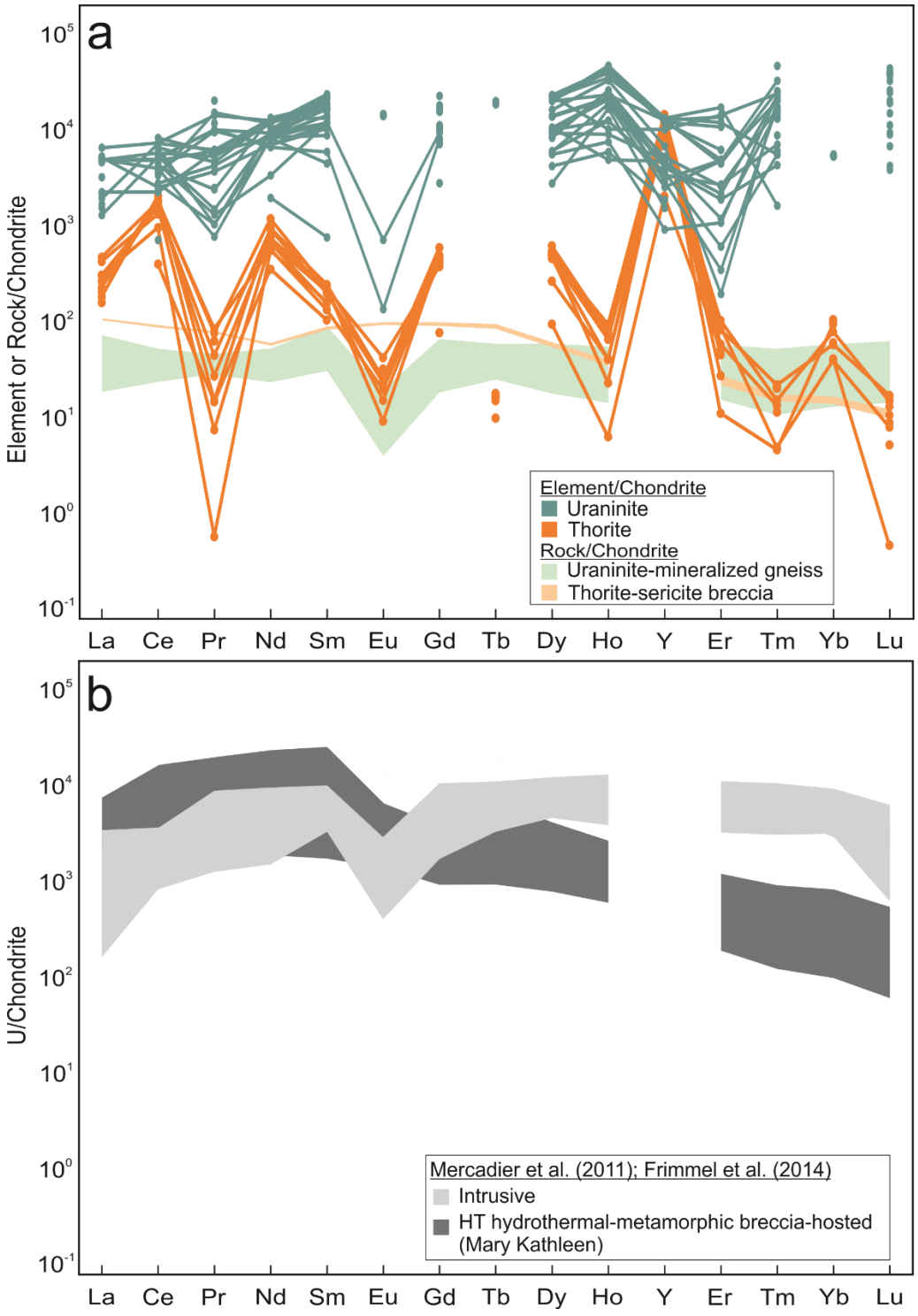

Figure 2-8: Chondrite normalized (McDonough and Sun 1995) REE + Y diagrams for (a) trace element (lines) and whole-rock geochemical (fields) data of the Hope uraninite (blue) and thorite (orange). Analyses that fall below the limits of detection of the EPMA are plotted as ½ their respective detection limit, as a single dot; (b) uraninite data from several global intrusive deposits (Frimmel et al. 2014 and Mercadier et al. 2011; light grey) and the Mary Kathleen deposit (dark grey; Frimmel et al. 2014).

2.4.4. Whole-Rock Geochemistry

Four representative samples of uraninite mineralized samples (H-10, H-11, H-12, H-14) and one sample of thorite-sericite stockwork in quartz (H-09) were sent for whole-rock geochemical analyses to determine major and trace element compositions. Major and trace elements, including REE are presented in **Table A2-2**.

The whole-rock geochemistry of uraninite mineralized samples are consistent with observed mineralogy. Samples containing abundant albite clasts (e.g., H-11), contain 2.12 wt.% Na and 7.20 wt.% Al while biotite-rich samples (e.g., H-12 and H-14) contain 3.94–6.34 wt.% Fe and 1.99–2.98 wt.% K and variable Al (4.1–7.88 wt.%). In general, mineralized samples contain 728–3870 ppm U, 713–1470 ppm Zr, 379–2090 ppm Pb, 263–439 ppm Mo and 107 to > 500 ppm Th, with have high U/Th ratios (4–7) and Zr/Hf ratios (27–36). Chondrite normalized REE signatures (**Figure 2-8a**; McDonough and Sun 1995) are relatively flat and have a negative Eu anomaly.

Sample H-09 of the thorite-sericite stockwork contain Th concentrations greater than the detection limit (> 500 ppm Th), 1.76 wt.% K, consistent with abundant sericite and thorite observed optically, and they also contain 1.88 ppm Ag (**Table A2-2**). The stockwork is depleted in Cs, U (46.3 ppm), Ta, Nb, Pb (94.7 ppm), Sr and Zr (32 ppm) relative to uraninite-mineralized samples. They contain low U/Th values (0.09), but have high Zr/Hf ratios (53.3) due to low Hf (0.6 ppm). Chondrite normalized REE signatures (**Figure 2-8a**; McDonough and Sun 1995) are enriched in La, Ce, Pr and Eu relative to uraninite-mineralized samples. The MREE and HREE form a convex bell, where HREE are depleted (**Figure 2-8a**).

2.4.5. Geochronology

U-Pb Geochronology of Uraninite

In-situ U-Pb isotope analyses were determined by SIMS. Seventy-nine measurements were collected from homogeneous, least altered and fractured uraninite that displayed low Si and Ca contents and high Pb contents in EPMA data (**Table A2-4**, **Table A2-5**). To refine the dataset, overlapping ellipses on Wetherill Concordia diagrams were grouped and averaged (**Table 2-3**).

Five distinct Discordia ages were apparent on Concordia diagrams (**Figure 2-9**). The oldest ages are apparent in two Discordia with upper age intercepts at 2790 ± 22 Ma and 2784 ± 22 Ma, with an MSWD of 0.46 (n = 5) and an MSWD of 0.28 (n = 5), respectively (T0; **Figure 2-9**). Younger ages include (T1 and T2) 2614 ± 11 Ma, with an MSWD of 1.7 (n = 7); (T1 and T2; **Figure 2-9c**) and 2531 ± 17 Ma with an MSWD of 0.86 (n = 5); (**Figure 2-9**). The youngest Discordia age has an upper intercept of 1778 ± 14 Ma with an MSWD of 1.3 (n = 3); (T3; **Figure 2-9e**).

Table 2-3: SIMS analyses of Hope uraninite separated into stages based on ellipse overlap

	$^{207}Pb/^{206}Pb$*	2σ*	$^{207}Pb/^{235}U$*	2σ*	$^{206}Pb/^{238}U$*	2σ*	Upper Intercept Age (Ma)	MSWD	Lower Intercept Age (Ma)
T0									
	0.0775	0.3	1.0184	0.5	0.0920	0.1			
	0.0935	0.3	1.3969	0.5	0.1042	0.1			
	0.0989	0.3	1.6045	0.4	0.1122	0.1	**2790±22**	**0.46**	**490±5.5**
	0.1122	0.3	2.0618	0.4	0.1270	0.1			
	0.1393	0.3	3.6175	0.5	0.1778	0.1			
T0									
	0.1373	0.2	3.9211	0.4	0.1947	0.1			
	0.1259	0.2	3.2743	0.4	0.1739	0.1			
	0.0954	0.3	1.6784	0.5	0.1222	0.1	**2784±22**	**0.28**	**562±6.8**
	0.0927	0.3	1.5539	0.5	0.1171	0.1			
	0.0884	0.3	1.4545	0.5	0.1147	0.1			
T1									
	0.1307	0.2	3.1422	0.5	0.1652	0.1			
	0.1086	0.3	1.8161	0.5	0.1158	0.1			
	0.1235	0.2	2.4974	0.5	0.1405	0.1			
	0.1182	0.2	2.1923	0.5	0.1294	0.1	**2615±10**	**1.7**	**409±5**
	0.1038	0.3	1.5550	0.5	0.1048	0.1			
	0.1162	0.3	2.0168	0.4	0.1207	0.1			
	0.1534	0.1	8.9223	0.5	0.3795	0.1			
T2									
	0.0762	0.4	0.8744	0.5	0.0815	0.1			
	0.0774	0.3	0.9291	0.5	0.0847	0.1			
	0.0945	0.3	1.3769	0.4	0.1014	0.1	**2531±17**	**0.86**	**425±4.8**
	0.1164	0.2	2.4199	0.4	0.1430	0.1			
	0.1239	0.3	2.9173	0.5	0.1612	0.1			
T3									
	0.1033	0.3	2.2522	0.5	0.1512	0.1			
	0.1015	0.3	2.0570	0.5	0.1395	0.1	**1778±14**	**1.3**	**33±15**
	0.1020	0.3	1.2844	0.5	0.0878	0.1			

*****Values grouped and averaged based on overlapping ellipses.
Notes: Grouped full data set found in **Table A2-4, Table A2-5**

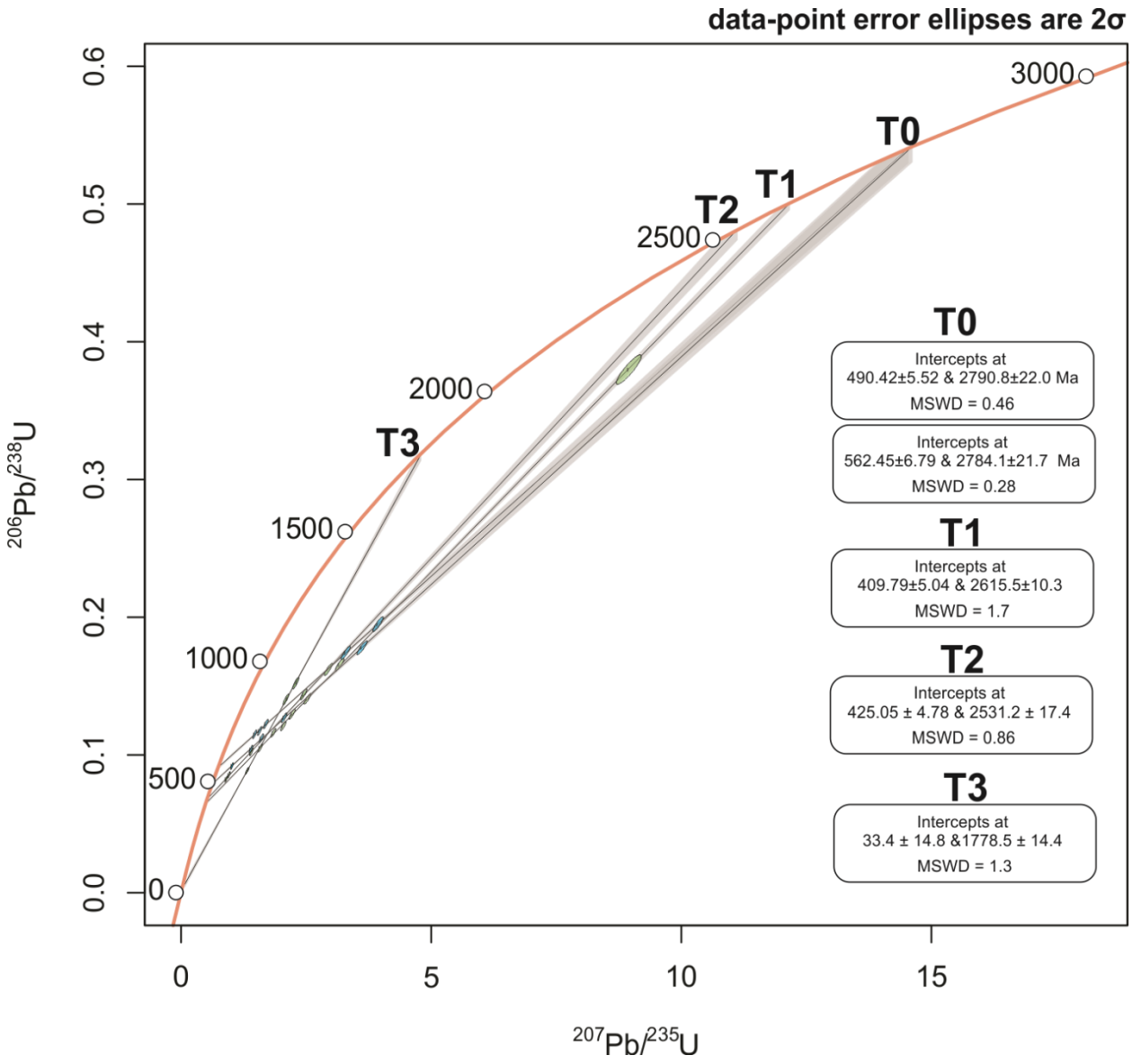

Figure 2-9: Wetherill diagram of $^{206}Pb/^{238}U$ versus $^{207}Pb/^{235}U$ with ages in millions of years (Ma) along Concordia (orange line). Averaged U-Pb results from in situ isotopic analyses of uraninite, with T0 representing primary crystallization ages of uraninite; T1 (blue ellipses), T2 and T3 (green ellipses) representing various alteration and isotopic resetting events throughout the evolution of the Hope occurrence.

$^{40}Ar/^{39}Ar$ Geochronology of Biotite

In situ $^{40}Ar/^{39}Ar$ geochronology of 17 grains of biotite in the shear zones at the Hope yield plateau ages from 1822 ± 5 Ma to 1850 ± 5 Ma, with a weighted mean age of 1834 ± 1 Ma with an MSWD of 2.47 (*n*=17); (**Figure A2-4**). The high MSWD (> 1) represents overdispersion between ages of different grains.

$^{187}Re/^{187}Os$ Geochronology of Molybdenite

Two analyses of molybdenite contain significant common Os, such that the Model Age calculated is dependent on the value of initial $^{187}Os/^{188}Os$. However, the total amount of ^{187}Os (radiogenic and common) for the two analyses can be quantified using a triple spike and regressed versus ^{187}Re to yield a two-point age of 1794 ± 28 Ma (**Table A2-3**, **Figure A2-5**).

2.5. Discussion

Pure uranium oxides are not known in nature, and are always at least partially oxidized and contain additional elements (Finch and Murakami 1999). Thorium can readily replace U^{4+} in uraninite, reflected in the solid solution between thorianite (ThO_2) and uraninite. Considering Th is relatively immobile in aqueous fluids, the Th content of uraninite is a function of origin (i.e., hydrothermal vs. magmatic uraninite; **Figure 2-10**; Alexandre et al. 2015). The ionic radii of Y^{3+} and REE^{3+} are close to that of U^{4+}, allowing them to easily substitute for U^{4+}, and their low susceptibility to redox changes, make the REE+Y signatures of uraninite a powerful tool to distinguish the deposit type (Mercadier et al. 2011). The highest concentrations of REE+Y occur within high temperature intrusive-related deposits, relative to tabular, unconformity-type, vein-type and metasomatic uranium deposits (**Figure 2-12**; Mercadier et al. 2011, Alexandre et al. 2015). The accumulation of radiogenic Pb in uraninite destabilizes the uraninite structure leaving it susceptible to alteration by fluids (Kotzer and Kyser 1993, Alexandre et al. 2005). A variety of

elements substitute for Pb during alteration (e.g., Si, Fe, Ca, P; Finch and Murakami 1999). Because of its chemical diversity, the composition of uraninite may be used as a provenance tool (i.e., **Figure 2-11**; Mercadier et al. 2011, Frimmel et al. 2014, Alexandre et al. 2015) and as an indicator for geochemical environments (Finch and Murakami 1999).

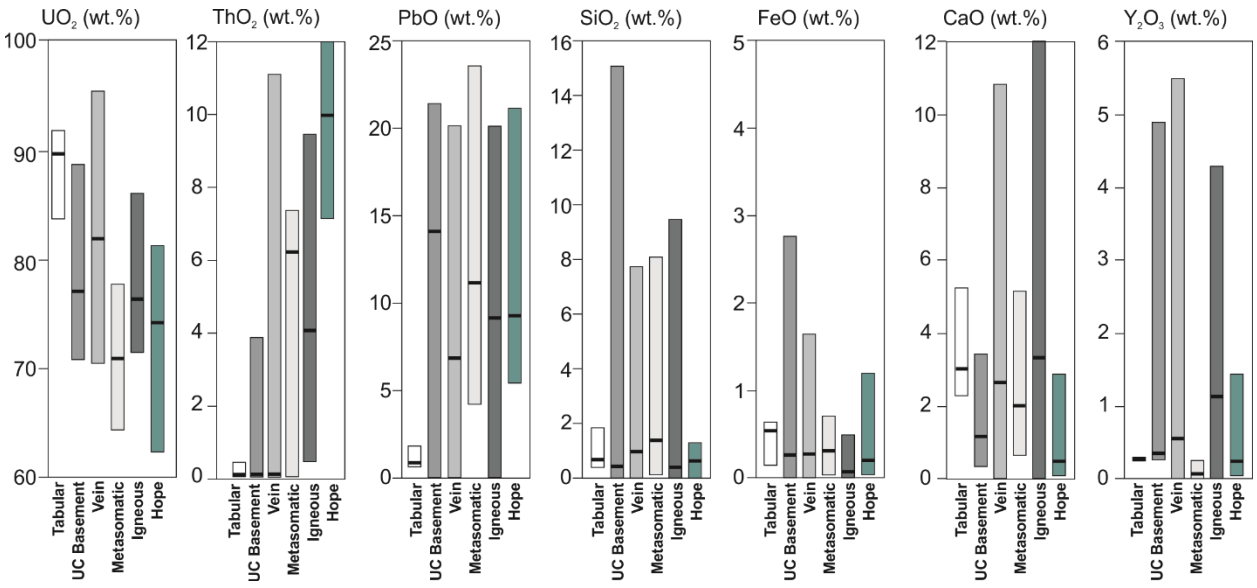

Figure 2-10: Ranges (boxes) and medians (bold lines) for EPMA major element concentrations in uraninite by deposit type, compared to the Hope occurrence (this study). Modified from (Alexandre et al. 2015).

The uraninite at the Hope occurrence contains elevated Th (up to 12.9 wt.% ThO_2; **Table 2-**), Y (up to 2.63 wt.% Y_2O_3), and high ΣREE (up to 3.2 wt.%; **Table 2-1**) concentrations, suggesting a magmatic origin (**Figure 2-11**). In EPMA-WDS elemental maps, Th and REE (represented by Y) occur as primary zonations within uraninite grains (**Figure 2-7**), interpreted to represent the initial substitution into Hope uraninite during its crystallization (**Figure 2-7i**; Alexandre et al. 2015). The Th and REE contents also discriminate the temperature of crystallization, where U/Th > 100 and ΣREE > 1 wt.% are indicative of crystallization temperatures of > 350 °C (**Figure 2-11**; Mercadier et al. 2011, Frimmel et al. 2014), consistent with a magmatic origin for uraninite.

The Hope uraninite shows similarities in mineral chemistry compared to uraninite from high-temperature intrusive (i.e., Moore Lake [Canada], Kola [Russia], Luthi [Finland], and Rössing [Namibia] deposits; Mercadier et al. 2011; and the Dörrmorsbach [Germany] and Ekomedion [Cameroon] deposits; Frimmel et al. 2014; **Figure 2-11**) and hydrothermal deposits (i.e., Mary-Kathleen [Australia]; Frimmel et al. 2014; **Figure 2-11**), globally. These deposits may be further discriminated by their chondrite normalized REE signatures (**Figure 2-8b**), which reflect the origin of uranium mineralization (Mercadier et al. 2011, Frimmel et al. 2014). At high-temperatures (> 350 °C), large amounts of REE are able to be incorporated into uraninite, without fractionation between LREE and HREE ($LREE_N/HREE_N \approx 1$; intrusive and metamorphic deposits; Mercadier et al. 2011). The ΣREE, LREE/HREE ratios and variable Y concentrations (1000–12000 ppm) of Hope uraninite are most similar to uraninite of intrusive deposits (Frimmel et al. 2014; **Figure 2-12**). Although uranium oxides at the Mary Kathleen deposit have similar high ΣREE and U/Th ratios (**Figure 2-11**), they have distinguishably higher LREE/HREE ratios (**Figure 2-8**; **Figure 2-12a**) and Y concentrations (up to 2000 ppm; **Figure 2-12b**) than the Hope occurrence. These inconsistencies rule out the possibility of a hydrothermal-metasomatic origin for the Hope uraninite.

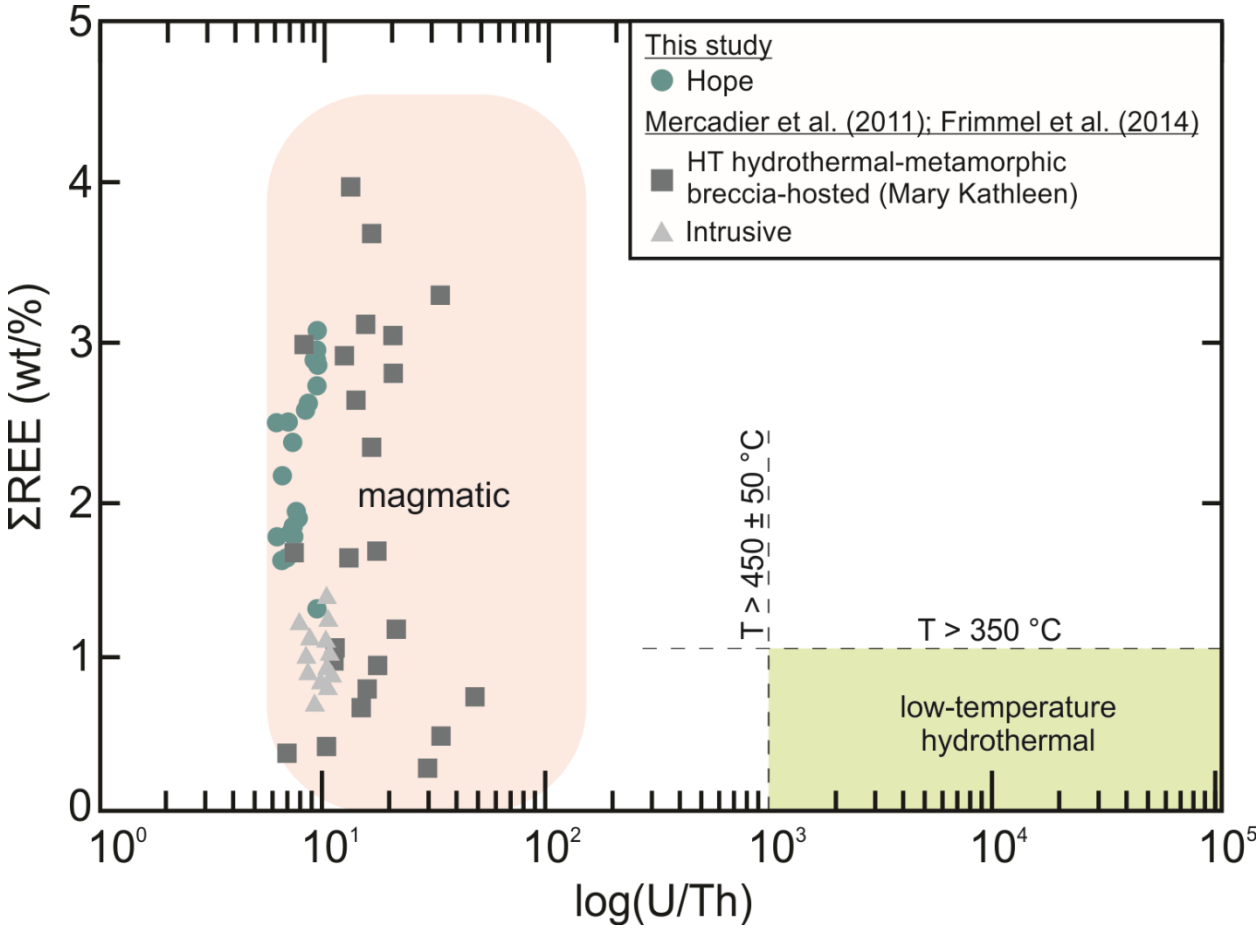

Figure 2-11: Total REE (ΣREE) content (wt.%) versus U/Th of uraninite from Hope analyzed by EPMA, compared to global igneous and hydrothermal deposits with similar signatures from (Mercadier et al. 2011, Frimmel et al. 2014). Figure modified from (Frimmel et al. 2014).

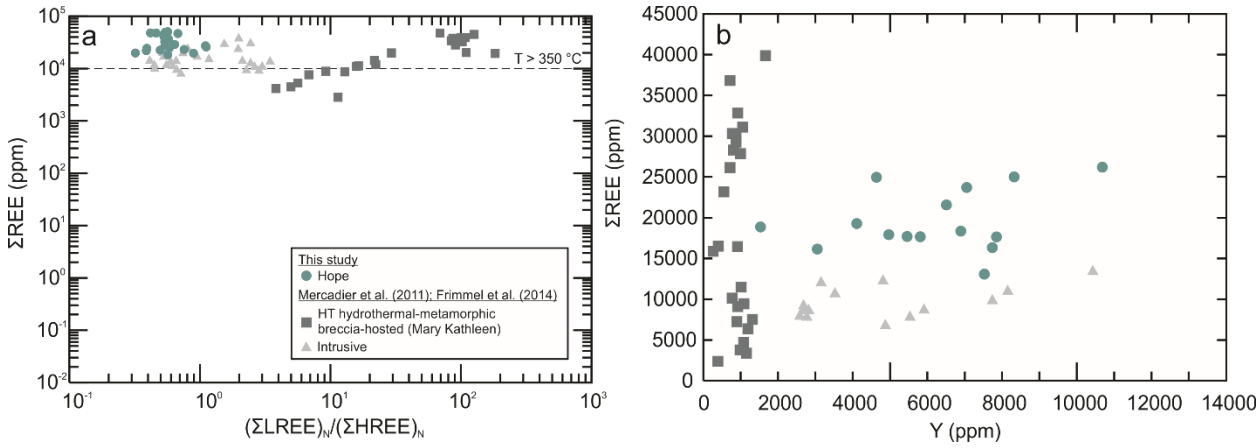

Figure 2-12: Total rare earth element (ΣREE) content (ppm) from the Hope occurrence and global igneous and hydrothermal deposits versus (a) chondrite-normalized (McDonough and Sun 1995) light over heavy rare earth element ratios $(\Sigma LREE)_N/(\Sigma HREE)_N$ with high-temperature (> 350 °C) threshold from Mercadier et al. (2011) and; (b) versus Y (ppm); Modified from Mercadier et al. (2011), and Frimmel et al. (2014).

The oldest uraninite ages determined by in-situ SIMS U-Pb analyses are apparent in two Discordia with upper age intercepts at 2790 ± 22 Ma and 2784 ± 22 Ma (T0; **Figure 2-9**). Due to their overlap, these ages are interpreted to be the same generation of primary uraninite. Considering the assumed magmatic origin for uraninite, and the textural and paragenetic relationships of uraninite with coarse-grained zircon (up to 100 μm) and oligoclase (up to 2 cm); (**Figure 2-5g**), the quartz-biotite-albite breccias at Hope may be reworked/brecciated granitic pegmatites. This is consistent with the formation of the first granitic pegmatites able to crystallize magmatic uraninite in Earth's history between 3.1 and 2.2 Ga (Cuney 2010). However, the timing of uraninite mineralization at ~2.79 Ga is too old in comparison with the depositional age of the host Stewart River biotite-paragneiss based on detrital zircon results (2.52–2.38 Ga; Neil, pers. Comm). The uraninite at Hope are instead interpreted to be detrital in origin with a magmatic provenance. This explains the older age of uraninite from detrital zircons in the host biotite-paragneiss.

Although a similar origin has been interpreted for primary 3.2 Ga detrital, igneous uraninite is hosted within the 3.0 Ga Dominion Reef sediments of the Witwatersrand Basin (Burron et al. 2018). Using detrital uraninite as a proxy provides further support for an oxygen depleted atmosphere prior to the Great Oxidation Event (Bekker et al. 2004), and the formation of the oldest uranium deposits on Earth (Cuney 2010).

Prior to this work, the oldest recorded uranium mineralization in the Rae craton was the 2.29 Ga uraninite at the Fay deposit within the Beaverlodge Uranium District (Dieng et al. 2015). New data from the Hope occurrence in the Nonacho Basin presented in this study records primary magmatic uraninite mineralization ~2780 to 2790 Ma, providing evidence for early uranium

enrichment of the Rae craton, nearly 500 million years earlier than what was previously documented.

There are a few discrepancies with the interpretation of a detrital origin for uraninite and the proposed age of crystallization at Hope that should be acknowledged. Primarily, there are no recorded 2.78 Ga granites or pegmatites nearby that could have been the source for uraninite. However, this area is largely unmapped and understudied, thus there could be undiscovered granite source rocks. Utilizing other geochronometers on mineral phases in equilibrium with uraninite, such as zircon, could help validate or negate, the 2.79 Ga crystallization ages and to further constrain the geological origin for uraninite. Unfortunately, the zircon at Hope are highly metamict and are likely unreliable for U-Pb geochronology. Additionally, these uraninite ages are older than the reported detrital zircon ages of 2.52–2.38 Ga of the host paragneiss (Neil pers. comm). Furthermore, the host paragneiss has undergone amphibolite-facies metamorphism and because of the extremely low stability of uraninite in metamorphic conditions (Janeczek and Ewing 1992, Finch and Murakami 1999), it is improbable that detrital uraninite could survive these conditions. Despite these discrepancies, we suggest an Archean age for uraninite is probable, especially when considering the T1 Discordia age of 2.61 ± 0.01 Ga, which is strengthened with a <10% discordant ellipse (***Figure 2-9***; **Table A2-5**). Further mapping and study of the area, as well as geochronology of detrital zircons in the host rocks, are required to identify possible granite source rocks and to evaluate a detrital origin for uraninite.

The uraninite is highly fractured and records various stages of alteration (**Figure 2-7 b-h**). Uraninite contains variable Pb (5.8–18.2 wt.% PbO), which negatively correlates with UO_2, reflecting the radioactive decay of U to Pb (**Figure 2-7j**). The incompatible nature of radiogenic Pb^{2+} with the crystal structure of uraninite and loss during alteration events is reflected in the

scatter in **Figure 2-7j**. During alteration of Hope uraninite, Ca (up to 3.54 wt.% CaO) substituted for Pb in areas with a high density of fractures, and Pb precipitated along fractures and grain boundaries (**Figure 2-7c, f**). The substitution for these elements is supported by increasing CaO, SiO_2 and FeO, with decreasing PbO (**Figure 2-7k**; **Table 2-**). Some of the Pb released during alteration was incorporated into galena (Janeczek and Ewing 1992), which is a late phase spatially associated with uraninite (**Figure 2-5**) and occurs within local reaction rims alongside K-feldspar and calcite between uraninite and albite and quartz (**Figure 2-7**).

The U-Pb system of uraninite acts as an open system, which leads to the loss or gain of U and/or Pb (Corcoran and Simonetti 2020). The highly discordant ages (**Figure 2-9**) at Hope are attributed to the inherent open system behaviour of uraninite (Kotzer and Kyser 1993, Finch and Murakami 1999, Sharpe and Fayek 2016), and the heterogeneity of mineral grains at micrometer scale (Kotzer and Kyser 1993, Sharpe and Fayek 2016). The upper intercept ages of the Discordia for stages following primary uraninite crystallization, are representative of disturbance or alteration events that led to isotopic resetting of the U-Pb system. These isotopic resetting events may be attributed to several coinciding magmatic and/or hydrothermal events that occurred throughout the Rae.

The first stage of alteration and/or isotopic resetting at 2614 ± 11 Ma (T1; **Figure 2-9**), is coincident with the emplacement of the Snow Island Suite, an event that records extensive plutonism throughout the Rae from 2.61–2.59 Ga (Jefferson et al. 2015a, 2015b, Peterson et al. 2015). The intrusive suite is widespread and extends from the southern Rae (Davis et al. 2015) to Dubwant Lake (Peterson 2006), the central Rae (Kjarsgaard et al. 1997, Pehrsson et al. 2013b, Peterson et al. 2015) and to the Thelon front (Davis et al. 2014; **Figure 2-1**). The second stage of alteration and/or isotopic resetting is recorded at 2531 ± 17 Ma (T2; **Figure 2-9**), coincident with

the emplacement of local 2.50 Ga granitoids in the Hope area (Neil, pers. Comm), and a suite of 2.53–2.52 magmatism along the western Rae (Ashton et al. 2014, Davis et al. 2014, Cloutier et al. 2021), which may be related to an early phase of the 2.5–2.3 Ga Arrowsmith orogeny that affected the western margin of the Rae craton (Berman et al. 2013b).

Widespread 1.83 Ga magmatism is recorded throughout the entirety of the western Churchill Province (McGlynn et al. 1974, Bostock et al. 1991, Bostock and van Breemen 1992, Cousens et al. 2001, Morelli et al. 2009, D'Souza 2012), and the intrusions exposed within the Nonacho Basin are no exception. The emplacement of the Sparrow Dike swarm constrains the minimum age of Nonacho Group deposition to 1827 ± 4 Ma (McGlynn et al. 1974, Bostock and van Breemen 1992), coincident with 1834 ± 1 Ma Ar-Ar ages of biotite associated with uraninite mineralization at Hope determined in this study, and the emplacement of the 1813 ± 5 Ma Thekuthili Stock (Bostock et al. 1991). The textural equilibrium of biotite with much older (~2.79 Ga) uraninite suggests that the 1813 Ma age for biotite represents a resetting age coincident with magmatic activity, rather than a primary crystallization age.

Hydrothermal alteration of the Nonacho Basin is recorded at 1778 ± 14 Ma (T3; **Figure 2-9**), with coeval molybdenite mineralization (1794 ± 28 Ma; Re-Os) and chlorite alteration of earlier biotite. Canam et al., (2021) obtained an $^{40}Ar/^{39}Ar$ date of biotite at 1.78 Ga, reflecting sinistral strike-slip reactivation of the King Shear Zone, a regional north-northeast trending shear zone adjacent to the Hope uranium occurrence, striking ~100 km through the Nonacho Basin (**Figure 2-2**). The 1.78 Ga reactivation of the King Shear Zone is coincident with the extensional collapse of the Trans-Hudson orogeny proposed for the southern Rae craton (Hoffman 1988, Ashton et al. 2009, Pehrsson et al. 2013a) and the initial emplacement of the Nueltin Granite Suite to the northeast (Peterson et al. 2002). We suggest that hydrothermal activity focused along the 1.78 Ga

King Shear Zone (Canam et al., 2021) precipitated molybdenite and is recorded in the latest stage of uraninite alteration and resetting.

During phases of alteration, U^{6+} may be transported by oxidizing hydrothermal fluids up to a few hundred kilometers (Cuney 2014). At the Hope occurrence, the presence of a SO_3-rich thorite-sericite breccia (up to 3.19 wt. % SO_3; **Table 2-2**) is evidence of oxidized fluids that mobilized U from uraninite, leaving residual Th as fine-grained thorite with a low-temperature alteration assemblage (i.e., sericite, K-feldspar, chlorite; **Figure 2-6**), supported by Al-in-chlorite thermometry (Average of 269 °C; **Table A2-6**). In the MacInnis Lake sub-basin, over 50 km southwest of the Hope occurrence (**Figure 2-2**), REE-rich hydrothermal uranium minerals (uranophane ± uraninite) associated with structural conduits in the basement and basinal rocks, contain SO_3 (up to 2.26 wt.%; Landry et al. 2022), and occur with low-temperature mineral assemblages including sericite, Ba-rich K-feldspar, chlorite and sulphides, and locally with oxidized mineral assemblages (e.g., hematite-uranophane-sericite breccias; Landry et al. 2022), similar to the low-temperature, oxidized sericite-thorite breccias at Hope (e.g., sericite, K-feldspar, chlorite, pyrite). We suggest that primary uraninite, as observed at the Hope occurrence, may be sources for hydrothermal uranium mineralization in the MacInnis Lake sub-basin and elsewhere in the Nonacho Basin, recording late crustal reworking of uranium in the Rae craton. Argon-argon dating of the sericite from Hope and MacInnis Lake may be warranted, to determine if these alteration assemblages are temporally related.

2.6. Conclusion

The Hope uranium occurrence is characterized by Th and REE-rich uraninite in highly deformed quartz-biotite-albite breccias, reflecting high-temperature (> 350 °C) magmatic crystallization between 2790 ± 22 Ma and 2784 ± 22 Ma, nearly 300 million years older than the maximum depositional age host paragneiss. The high Th, REE, magmatic origin and age discrepancy suggest a detrital origin for the uraninite. The Hope uraninite is the oldest recorded uranium mineralization in the Rae craton to date, and provides evidence for early uranium enrichment in the Rae, one of Canada's most uraniferous geological provinces.

Geochronological data on uraninite, biotite and molybdenite reveal stages of isotopic resetting and alteration by later fluids, coincident with a suite of magmatic and hydrothermal activity in the Rae craton including: i) 2614 ± 11 Ma corresponding to the emplacement of the Snow Island Suite (Jefferson et al. 2015a, 2015b, Peterson et al. 2015); (ii) 2531 ± 17 Ma corresponding to local granites at Hope (Neil pers. comm) and widespread magmatism throughout the western Rae (Ashton et al. 2014, Davis et al. 2014, Cloutier et al. 2021) and; (iii) 1778 ± 14 Ma recording alteration by hydrothermal fluids, which also precipitated molybdenite (1794 ± 28 Ma; Re–Os), coincident with reactivation of the King Shear Zone (Canam et al. 2021). Widespread magmatic activity throughout the Rae around 1.83 Ga (McGlynn et al. 1974, Bostock et al. 1991, Bostock and van Breemen 1992, Cousens et al. 2001, Morelli et al. 2009, D'Souza 2012), is also coincident with biotite (1834 ± 1 Ma; Ar-Ar) at Hope. Remobilization of U from uraninite by low-temperature oxidizing fluids left residual Th to precipitate thorite in a sericite breccia alongside apatite and pyrite, similar to hydrothermal uranium mineralization at MacInnis Lake (Landry et al. 2022).

Evidence from mineral chemistry and geochronology of uraninite (as well as biotite and molybdenite) at the Hope uranium occurrence suggests a long-lived system of uranium recycling

within the Rae craton, where widespread magmatic and/or hydrothermal events may have transported uranium from primary uraninite mineralization at occurrences such as Hope, throughout the basement and basinal rocks of the Nonacho Basin to form secondary hydrothermal uranium occurrences, such as those at MacInnis Lake.

2.7. References

Abd El-Naby, H.H. 2009. High and low temperature alteration of uranium and thorium minerals, Um Ara granites, south Eastern Desert, Egypt. Ore Geology Reviews, **35**: 436–446. doi:10.1016/j.oregeorev.2009.02.006.

Abrecht, J., and Hewitt, D.A. 1988. Experimental evidence on the substitution of Ti in biotite. American Mineralogist, **73**: 1275–1284.

Adlakha, E.E., and Hattori, K. 2016. Paragenesis and composition of tourmaline types along the P2 fault and McArthur river uranium deposit, Athabasca Basin, Canada. Canadian Mineralogist,. doi:10.3749/canmin.1500057.

Adlakha, E.E., Hattori, K., Davis, W.J., and Boucher, B. 2017. Characterizing fluids associated with the McArthur River U deposit, Canada, based on tourmaline trace element and stable (B, H) isotope compositions. Chemical Geology,. doi:10.1016/j.chemgeo.2017.06.030.

Aitchison, J. 1982. The Statistical Analysis of Compositional Data. Journal of the Royal Statistical Society: Series B (Methodological), **44**: 139–160. doi:10.1111/j.2517-6161.1982.tb01195.x.

Alexandre, P. 2009. Mineralogy and geochemistry of the sodium metasomatism-related uranium occurrence of Aricheng South , Guyana. Mineralium Deposita,. doi:10.1007/s00126-010-0278-7.

Alexandre, P., Kyser, K., and Jiricka, D. 2009. Critical geochemical and mineralogical factors for the formation of unconformity-related uranium deposits:Comparison between barren and mineralized systems in the athabasca basin, Canada. Economic Geology, **104**: 413–435. doi:10.2113/gsecongeo.104.3.413.

Alexandre, P., Kyser, K., Jiricka, D., and Witt, G. 2012a. Formation and evolution of the centennial unconformity-related uranium deposit in the South-Central Athabasca Basin, Canada. Economic Geology, **107**: 385–400. doi:10.2113/econgeo.107.3.385.

Alexandre, P., Kyser, K., Layton-Matthews, D., Joy, B., and Uvarova, Y. 2015. Chemical compositions of natural uraninite. Canadian Mineralogist, **53**: 595–622. doi:10.3749/canmin.1500017.

Alexandre, P., Kyser, K., Polito, P., and Thomas, D. 2005. Alteration mineralogy and stable isotope geochemistry of Paleoproterozoic basement - Hosted unconformity-type uranium deposits in the Athabasca Basin, Canada. Economic Geology, **100**: 1547–1563. doi:10.2113/gsecongeo.100.8.1547.

Alexandre, P., and Kyser, T.K. 2005. Effects of cationic substitutions and alteration in uraninite, and implications for the dating of uranium deposits. Canadian Mineralogist, **43**: 1005–1017. doi:10.2113/gscanmin.43.3.1005.

Alexandre, P., Uvarova, Y., and Kyser, T.K. 2012b. Origin of uranous and uranyl minerals at the centennial deposit, Athabasca Basin, northern Saskatchewan, Canada. Canadian Mineralogist, **50**: 693–704. doi:10.3749/canmin.50.3.693.

Alkis Kontonikas-Charos, Cristiana L. Ciobanu, N.J.C. 2014. Albitization and redistribution of REE and Y in IOCG systems: Insights from Moonta-Wallaroo, Yorke Peninsula, South Australia,. Lithos, **208**–**209**: 178–201. doi:https://doi.org/10.1016/j.lithos.2014.09.001.

Ashton, K.E., Hartlaub, R.P., Heaman, L.M., Morelli, R.M., Card, C.D., Bethune, K., and Hunter, R.C. 2009. Post-Taltson sedimentary and intrusive history of the southern Rae Province along the northern margin of the Athabasca Basin, Western Canadian Shield. Precambrian

Research. doi:10.1016/j.precamres.2009.

Ashton, K.E., Rayner, N.M., Heaman, L.M., Creaser, R.A., and Sm-nd, R.A.N. 2014. New Sm-Nd and U-Pb Ages from the Zemlak and South-Central Beaverlodge Domains : A Case for Amalgamated Taltson Basement Complex and Proto-Rae Cratonic Blocks within the Rae Province of Northwestern Saskatchewan. **2**: 1–26.

Aspler, L.B. 1985, GEOLOGY OF NONACHO BASIN (EARLY PROTEROZOIC) NWT; LAWRENCE B. ASPLER

Aspler, L.B., and Donaldson, J.A. 1985. The Nonacho Basin (Early Proterozoic), Northwest Territories, Canada: sedimentation and deformation in a strike-slip setting. Strike-slip deformation, basin formation, and sedimentation,: 193–209. SEPM, Tulsa; Special Publication 37. doi:10.2110/pec.85.37.0193.

Bekker, A., Holland, H.D., Wang, P.-L., Rumble, D., I., Stein, H.J., Hannah, J.L., Coetzee, L.L., and Beukes, N.J. 2004. Dating the rise of atmospheric oxygen. Nature, **427**: 117–120.

Belevtsev, Y.. 1980. Endogenic uranium deposits of precambrian shields: Environment of deposition. Albitized Uranium Deposits: Six Articles Translated from Russian Literature; Abou-Zied, S., Kerns, G., Eds.; U.S. Department of Energy: Washington, DC, USA, 1980,: 55–80.

Berman, R.G. 2010. Metamorphic map of the western Churchill Province. Geological Survey Canada Open File 5279 (3 sheets, 49 p. report),.

Berman, R.G., Davis, W.J., and Pehrsson, S. 2007. Collisional Snowbird tectonic zone resurrected: Growth of Laurentia during the 1.9 accretionary phase of the Hudsonian orogeny. Geology,

35: 911–914. doi:10.1130/G23771A.1.

Berman, R.G., Davis, W.J., Whalen, J.B., Taylor, B.E., Mcmartin, I., Mccurdy, M.W., Mitchell, R.K., Ma, S., Coyle, M., Roberts, B., and Craven, J.A. 2018. Report of activities for the GEM-2 Chantrey-Thelon activity : Thelon tectonic zone project , Nunavut. Geological Survey of Canada, Open File,: 22.

Berman, R.G., Pehrsson, S., Davis, W.J., Ryan, J.J., Qui, H., and Ashton, K.E. 2013a. The Arrowsmith orogeny: Geochronological and thermobarometric constraints on its extent and tectonic setting in the Rae craton, with implications for pre-Nuna supercontinent reconstruction. Precambrian Research, **232**: 44–69. Elsevier B.V. doi:10.1016/j.precamres.2012.10.015.

Berman, R.G., Pehrsson, S., Davis, W.J., Ryan, J.J., Qui, H., and Ashton, K.E. 2013b. The Arrowsmith orogeny: Geochronological and thermobarometric constraints on its extent and tectonic setting in the Rae craton, with implications for pre-Nuna supercontinent reconstruction. Precambrian Research, **232**: 44–69. Elsevier. doi:10.1016/J.PRECAMRES.2012.10.015.

Berman, R.G., Sanborn-Barrie, M., Stern, R.A., and Carson, C.J. 2005. Tectonometamorphism at ca. 2.35 and 1.85 Ga in the rae domain, western Churchill Province, Nunavut, Canada: Insights from structural, metamorphic and in situ geochronological analysis of the southwestern Committee Bay Belt. Canadian Mineralogist, **43**: 409–442. Mineralogical Association of Canada. doi:10.2113/GSCANMIN.43.1.409.

Berman, R.G., Sandeman, H.A., and Camacho, A. 2010. Diachronous Palaeoproterozoic deformation and metamorphism in the Committee Bay belt, Rae Province, Nunavut: insights

from 40Ar-39Ar cooling ages and thermal modelling. Journal of Metamorphic Geology, **28**: 439–457. doi:10.1111/J.1525-1314.2010.00873.X.

Bostock, H.H., van Breemen, O. 1992. Thetiming ofemplacement,and distribution of the Sparrow diabase dyke swarm, District of Mackenzie, Northwest Territories. In: Radiogenic Age and Isotopic Studies: Report 6, Geological Survey of Canada. *In* Paper 92-2. Geological Survey of Canada.

Bostock, H.H., van Breeman, O., and Loveridge, W.D. 1991. Further geochronology of plutonic rocks in the northern Taltson Magmatic Zone, District Mackenzie, N.W.T. Geological Survey Canada, **90**: 67–78.

Bowles, J.F.W. 1990. Age dating of individual grains of uraninite in rocks from electron microprobe analyses. Chemical Geology, **83**: 47–53.

Bowles, J.F.W. 2015. Age Dating from Electron Microprobe Analyses of U, Th, and Pb: Geological Advantages and Analytical Difficulties. Microscopy and Microanalysis, **21**: 1114–1122. doi:10.1017/S1431927615000446.

Van Breemen, O., Kjarsgaard, B.A., Tella, S., Lemkow, D., Aspler, L. 2013. . U-Pb detrital zircon geochronology of clastic sedimentary rocks of the Paleoproterozoic Nonacho and East Arm basins, Thaidene Nena MERA study area. In: Wright, D.F., Ambrose, E. J., Lemkow, D., Bonham-Carter, G. (Eds.), Mineral and Energy Resource Assessment of the proposed Thaidene Nene National Park Reserve in the area of the east arm of Great Slave Lake, Northwest Territories. Geological Survey of,: 119142. doi:https://doi.org/10.4095/292453.

Van Breemen, O., Bostock, H.., and Loveridge, W.D. 1992. Geochronology of granites along the margin of the northern Taltson magmatic zone and western Rae Province, Northwest

Territories. Geological Survey of Canada Paper, **91**: 17–24.

Burron, I., da Costa, G., Sharpe, R., Fayek, M., Gauert, C., and Hofmann, A. 2018. 3.2 Ga detrital uraninite in the Witwatersrand Basin, South Africa: Evidence of a reducing Archean atmosphere. Geology, **46**: 295–298. doi:10.1130/G39957.1.

Campbell Todd, R. 1956. Report on exploration on the MacInnis Lake property of Canadian Pipelines and Petroleum Limited, Northwest Territories; Scurry-Rainbow Oil Limited, unpublished report,.

Canam, R., Gibson, H. d., Martel, E., and Kellet, D. 2021. The Timing of Deformation and Kinematics of Shear Zones in the Nonacho Lake area. *In* Yellowknife Geoscience Forum: Geoscience and Exploration.

de Caritat, P., Hutcheon, I., and Walshe, J.L. 1993. Chlorite geothermometry: A review. Clays and Clay Minerals, **41**: 219–239. doi:10.1346/CCMN.1993.0410210.

Cathelineau, M. 1988. Cation site occupancy in chlorites and illites as a function of temperature. Clay Minerals, **23**: 471–485. doi:https://doi.org/10.1180/claymin.1988.023.4.13.

Checklin, G.A. 1968. MacInnis Lake project (AFE 2-27); Scurry-Rainbow Oil Limited, unpublished report.

Chen, S., Hattori, K., and Grunsky, E.C. 2016. Multivariate statistical analysis of the REE-mineralization of the Maw Zone, Athabasca Basin, Canada. Journal of Geochemical Exploration, **161**: 98–111. Elsevier B.V. doi:10.1016/j.gexplo.2015.11.009.

Chi, G., Haid, T., Quirt, D., Fayek, M., Blamey, N., and Chu, H. 2016. Petrography, fluid inclusion analysis and geochronology of the End uranium deposit, Kiggavik, Nunavut, Canada [online].

Mineralium Deposita, **52**: 211–232. doi:10.1007/s00126-016-0657-9.

Cinelu, S.; Cuney, M. 2006. Sodic metasomatism and U-Zr mineralization: A model based on the Kurupung batholith (Guyana). Geochimica et Cosmochimica Acta, **70**. doi:doi:10.1016/j.gca.2006.06.120.

Ciobanu, C.L., Wade, B.P., Cook, N.J., Schmidt Mumm, A., and Giles, D. 2013. Uranium-bearing hematite from the Olympic Dam Cu-U-Au deposit, South Australia: A geochemical tracer and reconnaissance Pb-Pb geochronometer. Precambrian Research, **238**: 129–147. Elsevier B.V. doi:10.1016/j.precamres.2013.10.007.

Cloutier, M.A., Bethune, K.M., Ashton, K.E., and Deane, J.M.K. 2021. U-Pb geochronology, geochemistry, and isotopic composition of granitoids across the Nolan-Zemlak domain boundary in the SW Rae craton, Laurentia: Evidence for a late Neoarchean suture reworked during Arrowsmith orogen. Precambrian Research, **362**: 106303. Elsevier B.V. doi:10.1016/j.precamres.2021.106303.

Comas-Cufí, M., and Hió-Henestrosa, T. 2011. CoDaPack 2.0: a stand-alone, multi-platform compositional software. *In* Egozcue JJ, Tolosana-Delgado R, Ortego MI, eds. CoDaWork'11: 4th International Workshop on Compositional Data Analysis. Sant Feliu de Guíxols;

Corcoran, L., and Simonetti, A. 2020. Geochronology of uraninite revisited. Minerals, **10**. doi:10.3390/min10030205.

Corrigan, D., Pehrsson, S., Wodicka, N., and de Kemp, E. 2009. The Palaeoproterozoic Trans-Hudson Orogen: A prototype of modern accretionary processes. Geological Society Special Publication, **327**: 457–479. doi:10.1144/SP327.19.

Corriveau, L., Hamid Mumin, A., and Potter, E.G. 2019. Mineral systems with iron oxide copper-gold (Ag-Bi-Co-U-REE) and affiliated deposits: introduction and overview. *In* Corriveau, L., Potter, E.G. and Mumin, A.H., eds., Mineral systems with iron oxide copper-gold (IOCG) and affiliated deposits: Geological Association of Canada, Special Paper 52. pp. 1–26.

Corriveau, L., Montreuil, J.-F., De Toni, A.F., Potter, E.G., and Percival, J.B. 2022. Mapping mineral systems with IOCG and affiliated deposits: a facies approach. Corriveau, L., Potter, E.G. and Mumin, A.H., eds., Mineral systems with iron oxide copper-gold (IOCG) and affiliated deposits: Geological Association of Canada, Special Paper 52,: 69–111.

Corriveau, L., Montreuil, J.F., and Potter, E.G. 2016. Alteration facies linkages among iron oxide copper-gold, iron oxide-apatite, and affiliated deposits in the great bear magmatic zone, Northwest Territories, Canada. Economic Geology, **111**: 2045–2072. doi:10.2113/econgeo.111.8.2045.

Cousens, B., Chiarenzelli, J., Donaldson, J., Peterson, T., and Lecheminant, A. 2001. Enriched Archean lithospheric mantle beneath western Churchill Province tapped during Paleoproterozoic orogenesis. Geological Society of America, **29**: 827–830.

Cuney, M. 2009. The extreme diversity of uranium deposits. Mineralium Deposita, **44**: 3–9. doi:10.1007/s00126-008-0223-1.

Cuney, M. 2010. Evolution of uranium fractionation processes through time: Driving the secular variation of uranium deposit types. Economic Geology, **105**: 553–569. doi:10.2113/gsecongeo.105.3.553.

Cuney, M. 2014. Felsic magmatism and uranium deposits. Bulletin de la Societe Geologique de France, **185**: 75–92. doi:10.2113/gssgfbull.185.2.75.

D’Souza, R.J. 2012. Geochemistry and source-tracing of the Sparrow Dyke Swarm, the Tsu Lake dykes, the Martin Group Igneous Rocks and the Christopher Island Formation.

Davis, W.J., Berman, R.G., Nadeau, L., and Percival, J.A. 2014. U-Pb zircon geochronology of a transect across the Thelon tectonic zone, Queen Maud region, and adjacent Rae craton, Kitikmeot Region, Nunavut, Canada. doi:doi:10.4095/295177.

Davis, W.J., Pehrsson, S.J., and Percival, J.. 2015. Results of a U-Pb zircon geochronology transect across the southern Rae craton, Northwest Territories, Canada.

Dazé, A., Lee, J.K.W., and Villeneuve, M. 2003. An intercalibration study of the Fish Canyon sanidine and biotite 40Ar/39Ar standards and some comments on the age of the Fish Canyon Tuff. Chemical Geology, **199**: 111–127.

Dieng, S., Kyser, K., and Godin, L. 2013. Tectonic history of the North American shield recorded in uranium deposits in the Beaverlodge area, northern Saskatchewan, Canada. Precambrian Research, **224**: 316–340. Elsevier B.V. doi:10.1016/j.precamres.2012.09.011.

Dieng, S., Kyser, K., and Godin, L. 2015. Genesis of multifarious uranium mineralization in the Beaverlodge area, Northern Saskatchewan, Canada. Economic Geology, **110**: 209–240. doi:10.2113/econgeo.110.1.209.

Doi, K., Yamamoto, I., Arden, J., and Thorne, D. 1971. Geological Report on the Hope Group, Nonacho Lake Area, NWT.

Ehrig, K., McPhie, J., and Kamenetsky, V. 2012. Geology and Mineraligocal Zonation of the Olympic Dam Iron Oxide Cu-U-Au-Ag Deposit, South Australia. Society of Economic Geologists Special Publication,: 237–267. doi:10.5382/sp.17.

Farkas, A. 1984. Mineralogy and host rock alteration of the Lone Gull deposit: Urangesellschaft Internal Report.

Fayek, M., and Kyser, T.K. 1997. Characterization of multiple fluid-flow events and rare-earth-element mobility associated with formation of unconformity-type uranium deposits in the Athabasca Basin, Saskatchewan. Canadian Mineralogist, **35**: 627–658.

Finch, R., and Murakami, T. 1999. Systematics and paragenesis of uranium minerals. Uranium: Mineralogy, Geochemistry, and the Environment,: 91–179. doi:10.1515/9781501509193-008.

Frimmel, H.E., Schedel, S., and Brätz, H. 2014. Uraninite chemistry as forensic tool for provenance analysis. Applied Geochemistry, **48**: 104–121. Elsevier Ltd. doi:10.1016/j.apgeochem.2014.07.013.

Gandhi, S.S., and Prasad, N. 1980. Geology and Uranium Occurrences of the MacInnis Lake Area, District of MacKenzie. Geological Survey of Canada, Paper 80-1B.

Gatzweiler, R., Von Pechmann, E., Loewer, R., Strnad, G., and Fritsche, R. 1987. Albitite-type uranium mineralization in the Nonacho Basin area, Northwest Territories, Canada. Uranium Resources and Geology of North America for the International Atomic Energy Agency (IAEA),: 491–518.

Grechishnicov, N.. 1980. Structural setting of one type of uranium-albitite mineralisation in Precambrian rocks. Albitized Uranium Deposits: Six Articles Translated from Russian Literature; Abou-Zied, S., Kerns, G., Eds.; U.S. Department of Energy: Washington, DC, USA1,.

Hammer, Ø., Harper, D.A.T., and Ryan, P.D. 2001. PAST: Paleontological statistics software package for education and data analysis. Palaeontologia Electronica, **4**: 99. Available from http://palaeo-electronica.org/2001_1/past/issue1_01.htm.

Harrington, E. 1980. Thekuthili Lake Project, Northwest Territories, Assessment Work Report-1979; PNC Exploration (Canada) Limited; unpublished report.

Hartlaub, A.R.P., Heaman, L.M., Chacko, T., Ashton, K.E., The, S., March, N., Hartlaub, R.P., Heaman, L.M., Chacko, T., and Ashton, K.E. 2007. Circa 2 . 3 - Ga Magmatism of the Arrowsmith Orogeny , Uranium City Region , Western Published by : The University of Chicago Press Circa 2 . 3-Ga Magmatism of the Arrowsmith Orogeny , Uranium City Region , Western Churchill Craton , Canada. University of Chicago Press, **115**: 181–195.

Hegge, M.R., and Trigg, C.M. 1967. Results of diamond drilling on claim no. 22, Pyramid group, MacInnis Lake, Northwest Territories; Territorial Uranium Miners Limited; Department of Indian and Northern Affairs document no. N019973.

Henderson, J.F. 1937. NONACHO LAKE AREA , NORTHWEST TERRITORIES. Geol. Surv. of Can., **Paper 37-2**: 22.

Hillacre, S., Ansdell, K., and McEwan, B. 2021. Geology, structural analysis, and paragenesis of the arrow uranium deposit, Western Athabasca Basin, Saskatchewan, Canada: Implications for the development of the patterson lake corridor. Economic Geology, **116**: 285–321. doi:10.5382/ECONGEO.4797.

Hitzman, M.C., Oreskes, N., and Einaudi, M.T. 1992. Geological characteristics and tectonic setting of Properozoic iron oxide (Cu-U-Au-REE) deposits. Precambrian Research, **58**: 241–287.

Hitzman, M.C., and Valenta, R.K. 2005. Uranium in iron oxide-copper gold (IOCG) systems. Economic Geology, **100**: 1657–1661.

Hoffman, P.F. 1988. United plates of America, the birth of a craton: Early Proterozoic assembly and growth of Laurentia. doi:10.1146/annurev.ea.16.050188.002551.

Ielpi, A., Martel, E., Fischer, B., Pehrsson, S.J., Tullio, M., and Neil, B.J.C. 2021. A reappraisal of the Nonacho Basin (Northwest Territories, Canada): Record of post-orogenic collapse and marine flooding in the Palaeoproterozoic of the Rae Craton. Precambrian Research, **358**: 106140. Elsevier. doi:10.1016/J.PRECAMRES.2021.106140.

International Atomic Energy Agency (IAEA). 2009. World distribution of uranium deposits (UDEPO) with uranium deposit classification. IAEA-TECDOC-1629, Division of Nuclear Fuel Cycle,: 58–61. doi:ISBN 978-92-0-1-110509-7 NV - 1629.

Janeczek, J., Ewing, R.C. 1992. Dissolution and alteration of uraninite under reducing conditions. Journal of Nuclear Materials, **190**: 157–173.

Janeczek, Janusz; Ewing, R.C. 1992. Structural formula of uraninite. Journal of Nuclear Materials, **190**: 128–132.

Jefferson, C.W. 2013. Uranium Potential and Levels of Radioactivity in the Proposed National Park Area:

Jefferson, C.W., Pehrsson, S.J., Peterson, T., Tschirhart, V., Anand, A., Wollenberg, P., LeCheminant, A.N., Riegler, T., Bethune, K., Chorlton, L.B., McEwan, B., Tschirhart, P., Scott, J.M.J., Davis, W., McNicoll, V., Riemer, W., Patterson, J., Morris, W.A., and Stieber, C. 2015a. Outcrop and remote predictive geology of the western Marjorie–Tehek supracrustal

belt and Northeast Thelon Basin margin in parts of NTS 66A and 66B, Nunavut.

Jefferson, C.W., Thomas, D.J., Gandhi, S.S., Ramaekers, P., Delaney, G., Brisbin, D., Cutts, C., Quirt, D., Portella, P., and Olson, R.A. 2007. Unconformity associated uranium deposits of the Athabasca Basin, Saskatchewan and Alberta. : 273–305.

Jefferson, C.W., White, J.C., Young, G.M., Patterson, J., Tschirhart, V., Pehrsson, S.J., Calhoun, L., Rainbird, R.H., Peterson, T., Davis, W.J., Tella, S., Chorlton, L.B., Scott, J.M.J., Davis, W.J., Percival, J.A., Morris, W.A., Keating, P., Anand, A., Shelat, Y., and MacIsaac, D. 2015b. Outcrop and remote predictive geology of the Amer Belt and basement beside and beneath the northeast Thelon Basin in parts of NTS 66A, B, C, F, G and H, Nunavut.

Johnstone, D.D., Bethune, K.M., Card, C.D., and Tschirhart, V. 2020. Structural evolution and related implications for uranium mineralization in the patterson lake corridor, southwestern athabasca basin, saskatchewan, canada. Geochemistry: Exploration, Environment, Analysis, **21**. doi:10.1144/geochem2020-030.

Jolliffe, I.T. 1986. Principal Component Analysis. Encyclopedia of Statistics in Behavioral Science,.

Kjarsgaard, B.A., Kerswill, J.A., and Jenner, G.. 1997. Lithostratigraphy and metallogenic implications of komatiite - banded iron formation - felsic volcanic rocks of the Archean Woodburn Lake group, Pipedream lake, central Churchill Province, Northwest Territories.

Koehler, G.J. 1957. Geological Report, MacInnis Property, Island Zone; Mackenzie Mining District, N.W.T.; Consolidated Mining and Smelting Company Limited, unpublished report.

Kotzer, T.G., and Kyser, T.K. 1993. O, U, and Pb isotopic and chemical variations in uraninite:

implications for determining the temporal and fluid history of ancient terrains. American Mineralogist, **78**: 1262–1274.

Kotzer, T.G., and Kyser, T.K. 1995. Petrogenesis of the Proterozoic Athabasca Basin, northern Saskatchewan, Canada, and its relation to the diagenesis, hydrothermal uranium mineralization, and paleohydrology. Chemical Geology, **120**: 45–89.

Kuiper, K.F., Deino, A., Hilgen, F.J., Krijgsman, W., Renne, R., and Wijbrans, J.. 2008. Synchronizing Rock Clocks of Earth History. Science, **320**: 500–504.

Kuronuma, C. 1984. Assessment Report of the Thekuthili Lake Project on Mineral Claims Kule 13, 41, 48, 51, 52, 53, 59, 71, 72, 74, 75, 76, 77, 78, 79, 80, 81, 82.

Kyser, T.K., Kotzer, T., and Sibbald, T.I.I. (n.d.). Oxygen, U-Pb and Pb-Pb Isotope Systematics in Uraninite from Complex U-Au-PGE Vein-Type and Unconformity-type Uranium Deposits in Northern Saskatchewan.

Landry, K., Adlakha, E.E., Hanley, J.J., Roy-Garand, A., Terekhova, A., Martel, E., and Falck, H. 2022. Metasomatic uranium mineralization in the MacInnis Lake Area, Nonacho Basin, Northwest Territories: Potential linkages to IOCG and affiliated deposits.

LeCheminant, A.N., and Heaman, L.M. 1989. Mackenzie igneous events, Canada: Middle Proterozoic hotspot magmatism associated with ocean opening. Earth and Planetary Science Letters, **96**: 38–48. doi:10.1016/0012-821X(89)90122-2.

LeCheminant, A.N., Tella, S., Sanborn-Barrie, M., and Venance, K.. 1997. Geology, Parker Lake South, District of Keewatin, North- west Territories. Geological Survey of Canada, Open File Map 3405, scale 1:50,000.

MacDonald, B.. 1956. Report on exploration on the MacInnis Lake property of Canadian Pipelines and Petroleum Limited, Northwest Territories; Scurry-Rainbow Oil Limited, unpublished report,.

MacLeod, W.A., and Brander, J.M. 1975. Assessment report: Mining claims BM 1-36, claim map no. 75E-8 (Lat. 61°20'; Long. 110°10') August 1, 1974-October 1, 1974; Shell Canada Limited, Department of Indian and Northern Affairs document no. N 080170.

Makela, K. 1970. MacInnis Lake property evaluation; Scurry-Rainbow Oil Limited, unpublished report.

Maurice, Y.T. 1984. Gold, tin, uranium and other elements in the Proterozoic Nonacho sediments and adjacent basement rocks near MacInnis Lake, District of MacKenzie. Geological Survey of Canada, Part A, Paper 84-1A.

McDonough, W.F., and Sun, S.S. 1995. The composition of the Earth. Chemical Geology, **120**: 223–253.

Mcglynn, J.C., Irving, E., and Park, J.K. 1974. Paleomagnetism and Age of Nonacho Group Sandstone and Associated Sparrow Dikes , District of Mackenzie. Canadian Journal of Earth Sciences, **11**: 30–42.

McVittie G.A. 1956. Report on Packsack Drilling: Bragon Zone; Consolidated Mining and Smelting Company of Canada Limited, unpublished report.

Meagher J.T. 1955. Report on the BAG claim group, MacInnis Lake, Northwest Territories, Iso Uranium Mined Limited, Department of Indian and Northern Affairs document no. N017070.

Mellion J.J. 1965. Report on the Nonacho project, Summer 1965; International Mine Services

Limited, unpublished report,.

Mercadier, J., Cuney, M., Lach, P., Boiron, M.C., Bonhoure, J., Richard, A., Leisen, M., and Kister, P. 2011. Origin of uranium deposits revealed by their rare earth element signature. Terra Nova, **23**: 264–269. doi:10.1111/j.1365-3121.2011.01008.x.

Moffat, G.W. 1974. An investigation of the radioactive mineral occurrences of the Great Slake Lake-Athabasca Lake region of the District of Mackenzie in the Northwest Territories; unpublished B.Sc. thesis, University of Toronto.

Montreuil, J.F., Corriveau, L., and Potter, E.G. 2015a. Formation of albitite-hosted uranium within IOCG systems: the Southern Breccia, Great Bear magmatic zone, Northwest Territories, Canada. Mineralium Deposita, **50**: 293–325. doi:10.1007/s00126-014-0530-7.

Montreuil, J.F., Corriveau, L., and Potter, E.G. 2015b. Formation of albitite-hosted uranium within IOCG systems: the Southern Breccia, Great Bear magmatic zone, Northwest Territories, Canada. Mineralium Deposita, **50**: 293–325. doi:10.1007/s00126-014-0530-7.

Montreuil, J.F., Potter, E.G., Corriveau, L., and Davis, W.J. 2016. Element mobility patterns in magnetite-group IOCG systems: The Fab IOCG system, Northwest Territories, Canada. Ore Geology Reviews, **72**: 562–584. Elsevier B.V. doi:10.1016/j.oregeorev.2015.08.010.

Morelli, R.M., Hartlaub, R.P., Ashton, K.E., and Ansdell, K. 2009. Evidence for enrichment of subcontinental lithosperic mantle from Paleoproterozoic intracratonic magmas: Geochemistry and U-Pb grochronology of Martin Group igneous rocks, western Rae Craton, Canada. Precambrian Research. doi:10.1016/j.precamres.2009.04.005.

Neil, B.J.C., Gibson, H.D., Pehrsson, S.J., Martel, E., Thiessen, E.J., and Crowley, J.L. 2021.

Provenance, stratigraphic and precise depositional age constraints for an outlier of the 1.9 to 1.8 Ga Nonacho Group, Rae craton, Northwest Territories, Canada. Precambrian Research, **352**: 105999. Elsevier B.V. doi:10.1016/j.precamres.2020.105999.

Ng, R., Alexandre, P., Kyser, K., Cloutier, J., Abdu, Y.A., and Hawthorne, F.C. 2013. Oxidation state of iron in alteration minerals associated with sandstone-hosted unconformity-related uranium deposits and apparently barren alteration systems in the Athabasca Basin, Canada: Implications for exploration. Journal of Geochemical Exploration, **130**: 22–43. Elsevier B.V. doi:10.1016/j.gexplo.2013.02.009.

NORMIN. 2019. NORMIN showings [online]. Northwest Territories Geological Survey, Yellowknife. Accessed at http://www.ntgomap.nwtgeoscience.ca.

Ono, S., and Fayek, M. 2011. Decoupling of O and Pb isotope systems of uraninite in the early Proterozoic Conglomerates in the Elliot Lake district. Chemical Geology, **288**: 1–13. doi:https://doi.org/10.1016/j.chemgeo.2010.03.015.

Ootes, L., Goff, S., Jackson, V.A., Gleeson, S.A., Creaser, R.A., Samson, I.M., Evensen, N., Corriveau, L., and Mumin, A.H. 2010. Timing and thermochemical constraints on multi-element mineralisation at the Nori/RA Cu-Mo-U prospect, Great Bear magmatic zone, Northwest Territories, Canada. Mineralium Deposita, **45**: 549–566. doi:10.1007/s00126-010-0291-x.

Pagel, M., Poty, B., and Sheppard, S.M.F. 1980. Contributions to some Saskatchewan uranium deposits mainly from fluid inclusions and isotopic data. Uranium in Pine Creek Geosyncline (S. Ferguson and A. Gobely, editors). IAEA, Vienna.,: 639–654.

Pehrsson, S.J., Berman, R.G., and Davis, W.J. 2013a. Paleoproterozoic orogenesis during Nuna

aggregation: A case study of reworking of the Rae craton, Woodburn Lake, Nunavut. Precambrian Research, **232**: 167–188. Elsevier. doi:10.1016/J.PRECAMRES.2013.02.010.

Pehrsson, S.J., Berman, R.G., Eglington, B., and Rainbird, R. 2013b. Two Neoarchean supercontinents revisited: The case for a Rae family of cratons. Precambrian Research, **232**: 27–43. Elsevier B.V. doi:10.1016/j.precamres.2013.02.005.

Peterson, T.D. 2006. Geology of the Dubawnt Lake area, Nunavut-Northwest Territories.

Peterson, T.D., Van Breemen, O., Sandeman, H., and Cousens, B. 2002. Proterozoic (1.85-1.75 Ga) igneous suites of the Western Churchill Province: Granitoid and ultrapotassic magmatism in a reworked Archean hinterland. Precambrian Research, **119**: 73–100. doi:10.1016/S0301-9268(02)00118-3.

Peterson, T.D., Jefferson, C.W., and Anand, A. 2015. Geological setting and geochemistry of the ca. 2.6 Ga Snow Island Suite in the central Rae Domain of the Western Churchill Province, Nunavut - Report: Geological Survey of Canada Open File 7841. Geological Survey of Canada Open File 7841,: 29. doi:10.4095/296599.

Potter, E.G., Acosta-Góngora, P., Corriveau, L., Montreuil, J.-F., and Yang, Z. 2022. Uranium enrichment processes in metasomatic iron oxide and alkali-calcic systems as revealed by uraninite trace element chemistry. Corriveau, L., Potter, E.G. and Mumin, A.H., eds., Mineral systems with iron oxide copper-gold (IOCG) and affiliated deposits: Geological Association of Canada, Special Paper 52,: 325–345.

Potter, E.G. 2021. GEOLOGICAL SURVEY OF CANADA OPEN FILE 7873 Geochemistry of uranium- bearing veins from the Uranium City-Beaverlodge district , northern OPEN FILE 7873 Geochemistry of uranium-bearing veins from the Uranium City-Beaverlodge district ,

northern Saskatchewan. doi:10.4095/328980.

Potter, E.G., Corriveau, L., and Kjarsgaard, B.A. 2019a. Paleoproterozoic Iron Oxide Apatite (IOA) and Iron Oxide-Copper-Gold (IOCG) mineralization in the East Arm Basin, Northwest Territories, Canada. Canadian Journal of Earth Sciences,: 1–17. doi:10.1139/cjes-2018-0171.

Potter, E.G., Corriveau, L., Montreuil, J., Yang, Z., Potter, E.G., Corriveau, L., and Montreuil, J. 2021. Uranium enrichment processes in metasomatic iron oxide and alkali-calcic systems as revealed by uraninite trace element chemistry — supplementary data. Geological Survey of Canada, Open File,.

Potter, E.G., Montreuil, J. -F., Corriveau, L., and Davis, W.J. 2019b. The Southern Breccia Metasomatic Uranium System of the Great Bear Magmatic Zone, Canada. : 109–130. doi:10.1002/9781119290544.ch5.

Putnis, A., Hinrichs, R., Putnis, C. V., Golla-Schindler, U., and Collins, L.G. 2007. Hematite in porous red-clouded feldspars: Evidence of large-scale crustal fluid-rock interaction. Lithos, **95**: 10–18. doi:10.1016/j.lithos.2006.07.004.

Quirt, D. 2012. Clay alteration mineralogy comparisons between the Athabasca and Thelon Basins – basement alteration. **2012**.

Read, D., Black, S., Buckby, T., Hellmuth, K.H., Marcos, N., and Siitari-Kauppi, M. 2008. Secondary uranium mineralization in southern Finland and its relationship to recent glacial events. Global and Planetary Change, **60**: 235–249. doi:10.1016/j.gloplacha.2007.02.006.

Reid, J.D. 1955. MacInnis Lake: Report on area for exploration; Scurry-Rainbow Oil Limited, unpublished report.

Reid, K.D., and Ansdell, K. 2012. Elemental changes in variably altered granitoid rocks in the vicinity of the Centennial unconformity-related uranium deposit, northern Saskatchewan, and implications for uranium mineralization. GAC-MAC,.

Richard, A., Rozsypal, C., Mercadier, J., Banks, D.A., Cuney, M., Boiron, M.C., and Cathelineau, M. 2012. Giant uranium deposits formed from exceptionally uranium-rich acidic brines. Nature Geoscience, **5**: 142–146. Nature Publishing Group. doi:10.1038/ngeo1338.

Riegler, T. 2013. , Système d'altération et minéralisation en uranium le long du faisceau structural Kiggavik-Andrew Lake (Nunavut, Canada): Modèle génétique et guides d'éxploration: Ph.D. thesis, Poitiers, France, Université de Poitiers.

Selby, D., and Creaser, R.A. 2004. Macroscale NTIMS and microscale LA-MC-ICP-MS Re-Os isotopic analysis of molybdenite: Testing spatial restrictions for reliable Re-Os age determinations, and implications for the decoupling of Re and Os within molybdenite. Geochimica et Cosmochimica Acta, **68**: 3897–3908.

Shabaga, B.M., Fayek, M., Quirt, D., Jefferson, C.W., and Camacho, A. 2017. Mineralogy, geochronology, and genesis of the Andrew lake ranium deposit, Thelon basin, Nunavut, Canada. Canadian Journal of Earth Sciences, **54**: 850–868. doi:10.1139/cjes-2017-0024.

Shabaga, B.M., Fayek, M., Quirt, D., Jefferson, C.W., and Ledru, P. 2021. Geochemistry and geochronology of the Kiggavik uranium deposit, Nunavut, Canada. Mineralium Deposita, **56**: 1245–1262. Mineralium Deposita. doi:10.1007/s00126-020-01001-8.

Sharpe, R., and Fayek, M. 2016. Mass bias corrections for U-Pb isotopic analysis by secondary ion mass spectrometry: Implications for U-Pb dating of uraninite. Rapid Communications in Mass Spectrometry,: 1601–1611. doi:10.1002/rcm.7595.

Sharpe, R., Fayek, M., Quirt, D., and Jefferson, C.W. 2015. Geochronology and genesis of the bong uranium deposit, Thelon Basin, Nunavut, Canada. Economic Geology, **110**: 1759–1777. doi:10.2113/econgeo.110.7.1759.

Spencer, R.. 1955. MacInnis Group: Engineering Report No. 1 (Mine Series No. 5831) Consolidated Mining and Smelting Company of Canada limited, unpublished report.

Stephen, H.C. 1956. Geological report on the WALT claim group, MacInnis Lake, Taltson Lake map area, District of Mackenzie, Northwest Territories; Newkirk Mining Corporation Limited; Department of Indian and Northern Affairs, document no. N017080,.

Stohl, F. V., and Smith, D.K. 1981. The crystal chemistry of the uranyl silicate minerals. American Mineralogist, **66**: 610–625.

Sun, S.S., and McDonough, W.F. 1989. Chemical and isotopic systematics of oceanic basalts: Implications for mantle composition and processes. Geological Society Special Publication, **42**: 313–345. doi:10.1144/GSL.SP.1989.042.01.19.

Tschirhart, V., Jefferson, C.W., and Morris, W.A. 2017. Basement geology beneath the northeast Thelon Basin, Nunavut: insights from integrating new gravity, magnetic and geological data. Geophysical Prospecting,. doi:10.1111/1365-2478.12430.

Viswanathan, K., and Harnet, O. 1986. Refined crystal structure of beta-uranophane, Ca(UO2)2(SiO3OH)2•5H2O. American Mineralogist, **71**: 1489–1493.

Wiewióra, A. and Weiss, Z. 1990. Crystallochemical classifications of phyllosilicates based on the unified system of projection of chemical composition: III. The serpentine-kaolin group. Clay Minerals, **25**: 93–98. doi:10.1180/claymin.1990.025.1.10.

Wilde, A. 2013. Towards a model for albitite-type uranium. Minerals, **3**: 36–48. doi:10.3390/min3010036.

Yeo, G.M., and Potter, E.G. 2010. Review of Reducing Mechanisms Potentially Involved in the Formation of Unconformity-type Uranium Deposits and their Relevance to Exploration. Saskatchewan Geological Survey, **2**: 13.

Chapter 3: Metasomatic uranium mineralization in the MacInnis Lake Area, Nonacho Basin, Northwest Territories: Potential linkages to IOCG and affiliated deposits

Kerstin Landry[a,*], Erin Adlakha[a], Andree Roy-Garand[a], Anna Terekhova[a], Jacob Hanley[a], Hendrik Falck[b], Edith Martel[c]

[a]*Department of Geology, Saint Mary's University, 923 Robie St., Halifax, Nova Scotia, B3H 3C3*
[b]*Department of Industry, Tourism and Investment, Government of the Northwest Territories, 5102 50th Avenue, Yellowknife, Northwest Territories, X1A 2L9*
[c]*Northwest Territories Geological Survey, 4601-B 52 Avenue, Yellowknife, Northwest Territories, X1A 1K3*

Keywords:
Nonacho Basin
Rae craton
Paleoproterozoic
Uranium
Albite
IOCG

*Corresponding author
E-mail address: Kerstin.Landry@smu.ca

Abstract

The intracratonic Paleoproterozoic Nonacho Basin, deposited on the western margin of the Rae craton, contains historic polymetallic (i.e., U, Cu, Fe, Pb, Zn, Ag) occurrences near its unconformable contact with crystalline basement rocks. Exploration began in the 1950s following detection of anomalous radioactivity, leading to preliminary investigations of numerous uranium occurrences. This study presents the paragenesis and trace-element chemistry of uranium minerals at the occurrences in the MacInnis Lake sub-basin of the Nonacho Basin, to evaluate the style and relative timing of uranium mineralization. The microscopic and compositionally heterogeneous Ba-rich uranium minerals (uraninite and uranophane) occur in quartz-chlorite ± calcite veins and sericitized chlorite ± quartz breccia and stockwork where they are spatially associated with hematite, rutile, and sulphides, namely pyrite, bornite and chalcopyrite. Uranium-bearing veins post-date pervasive albitization and locally Ba-rich K-feldspar alteration of host rocks. Uranium mineralization has two main mineral associations: (1) as overgrowths on earlier, partially dissolved

bornite and chalcopyrite; and (2) intergrown with hematite, rutile and sericite. Rare-earth element (+Y) concentrations of the uranium minerals are high, up to 9.5 wt.% ΣREE+Y and have $LREE_N/HREE_N$ values > 1, which are similar to REE signatures of uraninite in low-temperature, hematite-type IOCG-deposits (e.g., Olympic Dam, Gawler Craton, Australia) and albitite hosted uranium deposits (e.g., Southern Breccia, Great Bear Magmatic Zone, Canada). Extensive albitization and localized potassic-iron alteration associated with remobilized vein- and stockwork-hosted uranium also resembles albitite-hosted uranium (+hematite+chlorite+K-feldspar) of the Southern Breccia. MacInnis Lake uranium occurrences have been remobilized from earlier uranium occurrences in the Nonacho Basin by hydrothermal fluids along regional-scale faults. We suggest uranium minerals precipitated on earlier sulfides and silicates, which acted as a redox trap for mineralization, in low-temperature (313-333 °C) quartz-chlorite ± calcite veins and hematite-sericite ± quartz breccias and stockwork zones late in a complex metasomatic iron and alkali calcic alteration system.

3.1. Introduction

The Nonacho Basin, a fault-bound Paleoproterozoic siliciclastic basin in southeastern Northwest Territories (**Figure 3-1**), is the host of over 60 uranium occurrences, as well as a variety of polymetallic and critical metal (Cu, Pb, Zn, Ni, Au, Th, Pt, Ta and Sn) occurrences, which have been the subject of mineral exploration since the 1950s (Meagher J.T. 1955, Reid 1955, Spencer 1955, Campbell Todd 1956, McVittie G.A. 1956, Stephen 1956, MacDonald 1956, Koehler 1957, Mellion J.J. 1965, Hegge and Trigg 1967, Checklin 1968, Makela 1970, Moffat 1974, MacLeod and Brander 1975, Gandhi and Prasad 1980, Harrington 1980, Kuronuma 1984). Despite over 70 years of exploration, the ore and alteration mineralogy, mineral chemistry and conditions that allowed for the precipitation of uranium mineralization are poorly understood and yet to be

property identified under the International Atomic Energy Agency (IAEA); (2009) classification (e.g., unconformity-related deposits, sandstone deposits, hematite breccia complex deposits, metasomatic deposits, vein-type deposits, etc.).

Several uranium occurrences have been described in the MacInnis Lake area, a roughly 200 km^2 northeast-trending sub-basin, in the larger Nonacho Basin. Gandhi and Prasad (1980) and Kuronuma (1984) describe the uranium mineralization in the MacInnis Lake area as predominantly pitchblende, commonly associated with yellow, secondary uranium minerals (e.g., uranophane) that occur in stockwork-like veins, as sporadic mineralization along fractures and disseminated within basement rocks, overlying Nonacho sediments and gabbroic intrusions. Uranium minerals display structural and chemical diversity, governed by the chemical conditions under which the minerals formed (Finch and Murakami 1999). The mineralogy, oxidation conditions, susceptibility to alteration by later fluids (Kotzer and Kyser 1993, Alexandre and Kyser 2005), and their ability to incorporate a variety of elements during alteration (i.e., Pb, Th, Si, Fe, Ca, P, REE; Finch and Murakami 1999) are all factors that result in the precipitation of uranium minerals and/or influence their composition. These factors allow the utilization of uranium minerals as indicators for geochemical environments (Finch and Murakami 1999).

The purpose of this study is to describe and characterize the uranium mineralization of the MacInnis Lake sub-basin that hosts twenty-one noted uranium occurrences. Six occurrences, hosted in basement or sedimentary rocks of the Nonacho Basin —Kult-82, Island, Pyramid, Cole, Welch and Dussault—were selected for petrographic (i.e., scanning electron microscope and electron microprobe) and whole-rock geochemical (i.e., ICP-MS and ICP-OES) analyses in effort to determine the paragenetic relationship and the origin for hydrothermal uranium occurrences in

the MacInnis Lake area, which may be an analogue for other uranium occurrences in the Nonacho Basin and Paleoproterozoic basins with similar metallogeny.

3.2. Geological Setting

3.2.1. Regional Geology

The Nonacho Basin overlies the Rae craton of the western Churchill Province. The western Churchill Province is composed of two Meso-Neoarchean cratons; the Rae and the Hearne. The Rae craton is a crustal block, which extends > 1000 km from northern Canada into Greenland (Pehrsson et al. 2013b). The Rae is bounded by 2.0 to 1.9 Ga orogenic and tectonic belts (**Figure 3-1**) that formed during the amalgamation of Laurentia, the ancestral North American core (Hoffman 1988), and supercontinent, Nuna (Pehrsson et al. 2013b). The 2.0–1.9 Ga Taltson and Thelon suture zones border the Rae to the west (**Figure 3-1**) and formed during the collision of the Slave craton and Buffalo Head terrane with the Rae craton (Hoffman 1988; Berman et al. 2018). This collision caused lateral escape at 1.93 to 1.94 Ga and sinistral strike-slip faulting that bounds the Nonacho Basin (Aspler and Donaldson 1985, Ashton et al. 2009, Van Breemen et al. 2013).

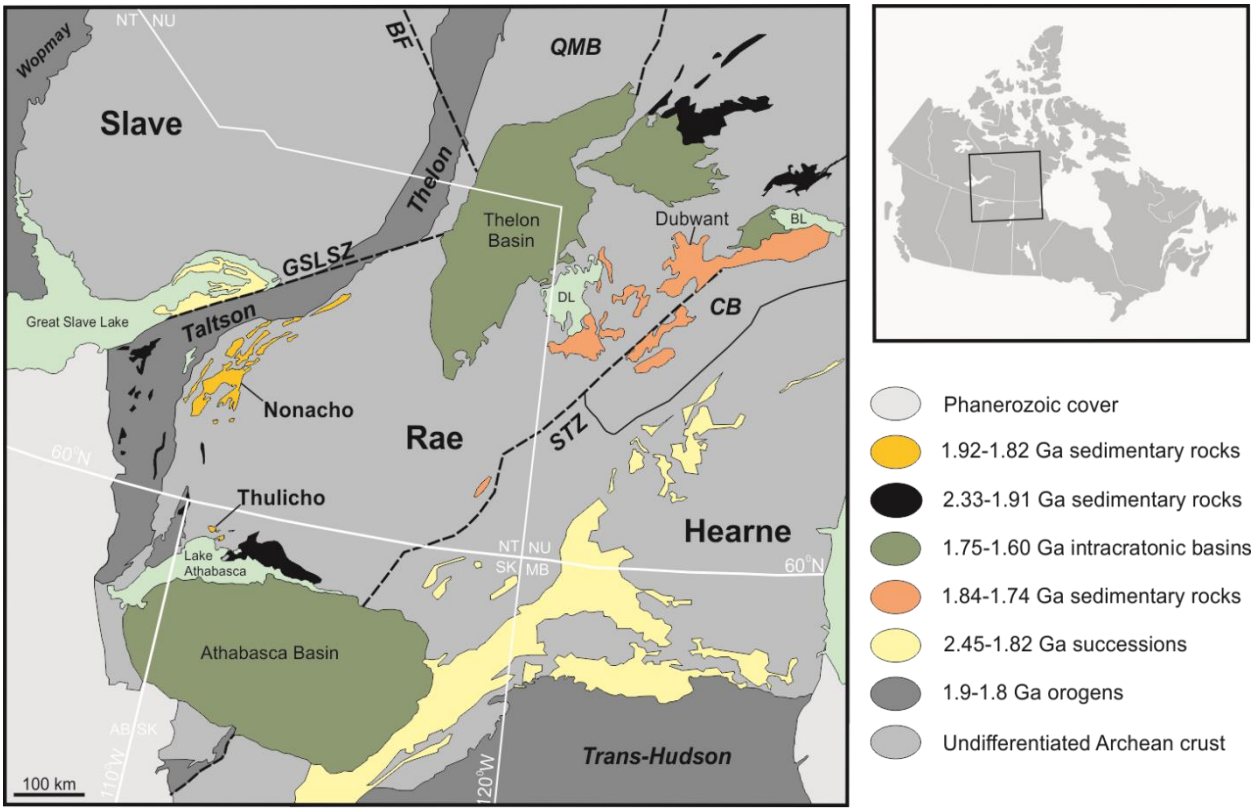

Figure 3-1: Generalized regional map showing the location of the Nonacho Basin relative to major lithotectonic domains. Abbreviations: BF–Bathurst Fault; BL–Baker Lake; CB–Chesterfield Block; DL–Dubwant Lake; GSLSZ–Great Slave Lake Shear Zone; STZ–Snowbird Tectonic Zone; QMB; Queen Maud block. Canadian Provinces and Territories: AB–Alberta; MB–Manitoba; NT–Northwest Territories; NU–Nunavut; SK–Saskatchewan. Dashed lines mark major structures and faults. Figure modified after Ashton et al., (2013) and Neil et al. (2021).

3.2.2. Local Geology

The Nonacho Basin is a northeast-striking Paleoproterozoic basin, measuring 200 × 60 km in size (Ielpi et al. 2021), that lies southeast of Great Slave Lake (**Figure 3-1**). The Nonacho Basin formed in response to a sinistral strike-slip faulting regime, which also formed several rhomb, wedge, and rectangular sub-basins (e.g., MacInnis; Salkeld; Sparks; Taltson; Naskethey; **Figure 3-2a** Aspler 1985, Aspler and Donaldson 1985). The Archean basement rocks consist of variably metamorphosed gneisses, granitoids, metasedimentary and metavolcanics rocks (Aspler, 1985;

Aspler and Donaldson 1985), unconformably overlain by the Nonacho Group sedimentary sequence.

The Nonacho Group is a sedimentary siliciclastic succession deposited between 1.91 and 1.83 Ga (Aspler, 1985; Aspler and Donaldson 1985). Reconnaissance mapping of the Nonacho Basin dates back to Henderson (1937), while a comprehensive effort to reconstruct the stratigraphy and structural evolution of the basin was performed by Aspler (1985) and reappraised by Ielpi et al. (2021). The stratigraphic sequence is divided into six formations and three fining or coarsening upward sequences, which are subdivided into two groups based on differences in their clast compositions: the lower and upper Nonacho Groups (**Figure A3-1**; Aspler 1985). The lower Nonacho Group consists of the Hjalmar (conglomerate, sandstone), Tronka Chua (sandstone), Chief Nataway (sandstone, shale) and Newshethdezza (sandstone) formations (Aspler 1985, Ielpi et al. 2021), and lithic clasts are dominantly sourced from the local Archean basement rocks (granitoid, orthogneiss and amphibolite; Aspler 1985). The upper Nonacho Group consists of the Thekulthili (conglomerate, sandstone) and Taltson (sandstone, shale) formations, which locally and unconformably overly both the Tronka Chua formation and the crystalline basement (Aspler and Donaldson 1985), and contains a more diverse clast assemblage, including intrabasinal sandstones and conglomerates, vein quartz, granitoid rocks, quartz arenite and felsic-mafic volcanic rocks (Aspler 1985, Ielpi et al. 2021). Aspler (1985) interpreted the Nonacho Group formations to record scree-slope, alluvial fan, fluvial, and lacustrine depositional environments of a foreland molasse, which formed during the Trans-Hudson Orogeny. However, reappraisal by Ielpi et al. (2021) suggests alluvial (fluvial dominated), shoal-water deltaic, nearshore marine and deep-water-marine depositional settings. Along with a variety of sedimentological indicators (e.g.,

wave- and bimodal-ripple hummocky cross, and flaser stratifications) documented by Ielpi et al. (2021), rules out an entirely terrestrial origin for Nonacho Group sedimentation.

Detrital zircon geochronology by Neil et al. (2021) and Van Breemen et al. (2013) indicate an apparent change in provenance from the lower to upper Nonacho Group, where there is an increase in detritus up-stratigraphy derived from the 2.0 to 1.9 Ga Taltson-Thelon orogenies. This constrains the minimum depositional of the upper Nonacho Group to 1907 ± 15 Ma (Ielpi et al. 2021). The Sparrow Dike Swarm cross-cuts the Nonacho Group sediments, except for the lowermost Hjalmar Formation, thus constraining the maximum age of deposition to 1827 ± 4 Ma (Bostock and van Breemen 1992)

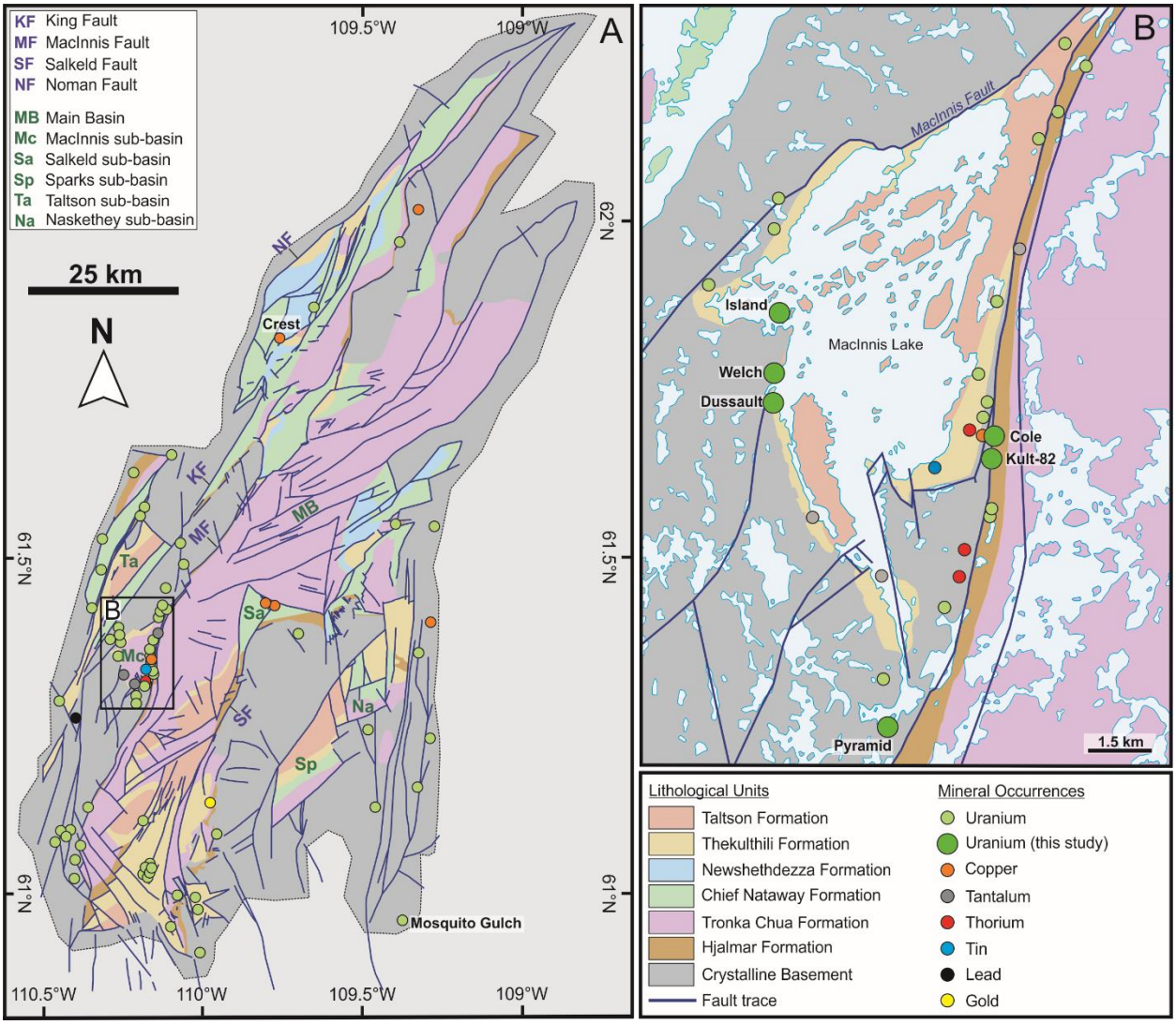

Figure 3-2: Geological sketches of the Nonacho Basin showing the location of notable uranium and base metal occurrences. A) The Nonacho Basin showing major faults, lithologies, and sub-basins (labeled), with the MacInnis Lake area outlined. Modified after Aspler (1985) and Ielpi et al. (2021); B) Geology and mineral occurrences of the MacInnis Lake Area. Uranium occurrences investigated in this study are labelled. Modified from Gandhi and Prasad (1978), Maurice (1984) and NORMIN (2019).

Geology and Mineral Occurrences at MacInnis Lake

The MacInnis Lake sub-basin is located along the western margin of the Nonacho Basin and bound by a series of north-northeast trending faults (**Figure 3-2a**) The MacInnis Lake area is host to numerous historic uranium and base-metal occurrences (**Figure 3-2b**), which were outlined in detail by Gandhi and Prasad (1980).

The lithology of the MacInnis Lake area includes crystalline basement granitoids unconformably overlain by the lowermost Hjalmar granite-pebble conglomerate, and the interbedded sandstones and mudstone of the Tronka Chua formation. There is a break in stratigraphy, with an absence of the upper-most Chief Nataway and Newshethdezza Formations of the lower Nonacho Group, resulting in the Thekulthili and Taltson Formations of the upper Nonacho Group unconformably overlying the basement granitoids (Gandhi and Prasad 1980).

Unaltered gabbroic dikes and intrusive bodies, which cross-cut the basement and overlying Nonacho sediments, are described by Gandhi and Prasad (1980); (**Figure 3-2b**). Gabbroic dikes cross-cutting the basement are noted to be up to 30m wide, and are visible in outcrop at the Island occurrence, covered in this study (Gandhi and Prasad 1980). In contrast, those cross-cutting the Nonacho sediments are noted to be relatively thin (Gandhi and Prasad 1980).

The MacInnis Lake sub-basin is variably faulted, sheared and deformed (Gandhi and Prasad 1980). The sub-basin is bordered along its western margin by the Taltson and Thekulthili formations (**Figure 3-2b**). Although their contact appears conformable, Jefferson (2013) suggests that this contact is a zone of repeated shearing and vein-hosted uranium, which has undergone a prolonged history of tectonically-driven uranium mineralization. Gandhi and Prasad (1980) note that the Taltson and Thekulthili sediments have undergone north-northeast trending synclinal folding, as well as varying east-northeast subsidiary and cross-folds. The less competent units of

the Taltson Formation have undergone more complex and severe drag-folding and crenulations (Gandhi and Prasad 1980). Several steeply-dipping north to northeast trending faults were observed in the area and are locally associated with a series of quartz veins (Gandhi and Prasad 1980). The eastern margin of the MacInnis Lake sub-basin is bordered by a high-strain zone within the Hjalmar formation (**Figure 3-2b**). The Hjalmar Formation is interpreted to have been deposited by strike-slip faulting during basin development (Aspler 1985, Aspler and Donaldson 1985), however incipient reactivation of faults likely resulted in shearing (Jefferson 2013). Canam et al. (2021) outline two deformation events; 2.3-2.2 Ga shearing and 1.78 Ga sinistral, trans-tensional, greenschist-facies reactivation, which flank the Nonacho basin and occurred following main basin development. Vein-hosted uranium occurrences are localized within the sheared western margin of the Hjalmar Formation and along other structurally disturbed settings of the MacInnis Lake sub-basin (Jefferson 2013; **Figure 3-2b**).

3.3. Methods

3.3.1. Field Work and Sampling

Six MacInnis Lake uranium occurrences, the Kult-82, Island, Pyramid, Cole, Welch and Dussault occurrences were examined and sampled for this study. Host rocks, alteration, mineralization and structures were documented in the field; however, extensive weathering and secondary uranium minerals made field observations challenging. Representative samples with uranium minerals (detected by high radioactivity) and associated alteration in a variety of host lithologies were collected and listed in **Table 3-1**. Samples were also provided by the Geological Survey of Canada (GSC) in Ottawa from a set of samples collected by Sunil Gandhi in 1978.

3.3.2. Petrographic Observations

Thirteen variably altered samples were sent to Precision Petrographics in Langley, British Columbia, for sodium cobaltinitrite staining to aid in distinguishing between potassic alteration (e.g., K-feldspar, sericite) and sodic alteration (e.g., albite) in highly altered samples.

Forty-four polished thin sections were prepared at Precision Petrographics and characterized using a petrographic microscope in both transmitted and reflected light. Compositional and textural analyses of uranium-bearing phases, associated sulphides and alteration minerals were determined using a TESCAN MIRA 3 LMU Variable Pressure Schottky Field Emission scanning electron microscope (SEM) at Saint Mary's University, equipped with an electron dispersive X-ray (EDS) Oxford INCA 80mm^2 silicon draft detector capable of quantitative analysis and a backscatter electron (BSE) detector for imaging. Measurements were conducted at a working distance of ~17 mm, with a beam current of 40 μA and accelerating voltage of 20 kV. Raw data (counts and keV) were reduced using the INCA software package.

False colour elemental maps were conducted using a Bruker M4 Tornado micro-Xray Florescence (micro-XRF) spectrometer at the University of New Brunswick to map elemental distribution within select hand samples. Analyses were conducted under vacuum using a Rh source at an accelerating voltage of 50 kV and beam current of 600 μA focussed to a 20 μm spot size. Data were processed using the Bruker M4 Tornado software.

3.3.3. Uranium and Chlorite Mineral Chemistry

Targeted uranium minerals and chlorite in polished thin sections were cut into chips with a dremel tool and mounted into 1-inch diameter epoxy pucks before analysis with the electron

probe X-ray microanalyzer (EPMA) at the University of Toronto. Analyses were performed using a JEOL JXA8230 5-WDS EPMA.

The composition of uranium minerals was completed using 40 EPMA measurements from six uranium mineralized samples (K82-C1, K82-C2, K82-10, C-02-1, I-12-1, W-01-1) with an accelerating voltage of 15 kV, a beam current of 30 nA and a 1 μm focused beam. Counts of characteristic X-rays for each element were quantified by comparison with analyses of known standards and energy lines: barite (Ba*Kα*), bustamite (Mn*Kα*), $CePO_4$ (Ce*Lα*), Cr-augite (Al*Kα*, Ca*Kα*, Mg*Kα*, Si*Kα*), $DyPO_4$ (Dy*Lα*), $ErPO_4$ (Er*Lα*), $EuPO_4$ (Eu*Lα*), galena (Pb*Mα*), $GdPO_4$ (Gd*Lα*), hematite (Fe*Kα*), $HoPO_4$ (Ho*Lα*), $LaPO_4$ (La*Lα*), $LuPO_4$ (Lu*Lα*), $NdPO_4$ (Nd*Lα*), $PrPO_4$ (Pr*Lα*), sanidine (K*Kα*), $SnPO_4$ (Sm*Lα*), $TbPO_4$ (Tb*Lα*), $ThSiO_4$ (Th*Mα*), TiO_2 (Ti*Kα*), $TmPO_4$ (Tm*Lα*), tugtupite (Cl*Kα*), UO_2 (U*Mα*), YPO_4 (Y*Lα*), $YbPO_4$ (Yb*Lα*).

A principal component analysis (PCA) was conducted using the open-source software PAST v.4.03 (Hammer et al. 2001) on the uranium mineral data in effort to reduce the dimensionality of the data set, since it contains a large number of variables. A centered log ratio (CLR) transformation was completed on the data using the open-source software CoDaPak v.2.02.21 (Comas-Cufí and Hió-Henestrosa 2011) set to overcome problems caused by constant-sum compositional data, while retaining as much of the variation in the variables as possible (Jolliffe 1986, Chen et al. 2016). A zero-replacement procedure was conducted, where all the zero elements are replaced by a value half of the detection limit of the EPMA, while all non-zero elements were reduced so that the sum of each sample composition remains constant, as suggested by Aitchison (1982).

Chemical U-Th-Pb ages of uranium minerals were determined using the Bowles (2015) method, where concentrations of U, Th and Pb were obtained in wt.% oxide using the EPMA. An

assumption was made that all of the uranium obtained is ^{238}U, since it accounts for 99.27% of the uranium present today (Bowles 2015).

Chlorite was analyzed with an accelerating voltage of 15 kV, a beam current of 10 nA and a 15 μm beam diameter. Counts of each element were quantified using counts produced by known standards and energy lines: albite (Na*Kα*), bustamite (Ca*Kα,* Mn*Kα*), chloriteSx2 (Al*Kα,* Si*Kα*), chlorite_118 (Mg*Kα*), Cr_2O_3 (Cr*Kα*), hematite (Fe*Kα*), MgF_2_halide (F*Kα*), pentlandite (Ni*Kα*), sanidine (K*Kα*), $SrTiO_3$ (Sr*Lα*), TiO_2 (Ti*Kα*) and tugtupite (Cl*Kα*).

The chemical formula of chlorite was calculated based on the ideal crystallochemical composition of chlorite, $(R_w^{2+}R_y^{3+}\square_z)^{VI}(Si_{(4-x)}Al_x)^{IV}O_{10}(OH)_8$, modified from Wiewióra and Weiss (1990), where $w + y + z = 6$, and □ represents structural vacancies. Octahedral (VI) sites house divalent cations (R^{2+}), primarily Mg^{2+}, Fe^{2+}, Mn^{2+} and Ni^{2+} and trivalent and quadrivalent cations (R^{3+}), such as Al^{3+}, Fe^{3+}, Cr^{3+}, and Ti^{4+} (Wiewióra and Weiss 1990). Tetrahedral (IV) sites host Si^{4+} in four tetrahedral positions, where x is the number of trivalent cations substituting for Si^{4+} (Wiewióra and Weiss 1990). For cation site assignment, the tetrahedral site is first filled with Si^{4+} then Al^{3+} to sum 4 cations. Aluminum can be accommodated in both tetrahedral and octahedral sites in chlorite, which makes it a useful geothermometer (de Caritat et al. 1993). Based on stoichiometric calculations, the tetrahedral aluminum (Al^{IV}) in chlorite is used as a geothermometer, based on Cathelineau (1988): $T(°C) = -61.92 + 321.98(Al^{IV})$.

3.3.4. Whole-Rock Geochemistry

A total of thirty-six representative host rock and mineralized samples were selected for whole-rock geochemistry. Sample preparation and analysis were performed at Activation Laboratories Inc. in Ancaster, Ontario. Major elements were analyzed using X-ray fluorescence

(XRF) on borate metafusion glass pellets. Trace elements were analyzed using Inductively Coupled Plasma Mass Spectrometry (ICP-MS) and Inductively Coupled Plasma Optical Emission Spectrometry (ICP-OES) on samples prepared using a closed vessel multi-acid digestion.

3.4. Results

3.4.1. Petrography and Paragenesis

Similar alteration mineral assemblages were observed at the uranium occurrences studied, despite having different host-rocks and variable modes of occurrence. The paragenetic sequence of all uranium occurrences are consistent and summarized in **Figure 3-3**. A summary of the styles and modes of uranium mineralization for the different occurrences (Kult-82, Island, Cole, Welch and Dussault), including uranium-species determined by EPMA compositional data, associated mineral assemblages, phases of chlorite, and host lithologies is presented in **Table 3-1**.

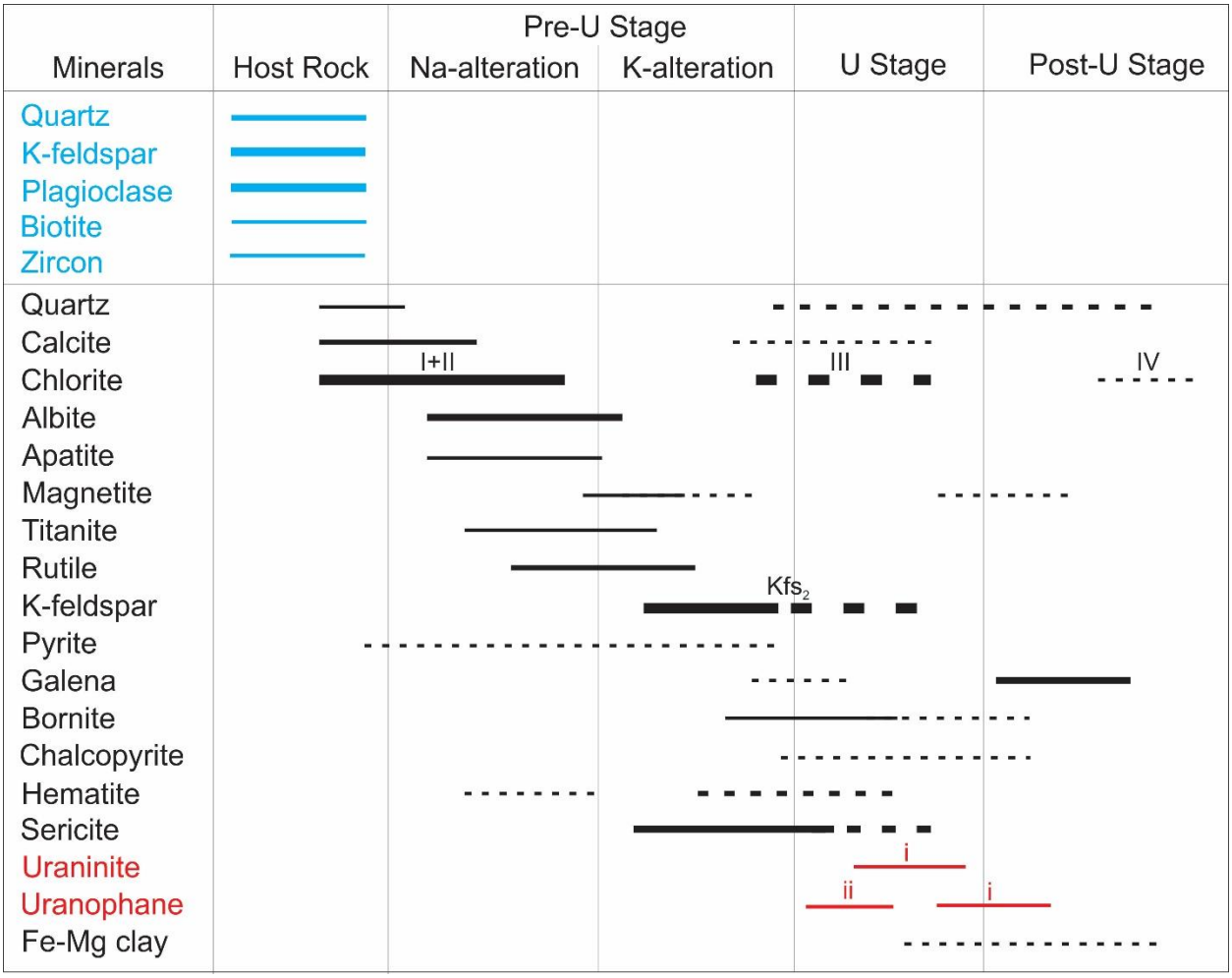

Figure 3-3: Mineral paragenesis of uranium occurrences at MacInnis Lake, Nonacho Basin. Weight of lines indicate relative abundance and dashed lines represent uncertainty in the sequence. Uranium minerals include uraninite and uranophane, and the different types, i and ii, are described in section 4.2. Stages of chlorite (I, II, III, and IV) are noted, and are described in detail in Section 4.3. Abbreviations: K-feldspar alteration (Kfs_2).

Table 3-1: Summary of representative mineralized samples and styles of uranium mineralization a the MacInnis Lake occurrences, Nonacho Basin

Occurrence	UTM Coordinates	Sample	Host Lithology	U-species	Habit, grain size and texture of U mineralization	U Associated minerals
Kult-82	12V 0546206, 6800134	K82-C1	Basement granitoid	Uran-Uph*	< 20µm overgrowths of Uran and Uph on Bn	$Chl_{(I)}$-Cal-Bn-Mag
Kult-82	12V 0546206, 6800134	K82-C2	Basement granitoid	Uran-Uph*	Fine-grained disseminations of Uran and Uph in Chl veinlets, as as overgrowths on Ccp	$Chl_{(I)}$-Ccp
Kult-82	12V 546245, 6800094	K82-10	Basement granitoid	Uran-Uph*	10µm anhedral clusters of Uran and Uph with 10µm lath-like Hem	Hem-Ser-Ab
Island	12V 0540868, 6803654	I-12-1	Basement granitoid + Gabbroic intrusion	Uran-Uph	Fine-grained disseminations of Uran and Uph with Gn in pits, overprinting Rt	Qz-Rt-Gn
Pyramid	12V 0543655, 6793727		Basement mafic gneiss	Unknown	Cal infilling cox-comb Qz giving high counts of radioactivity	Qz-Cal
Cole	12V 0546116, 6800677	C-02-2	Granite-pebble conglomerate (Hjalmar Fm)	Uph*	Aggregate of < 2µm globular Uph	Qz-$Chl_{(III)}$-Ser-Hem
Welch	12V 0540821, 6802158	W-01-1	Sandstone (Taltson Fm)	Uph	Uph micro-inclusions in dendritic Hem overprinting Rt and as very fine-grained Uph disseminations in stringers with Gn	Hem-Rt-Gn-$Chl_{(III)}$-Ser-Qz
Dussault	12V 0540845, 6801729	D-05	Sandstone (Taltson Fm)	Uph	Very fine-grained mix of U+Gn as overgrowths on Ccp	Qz-$Chl_{(III)}$-Cp-Gn

Abbreviations: albite (Ab), bornite (Bn), calcite (Cal), chalcopyrite (Ccp), chlorite (Chl), Formation (Fm) galena (Gn), hematite (Hem), magnetite (Mag), quartz (Qz), rutile (Rt), sericite (Ser), uraninite (Uran), and uranophane (Uph);*Determined using EPMA—See Section 3.4.2.

Basement Hosted Uranium Occurrences

Kult-82

The Kult-82 occurrence is hosted within a basement granitoid that contains predominantly coarse-grained to pegmatitic intermediate-sodic plagioclase ($Ab_{53–85}$), microcline and quartz, with interstitial biotite, pseudomorphed by chlorite (**Figure 3-4a**). Distal from deformation zones and lithological contacts, the granitoids are dark pink to brick-red in colour and have undergone sodic alteration (**Figure 3-4a**), whereby plagioclase and microcline are altered to secondary albite (Ab_{93-100}). Proximal to lithological contacts and deformation zones, the albitized granitoids are overprinted by brick-red potassic alteration consisting of fine-grained, hematized Ba-rich K-feldspar and very fine-grained interstitial sericite, that also locally altered chlorite veins. Veins of sericitized black chlorite ± calcite cross-cut the granitoids and earlier phases of alteration (**Figure 3-4b**). Remobilized uranium mineralization is evident by yellow radioactive surface staining (e.g., uranophane) along black chloritized fracture surfaces in outcrop and in hand specimens (**Figure 3-4c**).

Uranium mineralization is spatially associated with albitized and K-feldspar altered deformation zones that crosscut the altered granitoids close to the overlying unconformable contact with the Hjalmar conglomerates. There are two main styles of uranium mineralization: i) as overgrowths on partially dissolved Cu-sulphides and ii) disseminated within a hematite-sericite breccia. The first style of uranium mineralization is hosted in mm-scale black chlorite-calcite + quartz veins and occur as overgrowths on partially dissolved Cu-sulphides (bornite in sample K82-C1, and, to a lesser extent, chalcopyrite in sample K82-C2) and as disseminated fine-grained (< 20µm) blebs (**Figure 3-4e**). Bornite occurs as both coarse-grained (100-200µm), barren, anhedral inclusions in calcite, that contain laths of native Bi and are cross-cut by a ferromagnesian clay mineral (potentially stilpnomelane or minnesotatite; **Figure 3-4f**). Bornite also occurs as fine-

grained, anhedral blebs and is locally associated with uranium minerals and minor subhedral magnetite (**Figure 3-4f**, **g**). The second style of uranium mineralization occurs in the matrix of a hematite-sericite-uranium breccia (sample K82-10; **Figure 3-4h, i, j**). Brecciated clasts include secondary albite (Ab_{93-100}) and minor, locally Ba-rich, secondary K-feldspar (**Figure 3-4i**). In the hematite-sericite matrix, uranium mineralization occurs as anhedral, granular blebs (10-20 µm) coeval with bladed hematite of similar size (**Figure 3-4j**). Veinlets of calcite locally cross-cut the breccia (**Figure 3-4h, i**).

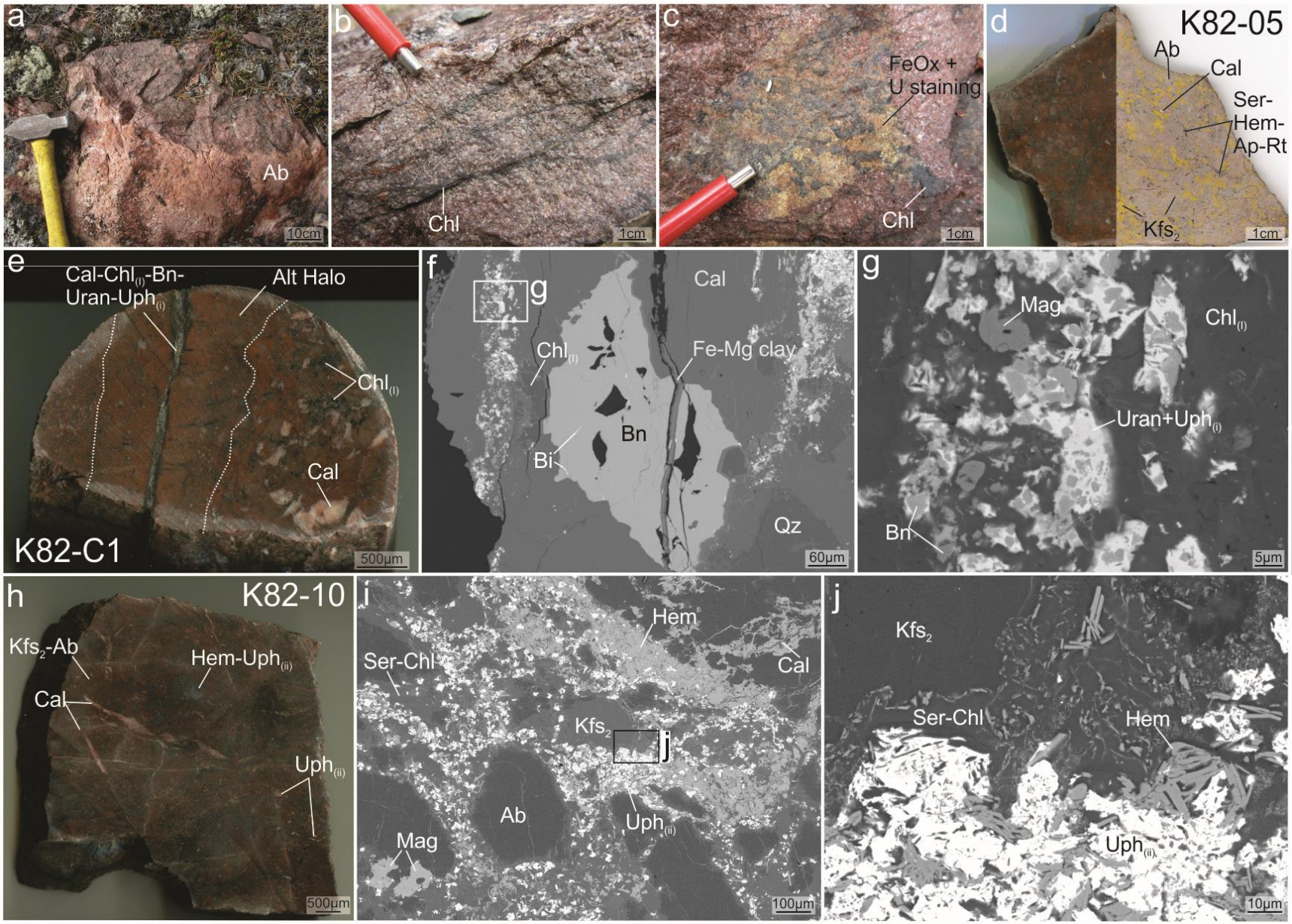
a
Ab
10cm
b
Chl
1cm
c
FeOx +
U staining
Chl
1cm
d
K82-05
Ab
Cal
Ser-
Hem-
Ap-Rt
Kfs2
1cm
e
Cal-Chl(i)-Bn-
Uran-Uph(i)
Alt Halo
Chl(i)
Cal
K82-C1
500µm
f
g
Cal
Chl(i)
Fe-Mg clay
Bn
Bi
Qz
60µm
g
Mag
Chl(i)
Uran+Uph(i)
Bn
5µm
h
K82-10
Kfs2-Ab
Hem-Uph(ii)
Cal
Uph(ii)
500µm
i
Hem
Ser-Chl
Cal
Kfs2
j
Ab
Uph(ii)
Mag
100µm
j
Kfs2
Ser-Chl
Hem
Uph(ii)
10µm

Figure 3-4: Images of the host rocks and uranium minerals at the Kult-82 occurrence. (a) Albitized granitoid host rock; (b) mm-scale black chlorite (Chl) veins; (c) Chorite on fracture surfaces coated with secondary Fe-oxide (FeOx) and yellow uranium staining; (d) Granitoid sample K82-05 showing pervasive albitization (Ab; pink) overprinted by Ba-rich K-feldspar (Kfs_2; yellow) alteration, as shown with sodium cobaltinitrite staining (right); (e) Sample K82-C1 with a very fine-grained albitized alteration halo (Alt Halo) surrounding a bornite (Bn), uraninite (Uran) and type-i uranophane ($Uph_{(i)}$) bearing type-i chlorite and calcite (Cal) vein; (f) SEM-BSE image of bornite in calcite with native Bi-inclusions cross-cut by an unidentified ferro-magnesian clay mineral; (g) SEM-BSE image of uraninite and $uranophane_{(i)}$ overgrowths on bornite with magnetite in chlorite-calcite vein; (h) Sample (K82-10) hosting type-ii uranophane ($Uph_{(ii)}$) in a hematite-chlorite-sericite breccia with late calcite veins; (i) Clasts of locally Ba-rich secondary K-feldspar and as well as minor blocky magnetite hosted in the Hem-Chl-Ser matrix (from h); (j) SEM-BSE enhanced image of box in (i) showing intergrown, coeval $hematite\text{-}uranophane_{(ii)}$ in the pervasively sericitized chlorite matrix.

Island

The Island occurrence is located along the western margin of MacInnis Lake and is hosted within a similar basement granitoid as the Kult-82 occurrence, in addition to a gabbroic intrusion (**Figure 3-2b**). A sharp contact (trending 120°) between potassic altered granitoids and the gabbroic intrusion, as well as inclusions of the granitoid within the gabbro, are visible in outcrop (**Figure 3-5a**). Gandhi and Prasad (1980), documented that the gabbro also crosscuts the sedimentary Taltson and Thekulthili formations of the basin; however, this was not confirmed in the field by the authors of the current paper.

The least altered granitoid is medium-grained, pink in colour and contains cm-scale saussueritized quartz-feldspar veins with clots of magnetite and/or specular hematite. The least-altered granitoid has undergone similar alteration as the granitoid at the Kult-82 occurrence, where secondary albite and fine-grained hematized and Ba-rich K-feldspar alteration with blebby quartz are cross-cut by veins of quartz and locally sericitized type-I and type-II black chlorite (**Figure 3-5b**). Near structures and lithological contacts, the granitoid has undergone pervasive potassic alteration by very fine-grained, Ba-rich and brick-red secondary K-feldspar alteration. The brick-red and Ba-rich K-feldspars contain micro-inclusions of hematite (e.g., sample I-09; **Figure 3-5c, d**) and Ba-zonation with higher Ba in the core (~11 wt.% BaO) than the rim (~4 wt.% BaO); (**Figure 3-5d**).

In the granitoid where K-feldspar alteration of the host rock is prominent, the late quartz-chlorite veins commonly contain pyrite, chalcopyrite, hematite, rutile (**Figure 3-5b**) and local uranophane mineralization (**Figure 3-5e**). Uranophane is spatially associated with two generations of rutile (primary blocky and altered aggregate; **Figure 3-5e**) and local pyrite, with galena rims (**Figure 3-5e**). Uranophane occurs as fine-grained disseminations with galena inclusions,

overprinting aggregates of altered rutile, spatially associated with primary blocky rutile and local pyrite ± galena (**Figure 3-5f, g**).

The Island gabbro varies from fine- to coarse-grained and is locally epidotized. The gabbro exhibits brick-red alteration in areas where secondary hematized Ba-rich K-feldspar alteration is pervasive and along the margins of veins (1-2 cm wide) of quartz, black chlorite and calcite (trending 330°) that contain a black radioactive mineral, tentatively identified as uraninite (**Figure 3-5h**). Although these veins were exposed in outcrop, sampling was unsuccessful.

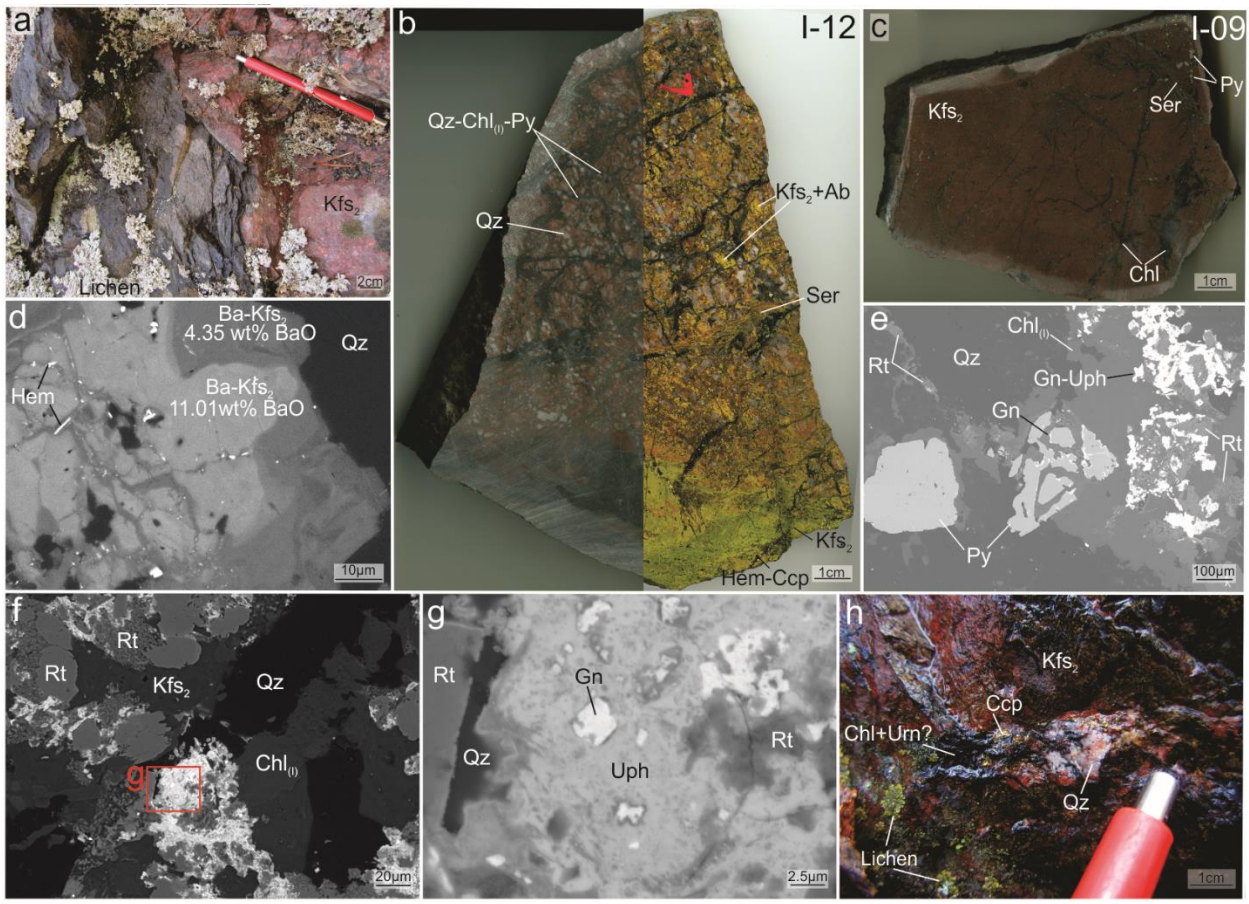

Figure 3-5: Host rocks and uranium minerals at the Island occurrence. (a) Contact between the gabbroic intrusion and brick-red K-feldspar altered (Kfs2) granitoid; (b) Granitoid sample I-12 with sodium cobaltinitrite staining (right) to show the distribution of potassic (yellow) and sodic (pink) alteration. The majority of the sample is altered by fine-grained secondary albite (Ab) overprinted by K-feldspar alteration with blebby quartz and cross-cut by chlorite-sericite (Ser) veins ± quartz and euhedral pyrite (Py). The lower portion of the slab is composed of very fine-

grained K-feldspar alteration with veinlets of chalcopyrite and hematite (Hem); (c) Gabbro sample I-09 showing brick-red K-feldspar alteration, sericitized chlorite veins, and euhedral pyrite; (d) SEM-BSE image of sample I-09 where zoned Ba-rich K-feldspar contain laths and fracture-filled hematite; (e) SEM-BSE image of a quartz-chlorite vein from I-12 containing galena and uranophane (Uph) mineralization, associated with rutile (Rt) and pyrite, locally overprinting galena (Gn); (f) SEM-BSE image of a quartz-chlorite vein in sample I-12 with Kfs_2 alteration containing blocky and aggregates of rutile (Rt); (g) Pb-rich uranophane with galena inclusions overprinting and spatially associated with rutile in quartz-chlorite vein; and (h) Centimetre-scale vein of chlorite, quartz (Qz) with chalcopyrite (Ccp) and with uraninite (?) in brick-red altered gabbro.

Pyramid

The Pyramid occurrence is located on the southern tip of MacInnis Lake (**Figure 3-2b**). There are two main lithologies in the area: i) felsic gneisses, which have been intruded by locally saussertized pegmatite dikes (**Figure 3-6a**), and ii) mafic gneisses, which have been variably chloritized and host uranium minerals (**Figure 3-6b, c**). The felsic gneisses are coarse grained and light pink in colour. They are cross-cut by various pegmatitic intrusions of euhedral K-feldspar and minor quartz which are, in turn, cross-cut by black chlorite veins. The mafic gneiss is fine-grained, weakly magnetic, pervasively chloritized, variably clay altered, and silicified (**Figure 3-6b, c**). Veins of vuggy quartz infilled by wispy calcite cross-cut the host in various locations (**Figure 3-6b**). Clasts of basement granitoid are suspended in the chloritized gneiss which contain disseminated pyrite and minor chalcopyrite (**Figure 3-6c**).

The Pyramid occurrence is hosted in brecciated mafic gneiss where veins composed of cm-scale cox-comb quartz are infilled with wispy calcite and minor mm-scale black sooty blebs (**Figure 3-6d**). The quartz-calcite veins and brecciated gneiss are radioactive, and yellow secondary uranophane staining and Fe-oxide weathering are common in exposed outcrops (**Figure 3-6e**). An alteration halo of highly silicified chloritized mafic gneiss surrounds the breccia zone. Although uranium mineralization was previously outlined by Gandhi and Prasad (1980), and radioactivity was high while conducting field observations, no uranium minerals were identified

during petrographic observations of thin sections. The radioactivity within the samples is from surface staining and yellow secondary uranium minerals, and not from uranium minerals within the samples. The origin of the remobilized secondary uranium is therefore unknown.

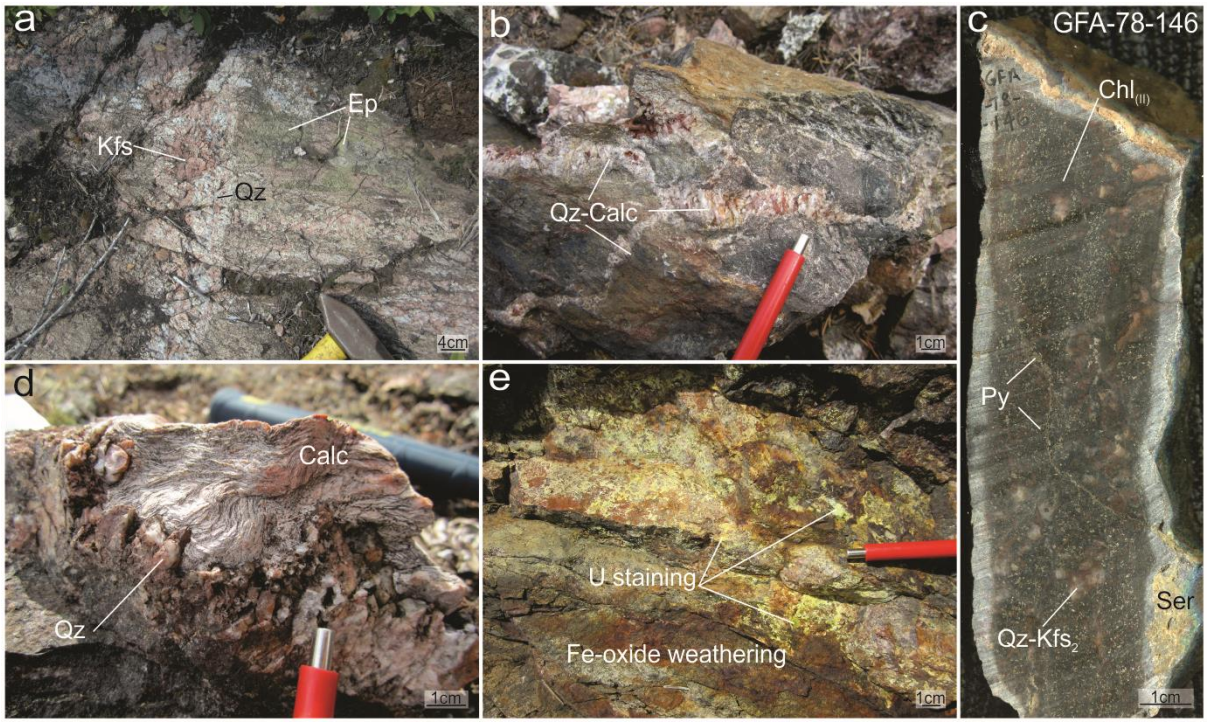

Figure 3-6: Representative lithologies and mineralized samples at the Pyramid occurrence: (a) Pegmatitic quartz (Qz) and K-feldspar (Kfs) crosscutting granitic gneiss with epidote (Ep) alteration of feldspars; (b) Miarolitic quartz veins infilled with calcite (Calc) cross-cutting host amphibolite; (c) Clasts of quartz and secondary K-feldspar (Kfs_2) suspended in highly chloritized matrix with sericite (Ser) infilling fractures and disseminated pyrite (Py); (d) Wispy calcite infilling cox-comb quartz vein; (e) Yellow secondary uranium staining and Fe-oxide weathering products are prominent near quartz-calcite veins in outcrop.

Sediment hosted uranium occurrences

Cole

Mineralization of the Cole occurrence occurs in shear and breccia zones within the basal granite-pebble conglomerate of the Hjalmar Formation, in close proximity to the unconformable contact with the basement granitoid (**Figure 3-2b**). The conglomerate contains cm-scale, sub-angular to sub-rounded clasts of basement granitoid within a chloritized greenish-grey arkosic sandstone matrix (**Figure 3-7a**). The underlying basement granitoids are also weakly sheared and

K-feldspar altered (**Figure 3-7b**). Where deformed, foliated and brecciated, conglomerates contain milled and rounded granitic clasts that have undergone secondary albite and potassic alteration, similar to basement granitoid rocks at the Kult-82 and Island occurrences. The milled clasts in sheared conglomerates are suspended in a sericitized chlorite matrix (**Figure 3-7c**).

Conglomerates are brecciated by quartz and locally host uranium mineralization (**Figure 3-7d, e**). The matrix of mineralized breccias consist of quartz and variably sericitized type-III chlorite with calcite, pyrite, hematite, apatite, rutile, titanite and minor uranium minerals (**Figure 3-7d, e**). Uranium minerals occur as small (1-2 μm) disseminated and globular grains of uranophane, hosted in the sericite-chlorite matrix and are spatially associated with bladed and lath-like clusters of hematite (**Figure 3-7e-i**). Veinlets of an unidentified ferromagnesian clay mineral with similar chemistry to the clay mineral at the Kult-82 occurrence (i.e., stilpnomelane or minnesotatite), overprints sericitization, cross-cuts granitic clasts, and exploits fractures in the quartz matrix (**Figure 3-7f, g**).

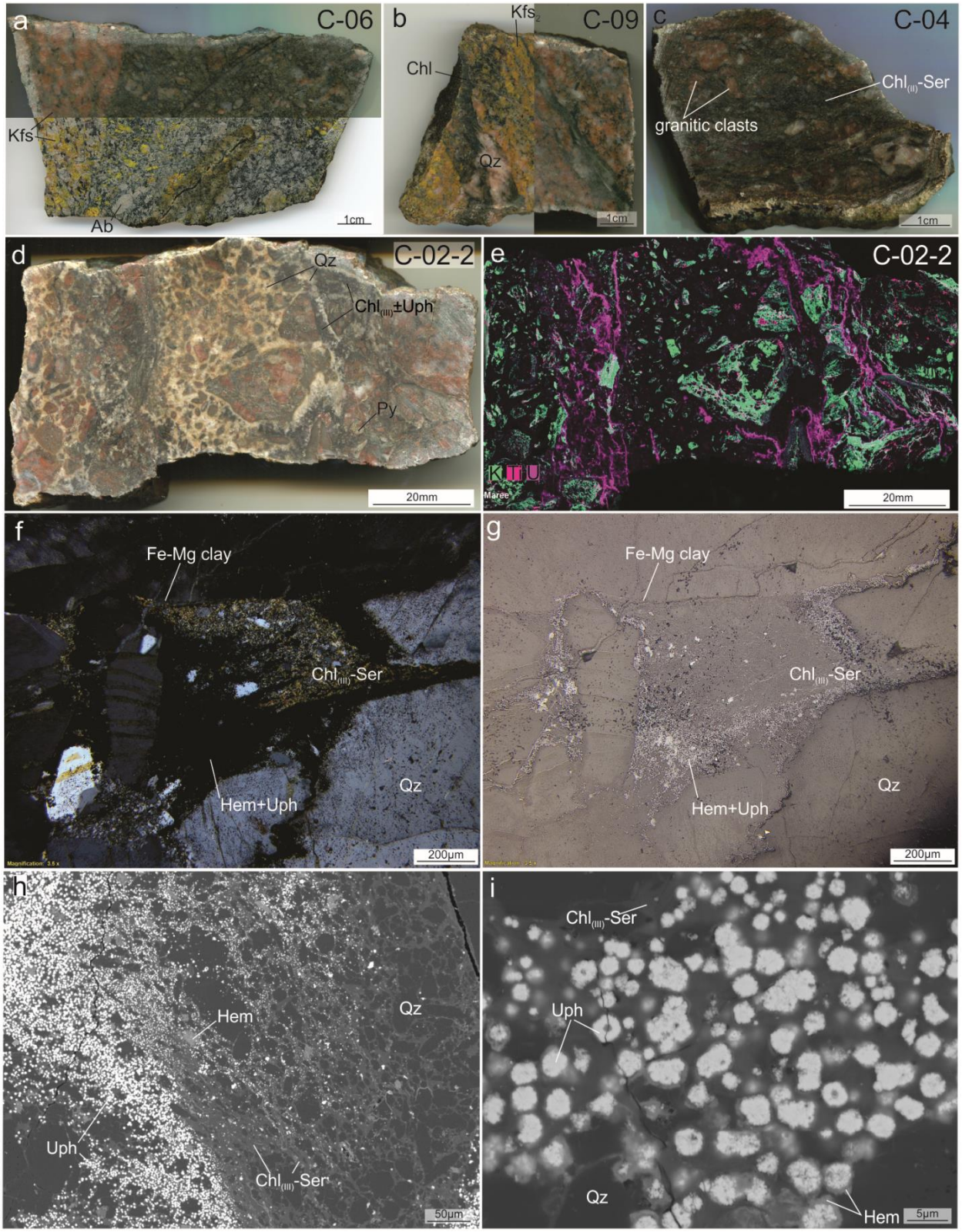

Figure 3-7: Host rocks and mineralization at the Cole occurrence. (a) Granite-pebble conglomerate of the Hjalomar Formation (sample C-06) showing sodium cobaltinitrite staining (bottom) and unstained surface (top) with clasts of predominantly secondary K-feldspar (Kfs) and

albite (Ab). (b) K-feldspar altered (Kfs_2) and sericitized basement granitoid (sample C-09) stained with sodium cobaltinitrite (right) with cross-cutting black chlorite (Chl) and quartz (Qz) veins. (c) Foliated and brecciated conglomerate (sample C-04) with milled and rounded granitic clasts suspended in a black matrix of sericite (Ser) and chlorite. (d) uranium-mineralized quartz-chlorite-sericite breccia (sample C-02-2) where type-III chlorite veins contain pyrite, rutile, hematite and uranium minerals; (e) False colour elemental map of (d) produced by micro-XRF showing the distribution of K (green), Ti (purple) and uranium (pink). Individual elemental maps in **Figure A3-2**; (f) cross-polarized transmitted light photomicrograph of uranophane (Uph) with hematite (Hem) in chlorite-sericite veins within the breccia, cross-cut by an unidentified ferromagnesian clay mineral; (g) reflected light photomicrograph of (f); (h-i) SEM-BSE images of very fine-grained bladed hematite with globular uranophane associated with sericitized chlorite in the breccia.

Welch and Dussault

The Taltson Formation hosts the Welch and Dussault occurrences, which are located along the western shoreline of MacInnis Lake, ~600 m apart (**Figure 3-2**). The interbedded sandstone-mudstone units of the uppermost Taltson Formation are composed of alternating layers of medium to fine-grained pink arkosic sandstone, and greenish-grey mudstone. The sedimentary rocks are deformed in shear zones, displaying minor folding and crenulations and are more broadly cross-cut by a large network of quartz veins spanning up to 5m wide (**Figure 3-8a; Figure 3-9a**). Both the Welch and Dussault occurrences are highly brecciated by vuggy quartz veins that contain black sericitized chlorite and are locally coated by secondary yellow uranophane (**Figure 3-8a**). Sericite occurs along fracture surfaces and along quartz vein margins (**Figure 3-8b; Figure 3-9c**). Despite their similar host and close proximity, the mineralogy of the uranium-bearing quartz veins at each occurrence are slightly different.

At the Welch occurrence, the host sedimentary unit has undergone chloritization, sericitization and locally Ba-rich K-feldspar alteration. The host rock is cross-cut by networking vuggy quartz veins containing type-III chlorite, rutile, hematite, galena and minor secondary uranium minerals (**Figure 3-8c, d, e, f**). The chloritized and sericitized sedimentary matrix host apatite and clusters of bladed hematite (**Figure 3-8c**).

Uranium minerals are minor and occur as micro-inclusions of uranophane in dendritic hematite, which overprint rutile (**Figure 3-8f**). The uranium-bearing hematite is concentrated along the margins of quartz veins, associated with sericitized chlorite (**Figure 3-8c, e**). The quartz veins contain clusters of book-like type-III chlorite, locally associated with subhedral galena and minor uranium minerals (**Figure 3-8c**, **d**). Galena occurs as disseminations and as stringers with micro-inclusions of uranophane interstitial to subhedral quartz grains (**Figure 3-8c, d, e**).

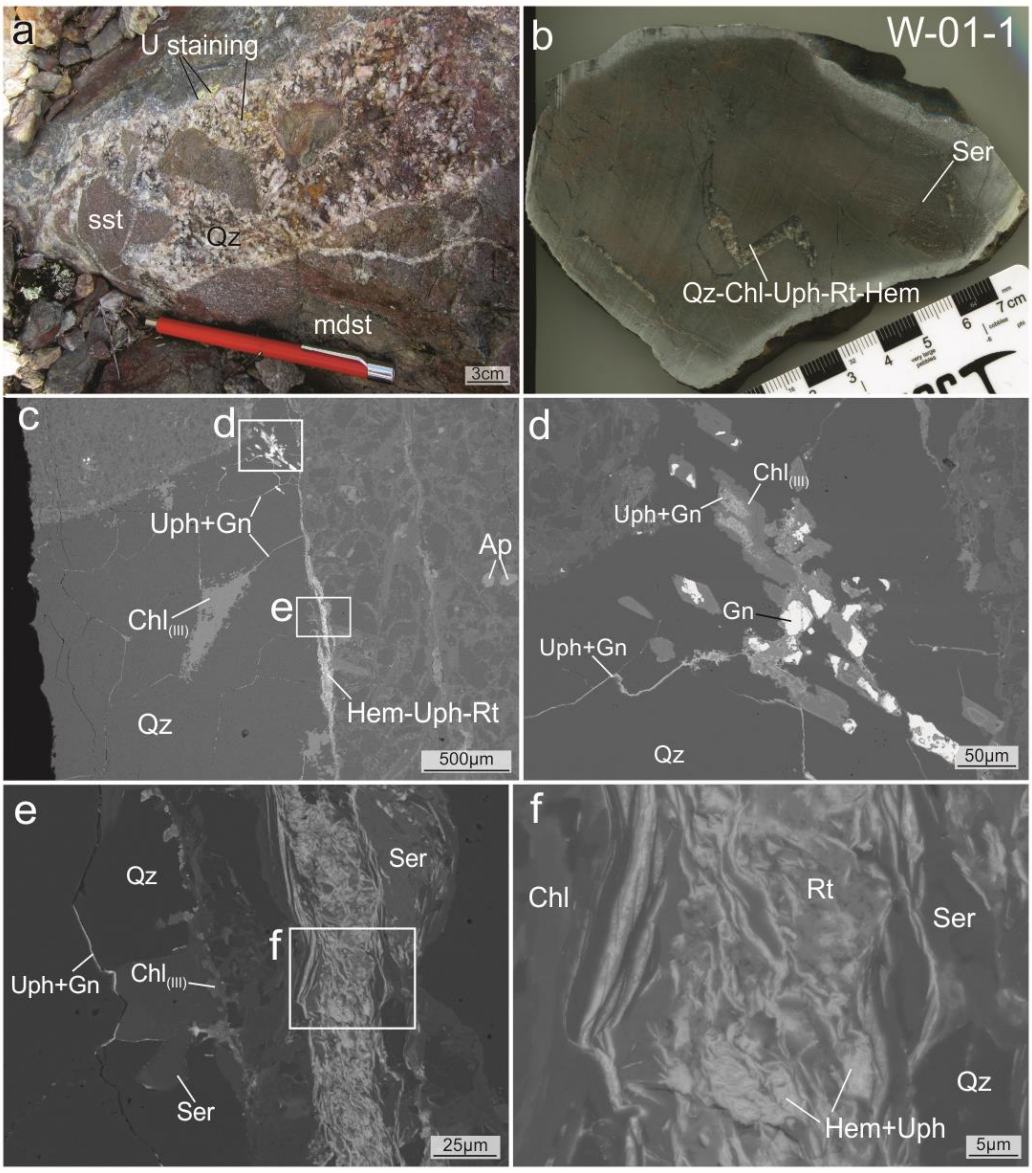

Figure 3-8: Host rocks and uranium mineralization at the Welch occurrence (a) Interbedded sandstone (sst) and mudstone (mdst) brecciated by vuggy quartz (Qtz) veins and local yellow

uranophane (Uph) surface staining. (b) Scanned slab of sample W-01 with miarolitic quartz veins bordered by chlorite (Chl) which contain rutile (Rt), hematite (Hem) and minor uranophane mineralization. (c) SEM-BSE image of the chloritized and sericitized matrix in sample W-01 which contains apatite (Ap) and is cross-cut by a quartz vein containing rutile, hematite and minor uranophane mineralization along vein margins. Stringers of uranophane and galena follow quartz grain boundaries overprinting type-III chlorite. (d) SEM-BSE image of type-III chlorite overprinted by galena with local uranophane in the cross-cutting quartz vein. (e) SEM-BSE image of sericitized chlorite along the margin of quartz vein and stringers of uranophane and galena following quartz grain boundaries. (f) SEM-BSE image of box outlined in (e) showing dendritic hematite containing micro-inclusions of uranium minerals overprinting rutile associated with sericitized chlorite along quartz vein margins.

The Dussault occurrence is hosted in pebbly arkosic sandstone to interbedded red and green sandstone-mudstone units, locally deformed and folded and cross-cut by large-scale, pervasive networking quartz veins (**Figure 3-9a**). The Dussault occurrence was described by Gandhi and Prasad (1980) as a series of radioactive lenses, where the main mineralized lens is 0.5-2m thick, 150m long and 60m wide, steeply dipping east, beneath MacInnis Lake and contains an estimated 27 000 metric tonnes averaging 0.17% U. Observations by Jefferson and Kjarsgaard (2009) outline crack-seal quartz veins and uraniferous quartz breccias that were confirmed through field observations by the authors.

Where mineralized, the sedimentary rocks are highly brecciated by vuggy quartz veins with sericite along fracture surfaces. Secondary yellow uranophane and Fe-oxide weathering are common along fracture surfaces (**Figure 3-9a**). Vuggy quartz veins contain abundant disseminations of chalcopyrite, interstitial to sericitized chlorite (**Figure 3-9b, c, d**). Galena overprints chalcopyrite and contains islands of native Bi (**Figure 3-9e, f**). Blebs of subhedral pyrite locally overprint chalcopyrite and galena (**Figure 3-9e**). Uranophane mineralization occurs with galena as fine-grained laths, associated with massive galena as overgrowths on chalcopyrite (**Figure 3-9e, f**).

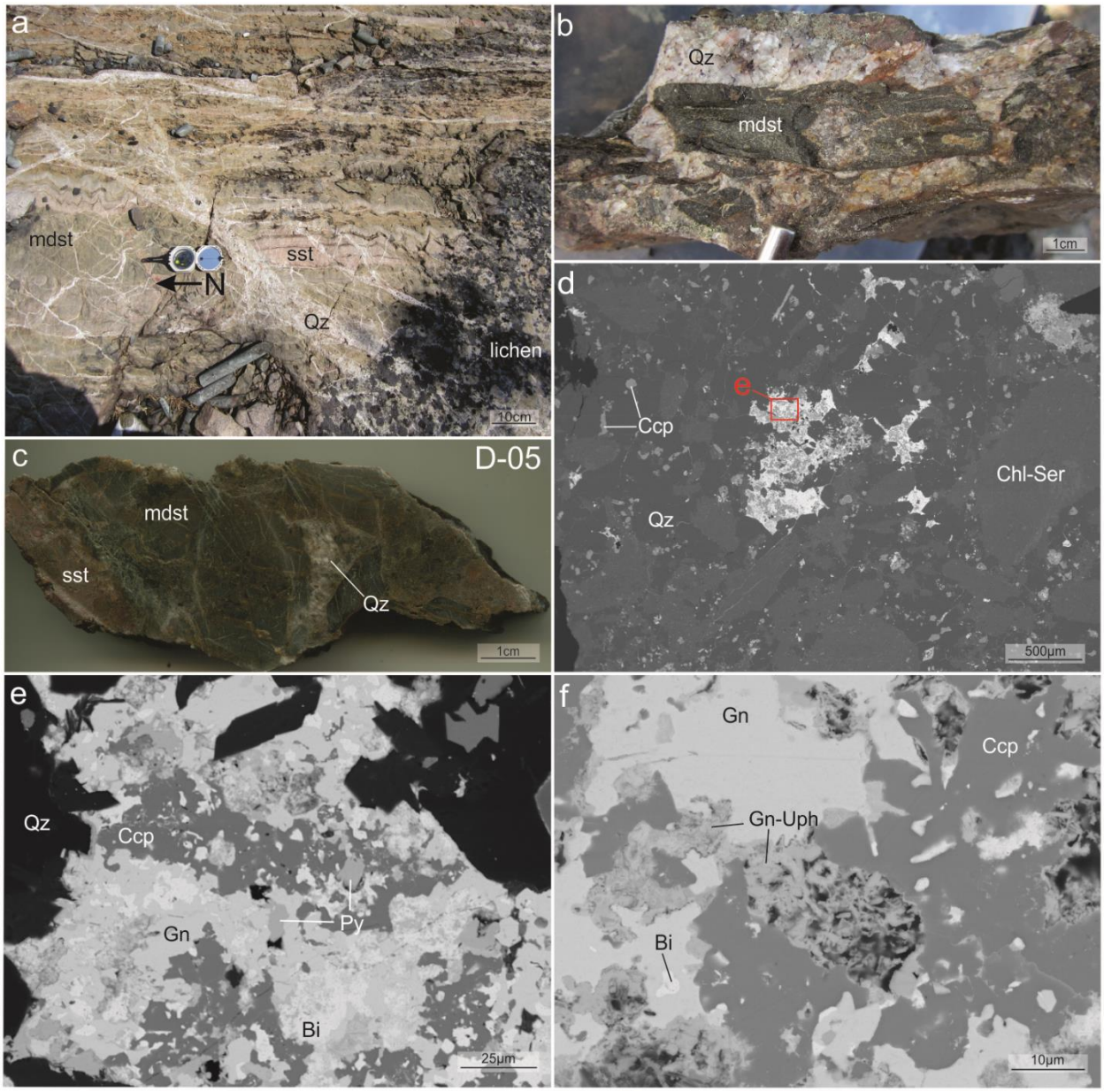

Figure 3-9: Host rocks and mineralization at the Dussault occurrence: (a) Interbedded sandstone (sst) and mudstone (mdst) of the Taltson Formation cross-cut by a series of networking quartz (Qz) veins. Bedding is locally folded and deformed. (b) Quartz brecciated sample D-05 with mudstone clasts and local Fe-oxide weathering and yellow uranophane staining (c) Sample D-05, showing vuggy quartz veins brecciating mudstone and sandstone clasts. (d) SEM-BSE image of abundant chalcopyrite (Ccp) disseminated in quartz breccia around chlorite (Chl) and sericite (Ser) altered clasts. (e) SEM-BSE image from box in (d) where galena (Gn) forms overgrowths on chalcopyrite and has local islands of native Bi hosted in quartz breccia. Local subhedral pyrite (Py) overprints chalcopyrite and galena. (f) SEM-BSE image where fine-grained laths of uranophane (Uph) and galena are spatially associated with massive galena as overgrowths on chalcopyrite.

3.4.2 Uranium Mineral Chemistry

The fine-grained nature of the uranium minerals and intergrowth with surrounding phases (e.g., chlorite, sericite, galena, quartz, hematite and rutile) made EMPA work difficult. Although over fifty EPMA measurements of uranium minerals were collected, only thirty-six analyses from Kult-82 and one analysis from Cole were not contaminated by surrounding mineral phases.

In general, the uranium minerals contain 61.55–81.09 wt% UO_2 and variable to high concentrations of Si (0.83–12.08 wt% SiO_2), Ca (0.96–8.20 wt% CaO), Ba (0.46–3.50 wt% BaO), Ti (0.14–1.55 wt% TiO_2), Fe (0.10–7.65 wt% FeO), and Pb (< 0.09–8.19 wt.% PbO). They are variably hydrous, considering low totals (89.5–99.63 wt.%; **Table 3-2**). Concentrations of Eu, Tb, Er, Tm, Yb, Lu and Th (with the exception of one target in the sample K82-C1) fell below the detection limits of the EPMA and are presented in **Table 3-2** as less than their respective detection limits.

The two styles of uranium minerals from the Kult-82 occurrence, i) vein hosted uranium minerals as overgrowths on partially dissolved Cu-sulphides (K82-C1, K82-C2; **Figure 3-4f**) and ii) anhedral granular blebs in a hematite-sericite breccia (K82-10; **Figure 3-4i**), are chemically distinct. Both styles of uranium mineralization at Kult-82 appear compositionally heterogeneous, confirmed by their variable distribution in $CaO\text{-}SiO_2\text{-}UO_2$ space that classifies uranium minerals such as uraninite (UO_2), uranophane ($Ca[UO_2]_2[SiO_2OH]_2$ and coffinite ($U[SiO_4]_{1-x}[OH]_{4x}$); (**Figure 3-10a**). Pure uranium oxides are not known in nature, and are always at least partially oxidized and contain additional elements (Finch and Murakami 1999). Uranium minerals typically have non-stoichiometric compositions due to presence of radiogenic Pb^{4+}, produced by the decay of ^{238}U and ^{235}U, which is a strong oxidizer and is unstable with U^{4+} (Finch and Murakami 1999). This causes auto-oxidation of U^{4+} to U^{6+}, and reduction of Pb^{4+} to Pb^{2+} (Finch and Murakami

1999). However, Pb^{2+} does not fit in the crystal structure of uraninite, and subsequent alteration and substitution of Pb^{2+} occurs with a variety of divalent cations (i.e., Ca, Si, Fe and REE); (Finch and Murakami 1999, Alexandre and Kyser 2005).

Type-i uranium minerals are classified as a mix of uraninite and uranophane (**Figure 3-10a**). This is confirmed by high U (70.69–81.09 wt.% UO_2) and low Si (0.83–6.41 wt.% SiO_2) and Ca (1.33–2.57 wt.% CaO) relative to type-ii uranium minerals (**Table 3-2**). Type-ii uranium minerals contain less U (61.55–75.30 wt.% UO_2) and higher Ca (3.27–4.39 wt.% CaO), Si (3.72–12.08 wt.% SiO_2) and Pb (3.30– 8.19 wt.% PbO) than type-i uranium (**Table 3-2**). Type-ii uranium has a highly variable distribution in the classification ternary (**Figure 3-10a**) and is classified as uranophane. Both styles of uranium minerals at the Kult-82 occurrence exhibit variably high Ba concentrations (0.46–3.50 wt.% BaO). Due to their similar charge and ionic radii, Ba^{2+} can easily substitute for Ca^{2+} therefore, their substitution is considered in **Figure 3-10b**. The compositions of the uranium minerals in (CaO+BaO)-SiO_2-UO_2 space shift slightly, relative to their position in CaO-SiO_2-UO_2 space, based on their respective Ba concentrations, however it does not drastically affect their classifications.

The uranium minerals at the Cole occurrence are associated with a similar mineral assemblage to type-ii uranium minerals at the Kult-82 occurrence (quartz-chlorite-sericite-hematite). The one available analysis shows that the Cole uranium minerals may be classified as uranophane (**Figure 3-10a**). They contain 67.00 wt.% UO_2, 6.14 wt.% PbO. 6.95 wt.% SiO_2 and 3.52 wt.% CaO, similar to the type-ii uranium minerals at Kult-82, with the exception of low Ba (0.20 wt.% BaO).

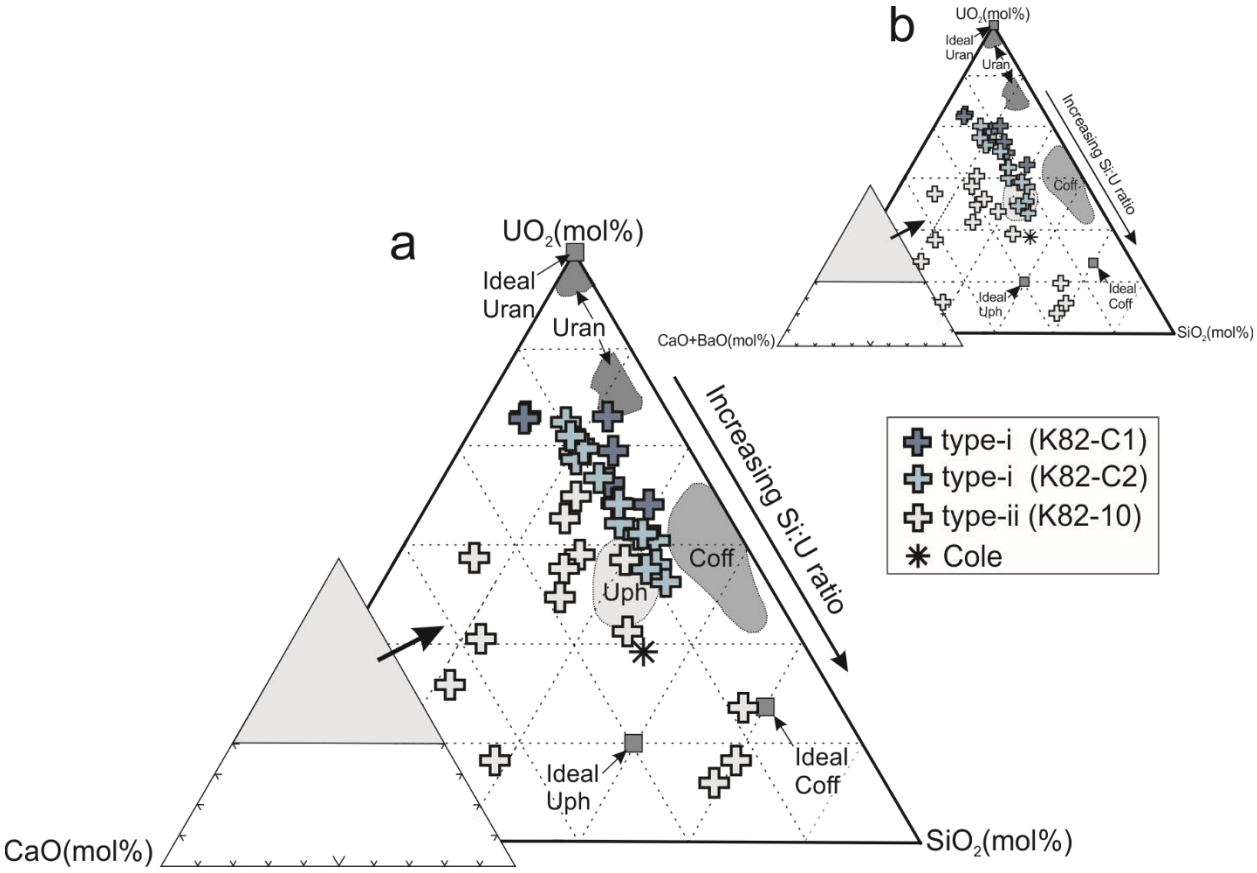

Figure 3-10: Molar proportions of major oxides the uranium minerals at the Kult-82 (K82) and Cole occurrences plotted on (a) CaO-UO_2-SiO_2 and (b) $CaO+BaO$-UO_2-SiO_2 ternary diagrams. The compositions of ideal uraninite (Uran), uranophane (Uph) and coffinite (Coff) are plotted, as well as fields for natural uranophane, coffinite, and uraninite from the Athabasca Basin (modified from Alexandre et al., 2012).

Table 3-2: Representative EPMA data (wt% oxide) of uranium minerals of the Kult-82 and Cole occurrences.

	K82-C1 (type-i)					K82-C2 (type-i)					K82-10 (type-ii)					C-02
SiO_2	3.06	2.16	0.83	0.85	4.37	6.41	5.52	4.47	5.75	5.77	3.72	11.88	6.61	4.05	12.08	6.95
TiO_2	0.58	1.11	1.55	1.55	0.62	0.25	0.18	0.25	0.31	0.25	0.29	0.18	0.14	0.22	0.19	*n.d.*
Al_2O_3	0.19	0.02	<0.02	0.01	0.27	0.17	0.26	0.20	0.29	0.19	0.19	1.85	0.25	0.30	2.02	2.66
MgO	0.06	0.03	0.02	0.03	0.12	0.07	0.03	0.05	0.06	0.05	0.08	0.09	0.05	0.04	0.35	*n.d.*
$FeO_{(total)}$	3.61	3.37	3.58	3.12	3.37	1.43	2.05	2.13	1.87	1.47	3.18	1.21	1.23	1.26	2.65	2.56
CaO	1.69	1.87	2.46	2.57	1.33	2.12	1.81	2.31	2.03	2.36	3.90	4.16	3.78	4.39	3.27	3.52
K_2O	0.02	0.02	0.01	0.02	0.03	0.01	<0.04	0.01	0.04	0.02	0.09	0.21	0.06	0.35	0.09	0.44
P_2O_5	1.07	0.14	0.09	0.12	0.15	0.57	0.21	0.21	0.34	0.34	0.21	0.09	0.11	0.09	0.13	*n.d.*
SO_3	1.56	1.44	1.40	0.59	1.30	<0.02	0.01	<0.02	1.29	<0.02	2.25	2.26	0.55	0.83	0.04	*n.d.*
Zr_2O_3	0.54	0.48	0.20	0.16	<0.08	0.01	<0.08	<0.08	<0.08	<0.08	0.19	<0.08	<0.08	0.12	<0.08	*n.d.*
BaO	0.94	0.78	0.46	0.62	1.12	2.85	1.85	1.89	2.20	2.74	2.43	2.44	2.03	2.99	2.89	0.22
La_2O_3	0.40	0.41	0.55	0.47	0.41	0.06	0.12	0.21	0.16	0.15	0.14	<0.20	<0.20	0.16	0.11	*n.d.*
Ce_2O_3	1.81	1.88	2.02	2.24	2.29	1.90	1.65	1.60	1.63	1.80	0.52	0.53	0.35	0.31	0.38	*n.d.*
Pr_2O_3	0.31	0.29	0.23	0.28	0.21	0.41	0.41	0.29	0.48	0.62	0.03	<0.16	0.04	<0.16	0.08	*n.d.*
Nd_2O_3	1.25	1.27	1.14	1.38	1.41	3.23	2.76	2.38	2.67	2.86	0.12	0.12	0.18	0.13	0.08	*n.d.*
Sm_2O_3	0.47	0.33	0.32	0.22	0.39	0.21	0.26	0.04	0.07	0.13	0.03	<0.14	0.09	<0.14	0.01	*n.d.*
Eu_2O_3	0.06	0.01	<0.16	<0.16	<0.16	0.07	<0.14	<0.14	<0.14	0.03	0.03	<0.14	<0.14	<0.14	0.04	*n.d.*
Gd_2O_3	0.36	0.35	0.43	0.33	0.19	0.02	<0.10	0.01	0.05	<0.10	<0.10	<0.10	<0.10	<0.10	<0.10	*n.d.*
Tb_2O_3	<0.12	<0.12	<0.12	<0.12	<0.12	<0.12	<0.12	<0.12	<0.12	<0.12	<0.12	<0.12	<0.12	<0.12	<0.12	*n.d.*
Dy_2O_3	0.66	0.61	0.60	0.59	0.6	0.03	0.11	0.13	0.11	0.05	0.16	0.03	0.09	0.09	0.23	*n.d.*
Ho_2O_3	0.10	0.21	0.12	0.16	0.16	<0.12	<0.12	<0.12	<0.12	0.03	<0.12	<0.12	<0.12	<0.12	<0.12	*n.d.*
Y_2O_3	3.87	2.08	2.15	2.10	1.72	0.13	0.06	0.04	0.04	0.08	<0.06	<0.06	<0.06	<0.06	<0.06	*n.d.*
Er_2O_3	0.12	0.05	0.02	0.03	<0.14	<0.14	<0.14	<0.14	<0.14	<0.14	<0.14	<0.14	<0.14	<0.14	0.01	*n.d.*
Tm_2O_3	0.10	0.08	<0.14	0.04	0.05	<0.14	<0.14	<0.14	<0.14	<0.14	<0.14	0.03	<0.14	<0.14	0.09	*n.d.*
Yb_2O_3	<0.16	<0.16	<0.16	0.07	0.11	0.09	<0.16	<0.16	<0.16	<0.16	<0.16	0.06	0.01	<0.16	<0.16	*n.d.*
Lu_2O_3	<0.02	<0.02	<0.02	<0.02	<0.02	<0.02	<0.02	<0.02	<0.02	<0.02	<0.02	<0.02	<0.02	<0.02	0.02	*n.d.*
PbO	0.87	0.48	2.37	1.22	1.07	<0.08	0.07	<0.08	2.35	<0.08	8.19	7.84	4.45	5.49	3.30	6.14
ThO_2	<0.12	<0.12	<0.12	<0.12	<0.12	<0.12	<0.12	<0.12	<0.12	<0.12	<0.12	<0.12	<0.12	<0.12	<0.12	<0.12
UO_2	70.69	76.37	76.99	78.52	74.66	76.32	79.84	81.09	75.53	77.51	73.90	61.55	75.3	71.87	64.44	67.00
Total	94.35	95.85	97.52	97.26	95.95	96.34	97.2	97.28	97.26	96.44	99.63	94.54	95.29	92.69	92.51	89.52
ΣREE + Y	9.50	7.60	7.57	7.91	7.54	6.16	5.37	4.68	5.20	5.73	1.02	0.76	0.75	0.69	1.05	*n.d.*
$LREE_N/HREE_N$ §	1.29	2.51	2.60	2.95	3.69	40.34	75.15	103.1	115.9	60.19	*n.d.*	*n.d.*	*n.d.*	*n.d.*	*n.d.*	*n.d.*

§ Chondrite normalized Ce and Y used as proxies for LREE and HREE, respectively

Abbreviations: not detected (*n.d.*).

Full data set in **Table A3-1**

The concentrations of Th, Pb, Ca, Si, Fe, Ce, Y, and Dy were chosen as main variables from the EPMA data sets for PCA analysis. The relative and actual contributions of the variables are shown in **Figure 3-11** for the first two principal components (PC), which account for more than 93.7% of the variation in the data. The UO_2, FeO, SiO_2, CaO and BaO are similar in PC1 and PC2, within quadrant IV, indicating their positive correlation. The ThO_2 and Ce_2O_3 plot in quadrant I with similar PC2 values as the UO_2 group, suggesting negative correlation between ThO_2 and Ce_2O_3 with the UO_2 group (**Figure 3-11**). No correlation between PbO is observed in PC1 and PC2 with other oxides, as it plots by itself in quadrant III and is controlled by the more Pb-rich type-ii uranium minerals at Kult-82 (**Figure 3-11**). Middle and heavy REE, represented by Dy_2O_3 and Y_2O_3, respectively, plot in quadrant II but have very different PC1 and PC2 values, suggest they do not correlate well. These elements are controlled by type-i uranium minerals (**Figure 3-11**). Similar PC2 values for Dy_2O_3 with Ce_2O_3 and ThO_2 suggest their negative correlation.

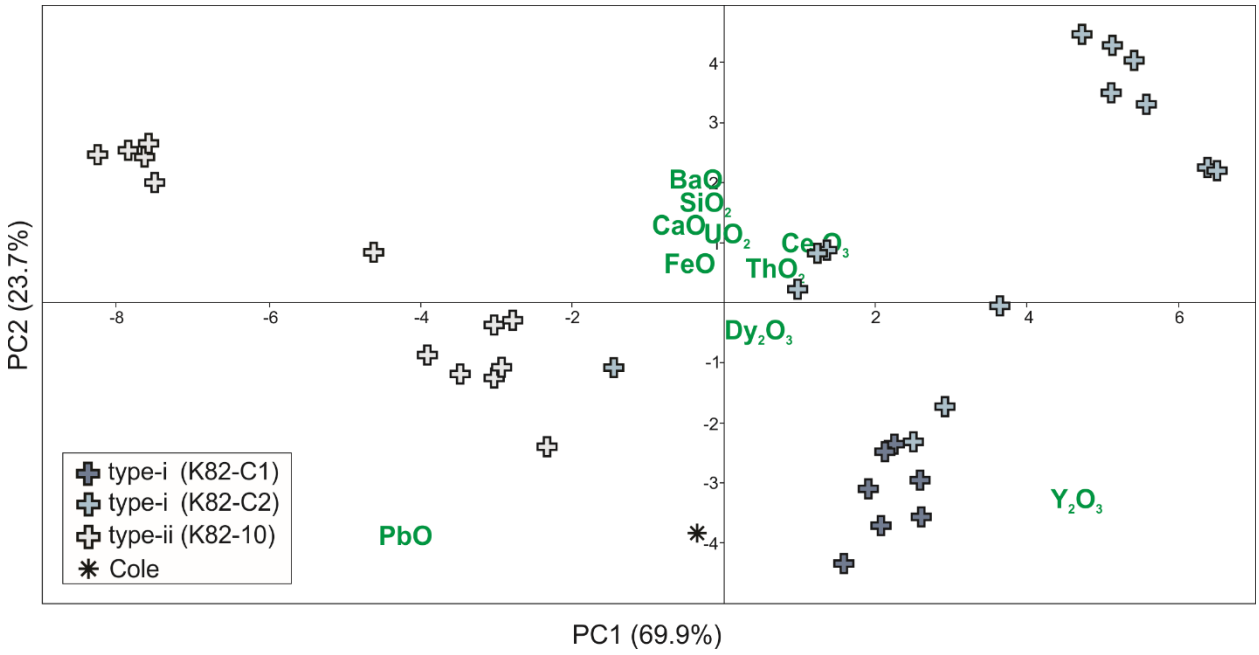

Figure 3-11: Biplots of Principal Component (PC) 1 vs. PC2 for uranium minerals from the Kult-82 and Cole occurrences.

Chemical U-Pb ages of uraninite and uranophane from the Kult-82 and Cole occurrences were determined using the Bowles (2015) method and EPMA analyses (**Table A3-2**), assuming all uranium present is ^{238}U, which accounts for 99.27% of the uranium present today (Bowles 2015). Several age groups were obtained for the uranium mineralization (**Figure 3-12**), outlining the variation in age from type-i and type-ii uranium minerals, and record more recent remobilization events for type-i uranophane. Type-ii and Cole uranophane are oldest, with four main age groups at 1749 ± 70 Ma, 1359 ± 54 Ma, 1170 ± 47 Ma and 895 ± 36 Ma. There are sporadic younger ages for type-ii uranium, recording more recent alteration, coincident with precipitation of type-i uraninite (~500Ma). The age of type-i uranium mineralization at Kult-82 ranges from 508 ± 20 Ma to a minimum age of 66 ± 3 Ma, recording recent remobilization and precipitation of uranophane, alerted from earlier uraninite.

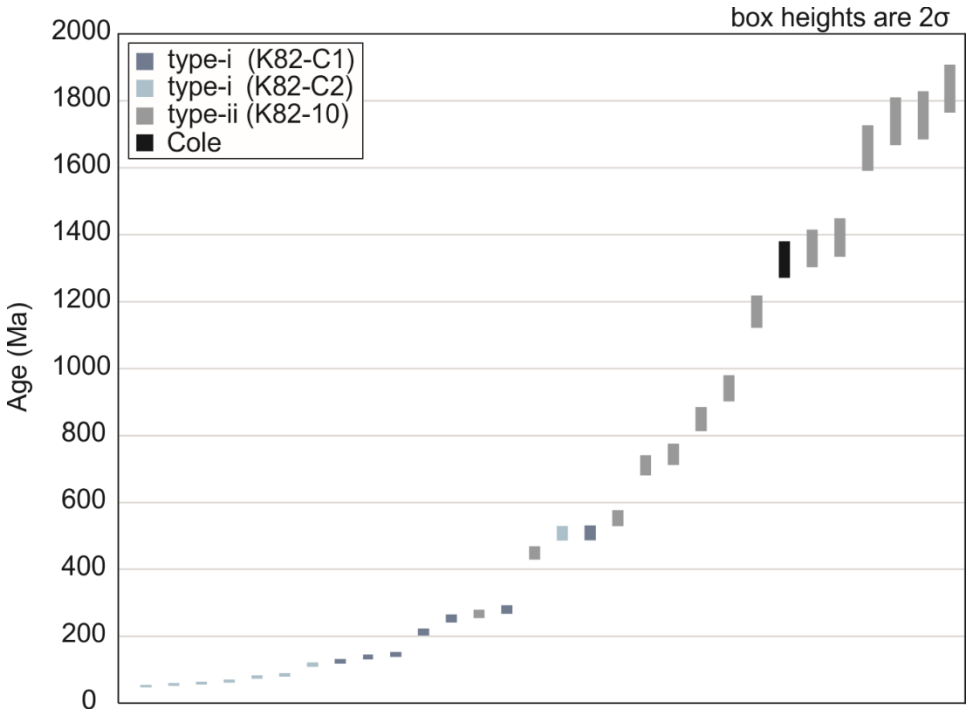

Figure 3-12: U-Pb ages based on uranium mineral EPMA data and Bowles (2015).

Although there were analytical difficulties (i.e., grain size and contamination from surrounding mineral phases) leading to uncertainty within the data (e.g., jagged normalized patterns close to detection limits; **Figure 3-13a**), the chondrite normalized REE signatures for the different styles of mineralization at the Kult-82 occurrence are similar, with high ΣREE+Y, and $LREE_N/HREE_N > 1$, (**Figure 3-13a**). The concentrations of Ce, Dy and Y are used as proxies for LREE, MREE and HREE, respectively. Overall, type-i uraninite and uranophane have higher ΣREE+Y (4.70–9.51 wt.% **Table 3-2**) than type-ii uranophane (0.69–1.05 wt.%; **Table 3-2**). Type-i uranium minerals can be subdivided into two groups based on distinctions in REE chemistry between samples K82-C1 and K82-C2 (**Figure 3-13**). Sample K82-C1 has the highest ΣREE+Y (7.54–9.51 wt.%) and relatively flat patterns, where $LREE_N/HREE_N$ ranges from 1.29–3.69 (**Table 3-2**). Sample K82-C2 contains 4.70–6.15 wt.% ΣREE+Y and high but variable $LREE_N/HREE_N$ ratios (40.34–115.90; **Table 3-2**; **Figure 3-13**). The REE pattern of type-i uranium minerals in sample K82-C2 is more similar with that of type-ii uranium minerals, than type-i uranium minerals in K82-C1, with the exception of much higher LREE in type-i uranium. Type-ii uranium minerals contain less ΣREE+Y overall, and their Eu, Tb, Ho, Y, Er, Tm, Yb and Lu concentrations fall beneath the detection limit for the EPMA (**Figure 3-13**).

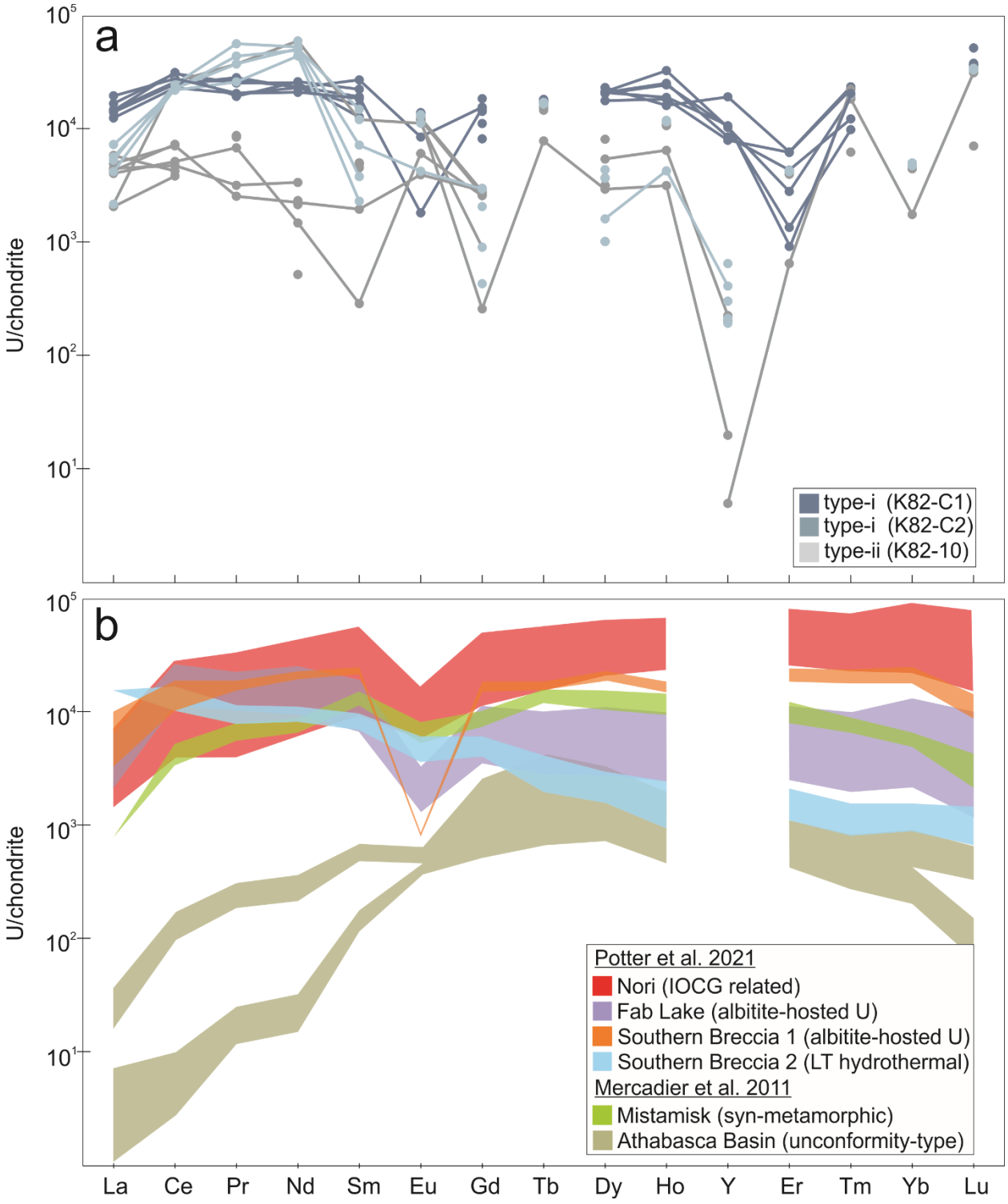

Figure 3-13: Chondrite normalized REE + Y patterns of (a) type-i and type-ii uranium minerals at the Kult-82 (K82) occurrence (full data set in **Table A3-1**). Analyses that fall below the limits of detection are plotted as ½ their respective detection limit, as a single dot; (b) REE signatures of uraninite from high-temperature K-Fe IOCG and albitite-hosted uranium (Fab Lake; Montreuil et al. 2015a; Potter et al. 2021; and Southern Breccia 1; Potter et al. 2021), low-temperature (LT) K-

Fe IOCG (Nori, Southern Breccia 2; Potter et al. 2021) deposits in the Great Bear Magmatic Zone (GBMZ) the Mistamisk syn-metamorphic uranium deposit (Mercadier et al. 2011) and the Unconformity-type uranium deposits from the Athabasca Basin (Mercadier et al. 2011). Chondrite values from (McDonough and Sun 1995).

3.4.3. Chlorite Thermometry

Through petrographic observations, four types of chlorite were distinguished at the MacInnis Lake uranium occurrences, based on crystal habit, colour and birefringence. The four types of chlorite are noted in the paragenetic sequence (**Figure 3-3**) as type-I, type-II, type-III and type-IV. At least ten grains from each textural type recognized were analyzed using EPMA, and the mean compositions are reported in **Table 3-3**. The data were plotted into an Al^{VI}-Fe-Mg ternary diagram (**Figure A3-3**) to classify the species of chlorite (i.e., Fe-rich chamosite or Mg-rich clinochlore).

Type-I chlorite occurs at the Kult-82, Island and Pyramid occurrences and occurs in veins as fine-grained granular to acicular clusters, locally occurring with calcite (± sulphides). At the Kult-82 occurrence, type-I chlorite veins occur with calcite, bornite, magnetite and pitchblende-uranophane mineralization. It can be classified as Mg-rich chamosite, with an average Fe# ranging from 0.55–0.72 which formed around 293– 329 °C (**Table 3-3**).

Type-II chlorite occurs at the Island, Pyramid and Cole occurrences as medium- to coarse-grained lath-like to massive chlorite in veins and interstitial to secondary K-feldspar and quartz and have been variably sericitized. Type-II chlorite is classified as a mix of Fe-rich clinochlore and minor Mg-rich chamosite with averaged Fe#'s ranging from 0.43–0.53 and temperatures ranging from 291–324 °C (**Table 3-3**). Interference colours range from blue-grey-brown in more Fe-rich chlorite to distinct Berlin blue interference colours in more Mg-rich chlorite.

Type-III chlorite occurs as worm-like clusters. Type-III chlorite occurs with quartz-sericite-hematite and uranium-hydroxides at the Cole and Welch occurrences. At the Welch occurrence, it is also associated with rutile and galena. This chlorite can be characterized as Fe-rich chamosite, with an average Fe# of 0.66–0.69 between samples, that formed around 313-323 °C (**Table 3-3**).

Type-IV chlorite occurs late in the paragenesis of MacInnis Lake uranium occurrences as massive chlorite in veins. The composition of type-IV chlorite varies from Fe- to Mg-rich, but has an average Fe# of 0.47 and a temperature of 311 °C (**Table 3-3**).

Table 3-3: Summary of chlorite species from MacInnis Lake uranium occurrences with mean Fe#, Al^{VI} and calculated temperatures for analyzed chlorites. Full data set presented in **Table A3-3**, **Table A3-4**, **Table A3-5**.

Sample No.	Species of chlorite	Petrographic Description of chlorite	Mineral Associations	Fe#*	1σ	Al^{VI}	*T* (°C)§	1σ
Type-I								
K82-C1 (K82)	Fe-rich	Fine-grained granular to acicular clusters in veins with blue-grey-brown interference colours	Chl-Calc-Mt-Bn-**U**	0.70	0.01	1.24	323	4.58
K82-05 (K82)			Chl	0.72	0.01	1.23	329	4.53
K82-01A (K82)			Chl-Calc	0.60	0.02	1.22	303	5.57
GFA-78-128-02 (Isl)			Chl	0.55	0.03	1.19	321	5.15
GFA-78-146A (Pyr)			Chl-Py	0.60	0.12	1.18	293	27.96
Type-II								
GFA-78-132 (Isl)	Mix of Fe- and Mg-rich	Medium- to coarse-grained lath-like to massive with variable blue-grey-brown to Berlin blue interference colours	Chl-Ser-Hem	0.45	0.01	1.14	294	5.10
GFA-78-146B (Pyr)			Chl-Ser-Kfs_2-Qtz	0.53	0.01	1.17	323	6.78
C-02 (Cole)			Chl±Ser	0.44	0.01	1.28	309	22.96
C-04A (Cole)			Chl-Ser-Kfs	0.43	0.01	1.23	324	5.50
C-04B (Cole)			Chl-Ser-Kfs	0.48	0.02	1.24	296	11.50
Type-III								
C-02-2 (Cole)	Fe-rich	Fine- to medium-grained worm-like clusters in veins	Qtz-Chl-Ser-Hm-**U**	0.66	0.03	1.25	333	6.84
W-01-1 (Wel)			Qtz-Chl-Ser-Hem-Rt-Gn-**U**	0.69	0.04	1.19	313	10.87
Type-IV								
C-09 (Cole)	Mg-rich	Massive in veins	Chl-Ser-Qtz-Kfs	0.47	0.05	1.18	311	16.28

Abbreviations: albite (Ab), bornite (Bn), calcite (Calc), chlorite (Chl), hematite (Hem), K-feldspar (Kfs), pyrite (Py), quartz (Qtz), sericite (Ser). Uranium occurrences: Cole, Island (Isl), Kult-82 (K82), Pyramid (Pyr), Welch (Wel).

*Fe# = Fe/(Fe+Mg), averaged by sample

§ Cathelineau (1988), averaged by sample

3.4.4. Whole-Rock Geochemistry

Thirty-six samples were sent for whole-rock geochemical analyses to determine major and trace element compositions using ICS-MS and ICP-OES, respectively. Analyzed rock types were variably altered and locally mineralized granitoids, mineralized sedimentary rocks and unmineralized representative host rocks. Major and trace elements are presented in **Table A3-6** and **Table A3-7**.

Granitoids and Intrusives

All basement granitoids have experienced varying degrees of albitization, locally overprinted by potassic alteration as both sericite and Ba-rich K-feldspar alteration. The variation in unmineralized samples is relatively minimal, but geochemical complexities arise within the mineralized samples (**Figure 3-14a**). In general, granitoids from Kult-82 and locally the Cole and Island occurrences, have lower K/Na ratios, attributed to more pervasive sodic alteration (**Figure 3-14a**). The variation is further established when considering the relationship between K/Al and Na/Al (**Figure 3-14b**), where the majority of the granitoids from Kult-82, Cole, Island and Pyramid vary from albite to potassic (K-feldspar and/or sericite) rich.

The K/Al values range from 0.18 to 0.68 (**Figure 3-14c**) indicating that potassic alteration comes from a mix of both K-feldspar (K/Al = 1) and sericite (K/Al = 0.33), which is consistent with petrographic observations. Chlorite veins are common throughout the granitoids; therefore, the Al content from chlorite should also be considered. There is a negative correlation between K/Al and Mg/Al values: granitoids with high K/Al ratios have low Mg/Al ratios (**Figure 3-14d**), suggesting a mixture of K-feldspar and sericite. Low K/Al ratios have high Mg/Al ratios, suggesting a greater abundance of chlorite at the Island occurrence. However, the Island granitoids

tend to have variable K/Al and Mg/Al contents (**Figure 3-14d**), attributed to a mixture of granitic K-feldspar alteration and sericitization of chlorite, based on petrographic observations.

In general, the basement granitoids show variability in their major element composition based on the relative amounts of quartz, plagioclase, K-feldspar, chlorite, sericite, hematite, rutile and pyrite in each sample. Potassic altered granitoids, however, tend to be Si and K rich and may contain > 5000 ppm Ba, reflecting the abundance of secondary Ba-rich K-feldspar (**Figure 3-14e**). The granitoids at Island contain the highest Ba concentrations (locally > 5000 ppm), whereas granitoids from Kult-82 and Cole contain mid-range Ba (1500-3000 ppm), with the exception of the type-ii uranophane mineralized sample from Kult-82 (K82-10), which contains similar Ba and K concentrations to pervasively potassic altered Island granitoids. The Pyramid granitoids contain low Ba, but variable K, higher in unmineralized samples than mineralized samples (**Figure 3-14e**).

Despite not finding visible mineralization in petrographic observations, the granitoids from Pyramid (sample PY-05) have the highest U/Th values (3008), and are the most enriched in base metals (i.e., Cu, Ag and Au) relative to other mineralized granitoids (**Figure 3-14f, g, h**).

At Kult-82, type-ii uranophane mineralized sample K82-10 is more closely related to albitization, with high U/Th ratios (1851), and low K/Na ratios (0.73; **Figure 3-14a**), despite containing K and Ba concentrations consistent with pervasively K-altered granitoids from Island (**Figure 3-14e**). In this case, type-ii uranophane is hosted within a hematite-sericite breccia, associated with albitized and local Ba-rich K-feldspar altered clasts (**Figure 3-4i**). The potassic alteration occurs as a mixture of both sericite and Ba-rich K-feldspar alteration consistent with petrographic observations (**Figure 3-4i**) and whole-rock geochemical data (**Figure 3-14c**), containing high U/Th values (1851), high Ba (4250 ppm; **Figure 3-14e**), Pb (2690 ppm), Cu (400 ppm; **Figure 3-14f**), Ag (5.15 ppm; **Figure 3-14g**) and Au (67 ppb; **Figure 3-14h**) at Kult-82.

At the Island occurrence, uranium mineralized samples contain the lowest SiO_2 have the highest Fe_2O_3, TiO_2 and locally high Cu (up to 886 ppm; **Figure 3-14e**) values, due to the presence of hematite, rutile and Cu-sulphides. They also contain high U/Th values (up to 1300), reflecting Th-poor uranium minerals, and contain high Pb (1030 ppm), Ag (up to 2.33 ppm; **Figure 3-14f**) and Au (up to 3.91 ppm; **Figure 3-14g**); (**Table A3-7**).

The gabbroic intrusion at the Island occurrence shows variations in major element composition based on alteration assemblages. Samples are characterized by typical gabbro compositions: with low Si (48.80–57.78 wt.% SiO_2), high Fe (13.24–15.23 wt.% Fe_2O_3), Mg (3.54–7.04 wt.% MgO), and Ti (1.13–1.53 wt.% TiO_2). The gabbro is variably sodic and potassic (K-feldspar) altered, confirmed by high Na (1.53–4.08 wt. % Na_2O) and K (0.71–2.03 wt. % K_2O) (**Figure 3-14a, b**) and variable Ba, up to 2230 ppm (**Figure 3-14e**). However, Ca concentrations are variable (0.21–9.28 wt.% CaO) with higher than normal Al (12.53–14.99 wt. % Al_2O_3), attributed to variable chlorite and epidote alteration. The low K/Al and high Mg/Al ratios confirm the presence of mafic minerals, predominately secondary chlorite with lesser primary ferromagnesian minerals (**Figure 3-14d**). When mineralized, U/Th values up to 1000, K/Na ratios are relatively high (**Figure 3-14a**), reflecting that mineralization is associated with potassic alteration, and elevated concentrations of various metals (i.e., Ni, Co, Zn, Ag, Cu) and up to 1180 ppm Pb.

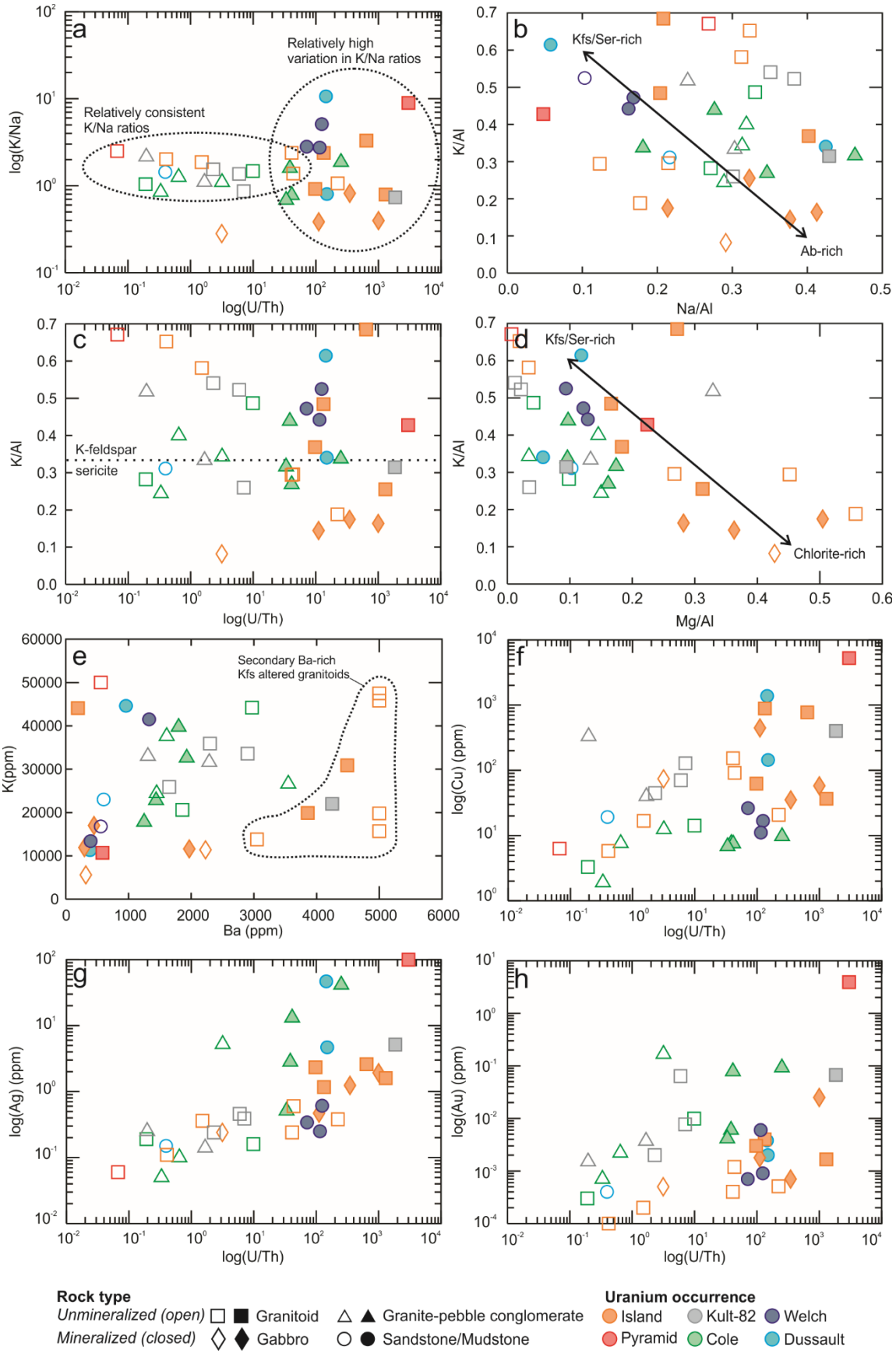
a
Relatively high variation in K/Na ratios
Relatively consistent K/Na ratios
log(K/Na)
log(U/Th)
b
Kfs/Ser-rich
Ab-rich
K/Al
Na/Al
c
K-feldspar sericite
K/Al
log(U/Th)
d
Kfs/Ser-rich
Chlorite-rich
K/Al
Mg/Al
e
Secondary Ba-rich Kfs altered granitoids
K(ppm)
Ba (ppm)
f
log(Cu) (ppm)
log(U/Th)
g
log(Ag) (ppm)
log(U/Th)
h
log(Au) (ppm)
log(U/Th)
Rock type
Unmineralized (open)
Mineralized (closed)
Granitoid
Gabbro
Granite-pebble conglomerate
Sandstone/Mudstone
Uranium occurrence
Island
Pyramid
Kult-82
Cole
Welch
Dussault

Figure 3-14: Biplot diagrams using whole rock geochemical data for mineralized and non-mineralized rock types from various occurrences. (a) log (U/Th) vs. log (K/Na), (b) Na/Al vs. K/Al, (c) log (U/Th) vs. K/Al, (d) K/Al vs. Mg/Al, (e) Ba (ppm) vs. K (ppm), (f) log (U/Th) vs. log (Cu) (ppm), (g) log (U/Th) vs. log (Ag) (ppm), (h) log (U/Th) vs. log (Au) (ppm). Abbreviations: albite (Ab), K-feldspar (Kfs), sericite (Ser).

Nonacho Sedimentary Rocks

The eight samples of variably chloritized conglomerates from the Hjalmar Formation have very similar major element compositions. In general, samples contain Si (48.66–71.12 wt.% SiO_2), Al (13.83–19.12 wt.% Al_2O_3), K (3.57–6.18 wt.% K_2O), Na (1.75–5.00 wt.% Na_2O), Mg (0.59–2.50 wt.% MgO) and variable Ca (0.44–7.16 wt.% CaO). Samples with relatively low Si contain relatively high Al, Ca and Na concentrations (**Table A3-6**).

The Hjalmar sediments contain relatively consistent K/Na values (**Figure 3-14a**) and variable K/Al and Na/Al values (**Figure 3-14b**), suggesting pervasive sodic and potassic alteration. **Figure 3-14c** demonstrates that the potassic alteration in the samples vary from K-feldspar to sericite dominant. Furthermore, the Mg/Al values are < 0.2, attributing the elevated Al concentrations to the potassic alteration of the sediments rather than chloritization (**Figure 3-14d**). The sediments also contain high Ba, up to 3550 ppm, which positively correlates with K concentrations (**Figure 3-14e**). Geochemical data is supported by petrographic observations, where the lack of quartz and the presence of chlorite, sericite and Ba-rich K-feldspar in hand sample and thin section.

At the Cole occurrence, uranium mineralized samples have similar major-element compositions to unmineralized samples, however they are relatively Si, Fe and Ti-rich, where uranophane is spatially associated with rutile and hematite, hosted in sericitized and chloritized quartz breccias (**Figure 3-7**). The trace element composition of mineralized samples varies,

reflected in relatively high U/Th values of up to 252, as well as up to 786 ppm Pb, 41.3 ppm Ag (**Figure 3-14f**) and 92 ppb Au (**Figure 3-14g**).

The Taltson Formation sediments of the Welch and Dussault occurrences are highly chloritized and brecciated by networking quartz veins, giving them a higher Si (70.20–88.03 wt.% SiO_2) content than their conglomeratic counterparts of the Hjalmar Formation. They contain variable K concentrations, but relatively lower Ba concentrations than the Hjalmar sediments (**Figure 3-14e**). The Taltson sediments contain relatively high K/Na ratios (**Figure 3-14a**), attributed to potassic alteration (**Figure 3-14b**). In general, the Dussault samples contain K-feldspar as their dominant potassic alteration phase due to increased K/Al ratios, while the Welch samples contain a mix of K-feldspar and sericite alteration (**Figure 3-14c**). The presence of high K/Al values and low Mg/Al values further supports that the K/Al ratios are related to potassic alteration rather than the presence of chlorite (**Figure 3-14d**). This data is consistent with petrographic observations, where chlorite is pervasively sericitized throughout both uranium occurrences.

The major element geochemical signatures of mineralized samples are consistent between occurrences, however there are apparent variations within trace element signatures, consistent with their respective mineralogy. For example, one uranium mineralized sample from Dussault (D-05) is characterized by elevated Fe (6.51 wt.% Fe_2O_3), 2090 ppm U, > 2000 ppm Bi, 1590 ppm Pb, 1380 ppm Cu (**Figure 3-14e**), 46.9 ppm Ag (**Figure 3-14f**), and 3.8 ppb Au (**Figure 3-14g**), relative to mineralized samples from Welch. The geochemical signatures of sample D-05 are consistent with the presence of disseminated chalcopyrite, galena, minor uranium and local Bi visible in thin section and through SEM analyses (**Figure 3-9e**).

Rare-Earth-Element Signatures

The majority of uranium mineralized and unmineralized samples from MacInnis Lake are characterized by high overall REE (**Figure 3-15a**); however, the uranium mineralized samples contain lower LREE/HREE ratios than unmineralized samples (**Figure 3-15b**), where Ce and Y are used as proxies for LREE and HREE, respectively. Uranium mineralized samples have high ΣREE and a gently negative slope from HREE to LREE and a slightly negative Eu anomaly when normalized to chondrite (**Figure 3-15c**; Sun and McDonough 1989). When normalized to Primitive Mantle (**Figure 3-15d**; Sun and McDonough 1989), the uranium mineralized samples have similar normalized patterns, regardless of their host lithology. They are characterized by a generally negative slope, reflecting relatively higher concentrations of incompatible elements such as large ion lithophiles (**Figure 3-15d**). They are characterized by weakly positive Ba and K anomalies, reflecting Ba-substitution in feldspars during potassic alteration, and strong positive U and Pb anomalies (**Figure 3-15d**). They also contain weak to no negative Eu anomaly, variable Ta, negative Sr and Zr anomalies (**Figure 3-15d**). Uranium mineralized samples from Welch and Dussault have lower overall REE (**Figure 3-15c**) and elevated Cs and Ta, negative Th anomaly and lower LREEs (**Figure 3-15d**).

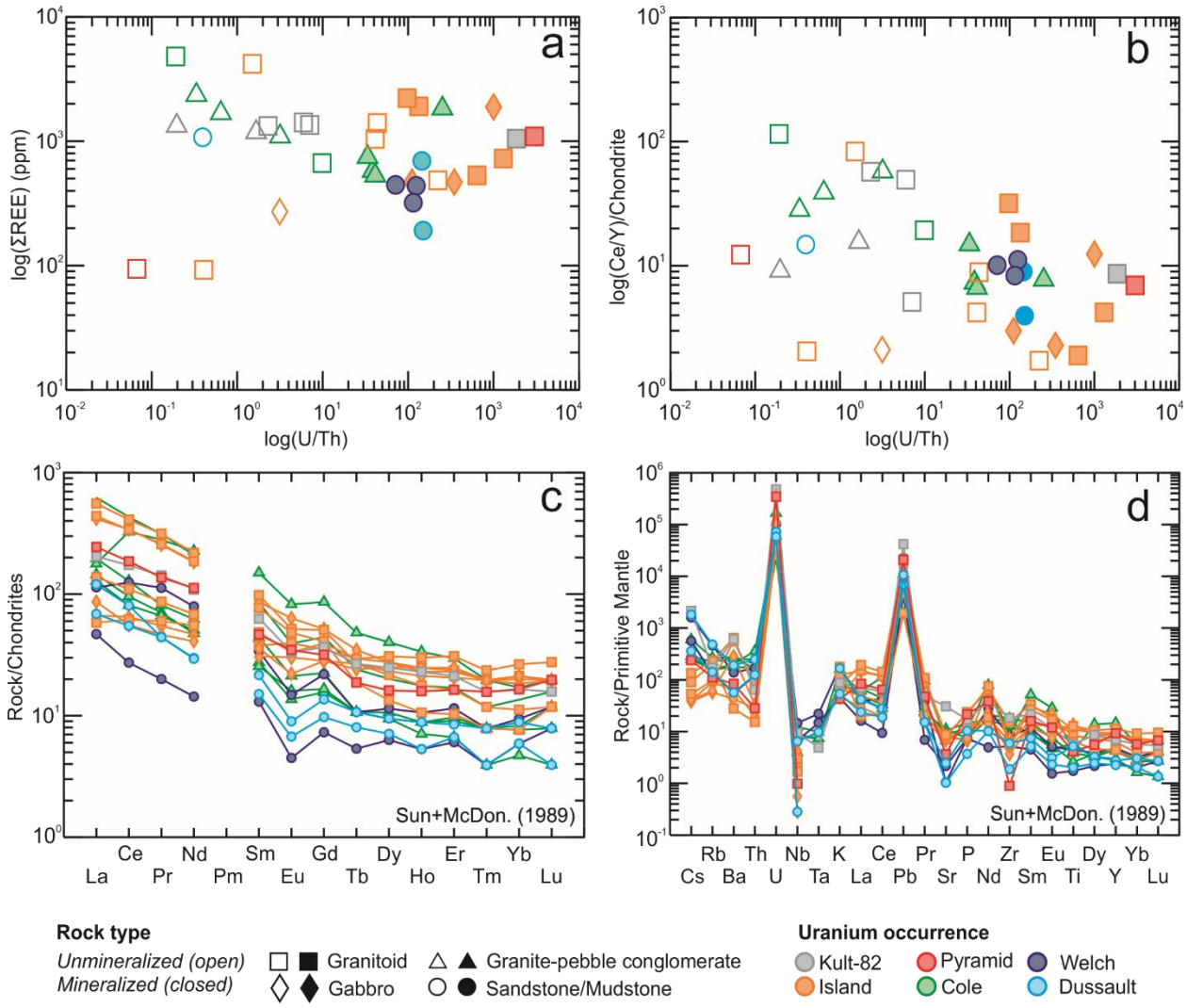

Figure 3-15: Biplot diagrams of mineralized and unmineralized samples showing (a) U/Th vs. log(ΣREE) and, (b) U/Th vs. log (Ce/Y); (REE are chondrite normalized; Sun and McDonough 1989). Mineralized samples distinguished by their occurrence as (c) Chondrite normalized (Sun and McDonough 1989) and (d) Primitive Mantle normalized (Sun and McDonough 1989) spider diagrams.

3.5. Discussion

3.5.1 Alteration Systematics and Paragenesis

The host granitoids and Nonacho sediments have undergone varying degrees of metasomatic alteration. Distinguishing between pervasive albitization and K-feldspar alteration in the field was difficult. Although intense brick-red hues are typically diagnostic of hydrothermal K-feldspar in metasomatic/hydrothermal environments (e.g., Corriveau et al. 2016), at MacInnis Lake, both pervasive albitization and K-feldspar alteration can have a brick-red appearance (i.e., brick-red albitized granitoids at Kult-82; **Figure 3-4d, e**; and brick red K-altered granitoids at Island; **Figure 3-5c**). This is attributed to the presence of fine-grained hematite in both albite and K-feldspar (**Figure 3-5d**), where hematite is precipitated into nano-pores in potassic and/or sodic altered plagioclase (Putnis et al. 2007, Wilde 2013). Utilizing analytical techniques such as colbatinitrite staining (Na–white to pink, K–yellow; i.e., **Figure 3-4d**) was critical in distinguishing the alteration facies in hand sample and determining their paragenetic relationship (**Figure 3-3**).

The pitted and porous end member albite (Ab_{93-100}) is locally infilled with sericite, consistent with low K/Al (~0.3; **Figure 3-14c**) and low Mg/Al values (0.03; **Figure 3-14d**) of the granitoids. The replacement of primary plagioclase and microcline during pseudomorphic albitization increases the porosity of the altered mineral and in turn, the host rocks, as the density of the newly formed albite is lower than that of plagioclase or microcline (Wilde 2013, Kontonikas-Charos et al., 2014). The albitized granitoids are also vuggy and infilled with calcite, that also occurs as veins with chlorite (**Figure 3-4e**). Chlorite also pseudomorphs primary biotite in the granite. Albitization of plagioclase requires dissolution of quartz to liberate Ca^{2+} and Al^{3+} following the reaction:

$$CaAl_3SiO_{8plagioclase} + Si^{4+}_{(aq)} + Na^{+}_{(aq)} \leftrightarrow NaAl_2Si_2O_{8albite} + Al^{3+}_{(aq)} + Ca^{2+}_{(aq)}.$$

It is possible that the calcite formed using the Ca^{2+} provided by albitization. We attribute sericite formation to the Al^{3+} and K^{+} liberated during albitization of plagioclase and microcline, and, K^{+} and H^{+} from the chloritization of biotite, following the reaction:

$$K(Fe_2Mg)AlSi_3O_{10}(OH)_{2biotite} + 2Fe^{2+}_{(aq)} + Al^{3+}_{(aq)} + 6H_2O_{(aq)} \leftrightarrow$$

$$(Fe_4MgAl)AlSi_3O_{10}(OH)_{8chlorite} + K^{+}_{(aq)} + 6H^{+}_{(aq).}$$

Based on the mineral assemblage (albite-sericite-chlorite-calcite) and calculations from Al in chlorite thermometry (**Table 3-3**), the albitization occurred at relatively low-temperatures (< 350 °C).

The brick-red K-feldspar post-dates albitization and is Ba-rich. The Ba-rich K-feldspar alteration is localized along structures and lithological contacts (e.g., the Island occurrence). Feldspars contain Ba-zonation with higher Ba in the core (~11 wt.% BaO) than the rim (~4 wt.% BaO); (**Figure 3-5d**). The K-feldspar altered granitoids are cross-cut by veins of quartz and sericitized chlorite, that contain pyrite, chalcopyrite, hematite, rutile and, locally, uranophane mineralization + galena (**Figure 3-5**). Rutile is present as an aggregate of blocky grains, possibly an alteration product of an earlier ferro-magnesian mineral such as biotite, which can easily undergo Ti-vacancy substitution (Abrecht and Hewitt 1988).

All uranium mineralization at MacInnis Lake post-dates earlier albitization and Ba-rich K-feldspar alteration (**Figure 3-3**). Both uranium mineral types at MacInnis Lake incorporated Si, Fe, Ca and Ba, indicated by EPMA results (**Table 3-2**) and their correlation with U in PCA biplots (**Figure 3-11**). It is typical of secondary uranyl minerals (i.e., uranophane) to commonly contain divalent cations (i.e., Ca^{2+}, Pb^{2+}, Ba^{2+}, Sr^{2+}) in their crystal structure (Finch and Murakami 1999).

The incorporation of Si, Fe and Ca into the crystal structure of uraninite is usually attributed to the substitution of radiogenic Pb during alteration events (Janeczek and Ewing 1992, Alexandre and Kyser 2005, Alexandre et al. 2015). Lead released during alteration is able to be incorporated into galena (i.e., Welch, Dussault and Island; **Figure 3-8d**, **Figure 3-9f**, **Figure 3-5g**), which is an indication of high sulfur fugacity (Janeczek and Ewing 1992; Ono and Fayek 2011). High Ba concentrations (**Table 3-2**), were likely provided by the alteration of earlier Ba-rich K-feldspar, where rims contain low Ba (~4 wt.% BaO) relative to cores (~11 wt.% BaO); (**Figure 3-5d**).

Type-i and type-ii uranium minerals are differentiated by their respective composition and timing (**Table 3-2**; **Figure 3-10**; **Figure 3-12**). Type-i uraninite and uranophane contain low Si (0.83–6.41 wt.% SiO_2) and Ca (1.33–2.57 wt.% CaO) relative to type-ii uranophane (3.72–12.08 wt.% SiO_2; 3.27–4.39 wt.% CaO). The low Pb concentrations of type-i uranium minerals (< 2.37 wt.% PbO) reflect their younger ages (508 ± 20 Ma and 66 ± 3 Ma; **Figure 3-12**), interpreted to record alteration and the recent dissolution-reprecipitation of primary uraninite, on partially dissolved Cu-sulphides, to uraninite + uranophane. Type-ii uranophane contain elevated Pb (3.30–8.19 wt.% PbO) and are distinctly older, with four main age groups at: 1749 ± 70 Ma, 1359 ± 54 Ma, 1170 ± 47 Ma and 895 ± 36 Ma (**Figure 3-12**). There are sporadic younger ages for type-ii uranophane, recording more recent alteration, which coincide with the younger alteration of type-i uranium minerals (~500 Ma; **Figure 3-12**). The chemical distinction and mineral associations between type-i and type-ii uranophane, namely their Pb, Ca and Si concentrations (**Table 3-2**), and variability within the CaO-SiO_2-UO_2 ternary (**Figure 3-10a**), is likely due to two different mineralizing events. One of these produced type-i uraninite with chlorite on Cu-sulfides in veins at some unknown time, as younger alteration disrupted the U-Pb system and formed uraninite+uranophane. The other produced type-ii uranophane with sericite and hematite in

breccias between 1800 and 1700 Ma. Both type-i and type-ii uranium minerals may have experienced similar alteration events ~500 Ma. Based on Al-in-chlorite thermometry, both type-i and type-ii uranium minerals are associated with relatively low-temperature chlorite, between 313-333 °C.

3.5.2 Controls on uranium mineralization

Uranium is highly soluble and mobile in its oxidized uranyl (U^{6+}) state; however, it must be reduced to its immobile, insoluble uranous (U^{4+}) state to form uraninite (Cuney 2009; Yeo and Potter 2010). Reduction can be done through a variety of mechanisms, including anaerobic bacteria, graphite, organic matter, methane, hydrogen sulphide (H_2S) or the presence of reduced Fe in oxides, sulfides and silicate minerals (e.g., magnetite, pyrite, chlorite); (Potter et al. 2019).

At the Kult-82 and Dussault occurrences, vein-hosted type-i uraninite and uranophane (± galena) are texturally associated with chlorite and partially dissolved Cu-sulphides, namely bornite and chalcopyrite (**Figure 3-10**). Considering the uranium minerals form overgrowths on the Cu-sulphides (**Figure 3-4g**; **Figure 3-9f**), we suggest that reduced Fe in the sulphides acted as a reductant for primary uraninite precipitation. These sulfides likely acted as redox buffer during later alteration of uraninite forming both secondary uranophane and uraninite, instead of just uranophane.

The oxidation and secondary alteration of primary uranous minerals, (i.e., uraninite and coffinite; Read et al. 2008, Abd El-Naby 2009), may form uranophane, a U^{6+} silicate mineral (Finch and Murakami 1999, Alexandre et al. 2012). However, uranophane can also precipitate directly form fluid. Uranophane is one of the most common uranyl minerals (Stohl and Smith 1981, Viswanathan and Harnet 1986), and possibly the most common uranium mineral after

uraninite (Finch and Murakami 1999, Alexandre et al. 2012). During the stage of type-ii uranophane mineralization, the conditions were highly oxidized, allowing the oxidized U^{6+} uranyl ions to precipitate directly from the fluid as uranophane alongside hematite (oxidized Fe^{3+}) and sericite, instead of as an alteration product from uraninite.

3.5.3. Classification of Deposit Type

Previous work by Gandhi and Prasad (1980) suggest similarities in the geological context of the Nonacho Basin (i.e., fault-bound sedimentary basin unconformably overlying metamorphosed basement rocks) with Paleoproterozoic basins that host unconformity-type uranium occurrences, such as the Athabasca Basin and the Thelon Basin, which also overly the Rae craton (**Figure 3-1**). While similarities exist between the MacInnis Lake uranium occurrences and unconformity-type uranium deposits (primarily their proximity to the unconformity and low-temperature mineralization), we also note several key differences. The MacInnis Lake uranium occurrences lack clay alteration (i.e., illite, kaolinite), a prominent feature in unconformity-type uranium deposits of the Athabasca and Thelon basins (Reid and Ansdell 2012; Richard et al. 2012; Quirt 2012; Ng et al. 2013; Adlakha and Hattori 2016). The uranium minerals at MacInnis Lake are a mixture of uranophane ± uraninite, whereas uranyl minerals are only observed in one area of the Athabasca Basin (Alexandre et al. 2012b). The chlorite associated with uranium minerals at MacInnis Lake are Fe-rich and relatively higher temperature (313-333 °C) than the ~200 °C sudoite in the Athabasca Basin (Pagel et al. 1980, Kotzer and Kyser 1995, Jefferson et al. 2007, Adlakha and Hattori 2016). Additionally, it is clear that at MacInnis Lake, reduced Fe and sulphide phases were the reductant for type-i mineralization, whereas this textural association for unconformity type uranium deposits is not evident, and still highly debated amongst authors (e.g.,

Kyser et al. 1990, Fayek and Kyser 1997, Alexandre et al. 2009, Yeo and Potter 2010; Ng et al. 2013).

Chondrite-normalized REE signatures of uraninite are interpreted to reflect the mineralizing fluid source or the deposit type (Mercadier et al. 2011), and these are also distinct between MacInnis Lake and unconformity-type uranium deposits. The chondrite normalized REE+Y signatures of MacInnis Lake uranium are high (over 10000X chondrite) and relatively flat lying (**Figure 3-13a**), while the signatures of unconformity-type uranium deposits contain lower REE (between 10 and 1000X chondrite), a slight bell-shaped signature, and lower $LREE_N/HREE_N$ ratios than MacInnis Lake (**Figure 3-13**; **Figure 3-16**; Mercadier et al. 2011). Although deposits of the Athabasca and Thelon basins have some similar structural and mineralogical features to the MacInnis Lake occurrences, we agree with other studies the likelihood of deposits comparable to unconformity-type uranium deposits is low for the Nonacho Basin (Aspler 1985, Jefferson et al. 2007, Jefferson 2013). Furthermore, the minimum age of Nonacho Group, constrained by the Sparrow Dike swarm (1827 Ma; McGlynn et al. 1974), is considered to be too old for unconformity-type uranium deposits that are said to have formed globally after ~1.75 Ga (Cuney 2009, Jefferson 2013).

Uranium enrichment is common in metasomatic iron and alkali calcic (MIAC) alteration systems that host U-bearing IOCG and albitite-hosted uranium deposits (Hitzman and Valenta 2005). The Mosquito Gulch occcurence, located in the southeastern Nonacho Basin, has been described as a albitite-hosted uranium by Gatzweiler et al. (1987); (**Figure 3-2a**). More recent work by Jefferson (2013) and Potter et al. (2013, 2019a) outline the potential for iron oxide copper-gold (IOCG), iron oxide-apatite (IOA) and affiliated deposits (polymetallic skarn, albitite-hosted uranium and epithermal deposits) at the Crest occurrence (**Figure 3-2a**) within the Nonacho Basin

and in the adjacent East Arm region of Great Slave Lake (**Figure 3-1**; Jefferson 2013; Potter et al. 2013, 2019a).

The style and mode of uranium occurrences at MacInnis Lake are similar to those in albitite-hosted uranium deposits by a variety of authors (Belevtsev 1980, Grechishnicov 1980, Cinelu and Cuney 2006, Alexandre 2009b, Wilde 2013). The uranium occurrences at MacInnis Lake post-date extensive albitization, and are hosted along deformation zones, such as the fault, mylonite and cataclasite host rocks that are associated with albitite-hosted uranium deposits. Similar to albitite-hosted uranium deposits, the uranium minerals at MacInnis Lake are locally a mix of uraninite ± uranophane that occur within veins or as micro-inclusions within hematite, and locally have a spatial association to Ti-bearing minerals (Wilde 2013). At Welch, uranophane is spatially associated with rutile and occurs as micro-inclusions within hematite, which is not uncommon for hematite, as it can host up to several wt.% U (i.e., Olympic Dam; Ciobanu et al. 2013). Inclusions of uranium in other phases (i.e., uraniferous titanite, rutile, ilmenite and magnetite) is also common in albitite-hosted uranium deposits (Belevtsev 1980, Grechishnicov 1980, Cinelu and Cuney 2006, Alexandre 2009b). In contrast, the uranium minerals are often associated with sulphides at MacInnis Lake, while sulphides are only present in small quantities in albitite-hosted uranium deposits (Wilde 2013). MacInnis Lake uranium minerals are also enriched in substitution elements (i.e., Si, Fe, Ca, Ba, REE), contain low Th (< 0.12 wt.% ThO_2) and elevated Y (up to 3.8 wt.% Y_2O_3). In contrast to albitite-hosted uranium deposits that characteristically contain elevated Th, intermediate substitution elements and low Y (Alexandre et al. 2015).

The ΣREE and $LREE_N/HREE_N$ ratios for MacInnis Lake uranium is similar to uraninite associated with high-temperature (> 350 °C; Mercadier et al. 2011; Frimmel et al. 2014) IOCG

and affiliated (i.e., albitite-hosted uranium) deposits (i.e., Southern Breccia and Fab from the Great Bear Magmatic Zone; **Figure 3-16**; Montreuil et al. 2015b, Potter et al. 2019b, 2021). Despite the elevated ΣREE at MacInnis Lake, their low Th concentrations and their relationship to low-temperature chlorite (313-333 °C) are inconsistent with high-temperature mineralization. The low Th concentrations in both uranium mineral types at MacInnis Lake (**Table 3-2**) and the lack of correlation with U in PCA space (**Figure 3-11**) eludes to the hydrothermal nature of the uranium minerals, where hydrothermal uranium minerals typically lack Th (Finch and Murakami 1999). Although there are similarities between the MacInnis Lake occurrences and albitite-hosted uranium deposits, there are many differences in mineralogy and uranium mineral chemistry suggesting an albitite-hosted uranium origin for the MacInnis Lake uranium occurrences is unlikely.

We note many similarities between the uranium occurrences at MacInnis Lake and U-bearing hematite group IOCG deposits of the low-temperature K-Fe alteration facies in MIAC alteration systems (Corriveau et al. 2016). The mineral assemblages at MacInnis Lake are similar to that of low-temperature (250–350 °C; Corriveau et al. 2016) K-Fe alteration facies, consisting of hematite, K-feldspar or sericite, ± calcite and chlorite, ± chalcopyrite, bornite, chalcocite, REE, or U-bearing minerals (Hitzman et al. 1992). Host rocks at MacInnis Lake have undergone extensive albitization, potassic alteration as Ba-rich K-feldspar and/or sericite that are locally associated with vein and breccia-hosted uranium mineralization. Similar to type-ii uranium minerals at MacInnis Lake, intense hematite and sericite breccias are also associated with uranium mineralization at the Olympic Dam deposit (Ehrig et al. 2012). The host rocks contain elevated Cu, Ag, LREE, Bi, Ba and U, similar to the signatures of low-temperature K-Fe alteration facies

(Ehrig et al. 2012; Corriveau et al. 2016) and have a spatial association of Cu, Au and Ag with U (**Figure 3-14f, g, h**), as seen at Olympic Dam (Ehrig et al. 2012).

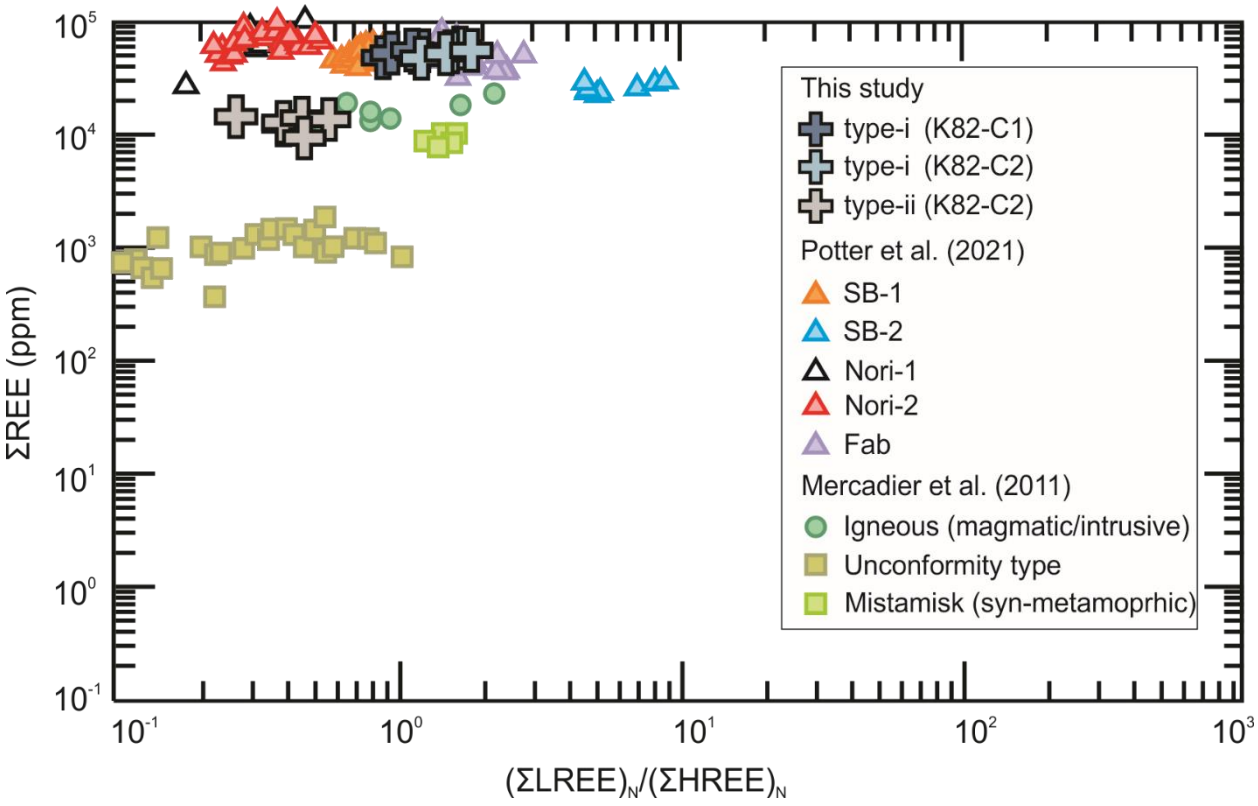

Figure 3-16: ΣREE versus chondrite-normalized light over heavy REE ratioe $(\Sigma LREE)_N/(\Sigma HREE)_N$ for uraninite from various deposit types compared to the MacInnis Lake uranium occurrences. Normalization values from McDonough and Sun (1985), including data from Potter et al. (2021) and Mercadier et al. (2011).

The MacInnis Lake uranium minerals have similar chondrite normalized REE signatures to uraninite from the Nori showing and the remobilized Southern Breccia uraninite in the Great Bear Magmatic Zone (**Figure 3-13**; **Figure 3-16**; Potter et al. 2021). The Nori showing is associated with low-temperature K-Fe alteration (Ootes et al. 2010), and hosts primary (Nori-1) and remobilized and/or altered uraninite (Nori-2) that contain elevated Si, Ca, Fe and Pb (Potter et al. 2021). The ΣREE of Nori uraninite are consistent with type-i uranium minerals, while the $LREE_N/HREE_N$ ratios are more similar to that of type-ii uranophane. The Southern Breccia (SB-2) mineralization occurs as pitchblende with elevated Si, Ca, Fe (+ hematite, chalcopyrite, pyrite,

rutile, F-bearing monazite) in chlorite veins, associated with low-temperature K-Fe alteration of primary (SB-1) uraninite (Montreuil et al. 2015b). The SB-2 mineralization has similar ΣREE but higher $LREE_N/HREE_N$ ratios than uranium minerals at Kult-82 (**Figure 3-16**). Despite having ΣREE > 1 wt.%, uraninite from Nori-1, Nori-2 and SB-2 have low Th (< 0.30 wt.% ThO_2; Potter et al. 2021), variable U/Th ratios (Montreuil et al. 2015b, Potter et al. 2019b, 2021), the result of low-temperature (< 350 °C) hydrothermal mineralization (Potter et al. 2021). Overall, the MacInnis Lake uranium minerals have similar high ΣREE, overall REE signatures, $LREE_N/HREE_N$ ratios, mineral chemistry (e.g., elevated Si, Ca, low Th), mineral associations (e.g., chlorite, hematite, chalcopyrite) and temperature (< 350 °C) to metasomatic uranium mineralization associated with the low-temperature K-Fe alteration facies at Nori and Southern Breccia.

In summary, at MacInnis Lake, the ΣREE are elevated, and $LREE_N/HREE_N$ ratios are relatively flat lying, with slight variations between type-i and type-ii uranium minerals. Their high REE signatures are comparable to magmatic, syn-metamorphic and IOCG style uraninite mineralization; however, the low Th contents (< 0.12 wt.% ThO_2), occurrence with low-temperature (313-333 °C) chlorite, is inconsistent with that of high-temperature IOCG of affiliated (e.g., albitite-hosted uranium) mineralization or other high-temperature (i.e., intrusive, metamorphic) mineralization. Instead, the low-temperature (< 350 °C) hydrothermal uranium minerals at MacInnis Lake show chemical (i.e., enriched Cu, Ag, LREE, Bi, Ba and U) and mineralogical similarities (i.e., hematite, K-feldspar, sericite, calcite, chlorite, chalcopyrite, bornite, and U-minerals) with the uraninite in low-temperature hematite group IOCG deposits of the K-Fe alteration facies in MIAC systems. Metasomatic iron and alkali-calcic mineral systems typically occur within geological belts, spanning hundreds of kilometers, where development of

alteration facies depends on a variety of factors (e.g., depth and metasomatic pathway of fluids; Corriveau et al. 2016, 2019, Montreuil et al. 2016). The low-temperature K-Fe alteration associated with uranium occurrences MacInnis Lake, and the geological context of the Nonacho Basin as a structurally controlled, highly deformed and altered basin that underwent multiple tectono-metamorphic events (e.g., Ashton et al., 2009, Hoffman 1988 Berman et al. 2005, 2010; Hartlaub et al. 2007; Pehrsson et al. 2013a, b) and is proximal to orogenic zones (i.e., Taltson and Thelon suture zones; Hoffman 1988) suggests high prospectivity for hematite-group IOCG deposits, and MIAC alteration systems in the area.

3.6. Conclusion

Uranium mineralization at MacInnis Lake is hosted in albitized and potassic altered basement granitoids and overlying sedimentary units along structural corridors surrounding, and within, the MacInnis Lake sub-basin. Two types of uranium minerals are characterized: type-i) uranophane ± uraninite, with or without galena, as overgrowths on earlier, partially dissolved bornite and chalcopyrite in quartz-chlorite ± calcite veins and stockwork (i.e., Kult-82 and Dussault and; type-ii) a chemically distinct earlier phase of uranophane spatially associated with, or as micro-inclusions within, hematite and/or rutile in quartz and pervasively sericitized chlorite veins, stockwork and breccias (i.e., Kult-82, Island, Cole and Welch). Both types of uranium minerals at MacInnis Lake contain elevated ΣREE+Y, and relatively flat lying $LREE_N/HREE_N$ ratios, with slight variations between type-i and type-ii. There are many similarities between the uranium mineral chemistry (e.g., elevated ΣREE+Y, Si, Ca, low Th), mineral associations (i.e., hematite, K-feldspar, sericite, calcite, chlorite, chalcopyrite, bornite, and U-minerals), and whole-rock geochemistry (Cu, Ag, LREE, Bi, Ba, U+/- Au) with those characteristic of low-temperature K-Fe alteration facies. The MacInnis Lake uranium occurrences are therefore, best classified as

metasomatic uranium, interpreted to be the result of remobilized uranyl minerals from low-temperature (< 350 °C) hydrothermal fluids associated with low-temperature K-Fe alteration. The differences in timing and uranium mineral chemistry point to a complex history of multiple mineralizing events at MacInnis Lake and various phases of MIAC alteration that may be related to a more complex and wide spread MIAC system throughout the Nonacho Basin.

3.7. References

Abd El-Naby, H.H. 2009. High and low temperature alteration of uranium and thorium minerals, Um Ara granites, south Eastern Desert, Egypt. Ore Geology Reviews, **35**: 436–446. doi:10.1016/j.oregeorev.2009.02.006.

Abrecht, J., and Hewitt, D.A. 1988. Experimental evidence on the substitution of Ti in biotite. American Mineralogist, **73**: 1275–1284.

Adlakha, E.E., and Hattori, K. 2016. Paragenesis and composition of tourmaline types along the P2 fault and McArthur river uranium deposit, Athabasca Basin, Canada. Canadian Mineralogist,. doi:10.3749/canmin.1500057.

Adlakha, E.E., Hattori, K., Davis, W.J., and Boucher, B. 2017. Characterizing fluids associated with the McArthur River U deposit, Canada, based on tourmaline trace element and stable (B, H) isotope compositions. Chemical Geology,. doi:10.1016/j.chemgeo.2017.06.030.

Aitchison, J. 1982. The Statistical Analysis of Compositional Data. Journal of the Royal Statistical Society: Series B (Methodological), **44**: 139–160. doi:10.1111/j.2517-6161.1982.tb01195.x.

Alexandre, P. 2009. Mineralogy and geochemistry of the sodium metasomatism-related uranium occurrence of Aricheng South , Guyana. Mineralium Deposita,. doi:10.1007/s00126-010-0278-7.

Alexandre, P., Kyser, K., and Jiricka, D. 2009. Critical geochemical and mineralogical factors for the formation of unconformity-related uranium deposits:Comparison between barren and mineralized systems in the athabasca basin, Canada. Economic Geology, **104**: 413–435. doi:10.2113/gsecongeo.104.3.413.

Alexandre, P., Kyser, K., Jiricka, D., and Witt, G. 2012a. Formation and evolution of the centennial unconformity-related uranium deposit in the South-Central Athabasca Basin, Canada. Economic Geology, **107**: 385–400. doi:10.2113/econgeo.107.3.385.

Alexandre, P., Kyser, K., Layton-Matthews, D., Joy, B., and Uvarova, Y. 2015. Chemical compositions of natural uraninite. Canadian Mineralogist, **53**: 595–622. doi:10.3749/canmin.1500017.

Alexandre, P., Kyser, K., Polito, P., and Thomas, D. 2005. Alteration mineralogy and stable isotope geochemistry of Paleoproterozoic basement - Hosted unconformity-type uranium deposits in the Athabasca Basin, Canada. Economic Geology, **100**: 1547–1563. doi:10.2113/gsecongeo.100.8.1547.

Alexandre, P., and Kyser, T.K. 2005. Effects of cationic substitutions and alteration in uraninite, and implications for the dating of uranium deposits. Canadian Mineralogist, **43**: 1005–1017. doi:10.2113/gscanmin.43.3.1005.

Alexandre, P., Uvarova, Y., and Kyser, T.K. 2012b. Origin of uranous and uranyl minerals at the centennial deposit, Athabasca Basin, northern Saskatchewan, Canada. Canadian Mineralogist, **50**: 693–704. doi:10.3749/canmin.50.3.693.

Alkis Kontonikas-Charos, Cristiana L. Ciobanu, N.J.C. 2014. Albitization and redistribution of REE and Y in IOCG systems: Insights from Moonta-Wallaroo, Yorke Peninsula, South

Australia,. Lithos, **208**–**209**: 178–201. doi:https://doi.org/10.1016/j.lithos.2014.09.001.

Ashton, K.E., Hartlaub, R.P., Heaman, L.M., Morelli, R.M., Card, C.D., Bethune, K., and Hunter, R.C. 2009. Post-Taltson sedimentary and intrusive history of the southern Rae Province along the northern margin of the Athabasca Basin, Western Canadian Shield. Precambrian Research. doi:10.1016/j.precamres.2009.

Ashton, K.E., Rayner, N.M., Heaman, L.M., Creaser, R.A., and Sm-nd, R.A.N. 2014. New Sm-Nd and U-Pb Ages from the Zemlak and South-Central Beaverlodge Domains : A Case for Amalgamated Taltson Basement Complex and Proto-Rae Cratonic Blocks within the Rae Province of Northwestern Saskatchewan. **2**: 1–26.

Aspler, L.B. 1985. GE : OLOGY OF NONACHO BASIN (EARLY PROTEROZOIC) NWT . LAWRENCE B ,. ASPlER.

Aspler, L.B., and Donaldson, J.A. 1985. The Nonacho Basin (Early Proterozoic), Northwest Territories, Canada: sedimentation and deformation in a strike-slip setting. Strike-slip deformation, basin formation, and sedimentation,: 193–209. SEPM, Tulsa; Special Publication 37. doi:10.2110/pec.85.37.0193.

Bekker, A., Holland, H.D., Wang, P.-L., Rumble, D., I., Stein, H.J., Hannah, J.L., Coetzee, L.L., and Beukes, N.J. 2004. Dating the rise of atmospheric oxygen. Nature, **427**: 117–120.

Belevtsev, Y.. 1980. Endogenic uranium deposits of precambrian shields: Environment of deposition. Albitized Uranium Deposits: Six Articles Translated from Russian Literature; Abou-Zied, S., Kerns, G., Eds.; U.S. Department of Energy: Washington, DC, USA, 1980,: 55–80.

Berman, R.G. 2010. Metamorphic map of the western Churchill Province. Geological Survey Canada Open File 5279 (3 sheets, 49 p. report),.

Berman, R.G., Davis, W.J., and Pehrsson, S. 2007. Collisional Snowbird tectonic zone resurrected: Growth of Laurentia during the 1.9 accretionary phase of the Hudsonian orogeny. Geology, **35**: 911–914. doi:10.1130/G23771A.1.

Berman, R.G., Davis, W.J., Whalen, J.B., Taylor, B.E., Mcmartin, I., Mccurdy, M.W., Mitchell, R.K., Ma, S., Coyle, M., Roberts, B., and Craven, J.A. 2018. Report of activities for the GEM-2 Chantrey-Thelon activity : Thelon tectonic zone project , Nunavut. Geological Survey of Canada, Open File,: 22.

Berman, R.G., Pehrsson, S., Davis, W.J., Ryan, J.J., Qui, H., and Ashton, K.E. 2013a. The Arrowsmith orogeny: Geochronological and thermobarometric constraints on its extent and tectonic setting in the Rae craton, with implications for pre-Nuna supercontinent reconstruction. Precambrian Research, **232**: 44–69. Elsevier B.V. doi:10.1016/j.precamres.2012.10.015.

Berman, R.G., Pehrsson, S., Davis, W.J., Ryan, J.J., Qui, H., and Ashton, K.E. 2013b. The Arrowsmith orogeny: Geochronological and thermobarometric constraints on its extent and tectonic setting in the Rae craton, with implications for pre-Nuna supercontinent reconstruction. Precambrian Research, **232**: 44–69. Elsevier. doi:10.1016/J.PRECAMRES.2012.10.015.

Berman, R.G., Sanborn-Barrie, M., Stern, R.A., and Carson, C.J. 2005. Tectonometamorphism at ca. 2.35 and 1.85 Ga in the rae domain, western Churchill Province, Nunavut, Canada: Insights from structural, metamorphic and in situ geochronological analysis of the

southwestern Committee Bay Belt. Canadian Mineralogist, **43**: 409–442. Mineralogical Association of Canada. doi:10.2113/GSCANMIN.43.1.409.

Berman, R.G., Sandeman, H.A., and Camacho, A. 2010. Diachronous Palaeoproterozoic deformation and metamorphism in the Committee Bay belt, Rae Province, Nunavut: insights from 40Ar-39Ar cooling ages and thermal modelling. Journal of Metamorphic Geology, **28**: 439–457. doi:10.1111/J.1525-1314.2010.00873.X.

Bostock, H.H., van Breemen, O. 1992. Thetiming ofemplacement,and distribution of the Sparrow diabase dyke swarm, District of Mackenzie, Northwest Territories. In: Radiogenic Age and Isotopic Studies: Report 6, Geological Survey of Canada. *In* Paper 92-2. Geological Survey of Canada.

Bostock, H.H., van Breeman, O., and Loveridge, W.D. 1991. Further geochronology of plutonic rocks in the northern Taltson Magmatic Zone, District Mackenzie, N.W.T. Geological Survey Canada, **90**: 67–78.

Bowles, J.F.W. 1990. Age dating of individual grains of uraninite in rocks from electron microprobe analyses. Chemical Geology, **83**: 47–53.

Bowles, J.F.W. 2015. Age Dating from Electron Microprobe Analyses of U, Th, and Pb: Geological Advantages and Analytical Difficulties. Microscopy and Microanalysis, **21**: 1114–1122. doi:10.1017/S1431927615000446.

Van Breemen, O., Kjarsgaard, B.A., Tella, S., Lemkow, D., Aspler, L. 2013. . U-Pb detrital zircon geochronology of clastic sedimentary rocks of the Paleoproterozoic Nonacho and East Arm basins, Thaidene Nena MERA study area. In: Wright, D.F., Ambrose, E. J., Lemkow, D., Bonham-Carter, G. (Eds.), Mineral and Energy Resource Assessment of the proposed

Thaidene Nene National Park Reserve in the area of the east arm of Great Slave Lake, Northwest Territories. Geological Survey of,: 119142. doi:https://doi.org/10.4095/292453.

Van Breemen, O., Bostock, H.., and Loveridge, W.D. 1992. Geochronology of granites along the margin of the northern Taltson magmatic zone and western Rae Province, Northwest Territories. Geological Survey of Canada Paper, **91**: 17–24.

Burron, I., da Costa, G., Sharpe, R., Fayek, M., Gauert, C., and Hofmann, A. 2018. 3.2 Ga detrital uraninite in the Witwatersrand Basin, South Africa: Evidence of a reducing Archean atmosphere. Geology, **46**: 295–298. doi:10.1130/G39957.1.

Campbell Todd, R. 1956. Report on exploration on the MacInnis Lake property of Canadian Pipelines and Petroleum Limited, Northwest Territories; Scurry-Rainbow Oil Limited, unpublished report,.

Canam, R., Gibson, H. d., Martel, E., and Kellet, D. 2021. The Timing of Deformation and Kinematics of Shear Zones in the Nonacho Lake area. *In* Yellowknife Geoscience Forum: Geoscience and Exploration.

de Caritat, P., Hutcheon, I., and Walshe, J.L. 1993. Chlorite geothermometry: A review. Clays and Clay Minerals, **41**: 219–239. doi:10.1346/CCMN.1993.0410210.

Cathelineau, M. 1988. Cation site occupancy in chlorites and illites as a function of temperature. Clay Minerals, **23**: 471–485. doi:https://doi.org/10.1180/claymin.1988.023.4.13.

Checklin, G.A. 1968. MacInnis Lake project (AFE 2-27); Scurry-Rainbow Oil Limited, unpublished report.

Chen, S., Hattori, K., and Grunsky, E.C. 2016. Multivariate statistical analysis of the REE-

mineralization of the Maw Zone, Athabasca Basin, Canada. Journal of Geochemical Exploration, **161**: 98–111. Elsevier B.V. doi:10.1016/j.gexplo.2015.11.009.

Chi, G., Haid, T., Quirt, D., Fayek, M., Blamey, N., and Chu, H. 2016. Petrography, fluid inclusion analysis and geochronology of the End uranium deposit, Kiggavik, Nunavut, Canada [online]. Mineralium Deposita, **52**: 211–232. doi:10.1007/s00126-016-0657-9.

Cinelu, S.; Cuney, M. 2006. Sodic metasomatism and U-Zr mineralization: A model based on the Kurupung batholith (Guyana). Geochimica et Cosmochimica Acta, **70**. doi:doi:10.1016/j.gca.2006.06.120.

Ciobanu, C.L., Wade, B.P., Cook, N.J., Schmidt Mumm, A., and Giles, D. 2013. Uranium-bearing hematite from the Olympic Dam Cu-U-Au deposit, South Australia: A geochemical tracer and reconnaissance Pb-Pb geochronometer. Precambrian Research, **238**: 129–147. Elsevier B.V. doi:10.1016/j.precamres.2013.10.007.

Cloutier, M.A., Bethune, K.M., Ashton, K.E., and Deane, J.M.K. 2021. U-Pb geochronology, geochemistry, and isotopic composition of granitoids across the Nolan-Zemlak domain boundary in the SW Rae craton, Laurentia: Evidence for a late Neoarchean suture reworked during Arrowsmith orogen. Precambrian Research, **362**: 106303. Elsevier B.V. doi:10.1016/j.precamres.2021.106303.

Comas-Cufí, M., and Hió-Henestrosa, T. 2011. CoDaPack 2.0: a stand-alone, multi-platform compositional software. *In* Egozcue JJ, Tolosana-Delgado R, Ortego MI, eds. CoDaWork'11: 4th International Workshop on Compositional Data Analysis. Sant Feliu de Guíxols;

Corcoran, L., and Simonetti, A. 2020. Geochronology of uraninite revisited. Minerals, **10**. doi:10.3390/min10030205.

Corrigan, D., Pehrsson, S., Wodicka, N., and de Kemp, E. 2009. The Palaeoproterozoic Trans-Hudson Orogen: A prototype of modern accretionary processes. Geological Society Special Publication, **327**: 457–479. doi:10.1144/SP327.19.

Corriveau, L., Hamid Mumin, A., and Potter, E.G. 2019. Mineral systems with iron oxide copper-gold (Ag-Bi-Co-U-REE) and affiliated deposits: introduction and overview. *In* Corriveau, L., Potter, E.G. and Mumin, A.H., eds., Mineral systems with iron oxide copper-gold (IOCG) and affiliated deposits: Geological Association of Canada, Special Paper 52. pp. 1–26.

Corriveau, L., Montreuil, J.-F., De Toni, A.F., Potter, E.G., and Percival, J.B. 2022. Mapping mineral systems with IOCG and affiliated deposits: a facies approach. Corriveau, L., Potter, E.G. and Mumin, A.H., eds., Mineral systems with iron oxide copper-gold (IOCG) and affiliated deposits: Geological Association of Canada, Special Paper 52,: 69–111.

Corriveau, L., Montreuil, J.F., and Potter, E.G. 2016. Alteration facies linkages among iron oxide copper-gold, iron oxide-apatite, and affiliated deposits in the great bear magmatic zone, Northwest Territories, Canada. Economic Geology, **111**: 2045–2072. doi:10.2113/econgeo.111.8.2045.

Cousens, B., Chiarenzelli, J., Donaldson, J., Peterson, T., and Lecheminant, A. 2001. Enriched Archean lithospheric mantle beneath western Churchill Province tapped during Paleoproterozoic orogenesis. Geological Society of America, **29**: 827–830.

Cuney, M. 2009. The extreme diversity of uranium deposits. Mineralium Deposita, **44**: 3–9. doi:10.1007/s00126-008-0223-1.

Cuney, M. 2010. Evolution of uranium fractionation processes through time: Driving the secular variation of uranium deposit types. Economic Geology, **105**: 553–569.

doi:10.2113/gsecongeo.105.3.553.

Cuney, M. 2014. Felsic magmatism and uranium deposits. Bulletin de la Societe Geologique de France, **185**: 75–92. doi:10.2113/gssgfbull.185.2.75.

D'Souza, R.J. 2012. Geochemistry and source-tracing of the Sparrow Dyke Swarm, the Tsu Lake dykes, the Martin Group Igneous Rocks and the Christopher Island Formation.

Davis, W.J., Berman, R.G., Nadeau, L., and Percival, J.A. 2014. U-Pb zircon geochronology of a transect across the Thelon tectonic zone, Queen Maud region, and adjacent Rae craton, Kitikmeot Region, Nunavut, Canada. doi:doi:10.4095/295177.

Davis, W.J., Pehrsson, S.J., and Percival, J.. 2015. Results of a U-Pb zircon geochronology transect across the southern Rae craton, Northwest Territories, Canada.

Dazé, A., Lee, J.K.W., and Villeneuve, M. 2003. An intercalibration study of the Fish Canyon sanidine and biotite 40Ar/39Ar standards and some comments on the age of the Fish Canyon Tuff. Chemical Geology, **199**: 111–127.

Dieng, S., Kyser, K., and Godin, L. 2013. Tectonic history of the North American shield recorded in uranium deposits in the Beaverlodge area, northern Saskatchewan, Canada. Precambrian Research, **224**: 316–340. Elsevier B.V. doi:10.1016/j.precamres.2012.09.011.

Dieng, S., Kyser, K., and Godin, L. 2015. Genesis of multifarious uranium mineralization in the Beaverlodge area, Northern Saskatchewan, Canada. Economic Geology, **110**: 209–240. doi:10.2113/econgeo.110.1.209.

Doi, K., Yamamoto, I., Arden, J., and Thorne, D. 1971. Geological Report on the Hope Group, Nonacho Lake Area, NWT.

Ehrig, K., McPhie, J., and Kamenetsky, V. 2012. Geology and Mineraligocal Zonation of the Olympic Dam Iron Oxide Cu-U-Au-Ag Deposit, South Australia. Society of Economic Geologists Special Publication,: 237–267. doi:10.5382/sp.17.

Farkas, A. 1984. Mineralogy and host rock alteration of the Lone Gull deposit: Urangesellschaft Internal Report.

Fayek, M., and Kyser, T.K. 1997. Characterization of multiple fluid-flow events and rare-earth-element mobility associated with formation of unconformity-type uranium deposits in the Athabasca Basin, Saskatchewan. Canadian Mineralogist, **35**: 627–658.

Finch, R., and Murakami, T. 1999. Systematics and paragenesis of uranium minerals. Uranium: Mineralogy, Geochemistry, and the Environment,: 91–179. doi:10.1515/9781501509193-008.

Frimmel, H.E., Schedel, S., and Brätz, H. 2014. Uraninite chemistry as forensic tool for provenance analysis. Applied Geochemistry, **48**: 104–121. Elsevier Ltd. doi:10.1016/j.apgeochem.2014.07.013.

Gandhi, S.S., and Prasad, N. 1980. Geology and Uranium Occurrences of the MacInnis Lake Area, District of MacKenzie. Geological Survey of Canada, Paper 80-1B.

Gatzweiler, R., Von Pechmann, E., Loewer, R., Strnad, G., and Fritsche, R. 1987. Albitite-type uranium mineralization in the Nonacho Basin area, Northwest Territories, Canada. Uranium Resources and Geology of North America for the International Atomic Energy Agency (IAEA),: 491–518.

Grechishnicov, N.. 1980. Structural setting of one type of uranium-albitite mineralisation in

Precambrian rocks. Albitized Uranium Deposits: Six Articles Translated from Russian Literature; Abou-Zied, S., Kerns, G., Eds.; U.S. Department of Energy: Washington, DC, USA1,.

Hammer, Ø., Harper, D.A.T., and Ryan, P.D. 2001. PAST: Paleontological statistics software package for education and data analysis. Palaeontologia Electronica, **4**: 99. Available from http://palaeo-electronica.org/2001_1/past/issue1_01.htm.

Harrington, E. 1980. Thekuthili Lake Project, Northwest Territories, Assessment Work Report-1979; PNC Exploration (Canada) Limited; unpublished report.

Hartlaub, A.R.P., Heaman, L.M., Chacko, T., Ashton, K.E., The, S., March, N., Hartlaub, R.P., Heaman, L.M., Chacko, T., and Ashton, K.E. 2007. Circa 2 . 3 - Ga Magmatism of the Arrowsmith Orogeny , Uranium City Region , Western Published by : The University of Chicago Press Circa 2 . 3-Ga Magmatism of the Arrowsmith Orogeny , Uranium City Region , Western Churchill Craton , Canada. University of Chicago Press, **115**: 181–195.

Hegge, M.R., and Trigg, C.M. 1967. Results of diamond drilling on claim no. 22, Pyramid group, MacInnis Lake, Northwest Territories; Territorial Uranium Miners Limited; Department of Indian and Northern Affairs document no. N019973.

Henderson, J.F. 1937. NONACHO LAKE AREA , NORTHWEST TERRITORIES. Geol. Surv. of Can., **Paper 37-2**: 22.

Hillacre, S., Ansdell, K., and McEwan, B. 2021. Geology, structural analysis, and paragenesis of the arrow uranium deposit, Western Athabasca Basin, Saskatchewan, Canada: Implications for the development of the patterson lake corridor. Economic Geology, **116**: 285–321. doi:10.5382/ECONGEO.4797.

Hitzman, M.C., Oreskes, N., and Einaudi, M.T. 1992. Geological characteristics and tectonic setting of Properozoic iron oxide (Cu-U-Au-REE) deposits. Precambrian Research, **58**: 241–287.

Hitzman, M.C., and Valenta, R.K. 2005. Uranium in iron oxide-copper gold (IOCG) systems. Economic Geology, **100**: 1657–1661.

Hoffman, P.F. 1988. United plates of America, the birth of a craton: Early Proterozoic assembly and growth of Laurentia. doi:10.1146/annurev.ea.16.050188.002551.

Ielpi, A., Martel, E., Fischer, B., Pehrsson, S.J., Tullio, M., and Neil, B.J.C. 2021. A reappraisal of the Nonacho Basin (Northwest Territories, Canada): Record of post-orogenic collapse and marine flooding in the Palaeoproterozoic of the Rae Craton. Precambrian Research, **358**: 106140. Elsevier. doi:10.1016/J.PRECAMRES.2021.106140.

International Atomic Energy Agency (IAEA). 2009. World distribution of uranium deposits (UDEPO) with uranium deposit classification. IAEA-TECDOC-1629, Division of Nuclear Fuel Cycle,: 58–61. doi:ISBN 978-92-0-1-110509-7 NV - 1629.

Janeczek, J., Ewing, R.C. 1992. Dissolution and alteration of uraninite under reducing conditions. Journal of Nuclear Materials, **190**: 157–173.

Janeczek, Janusz; Ewing, R.C. 1992. Structural formula of uraninite. Journal of Nuclear Materials, **190**: 128–132.

Jefferson, C.W. 2013. Uranium Potential and Levels of Radioactivity in the Proposed National Park Area:

Jefferson, C.W., Pehrsson, S.J., Peterson, T., Tschirhart, V., Anand, A., Wollenberg, P.,

LeCheminant, A.N., Riegler, T., Bethune, K., Chorlton, L.B., McEwan, B., Tschirhart, P., Scott, J.M.J., Davis, W., McNicoll, V., Riemer, W., Patterson, J., Morris, W.A., and Stieber, C. 2015a. Outcrop and remote predictive geology of the western Marjorie–Tehek supracrustal belt and Northeast Thelon Basin margin in parts of NTS 66A and 66B, Nunavut.

Jefferson, C.W., Thomas, D.J., Gandhi, S.S., Ramaekers, P., Delaney, G., Brisbin, D., Cutts, C., Quirt, D., Portella, P., and Olson, R.A. 2007. Unconformity associated uranium deposits of the Athabasca Basin, Saskatchewan and Alberta. : 273–305.

Jefferson, C.W., White, J.C., Young, G.M., Patterson, J., Tschirhart, V., Pehrsson, S.J., Calhoun, L., Rainbird, R.H., Peterson, T., Davis, W.J., Tella, S., Chorlton, L.B., Scott, J.M.J., Davis, W.J., Percival, J.A., Morris, W.A., Keating, P., Anand, A., Shelat, Y., and MacIsaac, D. 2015b. Outcrop and remote predictive geology of the Amer Belt and basement beside and beneath the northeast Thelon Basin in parts of NTS 66A, B, C, F, G and H, Nunavut.

Johnstone, D.D., Bethune, K.M., Card, C.D., and Tschirhart, V. 2020. Structural evolution and related implications for uranium mineralization in the patterson lake corridor, southwestern athabasca basin, saskatchewan, canada. Geochemistry: Exploration, Environment, Analysis, **21**. doi:10.1144/geochem2020-030.

Jolliffe, I.T. 1986. Principal Component Analysis. Encyclopedia of Statistics in Behavioral Science,.

Kjarsgaard, B.A., Kerswill, J.A., and Jenner, G.. 1997. Lithostratigraphy and metallogenic implications of komatiite - banded iron formation - felsic volcanic rocks of the Archean Woodburn Lake group, Pipedream lake, central Churchill Province, Northwest Territories.

Koehler, G.J. 1957. Geological Report, MacInnis Property, Island Zone; Mackenzie Mining

District, N.W.T.; Consolidated Mining and Smelting Company Limited, unpublished report.

Kotzer, T.G., and Kyser, T.K. 1993. O, U, and Pb isotopic and chemical variations in uraninite: implications for determining the temporal and fluid history of ancient terrains. American Mineralogist, **78**: 1262–1274.

Kotzer, T.G., and Kyser, T.K. 1995. Petrogenesis of the Proterozoic Athabasca Basin, northern Saskatchewan, Canada, and its relation to the diagenesis, hydrothermal uranium mineralization, and paleohydrology. Chemical Geology, **120**: 45–89.

Kuiper, K.F., Deino, A., Hilgen, F.J., Krijgsman, W., Renne, R., and Wijbrans, J.. 2008. Synchronizing Rock Clocks of Earth History. Science, **320**: 500–504.

Kuronuma, C. 1984. Assessment Report of the Thekuthili Lake Project on Mineral Claims Kule 13, 41, 48, 51, 52, 53, 59, 71, 72, 74, 75, 76, 77, 78, 79, 80, 81, 82.

Kyser, T.K., Kotzer, T., and Sibbald, T.I.I. (n.d.). Oxygen, U-Pb and Pb-Pb Isotope Systematics in Uraninite from Complex U-Au-PGE Vein-Type and Unconformity-type Uranium Deposits in Northern Saskatchewan.

Landry, K., Adlakha, E.E., Hanley, J.J., Roy-Garand, A., Terekhova, A., Martel, E., and Falck, H. 2022. Metasomatic uranium mineralization in the MacInnis Lake Area, Nonacho Basin, Northwest Territories: Potential linkages to IOCG and affiliated deposits.

LeCheminant, A.N., and Heaman, L.M. 1989. Mackenzie igneous events, Canada: Middle Proterozoic hotspot magmatism associated with ocean opening. Earth and Planetary Science Letters, **96**: 38–48. doi:10.1016/0012-821X(89)90122-2.

LeCheminant, A.N., Tella, S., Sanborn-Barrie, M., and Venance, K.. 1997. Geology, Parker Lake

South, District of Keewatin, North- west Territories. Geological Survey of Canada, Open File Map 3405, scale 1:50,000.

MacDonald, B.. 1956. Report on exploration on the MacInnis Lake property of Canadian Pipelines and Petroleum Limited, Northwest Territories; Scurry-Rainbow Oil Limited, unpublished report,.

MacLeod, W.A., and Brander, J.M. 1975. Assessment report: Mining claims BM 1-36, claim map no. 75E-8 (Lat. 61°20'; Long. 110°10') August 1, 1974-October 1, 1974; Shell Canada Limited, Department of Indian and Northern Affairs document no. N 080170.

Makela, K. 1970. MacInnis Lake property evaluation; Scurry-Rainbow Oil Limited, unpublished report.

Maurice, Y.T. 1984. Gold, tin, uranium and other elements in the Proterozoic Nonacho sediments and adjacent basement rocks near MacInnis Lake, District of MacKenzie. Geological Survey of Canada, Part A, Paper 84-1A.

McDonough, W.F., and Sun, S.S. 1995. The composition of the Earth. Chemical Geology, **120**: 223–253.

Mcglynn, J.C., Irving, E., and Park, J.K. 1974. Paleomagnetism and Age of Nonacho Group Sandstone and Associated Sparrow Dikes , District of Mackenzie. Canadian Journal of Earth Sciences, **11**: 30–42.

McVittie G.A. 1956. Report on Packsack Drilling: Bragon Zone; Consolidated Mining and Smelting Company of Canada Limited, unpublished report.

Meagher J.T. 1955. Report on the BAG claim group, MacInnis Lake, Northwest Territories, Iso

Uranium Mined Limited, Department of Indian and Northern Affairs document no. N017070.

Mellion J.J. 1965. Report on the Nonacho project, Summer 1965; International Mine Services Limited, unpublished report,.

Mercadier, J., Cuney, M., Lach, P., Boiron, M.C., Bonhoure, J., Richard, A., Leisen, M., and Kister, P. 2011. Origin of uranium deposits revealed by their rare earth element signature. Terra Nova, **23**: 264–269. doi:10.1111/j.1365-3121.2011.01008.x.

Moffat, G.W. 1974. An investigation of the radioactive mineral occurrences of the Great Slake Lake-Athabasca Lake region of the District of Mackenzie in the Northwest Territories; unpublished B.Sc. thesis, University of Toronto.

Montreuil, J.F., Corriveau, L., and Potter, E.G. 2015a. Formation of albitite-hosted uranium within IOCG systems: the Southern Breccia, Great Bear magmatic zone, Northwest Territories, Canada. Mineralium Deposita, **50**: 293–325. doi:10.1007/s00126-014-0530-7.

Montreuil, J.F., Corriveau, L., and Potter, E.G. 2015b. Formation of albitite-hosted uranium within IOCG systems: the Southern Breccia, Great Bear magmatic zone, Northwest Territories, Canada. Mineralium Deposita, **50**: 293–325. doi:10.1007/s00126-014-0530-7.

Montreuil, J.F., Potter, E.G., Corriveau, L., and Davis, W.J. 2016. Element mobility patterns in magnetite-group IOCG systems: The Fab IOCG system, Northwest Territories, Canada. Ore Geology Reviews, **72**: 562–584. Elsevier B.V. doi:10.1016/j.oregeorev.2015.08.010.

Morelli, R.M., Hartlaub, R.P., Ashton, K.E., and Ansdell, K. 2009. Evidence for enrichment of subcontinental lithosperic mantle from Paleoproterozoic intracratonic magmas: Geochemistry and U-Pb grochronology of Martin Group igneous rocks, western Rae Craton,

Canada. Precambrian Research. doi:10.1016/j.precamres.2009.04.005.

Neil, B.J.C., Gibson, H.D., Pehrsson, S.J., Martel, E., Thiessen, E.J., and Crowley, J.L. 2021. Provenance, stratigraphic and precise depositional age constraints for an outlier of the 1.9 to 1.8 Ga Nonacho Group, Rae craton, Northwest Territories, Canada. Precambrian Research, **352**: 105999. Elsevier B.V. doi:10.1016/j.precamres.2020.105999.

Ng, R., Alexandre, P., Kyser, K., Cloutier, J., Abdu, Y.A., and Hawthorne, F.C. 2013. Oxidation state of iron in alteration minerals associated with sandstone-hosted unconformity-related uranium deposits and apparently barren alteration systems in the Athabasca Basin, Canada: Implications for exploration. Journal of Geochemical Exploration, **130**: 22–43. Elsevier B.V. doi:10.1016/j.gexplo.2013.02.009.

NORMIN. 2019. NORMIN showings [online]. Northwest Territories Geological Survey, Yellowknife. Accessed at http://www.ntgomap.nwtgeoscience.ca.

Ono, S., and Fayek, M. 2011. Decoupling of O and Pb isotope systems of uraninite in the early Proterozoic Conglomerates in the Elliot Lake district. Chemical Geology, **288**: 1–13. doi:https://doi.org/10.1016/j.chemgeo.2010.03.015.

Ootes, L., Goff, S., Jackson, V.A., Gleeson, S.A., Creaser, R.A., Samson, I.M., Evensen, N., Corriveau, L., and Mumin, A.H. 2010. Timing and thermochemical constraints on multi-element mineralisation at the Nori/RA Cu-Mo-U prospect, Great Bear magmatic zone, Northwest Territories, Canada. Mineralium Deposita, **45**: 549–566. doi:10.1007/s00126-010-0291-x.

Pagel, M., Poty, B., and Sheppard, S.M.F. 1980. Contributions to some Saskatchewan uranium deposits mainly from fluid inclusions and isotopic data. Uranium in Pine Creek Geosyncline

(S. Ferguson and A. Gobely, editors). IAEA, Vienna.,: 639–654.

Pehrsson, S.J., Berman, R.G., and Davis, W.J. 2013a. Paleoproterozoic orogenesis during Nuna aggregation: A case study of reworking of the Rae craton, Woodburn Lake, Nunavut. Precambrian Research, **232**: 167–188. Elsevier. doi:10.1016/J.PRECAMRES.2013.02.010.

Pehrsson, S.J., Berman, R.G., Eglington, B., and Rainbird, R. 2013b. Two Neoarchean supercontinents revisited: The case for a Rae family of cratons. Precambrian Research, **232**: 27–43. Elsevier B.V. doi:10.1016/j.precamres.2013.02.005.

Peterson, T.D. 2006. Geology of the Dubawnt Lake area, Nunavut-Northwest Territories.

Peterson, T.D., Van Breemen, O., Sandeman, H., and Cousens, B. 2002. Proterozoic (1.85-1.75 Ga) igneous suites of the Western Churchill Province: Granitoid and ultrapotassic magmatism in a reworked Archean hinterland. Precambrian Research, **119**: 73–100. doi:10.1016/S0301-9268(02)00118-3.

Peterson, T.D., Jefferson, C.W., and Anand, A. 2015. Geological setting and geochemistry of the ca. 2.6 Ga Snow Island Suite in the central Rae Domain of the Western Churchill Province, Nunavut - Report: Geological Survey of Canada Open File 7841. Geological Survey of Canada Open File 7841,: 29. doi:10.4095/296599.

Potter, E.G., Acosta-Góngora, P., Corriveau, L., Montreuil, J.-F., and Yang, Z. 2022. Uranium enrichment processes in metasomatic iron oxide and alkali-calcic systems as revealed by uraninite trace element chemistry. Corriveau, L., Potter, E.G. and Mumin, A.H., eds., Mineral systems with iron oxide copper-gold (IOCG) and affiliated deposits: Geological Association of Canada, Special Paper 52,: 325–345.

Potter, E.G. 2021. GEOLOGICAL SURVEY OF CANADA OPEN FILE 7873 Geochemistry of uranium- bearing veins from the Uranium City-Beaverlodge district , northern OPEN FILE 7873 Geochemistry of uranium-bearing veins from the Uranium City-Beaverlodge district , northern Saskatchewan. doi:10.4095/328980.

Potter, E.G., Corriveau, L., and Kjarsgaard, B.A. 2019a. Paleoproterozoic Iron Oxide Apatite (IOA) and Iron Oxide-Copper-Gold (IOCG) mineralization in the East Arm Basin, Northwest Territories, Canada. Canadian Journal of Earth Sciences,: 1–17. doi:10.1139/cjes-2018-0171.

Potter, E.G., Corriveau, L., Montreuil, J., Yang, Z., Potter, E.G., Corriveau, L., and Montreuil, J. 2021. Uranium enrichment processes in metasomatic iron oxide and alkali-calcic systems as revealed by uraninite trace element chemistry — supplementary data. Geological Survey of Canada, Open File,.

Potter, E.G., Montreuil, J. -F., Corriveau, L., and Davis, W.J. 2019b. The Southern Breccia Metasomatic Uranium System of the Great Bear Magmatic Zone, Canada. : 109–130. doi:10.1002/9781119290544.ch5.

Putnis, A., Hinrichs, R., Putnis, C. V., Golla-Schindler, U., and Collins, L.G. 2007. Hematite in porous red-clouded feldspars: Evidence of large-scale crustal fluid-rock interaction. Lithos, **95**: 10–18. doi:10.1016/j.lithos.2006.07.004.

Quirt, D. 2012. Clay alteration mineralogy comparisons between the Athabasca and Thelon Basins – basement alteration. **2012**.

Read, D., Black, S., Buckby, T., Hellmuth, K.H., Marcos, N., and Siitari-Kauppi, M. 2008. Secondary uranium mineralization in southern Finland and its relationship to recent glacial events. Global and Planetary Change, **60**: 235–249. doi:10.1016/j.gloplacha.2007.02.006.

Reid, J.D. 1955. MacInnis Lake: Report on area for exploration; Scurry-Rainbow Oil Limited, unpublished report.

Reid, K.D., and Ansdell, K. 2012. Elemental changes in variably altered granitoid rocks in the vicinity of the Centennial unconformity-related uranium deposit, northern Saskatchewan, and implications for uranium mineralization. GAC-MAC,.

Richard, A., Rozsypal, C., Mercadier, J., Banks, D.A., Cuney, M., Boiron, M.C., and Cathelineau, M. 2012. Giant uranium deposits formed from exceptionally uranium-rich acidic brines. Nature Geoscience, **5**: 142–146. Nature Publishing Group. doi:10.1038/ngeo1338.

Riegler, T. 2013. , Système d'altération et minéralisation en uranium le long du faisceau structural Kiggavik-Andrew Lake (Nunavut, Canada): Modèle génétique et guides d'éxploration: Ph.D. thesis, Poitiers, France, Université de Poitiers.

Selby, D., and Creaser, R.A. 2004. Macroscale NTIMS and microscale LA-MC-ICP-MS Re-Os isotopic analysis of molybdenite: Testing spatial restrictions for reliable Re-Os age determinations, and implications for the decoupling of Re and Os within molybdenite. Geochimica et Cosmochimica Acta, **68**: 3897–3908.

Shabaga, B.M., Fayek, M., Quirt, D., Jefferson, C.W., and Camacho, A. 2017. Mineralogy, geochronology, and genesis of the Andrew lake ranium deposit, Thelon basin, Nunavut, Canada. Canadian Journal of Earth Sciences, **54**: 850–868. doi:10.1139/cjes-2017-0024.

Shabaga, B.M., Fayek, M., Quirt, D., Jefferson, C.W., and Ledru, P. 2021. Geochemistry and geochronology of the Kiggavik uranium deposit, Nunavut, Canada. Mineralium Deposita, **56**: 1245–1262. Mineralium Deposita. doi:10.1007/s00126-020-01001-8.

Sharpe, R., and Fayek, M. 2016. Mass bias corrections for U-Pb isotopic analysis by secondary ion mass spectrometry: Implications for U-Pb dating of uraninite. Rapid Communications in Mass Spectrometry,: 1601–1611. doi:10.1002/rcm.7595.

Sharpe, R., Fayek, M., Quirt, D., and Jefferson, C.W. 2015. Geochronology and genesis of the bong uranium deposit, Thelon Basin, Nunavut, Canada. Economic Geology, **110**: 1759–1777. doi:10.2113/econgeo.110.7.1759.

Spencer, R.. 1955. MacInnis Group: Engineering Report No. 1 (Mine Series No. 5831) Consolidated Mining and Smelting Company of Canada limited, unpublished report.

Stephen, H.C. 1956. Geological report on the WALT claim group, MacInnis Lake, Taltson Lake map area, District of Mackenzie, Northwest Territories; Newkirk Mining Corporation Limited; Department of Indian and Northern Affairs, document no. N017080,.

Stohl, F. V., and Smith, D.K. 1981. The crystal chemistry of the uranyl silicate minerals. American Mineralogist, **66**: 610–625.

Sun, S.S., and McDonough, W.F. 1989. Chemical and isotopic systematics of oceanic basalts: Implications for mantle composition and processes. Geological Society Special Publication, **42**: 313–345. doi:10.1144/GSL.SP.1989.042.01.19.

Tschirhart, V., Jefferson, C.W., and Morris, W.A. 2017. Basement geology beneath the northeast Thelon Basin, Nunavut: insights from integrating new gravity, magnetic and geological data. Geophysical Prospecting,. doi:10.1111/1365-2478.12430.

Viswanathan, K., and Harnet, O. 1986. Refined crystal structure of beta-uranophane, Ca(UO2)2(SiO3OH)2•5H2O. American Mineralogist, **71**: 1489–1493.

Wiewióra, A. and Weiss, Z. 1990. Crystallochemical classifications of phyllosilicates based on the unified system of projection of chemical composition: III. The serpentine-kaolin group. Clay Minerals, **25**: 93–98. doi:10.1180/claymin.1990.025.1.10.

Wilde, A. 2013. Towards a model for albitite-type uranium. Minerals, **3**: 36–48. doi:10.3390/min3010036.

Yeo, G.M., and Potter, E.G. 2010. Review of Reducing Mechanisms Potentially Involved in the Formation of Unconformity-type Uranium Deposits and their Relevance to Exploration. Saskatchewan Geological Survey, **2**: 13.

Chapter 4: Key Conclusions and Future Work

4.1. Key Conclusions from Chapter 2

The uraninite at the Hope occurrence was crystallized at high-temperatures (>350°C) and has U/Th ratios and REE signatures consistent with global magmatic/intrusive uraninite deposits. Magmatic signatures of uraninite and paragenetic and textural relationships between coarse-grained zircon and oligoclase suggest a pegmatitic origin for mineralization at Hope. An age discrepancy exists between the 2.79 Ga uraninite at Hope and the minimum depositional age of 2.35 Ga for the host basement paragneiss, indicating the uraninite is likely detrital in origin with a magmatic provenance. The preservation of detrital uraninite provides further evidence for an oxygen depleted environment before 2.2 Ga.

The implementation of multiple geochronometers (i.e., U-Pb, Re-Os and Ar-Ar), provides insight into the evolution of the Hope occurrence, and evidence of long-lived uranium recycling throughout the Rae craton. Detrital uraninite crystallization occurred at 2790 ± 22 Ma and 2784 ± 21.7 Ma, and is currently the oldest recorded uranium mineralization in the Rae craton, providing evidence for early uranium enrichment within the Rae craton. Geochronological data on uraninite also reveal three isotopic resetting and alteration events associated with magmatic and hydrothermal events throughout the Rae: i) 2614 ± 10.5 Ma, corresponding to the emplacement of the Snow Island Suite; (ii) 2531 ± 17.4 Ma, corresponding to widespread magmatism throughout the western Rae and the emplacement of local granites at Hope, and; (iii) 1778 ± 14.4 Ma, recording alteration by hydrothermal fluids, which also precipitated molybdenite (1794 ± 28 Ma; Re-Os) with chloritization of earlier biotite (1834 ± 1.17 Ma; Ar-Ar), coincident with reactivation of the King Shear Zone at 1.78 Ga (Canam et al. 2021).

There are similarities between the low-temperature mineral assemblages associated with thorite at Hope, and the mineral assemblages at MacInnis Lake associated with uraninite and uranophane mineralization. The alteration and remobilization of primary uraninite at the Hope occurrence may have been a source for hydrothermal uranium occurrences throughout the Nonacho Basin, such as the MacInnis Lake occurrences.

4.2. Key Conclusions from Chapter 3

At the MacInnis Lake showings, uranium mineralization is heterogeneous, Pb-poor, and occurs as a mix of uraninite and uranophane, with at least two generations of uranophane chemically associated with Cu, Ag +/- Au. There are two main styles of uranium mineralization at MacInnis Lake: type-i) uraninite and uranophane as overgrowths on partially dissolved Cu-sulphides (i.e., bornite and chalcopyrite), with or without galena, in quartz-chlorite ± carbonate veins and; type-ii) uranophane associated with, or as micro-inclusions within, hematite and/or rutile in sericitized veins and breccias. The partially dissolved Cu-sulphides acted as a reductant for type-i uraninite mineralization and later, a redox buffer, precipitating uranophane. Type ii uranophane occurs with oxidized mineral assemblages (i.e., hematite), which facilitated uranophane precipitation directly from fluid. Type-i and type-ii uranium minerals are chemically and geochronologically distinct: type-i uranium minerals have higher ΣREE + Y, but lower Pb, Ca and Si, and have distinctly younger ages, likely reflecting more recent alteration and/or resetting of uraninite that was altered and remobilized to precipitate uraninite + uranophane (508 ± 20 Ma and 66 ± 3 Ma). The type-ii uranophane, have lower ΣREE + Y, but higher Pb, Ca and Si, and precipitated as primary uranophane in highly oxidized conditions at 1749 ± 70 Ma, in an event genetically distinct from type-i mineralization.

Basement granitoids and overlying Nonacho sediments have undergone pervasive albitization and later Ba-rich K-feldspar alteration, that pre-date all uranium mineralization. Uranium minerals are Ba-rich, which was incorporated into the crystal structure during alteration of Ba-rich K-feldspar by mineralizing fluids. The low temperature (<350°C) alteration assemblages associated with mineralization (hematite, K-feldspar or sericite, ± calcite and chlorite, ± chalcopyrite, bornite, chalcocite, REE, and U-bearing minerals) and the Th, Pb and REE signatures of hydrothermal uranium mineral chemistry resemble low-temperature K-Fe alteration of metasomatic iron and alkali calcic alteration systems, such as those that host uraninite bearing hematite-group IOCG deposits like Olympic Dam in Australia.

Uranium mineral chemistry points to a complex history for the Nonacho Basin, which may have been altered by multiple mineralizing events at MacInnis Lake. These uranium occurrences formed as the result of remobilized uranyl minerals and may ultimately have been derived from early uranium occurrences, such as primary detrital uraninite from the Hope occurrence. Regional-scale faults (e.g., the King Shear Zone) acted as conduits for hydrothermal fluids associated with various phases of metasomatic iron and alkali calcic alteration. Uranium was ultimately remobilized and precipitated as hydrothermal uranium minerals along deformation zones and structural corridors in the Nonacho Basin, such as the MacInnis Lake sub-basin.

4.2. Future Work

Originally, this study was proposed to encompass several other notable uranium occurrences throughout the Nonacho Basin, to compare and contrast modes of mineralization and widespread alteration associated with uranium occurrences. However, financial and logistical constraints refocused the study to a detailed examination of uranium mineralization from two main showing areas: the MacInnis Lake area and the Hope occurrence. Future work, including

petrographic analyses coupled with trace and rare-earth element concentrations of uranium minerals (e.g., EPMA) from other occurrences around the Nonacho Basin, will aid in determining potential paragenetic and geochemical relationships between occurrences.

Additional work is required to further understand the origin of detrital uraninite mineralization at the Hope occurrence. Fluid inclusion analyses of quartz may provide insight into the temperature and conditions of mineralizing fluids. Analyses of Pb-Pb isotopes in galena associated with uraninite mineralization may be compared to Pb-Pb isotopes in galena from other areas of the basin (e.g., MacInnis Lake) and can provide insight into the age and origin of galena, to aid in distinguishing geochemical relationships between various occurrences. Aluminum in chlorite thermometry of chlorite associated with molybdenite at the Hope occurrence will tighten temperature constraints on the 1.78 Ga hydrothermal alteration associated with the reactivation of the King Shear Zone, the latest stage of uraninite resetting, and molybdenite mineralization. Geochronology of other minerals such as titanite and sericite at the Hope showing may further constrain timing and paragenesis.

Due to the fine-grained nature of the uranium minerals at MacInnis Lake, only two occurrences were geochemically analyzed by EPMA. Fluid inclusion analyses of quartz and/or carbonate minerals associated with uranium mineralization may provide insight into physicochemical conditions of ore-formation and the composition of fluids associated with, or responsible for, mineralization. Geochronology of sericite will aid in constraining the timing of type-ii uranium mineralization at MacInnis Lake, and may potentially tie low-temperature sericite alteration to the thorite-sericite breccia from the Hope occurrence.

Regional basin-scale mapping by the Nonacho Basin Bedrock Mapping Project, and alteration mapping associated with uranium and iron-oxide occurrences throughout the basin is

currently underway. Trace-element geochemistry of iron-oxides at occurrences such as MacInnis Lake and Hope may establish a relationship between them or other occurrences in the basin and the potential of the area for IOCG and affiliated deposits. This work includes detailed mapping and supporting whole-rock geochemical analyses, which will permit the creation of geochemical barcodes, proposed by (Corriveau et al. 2016) to aid in visualization in the evolution of regional-scale alteration facies. This will solidify the interpretation of presence of widespread MIAC alteration throughout the Nonacho Basin, locally associated with hydrothermal uranium mineralization.

4.3. References

Canam, R., Gibson, H. d., Martel, E., and Kellet, D. 2021. The Timing of Deformation and Kinematics of Shear Zones in the Nonacho Lake area. *In* Yellowknife Geoscience Forum: Geoscience and Exploration.

Corriveau, L., Montreuil, J.F., and Potter, E.G., 2016. Alteration facies linkages among iron oxide copper-gold, iron oxide-apatite, and affiliated deposits in the great bear magmatic zone, Northwest Territories, Canada. Economic Geology, **111**: 2045–2072. doi:10.2113/econgeo.111.8.2045.

Appendix 2

Table A2-1: EPMA data in wt.% for Hope uraninite samples H-12 and H-14

	La_2O_3	Ce_2O_3	Pr_2O_3	Nd_2O_3	Sm_2O_3	Eu_2O_3	FeO	MgO	SiO_2	Al_2O_3	Lu_2O_3	Yb_2O_3	Tm_2O_3	Er_2O_3	Ho_2O_3	Dy_2O_3	Tb_2O_3	Gd_2O_3	Cl	K_2O	CaO	BaO	TiO_2	UO_2	SO_3	ThO_2	PbO	ZrO_2	P_2O_5	Y_2O_3	OH	Total
H12-1-1	0.00	0.21	0.05	0.49	0.28	0.00	0.30	0.02	0.00	0.00	0.07	0.09	0.10	0.26	0.06	0.61	0.00	0.36	0.27	0.00	2.85	0.07	0.03	75.78	0.83	8.46	6.92	0.00	0.05	2.00	0.00	100.1
H12-1-2	0.13	0.31	0.03	0.70	0.31	0.00	0.26	0.00	0.00	0.00	0.00	0.01	0.08	0.00	0.20	0.45	0.00	0.36	0.30	0.01	2.83	0.05	0.00	75.50	1.07	8.19	7.91	0.00	0.08	1.35	0.00	100.1
H12-1-3	0.00	0.36	0.21	0.46	0.24	0.00	0.24	0.01	0.00	0.00	0.01	0.00	0.02	0.04	0.13	0.29	0.00	0.23	0.19	0.02	2.66	0.01	0.03	76.00	0.52	10.78	6.74	0.00	0.08	0.83	0.00	100.1
H12-1-4	0.18	0.53	0.15	0.66	0.32	0.00	0.25	0.00	0.00	0.00	0.03	0.00	0.06	0.00	0.10	0.08	0.00	0.23	0.45	0.01	1.75	0.01	0.05	72.79	0.80	12.86	8.59	0.06	0.08	0.32	0.00	100.3
H12-1-5	0.00	0.06	0.00	0.11	0.01	0.00	0.42	0.02	0.00	0.00	0.06	0.17	0.18	0.00	0.03	0.30	0.00	0.07	0.44	0.03	1.58	0.09	0.05	76.80	1.38	7.62	9.91	0.00	0.05	0.96	0.00	100.3
H12-1-6	0.00	0.29	0.01	0.44	0.15	0.00	0.28	0.01	0.00	0.00	0.00	0.00	0.02	0.01	0.08	0.17	0.00	0.25	0.46	0.01	1.21	0.03	0.02	74.04	0.76	11.10	10.22	0.01	0.09	0.74	0.00	100.3
H12-1-7	0.00	0.59	0.06	0.66	0.27	0.00	0.32	0.02	0.00	0.00	0.10	0.00	0.07	0.01	0.16	0.24	0.00	0.22	0.36	0.01	1.59	0.07	0.02	72.65	1.55	10.95	9.70	0.00	0.09	0.59	0.00	100.2
H12-1-8	0.06	0.52	0.07	0.68	0.28	0.00	0.23	0.02	0.00	0.00	0.12	0.03	0.07	0.05	0.13	0.39	0.00	0.16	0.12	0.02	2.84	0.04	0.00	76.47	0.49	10.21	6.00	0.02	0.08	1.06	0.00	100.1
H12-1-9	0.05	0.35	0.07	0.63	0.29	0.00	0.27	0.02	0.00	0.00	0.10	0.00	0.00	0.04	0.13	0.38	0.00	0.25	0.16	0.00	2.92	0.00	0.00	76.52	0.64	9.75	6.58	0.00	0.07	0.90	0.00	100.1
H12-1-10	nd	0.37	nd	nd	nd	nd	0.24	nd	0.14	0.00	nd	nd	nd	nd	nd	0.30	nd	nd	0.21	0.02	2.15	0.05	nd	77.67	nd	10.98	7.44	nd	nd	0.80	0.00	100.3
H12-1-11	nd	0.39	nd	nd	nd	nd	0.21	nd	0.25	0.00	nd	nd	nd	nd	nd	0.35	nd	nd	0.37	0.04	2.53	0.05	nd	76.39	nd	12.56	6.66	nd	nd	0.58	0.00	100.3
H12-1-12	nd	0.28	nd	nd	nd	nd	0.34	nd	0.18	0.00	nd	nd	nd	nd	nd	0.28	nd	nd	0.49	0.07	0.75	0.06	nd	75.88	nd	10.97	10.36	nd	nd	0.82	0.00	100.4
H12-1-13	nd	0.38	nd	nd	nd	nd	0.30	nd	0.15	0.00	nd	nd	nd	nd	nd	0.20	nd	nd	0.26	0.10	2.41	0.03	nd	78.73	nd	10.57	6.84	nd	nd	0.40	0.00	100.3
H12-1-14	nd	0.35	nd	nd	nd	nd	0.34	nd	0.14	0.00	nd	nd	nd	nd	nd	0.37	nd	nd	0.38	0.09	1.86	0.06	nd	79.44	nd	8.46	8.01	nd	nd	0.91	0.00	100.4
H12-1-15	nd	0.17	nd	nd	nd	nd	0.33	nd	0.09	0.00	nd	nd	nd	nd	nd	0.32	nd	nd	0.36	0.08	1.52	0.06	nd	78.80	nd	8.09	9.74	nd	nd	0.87	0.00	100.4
H12-1-16	nd	0.30	nd	nd	nd	nd	0.29	nd	0.11	0.00	nd	nd	nd	nd	nd	0.29	nd	nd	0.26	0.10	2.07	0.00	nd	77.35	nd	11.02	8.13	nd	nd	0.46	0.00	100.3
H12-1-17	nd	0.43	nd	nd	nd	nd	0.22	nd	0.11	0.00	nd	nd	nd	nd	nd	0.20	nd	nd	0.33	0.09	2.83	0.05	nd	75.85	nd	11.35	8.57	nd	nd	0.32	0.00	100.3
H12-1-18	nd	0.40	nd	nd	nd	nd	0.29	nd	0.06	0.00	nd	nd	nd	nd	nd	0.54	nd	nd	0.22	0.03	2.87	0.04	nd	78.23	nd	8.48	7.65	nd	nd	1.46	0.00	100.2
H12-1-19	nd	0.35	nd	nd	nd	nd	0.17	nd	0.04	0.00	nd	nd	nd	nd	nd	0.26	nd	nd	0.36	0.04	2.37	0.06	nd	76.95	nd	10.29	8.75	nd	nd	0.75	0.00	100.3
H12-1-20	nd	nd	nd	nd	nd	nd	0.27	nd	0.55	nd	nd	nd	nd	nd	nd	nd	nd	nd	nd	nd	2.81	nd	0.02	68.61	nd	16.64	8.29	nd	nd	0.65	nd	97.84
H12-1-21	nd	nd	nd	nd	nd	nd	0.27	nd	0.30	nd	nd	nd	nd	nd	nd	nd	nd	nd	nd	nd	2.16	nd	0.00	69.21	nd	16.69	7.77	nd	nd	0.61	nd	97.01
H12-1-22	nd	nd	nd	nd	nd	nd	0.26	nd	0.46	nd	nd	nd	nd	nd	nd	nd	nd	nd	nd	nd	2.18	nd	0.01	68.20	nd	18.70	6.89	nd	nd	0.60	nd	97.29
H12-1-23	nd	nd	nd	nd	nd	nd	0.32	nd	0.43	nd	nd	nd	nd	nd	nd	nd	nd	nd	nd	nd	1.13	nd	0.01	67.02	nd	15.61	11.33	nd	nd	0.71	nd	96.55
H12-1-24	nd	nd	nd	nd	nd	nd	0.30	nd	0.76	nd	nd	nd	nd	nd	nd	nd	nd	nd	nd	nd	2.45	nd	0.04	67.69	nd	16.95	7.82	nd	nd	0.72	nd	96.75
H12-1-25	nd	nd	nd	nd	nd	nd	0.30	nd	0.40	nd	nd	nd	nd	nd	nd	nd	nd	nd	nd	nd	2.40	nd	0.01	69.17	nd	16.52	6.66	nd	nd	0.58	nd	96.02

	La_2O_3	Ce_2O_3	Pr_2O_3	Nd_2O_3	Sm_2O_3	Eu_2O_3	FeO	MgO	SiO_2	Al_2O_3	Lu_2O_3	Yb_2O_3	Tm_2O_3	Er_2O_3	Ho_2O_3	Dy_2O_3	Tb_2O_3	Gd_2O_3	Cl	K_2O	CaO	BaO	TiO_2	UO_2	SO_3	ThO_2	PbO	ZrO_2	P_2O_5	Y_2O_3	OH	Total
H12-1-26	nd	nd	nd	nd	nd	nd	0.36	nd	0.36	nd	nd	nd	nd	nd	nd	nd	nd	nd	nd	nd	1.79	nd	0.02	69.03	nd	17.66	7.44	nd	nd	0.48	nd	97.14
H12-1-27	nd	nd	nd	nd	nd	nd	0.33	nd	0.40	nd	nd	nd	nd	nd	nd	nd	nd	nd	nd	nd	1.56	nd	0.01	68.82	nd	16.62	8.68	nd	nd	0.53	nd	96.94
H12-1-28	nd	nd	nd	nd	nd	nd	0.35	nd	0.38	nd	nd	nd	nd	nd	nd	nd	nd	nd	nd	nd	1.00	nd	0.02	68.05	nd	16.31	9.80	nd	nd	0.92	nd	96.83
H12-1-29	nd	nd	nd	nd	nd	nd	0.31	nd	0.45	nd	nd	nd	nd	nd	nd	nd	nd	nd	nd	nd	2.42	nd	0.03	70.17	nd	14.14	7.50	nd	nd	0.62	nd	95.65
H12-1-30	nd	nd	nd	nd	nd	nd	0.28	nd	0.21	nd	nd	nd	nd	nd	nd	nd	nd	nd	nd	nd	2.78	nd	0.01	69.72	nd	11.21	8.78	nd	nd	1.49	nd	94.48
H12-1-31	nd	nd	nd	nd	nd	nd	0.28	nd	0.24	nd	nd	nd	nd	nd	nd	nd	nd	nd	nd	nd	2.50	nd	0.02	69.79	nd	14.57	7.12	nd	nd	0.94	nd	95.46
H12-1-32	nd	nd	nd	nd	nd	nd	0.26	nd	0.26	nd	nd	nd	nd	nd	nd	nd	nd	nd	nd	nd	2.32	nd	0.01	69.02	nd	16.68	7.54	nd	nd	0.29	nd	96.39
H12-1-33	nd	nd	nd	nd	nd	nd	0.25	nd	0.39	nd	nd	nd	nd	nd	nd	nd	nd	nd	nd	nd	2.76	nd	0.02	71.22	nd	13.18	6.06	nd	nd	0.99	nd	94.86
H12-1-34	nd	nd	nd	nd	nd	nd	0.23	nd	0.45	nd	nd	nd	nd	nd	nd	nd	nd	nd	nd	nd	2.64	nd	0.00	69.64	nd	16.58	6.80	nd	nd	0.60	nd	96.93
H12-2-1	0.05	0.27	0.00	0.37	0.18	0.00	0.20	0.03	1.17	0.01	0.11	0.00	0.03	0.05	0.08	0.28	0.00	0.17	0.13	0.02	1.13	0.00	0.03	68.58	1.05	8.65	15.83	0.00	0.08	0.69	0.86	100.0
H12-2-2	0.00	0.37	0.00	0.49	0.20	0.00	0.49	0.00	0.00	0.00	0.03	0.00	0.00	0.02	0.05	0.16	0.00	0.17	0.40	0.02	2.24	0.05	0.06	75.18	1.33	9.05	9.71	0.01	0.06	0.20	0.00	100.2
H12-2-3	0.00	0.32	0.02	0.18	0.20	0.00	0.57	0.00	0.00	0.00	0.01	0.09	0.06	0.02	0.06	0.26	0.00	0.24	0.45	0.01	1.15	0.14	0.03	73.07	1.29	9.90	11.18	0.00	0.07	0.98	0.00	100.2
H12-2-4	nd	0.21	nd	nd	nd	nd	0.31	nd	0.49	0.00	nd	nd	nd	nd	nd	0.29	nd	nd	0.37	0.13	1.48	0.06	nd	76.79	nd	9.18	10.28	nd	nd	0.79	0.00	100.3
H12-2-5	nd	0.32	nd	nd	nd	nd	0.43	nd	0.34	0.00	nd	nd	nd	nd	nd	0.23	nd	nd	0.31	0.12	1.99	0.05	nd	76.56	nd	9.19	10.15	nd	nd	0.66	0.00	100.3
H12-2-6	nd	0.35	nd	nd	nd	nd	0.22	nd	0.17	0.00	nd	nd	nd	nd	nd	0.26	nd	nd	0.32	0.07	0.81	0.05	nd	70.38	nd	9.85	17.45	nd	nd	0.49	0.00	100.4
H12-2-7	nd	0.14	nd	nd	nd	nd	0.06	nd	0.00	0.00	nd	nd	nd	nd	nd	0.18	nd	nd	0.33	0.12	0.46	0.02	nd	68.22	nd	8.09	21.98	nd	nd	0.77	0.00	100.3
H12-2-8	nd	0.34	nd	nd	nd	nd	0.25	nd	0.44	0.00	nd	nd	nd	nd	nd	0.26	nd	nd	0.44	0.13	1.41	0.07	nd	74.65	nd	8.94	12.70	nd	nd	0.77	0.00	100.4
H12-2-9	nd	0.28	nd	nd	nd	nd	0.45	nd	0.20	0.00	nd	nd	nd	nd	nd	0.28	nd	nd	0.25	0.07	2.53	0.05	nd	74.47	nd	8.86	12.20	nd	nd	0.67	0.00	100.3
H12-2-10	nd	nd	nd	nd	nd	nd	0.50	nd	0.71	nd	nd	nd	nd	nd	nd	nd	nd	nd	nd	nd	3.28	nd	0.00	70.58	nd	14.05	7.55	nd	nd	0.61	nd	97.29
H12-2-11	nd	nd	nd	nd	nd	nd	0.44	nd	0.56	nd	nd	nd	nd	nd	nd	nd	nd	nd	nd	nd	2.13	nd	0.03	70.19	nd	13.37	8.97	nd	nd	0.68	nd	96.36
H12-2-12	nd	nd	nd	nd	nd	nd	0.30	nd	0.54	nd	nd	nd	nd	nd	nd	nd	nd	nd	nd	nd	1.62	nd	0.01	69.00	nd	13.73	10.55	nd	nd	0.67	nd	96.41
H12-2-13	nd	nd	nd	nd	nd	nd	0.25	nd	0.41	nd	nd	nd	nd	nd	nd	nd	nd	nd	nd	nd	1.53	nd	0.03	73.72	nd	14.39	6.29	nd	nd	0.88	nd	97.50
H12-2-14	nd	nd	nd	nd	nd	nd	0.21	nd	4.92	nd	nd	nd	nd	nd	nd	nd	nd	nd	nd	nd	0.66	nd	3.09	55.26	nd	7.52	24.48	nd	nd	1.36	nd	97.50
H12-2-15	nd	nd	nd	nd	nd	nd	0.16	nd	0.26	nd	nd	nd	nd	nd	nd	nd	nd	nd	nd	nd	0.15	nd	0.03	62.08	nd	14.18	22.76	nd	nd	0.32	nd	99.94
H12-2-16	nd	nd	nd	nd	nd	nd	0.19	nd	0.73	nd	nd	nd	nd	nd	nd	nd	nd	nd	nd	nd	1.44	nd	0.03	63.24	nd	14.58	17.39	nd	nd	0.34	nd	97.93
H12-2-17	nd	nd	nd	nd	nd	nd	0.47	nd	0.47	nd	nd	nd	nd	nd	nd	nd	nd	nd	nd	nd	1.91	nd	0.03	71.13	nd	14.66	9.36	nd	nd	1.02	nd	99.05
H12-2-18	nd	nd	nd	nd	nd	nd	0.31	nd	0.17	nd	nd	nd	nd	nd	nd	nd	nd	nd	nd	nd	0.18	nd	0.03	69.61	nd	12.79	15.06	nd	nd	0.42	nd	98.56
H12-2-19	nd	nd	nd	nd	nd	nd	0.25	nd	0.29	nd	nd	nd	nd	nd	nd	nd	nd	nd	nd	nd	0.34	nd	0.02	65.79	nd	14.77	17.42	nd	nd	0.38	nd	99.24
H12-3-1	0.00	0.25	0.16	0.62	0.39	0.00	0.08	0.02	0.00	0.00	0.02	0.23	0.00	0.11	0.24	0.63	0.00	0.37	0.02	0.01	2.11	0.03	0.03	78.82	0.00	7.94	5.60	0.00	0.06	2.34	0.00	100.0
H12-3-2	0.00	0.27	0.13	0.52	0.35	0.00	0.08	0.02	0.00	0.00	0.05	0.04	0.00	0.20	0.24	0.62	0.00	0.37	0.02	0.01	2.13	0.00	0.04	74.90	0.00	7.37	10.26	0.00	0.07	2.37	0.00	100.5

	La_2O_3	Ce_2O_3	Pr_2O_3	Nd_2O_3	Sm_2O_3	Eu_2O_3	FeO	MgO	SiO_2	Al_2O_3	Lu_2O_3	Yb_2O_3	Tm_2O_3	Er_2O_3	Ho_2O_3	Dy_2O_3	Tb_2O_3	Gd_2O_3	Cl	K_2O	CaO	BaO	TiO_2	UO_2	SO_3	ThO_2	PbO	ZrO_2	P_2O_5	Y_2O_3	OH	Total
H12-3-3	0.00	0.35	0.03	0.54	0.36	0.00	0.13	0.01	0.00	0.00	0.10	0.17	0.02	0.22	0.24	0.56	0.00	0.50	0.02	0.00	2.54	0.00	0.00	78.04	0.03	7.78	5.23	0.00	0.09	2.63	0.43	100.0
H12-3-4	0.00	0.42	0.06	0.61	0.37	0.00	0.14	0.00	0.00	0.00	0.07	0.16	0.01	0.31	0.28	0.56	0.00	0.38	0.02	0.00	2.47	0.14	0.01	77.28	0.01	7.66	6.40	0.00	0.10	2.60	0.00	100.0
H12-3-5	0.04	0.38	0.02	0.49	0.29	0.00	0.05	0.01	0.00	0.00	0.10	0.16	0.08	0.09	0.25	0.63	0.00	0.40	0.02	0.02	1.99	0.05	0.00	78.08	0.00	7.76	6.61	0.00	0.08	2.42	0.00	100.0
H12-3-6	0.00	0.46	0.01	0.53	0.38	0.00	0.07	0.01	0.07	0.00	0.12	0.13	0.10	0.08	0.21	0.60	0.00	0.35	0.01	0.01	2.25	0.04	0.01	78.74	0.00	8.04	5.10	0.00	0.10	2.51	0.10	100.0
H12-3-7	0.06	0.47	0.05	0.67	0.23	0.00	0.11	0.04	0.00	0.00	0.09	0.10	0.04	0.25	0.14	0.55	0.00	0.40	0.02	0.00	2.18	0.03	0.03	78.52	0.00	7.73	5.62	0.00	0.07	2.47	0.16	100.0
H12-3-8	nd	0.34	nd	nd	nd	nd	0.08	nd	0.13	0.00	nd	nd	nd	nd	nd	0.65	nd	nd	0.01	0.15	1.57	0.02	nd	79.32	nd	7.59	6.74	nd	nd	2.49	0.92	100.0
H12-3-9	nd	0.44	nd	nd	nd	nd	0.06	nd	0.08	0.00	nd	nd	nd	nd	nd	0.69	nd	nd	0.01	0.07	2.54	0.05	nd	78.59	nd	7.49	6.96	nd	nd	2.38	0.66	100.0
H12-3-10	nd	0.23	nd	nd	nd	nd	0.11	nd	0.05	0.00	nd	nd	nd	nd	nd	0.57	nd	nd	0.02	0.09	1.97	0.06	nd	80.41	nd	7.60	6.34	nd	nd	2.41	0.16	100.0
H12-3-11	nd	0.24	nd	nd	nd	nd	0.07	nd	0.23	0.00	nd	nd	nd	nd	nd	0.58	nd	nd	0.01	0.06	2.89	0.03	nd	74.55	nd	7.26	9.62	nd	nd	2.29	2.17	100.0
H12-3-12	nd	0.43	nd	nd	nd	nd	0.09	nd	0.22	0.00	nd	nd	nd	nd	nd	0.74	nd	nd	0.03	0.06	1.89	0.09	nd	78.19	nd	7.80	7.88	nd	nd	2.37	0.21	100.0
H12-3-13	nd	0.25	nd	nd	nd	nd	0.07	nd	0.14	0.00	nd	nd	nd	nd	nd	0.46	nd	nd	0.16	0.10	1.31	0.04	nd	77.12	nd	7.96	10.37	nd	nd	2.16	0.00	100.1
H12-3-14	nd	0.19	nd	nd	nd	nd	0.07	nd	0.26	0.00	nd	nd	nd	nd	nd	0.60	nd	nd	0.16	0.13	1.67	0.05	nd	76.66	nd	8.39	9.90	nd	nd	1.98	0.00	100.0
H12-3-15	nd	0.35	nd	nd	nd	nd	0.08	nd	0.13	0.00	nd	nd	nd	nd	nd	0.65	nd	nd	0.02	0.13	1.67	0.07	nd	78.06	nd	7.76	8.86	nd	nd	2.27	0.00	100.0
H12-3-16	nd	0.30	nd	nd	nd	nd	0.06	nd	0.08	0.00	nd	nd	nd	nd	nd	0.60	nd	nd	0.01	0.12	2.02	0.03	nd	80.13	nd	7.54	6.19	nd	nd	2.47	0.44	100.0
H12-3-17	nd	0.00	nd	nd	nd	nd	0.14	nd	0.29	0.00	nd	nd	nd	nd	nd	0.40	nd	nd	0.02	0.15	2.39	0.04	nd	77.76	nd	8.71	7.75	nd	nd	1.63	0.72	100.0
H12-3-18	nd	nd	nd	nd	nd	nd	0.06	nd	0.67	nd	nd	nd	nd	nd	nd	nd	nd	nd	nd	nd	3.54	nd	0.02	71.53	nd	10.99	5.21	nd	nd	2.26	nd	94.26
H12-3-19	nd	nd	nd	nd	nd	nd	0.09	nd	0.40	nd	nd	nd	nd	nd	nd	nd	nd	nd	nd	nd	2.16	nd	0.01	73.50	nd	10.98	5.44	nd	nd	2.26	nd	94.85
H12-3-20	nd	nd	nd	nd	nd	nd	0.06	nd	0.39	nd	nd	nd	nd	nd	nd	nd	nd	nd	nd	nd	2.23	nd	0.02	73.18	nd	11.16	5.73	nd	nd	2.28	nd	95.04
H12-3-21	nd	nd	nd	nd	nd	nd	0.03	nd	0.41	nd	nd	nd	nd	nd	nd	nd	nd	nd	nd	nd	2.43	nd	0.02	72.58	nd	10.91	5.72	nd	nd	2.32	nd	94.42
H12-3-22	nd	nd	nd	nd	nd	nd	0.11	nd	0.70	nd	nd	nd	nd	nd	nd	nd	nd	nd	nd	nd	2.45	nd	0.02	71.76	nd	10.96	6.44	nd	nd	2.18	nd	94.62
H12-3-23	nd	nd	nd	nd	nd	nd	0.10	nd	0.58	nd	nd	nd	nd	nd	nd	nd	nd	nd	nd	nd	2.37	nd	0.01	72.41	nd	12.18	7.72	nd	nd	1.80	nd	97.17
H12-3-24	nd	nd	nd	nd	nd	nd	0.05	nd	0.53	nd	nd	nd	nd	nd	nd	nd	nd	nd	nd	nd	2.08	nd	0.02	71.40	nd	10.88	6.79	nd	nd	2.37	nd	94.12
H12-3-25	nd	nd	nd	nd	nd	nd	0.12	nd	0.07	nd	nd	nd	nd	nd	nd	nd	nd	nd	nd	nd	0.29	nd	0.00	55.13	nd	12.61	14.07	nd	nd	0.36	nd	82.66
H12-3-26	nd	nd	nd	nd	nd	nd	0.07	nd	0.50	nd	nd	nd	nd	nd	nd	nd	nd	nd	nd	nd	0.97	nd	0.02	67.96	nd	11.30	13.32	nd	nd	1.92	nd	96.06
H12-3-27	nd	nd	nd	nd	nd	nd	0.10	nd	0.51	nd	nd	nd	nd	nd	nd	nd	nd	nd	nd	nd	1.55	nd	0.02	69.54	nd	11.16	9.30	nd	nd	2.26	nd	94.43
H12-4-1	0.00	0.18	0.00	0.38	0.19	0.00	0.24	0.00	0.19	0.00	0.00	0.00	0.13	0.00	0.11	0.17	0.00	0.24	0.43	0.03	1.54	0.03	0.00	73.51	1.62	9.04	11.66	0.00	0.08	0.52	0.00	100.3
H12-4-2	0.07	0.17	0.07	0.44	0.20	0.01	0.30	0.00	0.00	0.00	0.00	0.00	0.03	0.00	0.13	0.28	0.00	0.22	0.56	0.00	0.77	0.07	0.00	69.35	2.58	9.05	15.29	0.00	0.06	0.63	0.00	100.2
H12-4-3	0.09	0.37	0.00	0.35	0.10	0.00	0.26	0.02	0.00	0.00	0.04	0.00	0.00	0.00	0.14	0.26	0.00	0.19	0.29	0.04	0.29	0.05	0.00	74.62	2.25	9.45	10.52	0.00	0.09	0.88	0.00	100.2
H12-4-4	0.00	0.19	0.04	0.38	0.18	0.00	0.49	0.00	0.00	0.00	0.03	0.02	0.05	0.00	0.16	0.23	0.00	0.18	0.34	0.01	1.24	0.03	0.02	76.46	1.02	9.62	8.60	0.00	0.09	1.00	0.00	100.3
H12-4-5	0.00	0.20	0.01	0.44	0.08	0.00	0.31	0.00	0.47	0.00	0.05	0.05	0.00	0.00	0.04	0.12	0.00	0.23	0.18	0.02	0.60	0.03	0.05	68.70	0.13	9.80	18.16	0.00	0.11	0.39	0.00	100.1

	La_2O_3	Ce_2O_3	Pr_2O_3	Nd_2O_3	Sm_2O_3	Eu_2O_3	FeO	MgO	SiO_2	Al_2O_3	Lu_2O_3	Yb_2O_3	Tm_2O_3	Er_2O_3	Ho_2O_3	Dy_2O_3	Tb_2O_3	Gd_2O_3	Cl	K_2O	CaO	BaO	TiO_2	UO_2	SO_3	ThO_2	PbO	ZrO_2	P_2O_5	Y_2O_3	OH	Total
H12-4-6	nd	nd	nd	nd	nd	nd	0.47	nd	0.44	nd	nd	nd	nd	nd	nd	nd	nd	nd	nd	nd	0.28	nd	0.01	69.49	nd	13.60	11.20	nd	nd	0.71	nd	96.20
H12-4-7	nd	nd	nd	nd	nd	nd	0.22	nd	0.31	nd	nd	nd	nd	nd	nd	nd	nd	nd	nd	nd	0.35	nd	0.02	66.21	nd	14.58	16.13	nd	nd	0.38	nd	98.21
H12-4-8	nd	nd	nd	nd	nd	nd	0.18	nd	0.30	nd	nd	nd	nd	nd	nd	nd	nd	nd	nd	nd	0.41	nd	0.03	62.41	nd	13.27	20.87	nd	nd	0.38	nd	97.84
H12-4-9	nd	nd	nd	nd	nd	nd	0.15	nd	0.65	nd	nd	nd	nd	nd	nd	nd	nd	nd	nd	nd	0.62	nd	0.03	62.96	nd	12.38	20.74	nd	nd	0.49	nd	98.02
H12-4-10	nd	nd	nd	nd	nd	nd	0.19	nd	0.97	nd	nd	nd	nd	nd	nd	nd	nd	nd	nd	nd	2.21	nd	0.02	72.41	nd	14.10	6.86	nd	nd	0.82	nd	97.58
H12-4-11	nd	nd	nd	nd	nd	nd	0.22	nd	1.25	nd	nd	nd	nd	nd	nd	nd	nd	nd	nd	nd	0.56	nd	0.07	61.37	nd	11.43	21.66	nd	nd	0.20	nd	96.75
H12-4-12	nd	nd	nd	nd	nd	nd	0.44	nd	0.50	nd	nd	nd	nd	nd	nd	nd	nd	nd	nd	nd	1.59	nd	0.03	69.57	nd	14.17	9.29	nd	nd	0.83	nd	96.41
H12-4-13	nd	nd	nd	nd	nd	nd	0.41	nd	0.60	nd	nd	nd	nd	nd	nd	nd	nd	nd	nd	nd	1.38	nd	0.03	69.28	nd	13.51	12.20	nd	nd	0.39	nd	97.80
H12-5-1	nd	0.46	nd	nd	nd	nd	0.39	nd	0.15	0.00	nd	nd	nd	nd	nd	0.46	nd	nd	0.25	0.01	3.13	0.03	nd	75.77	nd	10.85	8.04	nd	nd	0.54	0.00	100.0
H12-5-2	nd	0.39	nd	nd	nd	nd	0.27	nd	0.14	0.00	nd	nd	nd	nd	nd	0.30	nd	nd	0.16	0.00	3.04	0.04	nd	76.48	nd	10.59	8.09	nd	nd	0.30	0.23	100.0
H12-5-3	nd	0.45	nd	nd	nd	nd	0.33	nd	0.11	0.00	nd	nd	nd	nd	nd	0.40	nd	nd	0.23	0.00	3.24	0.03	nd	77.18	nd	9.66	7.24	nd	nd	0.71	0.48	100.0
H12-5-4	nd	0.39	nd	nd	nd	nd	0.47	nd	0.06	0.00	nd	nd	nd	nd	nd	0.61	nd	nd	0.36	0.00	2.44	0.07	nd	76.81	nd	8.89	9.12	nd	nd	0.92	0.00	100.1
H12-5-5	nd	0.49	nd	nd	nd	nd	0.40	nd	0.11	0.00	nd	nd	nd	nd	nd	0.44	nd	nd	0.25	0.00	2.94	0.03	nd	76.69	nd	10.41	7.42	nd	nd	0.51	0.37	100.0
H12-5-6	nd	0.32	nd	nd	nd	nd	0.23	nd	0.15	0.00	nd	nd	nd	nd	nd	0.14	nd	nd	0.41	0.00	1.83	0.04	nd	74.89	nd	11.44	10.29	nd	nd	0.56	0.00	100.2
H12-5-7	nd	0.41	nd	nd	nd	nd	0.36	nd	0.10	0.00	nd	nd	nd	nd	nd	0.28	nd	nd	0.36	0.00	3.13	0.00	nd	75.99	nd	10.88	8.48	nd	nd	0.25	0.00	100.2
H12-5-8	nd	0.30	nd	nd	nd	nd	0.49	nd	0.32	0.00	nd	nd	nd	nd	nd	0.21	nd	nd	0.41	0.01	2.02	0.04	nd	73.21	nd	12.33	10.64	nd	nd	0.28	0.00	100.2
H12-5-9	nd	0.00	nd	nd	nd	nd	0.32	nd	0.36	0.00	nd	nd	nd	nd	nd	0.18	nd	nd	0.51	0.00	1.17	0.03	nd	77.42	nd	7.18	12.83	nd	nd	0.40	0.00	100.4
H12-5-10	nd	0.40	nd	nd	nd	nd	0.37	nd	0.14	0.00	nd	nd	nd	nd	nd	0.43	nd	nd	0.38	0.00	3.34	0.03	nd	77.20	nd	9.68	6.78	nd	nd	0.80	0.54	100.0
H14-1	nd	0.21	nd	nd	nd	nd	1.28	nd	0.39	0.00	nd	nd	nd	nd	nd	0.25	nd	nd	0.30	0.00	2.98	0.03	nd	77.55	nd	10.35	5.84	nd	nd	0.93	0.00	100.0
H14-2	nd	0.33	nd	nd	nd	nd	0.77	nd	0.43	0.00	nd	nd	nd	nd	nd	0.60	nd	nd	0.22	0.00	2.15	0.04	nd	73.57	nd	12.48	6.63	nd	nd	1.93	0.91	100.0
H14-3	nd	0.33	nd	nd	nd	nd	0.46	nd	0.16	0.00	nd	nd	nd	nd	nd	0.18	nd	nd	0.47	0.00	1.12	0.00	nd	72.55	nd	12.06	12.34	nd	nd	0.18	0.27	100.1
H14-4	nd	0.29	nd	nd	nd	nd	0.64	nd	0.08	0.00	nd	nd	nd	nd	nd	0.50	nd	nd	0.24	0.00	0.62	0.05	nd	74.84	nd	10.17	11.93	nd	nd	0.95	0.00	100.3
H14-5	nd	0.34	nd	nd	nd	nd	0.71	nd	0.23	0.00	nd	nd	nd	nd	nd	0.68	nd	nd	0.36	0.01	0.84	0.04	nd	76.41	nd	9.73	8.48	nd	nd	2.13	0.12	100.0
H14-6	nd	0.28	nd	nd	nd	nd	0.60	nd	0.27	0.00	nd	nd	nd	nd	nd	0.55	nd	nd	0.35	0.00	1.60	0.04	nd	77.40	nd	9.32	8.12	nd	nd	1.71	0.00	100.2
H14-7	nd	0.49	nd	nd	nd	nd	0.57	nd	0.31	0.00	nd	nd	nd	nd	nd	0.61	nd	nd	0.30	0.00	2.17	0.03	nd	75.84	nd	10.36	7.41	nd	nd	1.69	0.29	100.0
H14-8	nd	0.52	nd	nd	nd	nd	0.73	nd	0.34	0.00	nd	nd	nd	nd	nd	0.69	nd	nd	0.28	0.00	1.59	0.03	nd	75.12	nd	10.97	7.86	nd	nd	1.49	0.44	100.0
H14-9	nd	0.18	nd	nd	nd	nd	0.41	nd	0.35	0.00	nd	nd	nd	nd	nd	0.34	nd	nd	0.15	0.00	2.88	0.05	nd	76.68	nd	9.54	7.85	nd	nd	1.15	0.46	100.0
H14-10	nd	0.11	nd	nd	nd	nd	0.56	nd	0.44	0.00	nd	nd	nd	nd	nd	0.24	nd	nd	0.15	0.00	2.88	0.04	nd	74.16	nd	11.50	9.46	nd	nd	0.57	0.00	100.1
H14-11	nd	0.17	nd	nd	nd	nd	0.48	nd	0.34	0.00	nd	nd	nd	nd	nd	0.47	nd	nd	0.10	0.01	2.60	0.02	nd	74.84	nd	8.39	11.12	nd	nd	1.47	0.02	100.0
H14-12	nd	0.26	nd	nd	nd	nd	0.49	nd	0.34	0.00	nd	nd	nd	nd	nd	0.43	nd	nd	0.15	0.00	2.33	0.05	nd	75.95	nd	10.24	8.99	nd	nd	0.87	0.00	100.0

	La_2O_3	Ce_2O_3	Pr_2O_3	Nd_2O_3	Sm_2O_3	Eu_2O_3	FeO	MgO	SiO_2	Al_2O_3	Lu_2O_3	Yb_2O_3	Tm_2O_3	Er_2O_3	Ho_2O_3	Dy_2O_3	Tb_2O_3	Gd_2O_3	Cl	K_2O	CaO	BaO	TiO_2	UO_2	SO_3	ThO_2	PbO	ZrO_2	P_2O_5	Y_2O_3	OH	Total
H14-13	nd	0.24	nd	nd	nd	nd	0.60	nd	0.28	0.00	nd	nd	nd	nd	nd	0.35	nd	nd	0.20	0.03	2.39	0.05	nd	76.68	nd	9.74	9.04	nd	nd	0.65	0.00	100.2
H14-14	nd	0.27	nd	nd	nd	nd	0.50	nd	0.27	0.00	nd	nd	nd	nd	nd	0.31	nd	nd	0.16	0.00	2.95	0.05	nd	77.64	nd	9.53	7.52	nd	nd	1.04	0.00	100.2
H14-15	nd	0.27	nd	nd	nd	nd	0.28	nd	0.24	0.00	nd	nd	nd	nd	nd	0.31	nd	nd	0.11	0.00	3.05	0.04	nd	77.93	nd	10.61	6.19	nd	nd	1.10	0.00	100.1
H14-16	nd	0.34	nd	nd	nd	nd	0.16	nd	0.31	0.00	nd	nd	nd	nd	nd	0.28	nd	nd	0.07	0.00	1.85	0.06	nd	76.25	nd	10.50	9.47	nd	nd	0.98	0.00	100.2
H14-17	nd	0.09	nd	nd	nd	nd	0.17	nd	0.31	0.00	nd	nd	nd	nd	nd	0.17	nd	nd	0.49	0.04	1.14	0.02	nd	71.20	nd	10.54	14.50	nd	nd	0.53	0.90	100.1

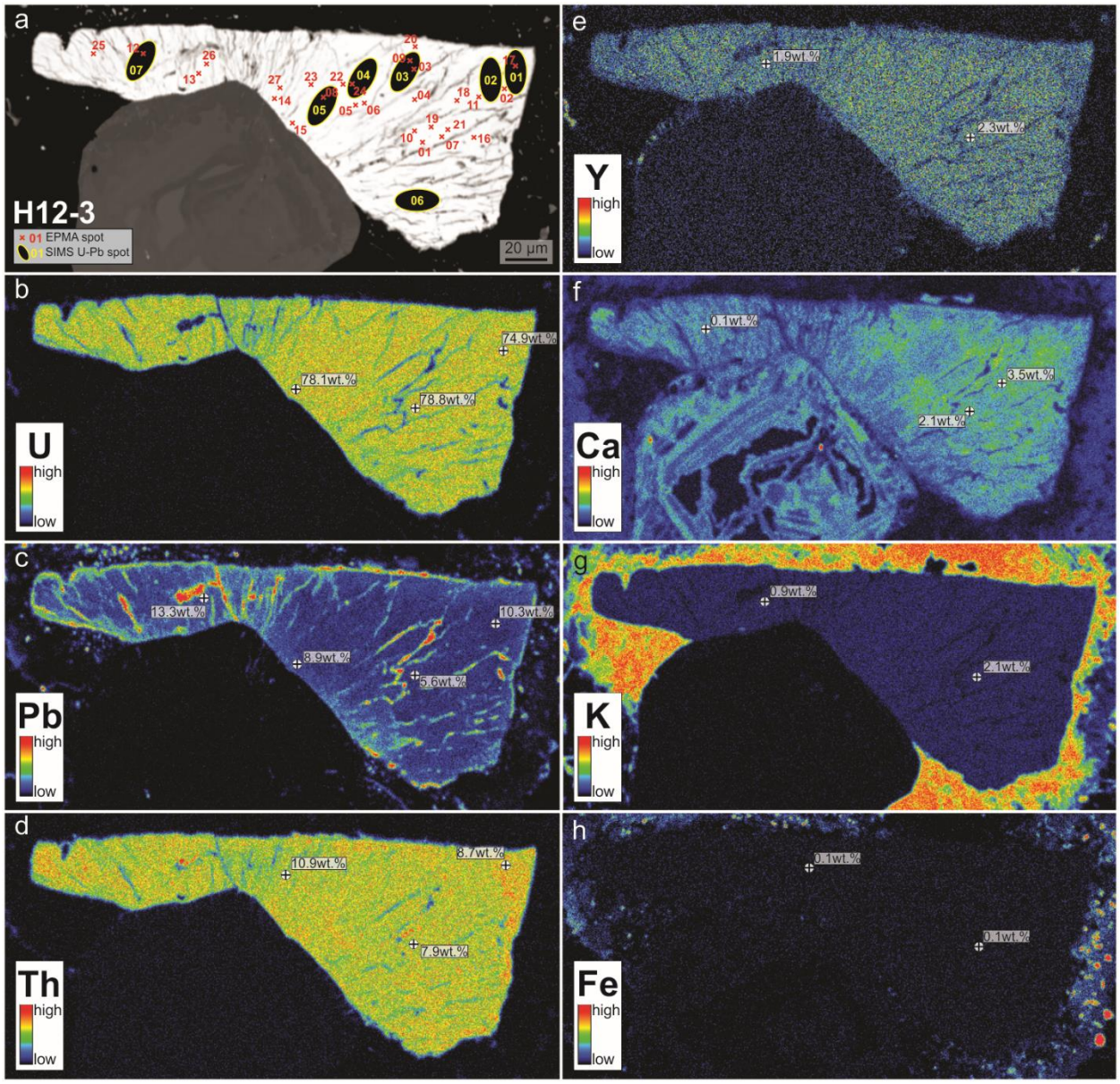

Figure A2-1: EPMA-WDS false colour elemental maps of coarse-grained uraninite and zircon from sample H12-3. The targets for EPMA and SIMS analyses outlined in (a) correlate to data presented in Table A2-1 and Table A2-4.

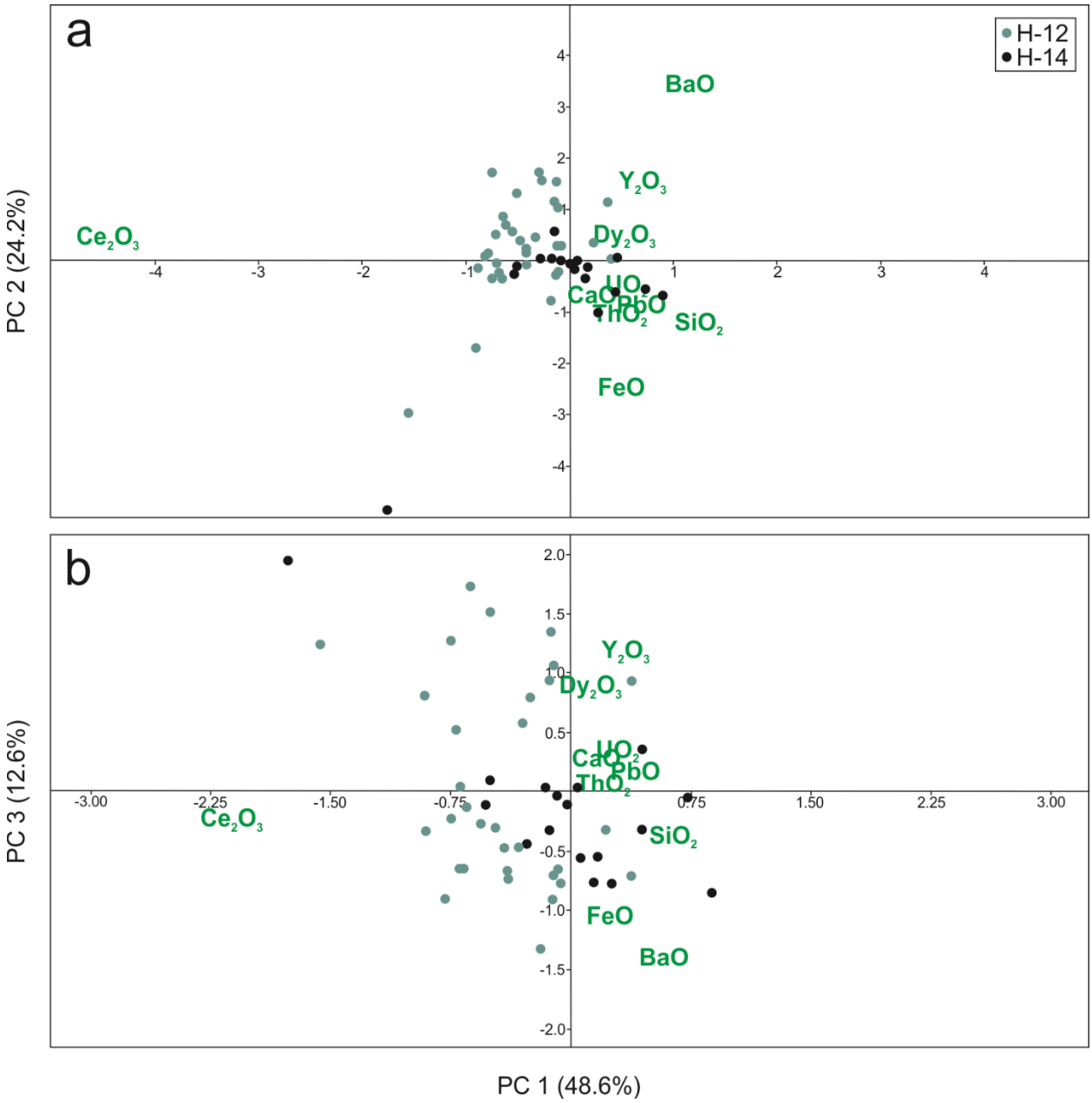

Figure A2-2: Principal Component (PC) analysis of uraninite from Hope (a) PC 1 vs. PC 2 and (b) PC 1 vs. PC 3

Table A2-2: Whole rock geochemical data in weight % and ppm

Analyte Symbol	Unit	Detection Limit	Analysis Method	H- 09	H- 10	H- 11	H- 12	H- 14
Co_3O_4	%	0.005	FUS-XRF	< 0.005	< 0.005	< 0.005	< 0.005	< 0.005
CuO	%	0.005	FUS-XRF	0.005	< 0.005	< 0.005	0.012	< 0.005
NiO	%	0.003	FUS-XRF	0.009	< 0.003	< 0.003	0.004	0.004
SiO_2	%	0.01	FUS-XRF	91.56	93.57	73.64	60.62	76.14
Al_2O_3	%	0.01	FUS-XRF	3.45	2.19	13.24	15.83	7.67
Fe_2O_3(T)	%	0.01	FUS-XRF	1.77	1.67	2.41	9.73	5.76
MnO	%	0.001	FUS-XRF	0.004	0.018	0.041	0.157	0.08
MgO	%	0.01	FUS-XRF	0.15	0.33	0.86	3.17	1.95
CaO	%	0.01	FUS-XRF	0.04	0.28	2.48	2.04	1.58
Na_2O	%	0.01	FUS-XRF	0.02	0.44	2.71	2.23	0.9
K_2O	%	0.01	FUS-XRF	1.96	0.7	2.14	3.36	2.27
TiO_2	%	0.01	FUS-XRF	0.02	0.21	0.36	0.72	0.92
P_2O_5	%	0.01	FUS-XRF	0.1	< 0.01	0.01	0.01	0.01
Cr_2O_3	%	0.01	FUS-XRF	0.01	0.01	0.01	0.01	0.02
V_2O_5	%	0.003	FUS-XRF	< 0.003	0.003	0.01	0.02	0.023
LOI	%		GRAV	1	0.57	1.61	2.76	1.81
Total	%	0.01	FUS-XRF	100.1	99.99	99.52	100.7	99.13
B	ppm	20	TD-MS	< 20	< 20	< 20	< 20	< 20
Li	ppm	0.5	TD-MS	5.2	6.5	20.8	47.8	36.7
Na	%	0.01	TD-MS	0.02	0.32	2.12	1.55	0.64
Mg	%	0.01	TD-MS	0.11	0.21	0.51	1.66	1.09
Al	%	0.01	TD-MS	1.93	1.17	7.2	7.88	4.1
K	%	0.01	TD-MS	1.76	0.64	2.01	2.98	1.99
Ca	%	0.01	TD-MS	0.03	0.19	1.75	1.37	1.07
Cd	ppm	0.1	TD-MS	< 0.1	< 0.1	< 0.1	< 0.1	< 0.1
V	ppm	1	TD-MS	23	28	58	114	149
Cr	ppm	1	TD-MS	41	64	40	79	88
Mn	ppm	1	TD-MS	45	151	329	1180	644
Fe	%	0.01	TD-MS	1.23	1.11	1.69	6.34	3.94
Hf	ppm	0.1	TD-MS	0.6	41.4	25.7	28.6	26.1
Ni	ppm	0.5	TD-MS	1	10.8	16.7	48.1	38.9
Er	ppm	0.1	TD-MS	4.1	4.4	2.8	10.3	9.3
Be	ppm	0.1	TD-MS	1.4	0.3	1.2	0.9	0.3
Ho	ppm	0.1	TD-MS	1.8	1.5	0.9	3.3	3.2
Hg	ppb	10	TD-MS	20	10	20	20	20
Ag	ppm	0.05	TD-MS	1.88	0.23	0.33	0.42	0.5
Cs	ppm	0.05	TD-MS	0.38	1.29	1.63	3.73	3.67
Co	ppm	0.1	TD-MS	1.9	4.2	7.1	30	19.7
Eu	ppm	0.05	TD-MS	5.11	0.3	1.23	1.24	0.77
Bi	ppm	0.02	TD-MS	1.96	0.13	0.32	0.22	0.33
Se	ppm	0.1	TD-MS	0.2	< 0.1	< 0.1	< 0.1	< 0.1
Zn	ppm	0.2	TD-MS	12.1	26.6	45.3	151	108
Ga	ppm	0.1	TD-MS	6.9	5	18.6	22.4	14.4
As	ppm	0.1	TD-MS	19.6	0.9	10	23.2	14.5
Rb	ppm	0.2	TD-MS	116	56.1	110	197	144
Y	ppm	0.1	TD-MS	44.6	30.8	20.3	77.4	65.3
Zr	ppm	1	TD-MS	32	1470	753	837	713
Nb	ppm	0.1	TD-MS	2.9	9.9	11.6	22.4	17
Mo	ppm	0.05	TD-MS	5.11	263	439	403	407
In	ppm	0.1	TD-MS	< 0.1	< 0.1	< 0.1	< 0.1	< 0.1
Sn	ppm	1	TD-MS	< 1	< 1	< 1	< 1	< 1
Sb	ppm	0.1	TD-MS	1.2	0.3	0.6	0.5	0.6
Te	ppm	0.1	TD-MS	0.2	< 0.1	0.1	0.1	0.2
Ba	ppm	1	TD-MS	306	81	348	509	274
La	ppm	0.1	TD-MS	26.3	5.3	16.4	13	7.5
Ce	ppm	0.1	TD-MS	58.7	15.7	30.7	23.5	21.2
Pr	ppm	0.1	TD-MS	7.7	2.8	3.9	3	4.1
Nd	ppm	0.1	TD-MS	28.9	14.8	15.4	12.4	25
Sm	ppm	0.1	TD-MS	14.2	6.6	4.7	5.7	13.2
Gd	ppm	0.1	TD-MS	18.3	5.6	4.5	7.8	13.3
Tb	ppm	0.1	TD-MS	2.4	1	0.7	1.8	2.3
Dy	ppm	0.1	TD-MS	12.7	7.2	5	15.1	16.2
Cu	ppm	0.2	TD-MS	34.4	10.1	9.9	77.1	27
Ge	ppm	0.1	TD-MS	< 0.1	< 0.1	0.2	0.2	0.2
Tm	ppm	0.1	TD-MS	0.4	0.5	0.3	1.4	1.1
Yb	ppm	0.1	TD-MS	2.5	3.8	2.4	10.6	7.5

Analyte Symbol	Unit	Detection Limit	Analysis Method	H- 09	H- 10	H- 11	H- 12	H- 14
Lu	ppm	0.1	TD-MS	0.3	0.6	0.4	1.7	1.1
Ta	ppm	0.1	TD-MS	< 0.1	0.6	0.7	1.4	0.9
Sr	ppm	0.2	TD-MS	10.8	30.9	277	165	70.8
W	ppm	0.1	TD-MS	0.7	0.6	0.6	0.6	0.9
Re	ppm	0.001	TD-MS	0.003	0.003	0.002	0.002	0.006
Tl	ppm	0.05	TD-MS	0.84	0.51	0.76	1.76	1.89
Pb	ppm	0.5	TD-MS	94.7	632	411	379	2090
Th	ppm	0.1	TD-MS	> 500	302	107	109	> 500
U	ppm	0.1	TD-MS	46.3	1190	728	810	3870

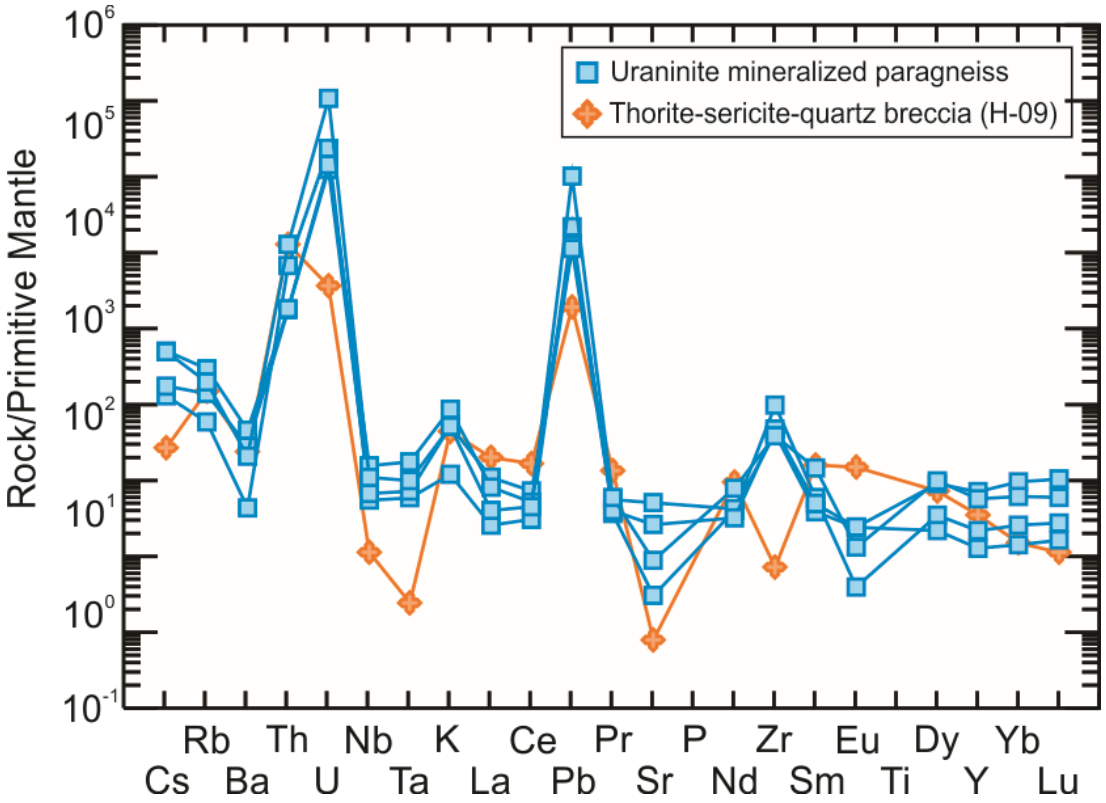

Figure A2-3: Trace-element whole-rock chemistry of Hope uraninite-bearing paragneiss and thorite-sericite breccia sample (H-09) normalized to Primitive Mantle (Sun and McDonough 1989).

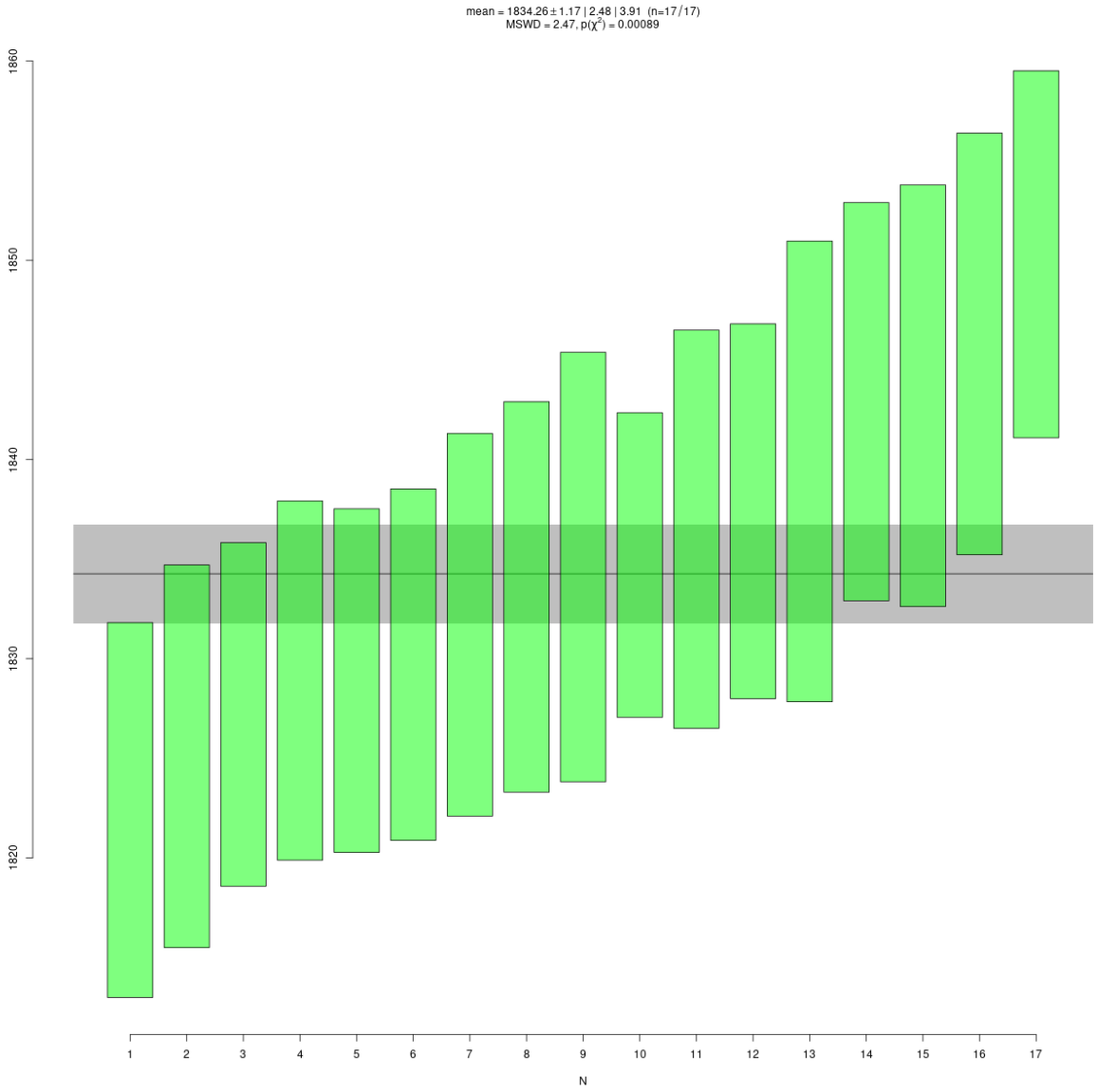

Figure A2-4: Biotite Ar-Ar plateau ages with weighted mean

Table A2-3: Re-Os isotopic age and data of molybdenite

Sample	Re (ppm)	±2σ	^{187}Re (ppb)	±2σ	^{187}Os (ppb)	2σ	Model Age (Ma)	±2σ with λ (Ma)
H-11	0.843	0.002	529.9	1.5	16.090	0.05	1938	9
H-11-RPT	1.093	0.002	687.0	1.5	20.848	0.18	1912	8

Notes: Age uncertainties include 187Re decay constant uncertainty. Model ages assume an initial ^{187}Os/^{188}Os ratio of 1.0. Abbreviations: Parts per billion (ppb), parts per million (ppm), repeat (RPT)

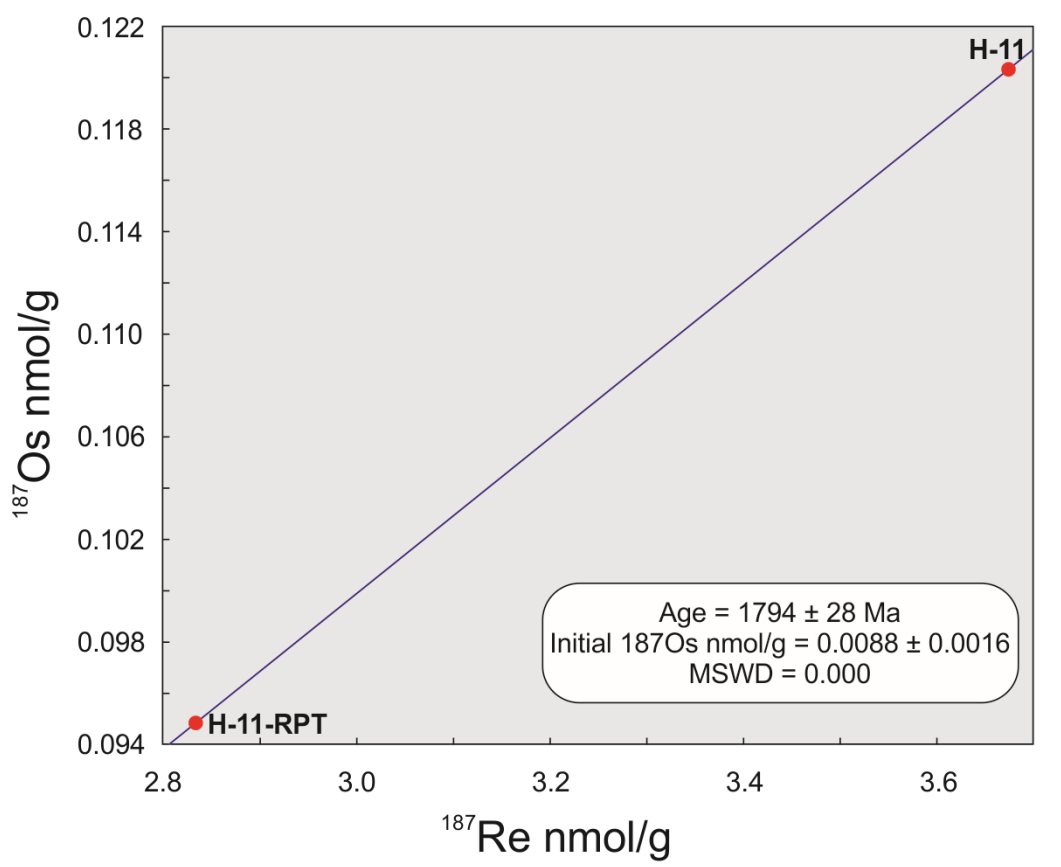

Figure A2-5: Two-point age of molybdenite from sample H-11.

Table A2-4: Full raw SIMS data set collected from 9 uraninite grains in two samples, H-12 and H-14

Sample	206Pb/204Pb	Error (%)	207Pb/204Pb	Error (%)	207Pb/206Pb	Error (%)	208Pb/204Pb	Error (%)	235U/238U	Error (%)	207Pb/235U	Error (%)	206Pb/238U	Error (%)
H12-1-1	36767.24	26.7	3326.09	26.7	0.0900	0.3	1790.62	26.7	0.00726	0.4	1.4582	0.5	0.1133	0.1
H12-1-2	38936.16	26.7	3380.33	26.7	0.0870	0.3	1748.64	26.7	0.00723	0.4	1.4547	0.5	0.1163	0.1
H12-1-3	39910.77	30.1	3354.70	28.9	0.0843	0.3	1887.96	30.1	0.00724	0.4	1.1785	0.5	0.0980	0.1
H12-1-4	38425.71	23.6	3471.35	23.6	0.0900	0.3	1800.00	23.6	0.00725	0.4	1.4283	0.5	0.1108	0.1
H12-1-5	50062.73	33.3	4385.12	33.3	0.0870	0.3	2076.14	31.6	0.00728	0.4	1.4156	0.5	0.1136	0.1
H12-1-6	53194.43	20.4	5506.10	20.4	0.1033	0.3	2398.36	20.4	0.00730	0.4	2.2522	0.5	0.1512	0.1
H12-1-7	35415.14	24.3	3585.00	24.3	0.1015	0.3	1530.27	24.3	0.00716	0.5	2.0570	0.5	0.1395	0.1
H12-1-8	45605.60	28.9	4366.73	28.9	0.0958	0.3	2101.78	28.9	0.00720	0.4	1.7043	0.5	0.1232	0.1
H12-1-9	47026.41	26.7	4331.49	26.7	0.0930	0.3	2196.36	26.7	0.00721	0.4	1.5864	0.5	0.1190	0.1
H12-1-10	44500.69	44.7	3926.25	44.7	0.0885	0.3	2061.28	44.7	0.00721	0.4	1.4932	0.5	0.1171	0.1
H12-1-11	38707.51	23.6	3582.23	23.6	0.0924	0.3	1691.12	23.6	0.00725	0.4	1.5214	0.5	0.1151	0.1
H12-1-12	39123.04	26.7	3502.17	26.7	0.0889	0.3	1539.27	26.0	0.00724	0.4	1.4698	0.5	0.1146	0.1
H12-1-13	38950.93	14.9	4274.39	14.9	0.1100	0.2	1533.68	14.9	0.00727	0.4	2.2504	0.5	0.1427	0.1
H12-1-14	41636.09	37.8	3508.03	37.8	0.0847	0.2	1828.42	37.8	0.00726	0.4	1.2975	0.5	0.1070	0.1
H12-1-15	40780.72	20.4	3621.47	20.4	0.0885	0.2	1927.45	20.4	0.00724	0.4	1.4731	0.5	0.1155	0.1
H12-1-16	43145.24	44.7	3508.08	44.7	0.0814	0.3	2006.30	44.7	0.00727	0.4	1.2275	0.5	0.1056	0.1
H12-1-17	43374.15	23.6	3882.17	23.6	0.0887	0.3	2012.89	23.6	0.00730	0.4	1.4467	0.5	0.1146	0.1
H12-1-18	43944.69	20.0	4167.51	20.0	0.0949	0.3	1680.22	20.0	0.00726	0.4	1.6525	0.5	0.1212	0.1
H12-2-1	55264.86	14.0	7046.61	14.0	0.1277	0.2	2100.38	14.0	0.00722	0.4	3.2716	0.4	0.1743	0.1
H12-2-2	44528.58	14.4	5193.95	14.4	0.1164	0.2	1692.69	14.4	0.00726	0.4	2.4199	0.4	0.1430	0.1
H12-2-3	64258.39	17.4	8228.13	17.4	0.1281	0.2	2594.99	17.4	0.00722	0.4	3.3248	0.4	0.1766	0.1
H12-2-4	58972.65	12.4	8112.05	12.4	0.1373	0.2	2372.83	12.4	0.00725	0.4	3.9211	0.4	0.1947	0.1
H12-3-1	25175.10	12.8	3104.88	12.8	0.1234	0.3	876.48	12.8	0.00725	0.5	2.9573	0.6	0.1640	0.1
H12-3-2	23960.37	13.6	2453.11	13.6	0.1024	0.3	830.31	13.6	0.00733	0.4	1.3104	0.5	0.0897	0.1
H12-3-3	12573.41	11.5	1509.40	11.5	0.1190	0.3	462.36	11.4	0.00723	0.7	3.1781	0.7	0.1795	0.1
H12-3-4	23166.48	14.4	2329.44	14.4	0.1005	0.3	780.44	14.4	0.00723	0.4	1.2863	0.5	0.0887	0.1
H12-3-5	22651.28	14.4	2345.05	14.0	0.1032	0.3	753.70	14.0	0.00730	0.4	1.2564	0.5	0.0850	0.1
H12-3-6	26939.69	13.7	2826.28	13.7	0.1048	0.3	938.02	13.7	0.00722	0.4	1.5671	0.5	0.1030	0.1
H12-3-7	26301.71	11.7	3381.91	11.7	0.1283	0.3	899.32	11.7	0.00726	0.5	3.2361	0.5	0.1736	0.1
H12-4-1	46601.11	25.8	5011.51	25.8	0.1071	0.3	1892.69	25.8	0.00723	0.4	1.7689	0.5	0.1136	0.1
H12-4-2	58479.04	14.7	7218.72	14.7	0.1236	0.2	2452.11	14.7	0.00729	0.4	3.1056	0.5	0.1724	0.1
H12-4-3	43194.06	20.0	5154.37	20.0	0.1193	0.2	1707.65	20.0	0.00725	0.4	2.3951	0.5	0.1379	0.1
H12-4-4	52224.91	18.3	5808.49	18.3	0.1115	0.2	2061.55	18.3	0.00723	0.4	2.0866	0.4	0.1289	0.1
H12-4-5	38409.72	16.4	4591.05	16.4	0.1194	0.2	1527.77	16.4	0.00730	0.4	2.2463	0.5	0.1306	0.1
H12-5-1	45323.00	23.6	4302.44	23.6	0.0945	0.3	1732.62	23.5	0.00720	0.4	1.3769	0.4	0.1014	0.1

Sample	206Pb/204Pb	Error (%)	207Pb/204Pb	Error (%)	207Pb/206Pb	Error (%)	208Pb/204Pb	Error (%)	235U/238U	Error (%)	207Pb/235U	Error (%)	206Pb/238U	Error (%)
H12-5-2	39468.27	24.3	3359.86	24.3	0.0853	0.3	1480.72	24.3	0.00728	0.4	1.2733	0.4	0.1052	0.1
H12-5-3	31996.36	21.8	2479.00	21.8	0.0775	0.3	1279.81	21.8	0.00726	0.4	1.0184	0.5	0.0920	0.1
H12-5-4	33968.48	30.2	2530.88	30.2	0.0762	0.4	1436.81	30.2	0.00728	0.4	0.8744	0.5	0.0815	0.1
H12-5-5	38042.58	26.7	2926.69	26.7	0.0774	0.3	1469.32	26.7	0.00726	0.4	0.9291	0.5	0.0847	0.1
H14-1-2-1	36833.24	20.9	3828.76	20.9	0.1041	0.3	1461.64	20.9	0.00728	0.4	1.5552	0.5	0.1057	0.1
H14-1-2-2	34753.11	11.5	4356.60	11.5	0.1252	0.2	1370.77	11.5	0.00724	0.4	2.5978	0.4	0.1447	0.1
H14-1-2-3	40902.78	17.5	4819.20	17.5	0.1178	0.2	1612.00	17.5	0.00723	0.4	2.0133	0.4	0.1200	0.1
H14-1-2-4	41853.19	22.4	4223.04	22.4	0.1010	0.3	1653.03	22.3	0.00723	0.4	1.5988	0.5	0.1107	0.1
H14-1-2-5	41382.36	15.1	4890.95	15.1	0.1178	0.2	1611.03	15.1	0.00727	0.4	2.2359	0.5	0.1333	0.1
H14-1-2-6	36583.64	19.2	3423.58	19.2	0.0935	0.3	1402.32	19.3	0.00724	0.4	1.3969	0.5	0.1042	0.1
H14-1-2-7	26737.57	14.0	3753.59	14.0	0.1405	0.3	1038.51	14.0	0.00713	0.4	3.6933	0.5	0.1806	0.1
H14-1-1-1	28779.86	16.9	3000.54	16.9	0.1042	0.3	1125.43	16.9	0.00725	0.4	1.5586	0.5	0.1049	0.1
H14-1-1-2	37414.37	13.4	4635.79	13.4	0.1244	0.3	1500.60	13.4	0.00722	0.4	2.4739	0.5	0.1387	0.1
H14-1-1-3	34937.43	18.6	3541.97	18.6	0.1010	0.3	1454.32	18.6	0.00723	0.4	1.4241	0.5	0.0986	0.1
H14-1-1-4	37212.96	18.3	3820.36	18.3	0.1027	0.3	1522.61	18.3	0.00724	0.4	1.5910	0.5	0.1082	0.1
H14-1-1-5	35906.94	13.9	4265.57	13.9	0.1189	0.2	1428.98	13.9	0.00725	0.4	2.1580	0.4	0.1275	0.1
H14-1-1-6	44247.54	20.0	4707.73	20.0	0.1104	0.3	1674.33	20.0	0.00719	0.4	1.8398	0.5	0.1162	0.1
H14-1-1-7	34039.39	14.1	4214.59	14.1	0.1246	0.2	1325.07	14.1	0.00732	0.4	2.4897	0.5	0.1414	0.1
H14-1-1-8	39023.70	16.7	4240.82	16.7	0.1080	0.3	1554.76	16.7	0.00724	0.4	1.7095	0.5	0.1110	0.1
H14-2-1	42539.68	22.4	4447.10	22.4	0.1048	0.3	1664.92	22.4	0.00728	0.4	1.5320	0.4	0.1019	0.1
H14-2-2	25943.24	31.6	3208.66	31.6	0.1232	0.3	1022.45	31.6	0.00729	0.6	2.4635	0.6	0.1381	0.1
H14-2-3	27801.92	25.0	3694.53	25.0	0.1312	0.3	1081.32	25.0	0.00730	0.6	3.0355	0.6	0.1600	0.1
H14-2-4	41756.78	23.6	4203.68	23.6	0.1008	0.3	1647.33	23.6	0.00728	0.4	1.4419	0.5	0.0996	0.1
H14-2-5	56915.56	16.2	7403.36	16.2	0.1282	0.2	2172.36	16.2	0.00723	0.4	3.3859	0.4	0.1756	0.1
H14-2-6	43059.50	9.1	6600.91	9.1	0.1534	0.1	1578.87	9.1	0.00726	0.5	8.9223	0.5	0.3795	0.1
H14-3-1	27933.24	15.4	3036.81	15.4	0.1090	0.3	1134.53	15.4	0.00723	0.4	1.6497	0.5	0.1050	0.1
H14-3-2	40039.94	21.8	4132.55	21.8	0.1034	0.3	1629.00	21.8	0.00727	0.4	1.5380	0.5	0.1033	0.1
H14-3-3	40876.34	25.8	3975.99	25.8	0.0968	0.3	1616.34	25.8	0.00721	0.4	1.6103	0.5	0.1136	0.1
H14-3-4	41377.80	13.1	4745.29	13.1	0.1146	0.3	1616.63	13.1	0.00725	0.4	2.0204	0.4	0.1214	0.1
H14-3-5	59820.70	16.7	7329.78	16.7	0.1226	0.2	2288.33	16.7	0.00728	0.4	2.4226	0.4	0.1372	0.1
H14-3-6	81410.49	19.6	10574.36	19.6	0.1300	0.2	3142.52	19.6	0.00720	0.4	3.2581	0.4	0.1709	0.1
H14-3-7	58979.22	21.8	6645.29	21.8	0.1126	0.2	2302.18	21.8	0.00723	0.4	2.2636	0.4	0.1378	0.1
H14-3-8	37124.81	28.9	3356.09	28.9	0.0903	0.3	1493.55	28.9	0.00724	0.4	1.0957	0.5	0.0842	0.1
H14-3-9	55946.53	16.7	7148.09	16.7	0.1275	0.2	2156.26	16.7	0.00723	0.4	3.1532	0.4	0.1692	0.1
H14-3-10	62244.53	16.0	8620.34	16.0	0.1382	0.2	2389.15	16.0	0.00721	0.4	3.5416	0.4	0.1750	0.1
H14-4-1	51058.16	18.6	5403.56	18.6	0.1070	0.2	2080.92	18.6	0.00723	0.4	1.8692	0.4	0.1202	0.1
H14-4-2	48205.49	19.3	5253.80	19.3	0.1092	0.2	1915.60	19.3	0.00723	0.4	1.8582	0.4	0.1173	0.1

Sample	206Pb/204Pb	Error (%)	207Pb/204Pb	Error (%)	207Pb/206Pb	Error (%)	208Pb/204Pb	Error (%)	235U/238U	Error (%)	207Pb/235U	Error (%)	206Pb/238U	Error (%)
H14-4-3	48826.41	20.0	5350.90	20.0	0.1097	0.2	1959.05	20.0	0.00724	0.4	1.8510	0.4	0.1165	0.1
H14-4-4	53019.34	19.6	5995.99	19.6	0.1129	0.3	2067.47	19.6	0.00729	0.4	2.0370	0.4	0.1250	0.1
H14-4-5	55296.93	20.4	6237.21	20.4	0.1132	0.2	2180.80	20.4	0.00731	0.4	2.2632	0.4	0.1381	0.1
H14-4-6	46493.70	16.7	5408.56	16.7	0.1167	0.2	1849.74	16.7	0.00725	0.4	2.1292	0.4	0.1261	0.1
H14-4-7	56655.57	14.6	7412.10	14.6	0.1308	0.2	2258.85	14.6	0.00726	0.4	3.1329	0.4	0.1647	0.1
H14-4-8	52829.70	13.5	6565.85	13.5	0.1244	0.2	2108.39	13.5	0.00722	0.4	2.8773	0.4	0.1584	0.1
H14-4-9	28060.74	15.1	3533.24	15.1	0.1252	0.2	1120.85	15.1	0.00723	0.5	2.6394	0.5	0.1456	0.1

Table A2-5: SIMS analyses of Hope uraninite, grouped into T0, T1, T2 and T3 based on ellipse overlap in Concordia space. Each grouping is averaged, representing a new ellipse (italicized). The number (n) is shown for each new ellipse, on how many data points were averaged. The number is also represented in Figure A2-6 by a red value next to their respective ellipse.

	Sample	207Pb/206Pb	2σ	207Pb/235U	2σ	206Pb/238U	2σ
T0							
	H12-5-3	0.0775	0.3	1.0184	0.5	0.0920	0.1000
0a (n=1)	*average*	*0.0775*	*0.3*	*1.0184*	*0.5*	*0.0920*	*0.1000*
	H14-1-2-6	0.0935	0.3	1.3969	0.5	0.1042	0.1000
0b (n=1)	*average*	*0.0935*	*0.3*	*1.3969*	*0.5*	*0.1042*	*0.1000*
	H14-1-2-4	0.1010	0.3	1.5988	0.5	0.1107	0.1000
	H14-3-3	0.0968	0.3	1.6103	0.4	0.1136	0.1000
0c (n=2)	*average*	*0.0989*	*0.3000*	*1.6045*	*0.4250*	*0.1122*	*0.1000*
	H12-4-4	0.1115	0.2	2.0866	0.4	0.1289	0.1000
	H14-4-4	0.1129	0.3	2.0370	0.4	0.1250	0.1000
0d (n=2)	*average*	*0.1122*	*0.2500*	*2.0618*	*0.4000*	*0.1270*	*0.1000*
	H14-1-2-7	0.1405	0.3	3.6933	0.5	0.1806	0.1000
	H14-3-10	0.1382	0.2	3.5416	0.4	0.1750	0.1000
0e (n=2)	*average*	*0.1393*	*0.2500*	*3.6175*	*0.4500*	*0.1778*	*0.1000*
T0							
	H12-2-4	0.1373	0.2	3.9211	0.4	0.1947	0.1000
0a (n=1)	*average*	*0.1373*	*0.2*	*3.9211*	*0.4*	*0.1947*	*0.1000*
	H12-2-1	0.1277	0.2	3.2716	0.4	0.1743	0.1000
	H12-2-3	0.1281	0.2	3.3248	0.4	0.1766	0.1000
	H12-3-7	0.1283	0.3	3.2361	0.5	0.1736	0.1000
	H14-2-5	0.1178	0.2	3.3859	0.5	0.1756	0.1000
	H14-3-9	0.1275	0.2	3.1532	0.4	0.1692	0.1000
0b (n=5)	*average*	*0.1259*	*0.2200*	*3.2743*	*0.4400*	*0.1739*	*0.1000*
	H12-1-8	0.0958	0.3	1.7043	0.5	0.1232	0.1000
	H12-1-18	0.0949	0.3	1.6525	0.5	0.1212	0.1000
0c (n=2)	*average*	*0.0954*	*0.3000*	*1.6784*	*0.5000*	*0.1222*	*0.1000*
	H12-1-9	0.0930	0.3	1.5864	0.5	0.1190	0.1000
	H12-1-11	0.0924	0.3	1.5214	0.5	0.1151	0.1000
0d (n=2)	*average*	*0.0927*	*0.3000*	*1.5539*	*0.5000*	*0.1171*	*0.1000*
	H12-1-2	0.0870	0.3	1.4547	0.5	0.1163	0.1000
	H12-1-4	0.0900	0.3	1.4283	0.5	0.1108	0.1000
	H12-1-5	0.0870	0.3	1.4156	0.5	0.1136	0.1000
	H12-1-10	0.0885	0.3	1.4932	0.5	0.1171	0.1000
	H12-1-12	0.0889	0.3	1.4698	0.5	0.1146	0.1000
	H12-1-15	0.0885	0.2	1.4731	0.5	0.1155	0.1000
	H12-1-17	0.0887	0.3	1.4467	0.5	0.1146	0.1000
0e (n=7)	*average*	*0.0884*	*0.2857*	*1.4545*	*0.5000*	*0.1147*	*0.1000*
T1							
	H14-4-7	0.1308	0.2	3.1329	0.4	0.1647	0.1000
	H14-2-3	0.1312	0.3	3.0355	0.6	0.1600	0.1000
	H14-3-6	0.1300	0.2	3.2581	0.4	0.1709	0.1000
1a (n=3)	*average*	*0.13*	*0.23*	*3.14*	*0.47*	*0.17*	*0.1000*
	H12-4-1	0.1071	0.3	1.7689	0.5	0.1136	0.1000
	H14-1-1-6	0.1104	0.3	1.8398	0.5	0.1162	0.1000
	H14-1-1-8	0.1080	0.3	1.7095	0.5	0.1110	0.1000
	H14-4-1	0.1070	0.2	1.8692	0.4	0.1202	0.1000
	H14-4-2	0.1092	0.2	1.8582	0.4	0.1173	0.1000
	H14-4-3	0.1097	0.2	1.8510	0.4	0.1165	0.1000
1b (n=6)	*average*	*0.11*	*0.25*	*1.82*	*0.45*	*0.12*	*0.1000*
	H12-4-3	0.1193	0.2	2.3951	0.5	0.1379	0.1000
	H14-1-2-2	0.1252	0.2	2.5978	0.4	0.1447	0.1000

	Sample	207Pb/206Pb	2σ	207Pb/235U	2σ	206Pb/238U	2σ
	H14-1-1-2	0.1244	0.3	2.4739	0.5	0.1387	0.1000
	H14-1-1-7	0.1246	0.2	2.4897	0.5	0.1414	0.1000
	H14-4-9	0.1252	0.2	2.6394	0.5	0.1456	0.1000
	H14-2-2	0.1232	0.3	2.4635	0.6	0.1381	0.1000
	H14-3-5	0.1226	0.2	2.4226	0.4	0.1372	0.1000
1c (n=7)	*average*	*0.12*	*0.23*	*2.50*	*0.49*	*0.14*	*0.1000*
	H12-4-5	0.1194	0.2	2.2463	0.5	0.1306	0.1000
	H14-1-2-5	0.1178	0.2	2.2359	0.5	0.1333	0.1000
	H14-1-1-5	0.1189	0.2	2.1580	0.4	0.1275	0.1000
	H14-4-6	0.1167	0.2	2.1292	0.4	0.1261	0.1000
1d (n=4)	*average*	*0.12*	*0.20*	*2.19*	*0.45*	*0.13*	*0.1000*
	H14-1-2-1	0.1041	0.3	1.5552	0.5	0.1057	0.1000
	H14-1-1-1	0.1042	0.3	1.5586	0.5	0.1049	0.1000
	H14-1-1-4	0.1027	0.3	1.5910	0.5	0.1082	0.1000
	H14-2-1	0.1048	0.3	1.5320	0.4	0.1019	0.1000
	H14-3-2	0.1034	0.3	1.5380	0.5	0.1033	0.1000
1e (n=5)	*average*	*0.10*	*0.30*	*1.55*	*0.48*	*0.10*	*0.1000*
	H14-3-4	0.1146	0.3	2.0204	0.4	0.1214	0.1000
	H14-1-2-3	0.1178	0.2	2.0133	0.4	0.1200	0.1000
1f (n=2)	*average*	*0.12*	*0.25*	*2.02*	*0.40*	*0.12*	*0.1000*
	H14-2-6	0.1534	0.1	8.9223	0.5	0.3795	0.1000
1g (n=1)	*average*	*0.15*	*0.10*	*8.92*	*0.50*	*0.38*	*0.1000*
T2							
	H12-5-4	0.0762	0.4	0.8744	0.5	0.0815	0.1000
2a (n=1)	*average*	*0.0762*	*0.4*	*0.8744*	*0.5*	*0.0815*	*0.1000*
	H12-5-5	0.0774	0.3	0.9291	0.5	0.0847	0.1000
2b (n=1)	*average*	*0.0774*	*0.3*	*0.9291*	*0.5*	*0.0847*	*0.1000*
	H12-5-1	0.0945	0.3	1.3769	0.4	0.1014	0.1000
2c (n=1)	*average*	*0.0945*	*0.3*	*1.3769*	*0.4*	*0.1014*	*0.1000*
	H12-2-2	0.1164	0.2	2.4199	0.4	0.1430	0.1000
2d (n=1)	*average*	*0.1164*	*0.2*	*2.4199*	*0.4*	*0.1430*	*0.1000*
	H12-3-1	0.1234	0.3	2.9573	0.6	0.1640	0.1000
	H14-4-8	0.1244	0.2	2.8773	0.4	0.1584	0.1000
2e (n=2)	*average*	*0.1239*	*0.2500*	*2.9173*	*0.5000*	*0.1612*	*0.1000*
T3							
	H12-1-6	0.1033	0.3	2.2522	0.5	0.1512	0.1000
3a (n=1)	*average*	*0.1033*	*0.3*	*2.2522*	*0.5*	*0.1512*	*0.1000*
	H12-1-7	0.1015	0.3	2.0570	0.5	0.1395	0.1000
3b (n=1)	average	0.1015	0.3	2.0570	0.5	0.1395	0.1000
	H12-3-2	0.1024	0.3	1.3104	0.5	0.0897	0.1000
	H12-3-4	0.1005	0.3	1.2863	0.5	0.0887	0.1000
	H12-3-5	0.1032	0.3	1.2564	0.5	0.0850	0.1000
3c (n=3)	*average*	*0.10*	*0.30*	*1.28*	*0.50*	*0.09*	*0.1000*

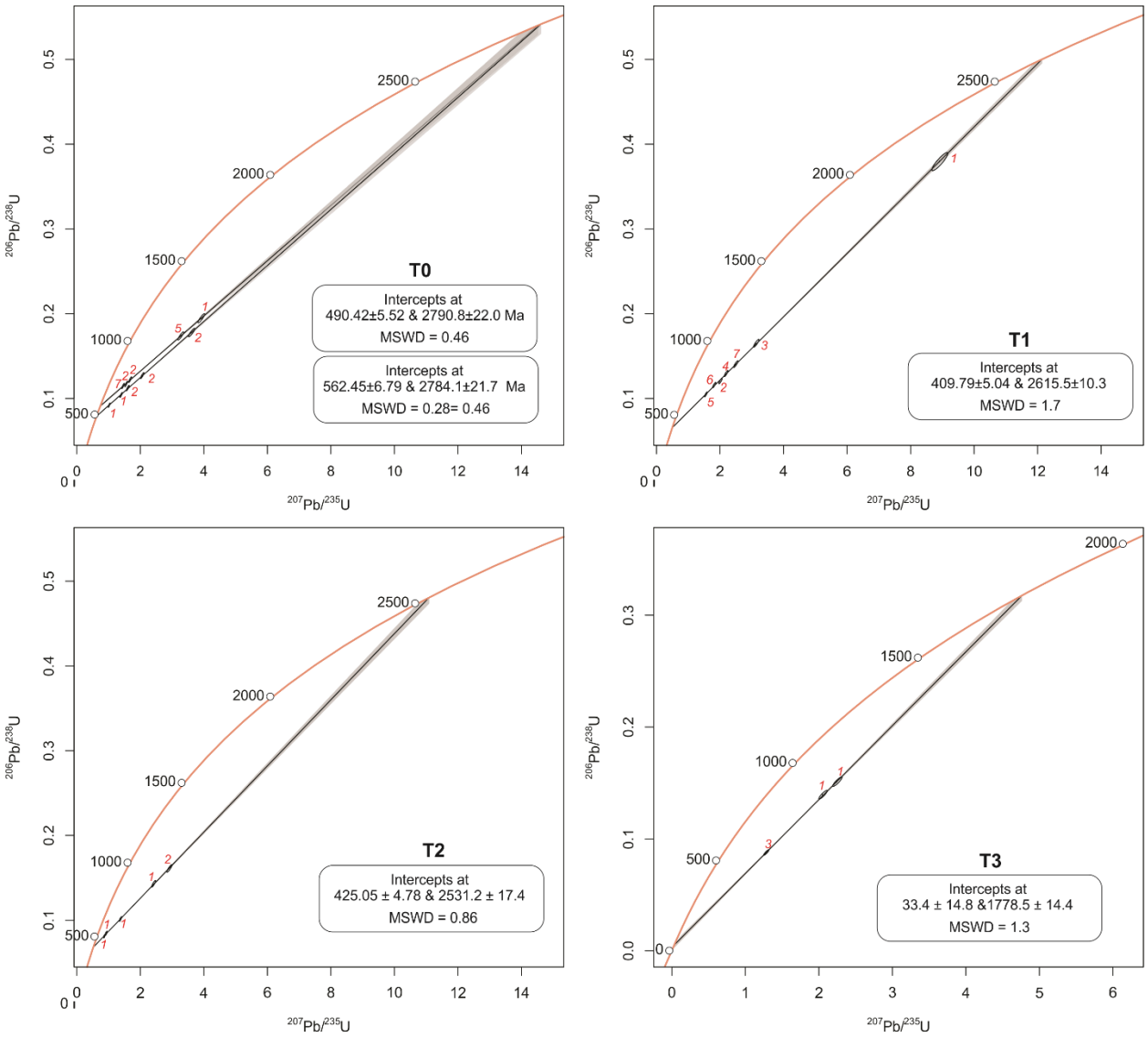

Figure A2-6: Wetherill diagram of $^{206}Pb/^{238}U$ versus $^{207}Pb/^{235}U$ with ages in millions of years (Ma) along Concordia (orange line). Averaged U-Pb results from in situ isotopic analyses of uraninite, with T0 representing primary crystallization ages of uraninite; T1, T2 and T3 representing various alteration and isotopic resetting events throughout the evolution of the Hope occurrence. Red numbers beside ellipses representing the number of averaged samples constituting that point.

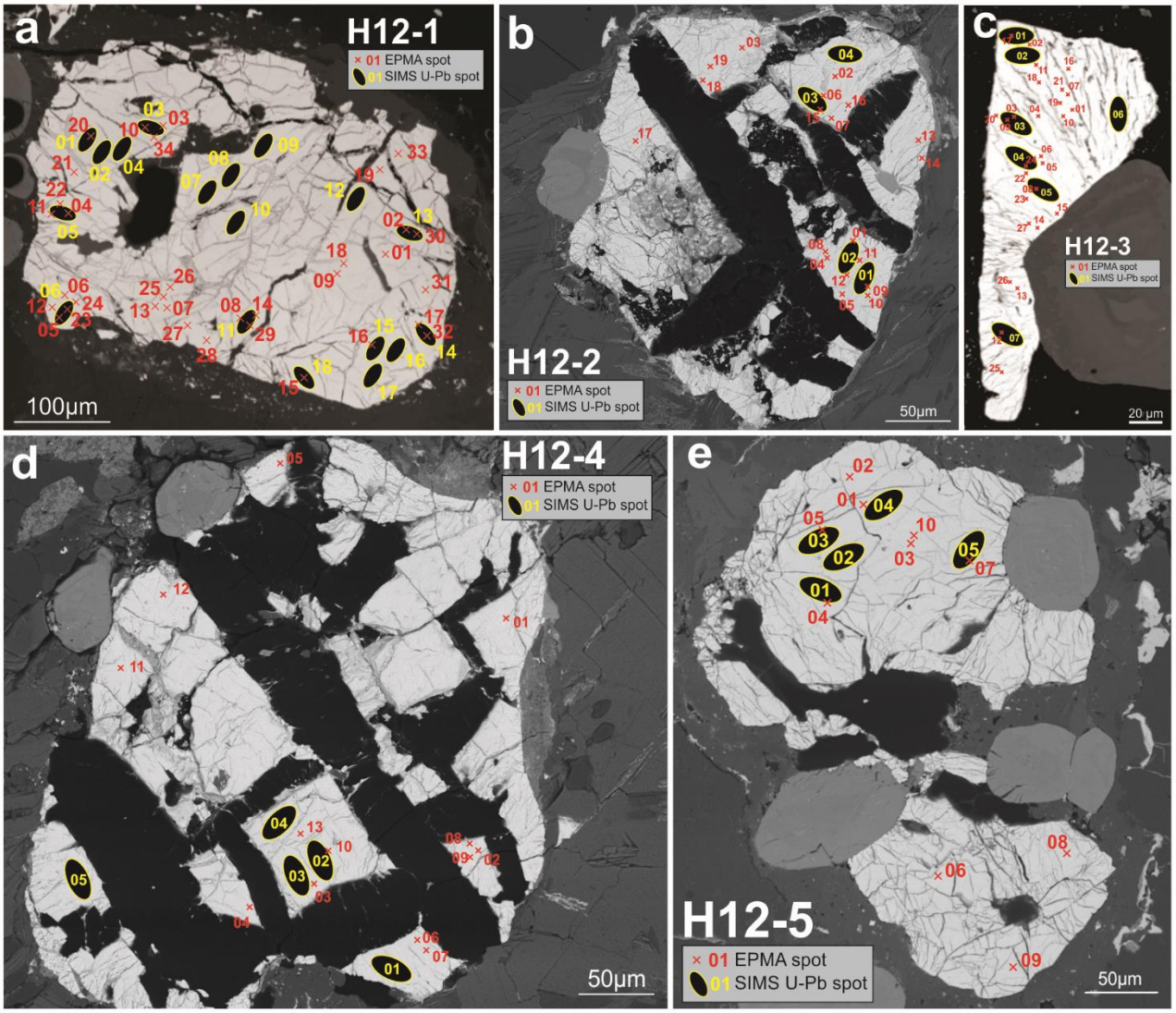

Figure A2-7: SEM BSE images with EPMA and SIMS U-Pb spot analyses from sample H-12. Data correlate with those outlined for respective sample numbers in Table A2-1 and Table A2-4.

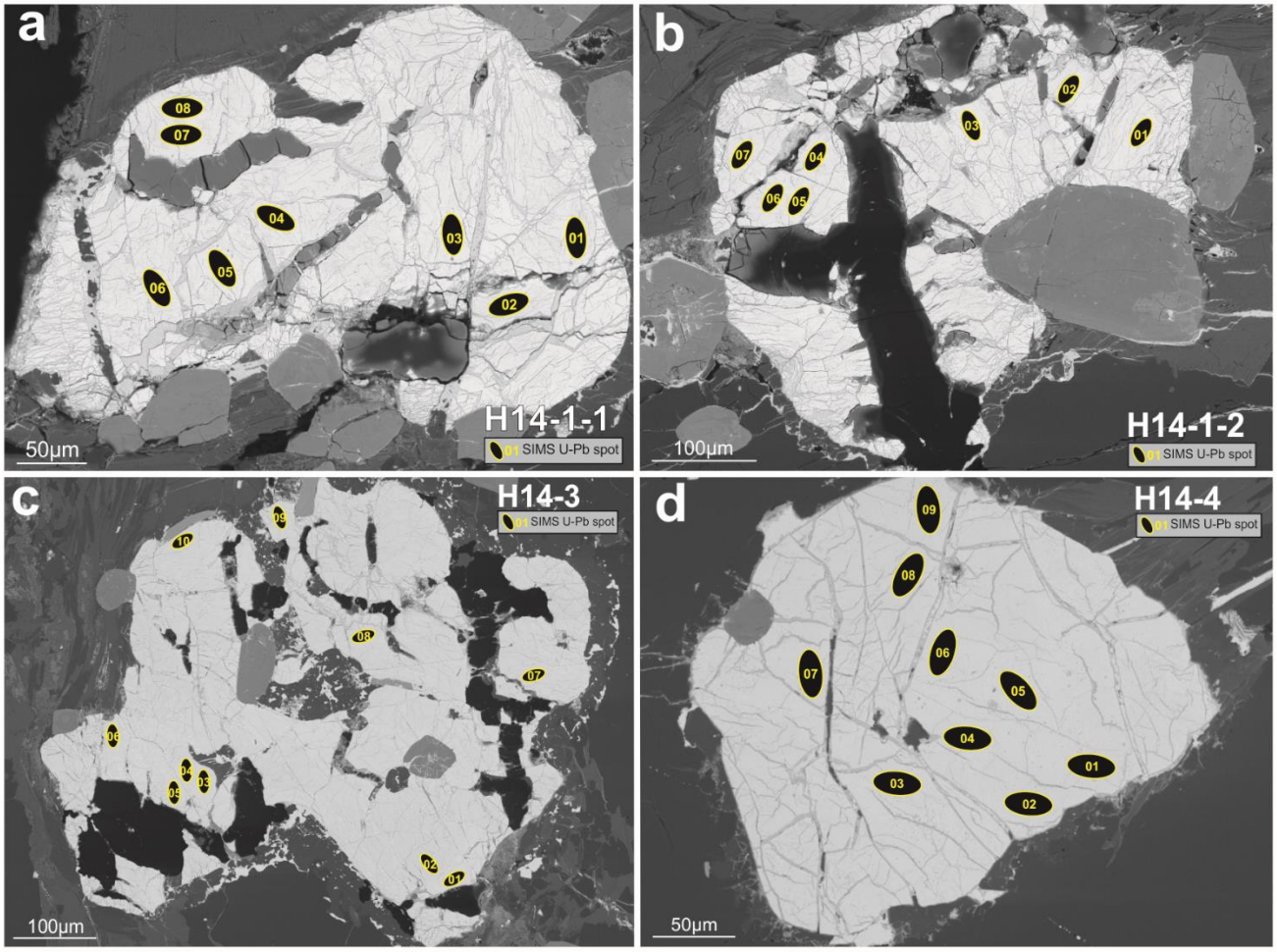

Figure A2-8: SEM BSE images with SIMS U-Pb spot analyses from sample H-14. Data correlate with those outlined for respective sample numbers in Table A2-4.

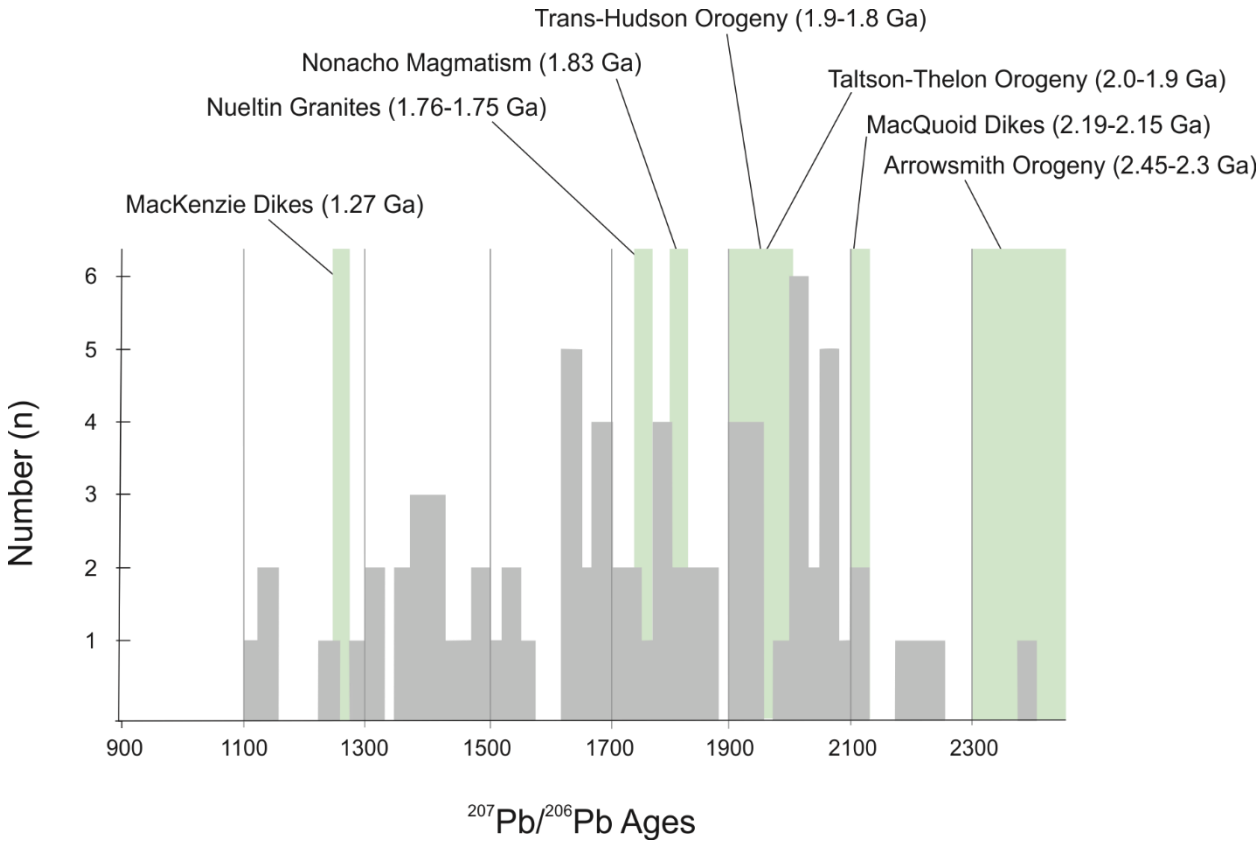

Figure A2-9: Histogram of the $^{207}Pb/^{206}Pb$ ages from Hope uraninite overlapping tectono-metamorphic events in the Rae craton. Noted events include: Arrowsmith orogeny (Berman et al. 2005, 2010, Hartlaub et al. 2007); MacQuoid Dikes (LeCheminant et al. 1997) ; Taltson-Thelon orogeny (Hoffman 1988); Trans-Hudson orogeny (Hoffman 1988, Ashton et al. 2009, Pehrsson et al. 2013a); Nonacho Magmatism (McGlynn et al. 1974, Bostock et al. 1991, Bostock and van Breemen 1992); Nueltin Granites (Peterson et al. 2002) and the MacKenzie Dikes (LeCheminant and Heaman 1989).

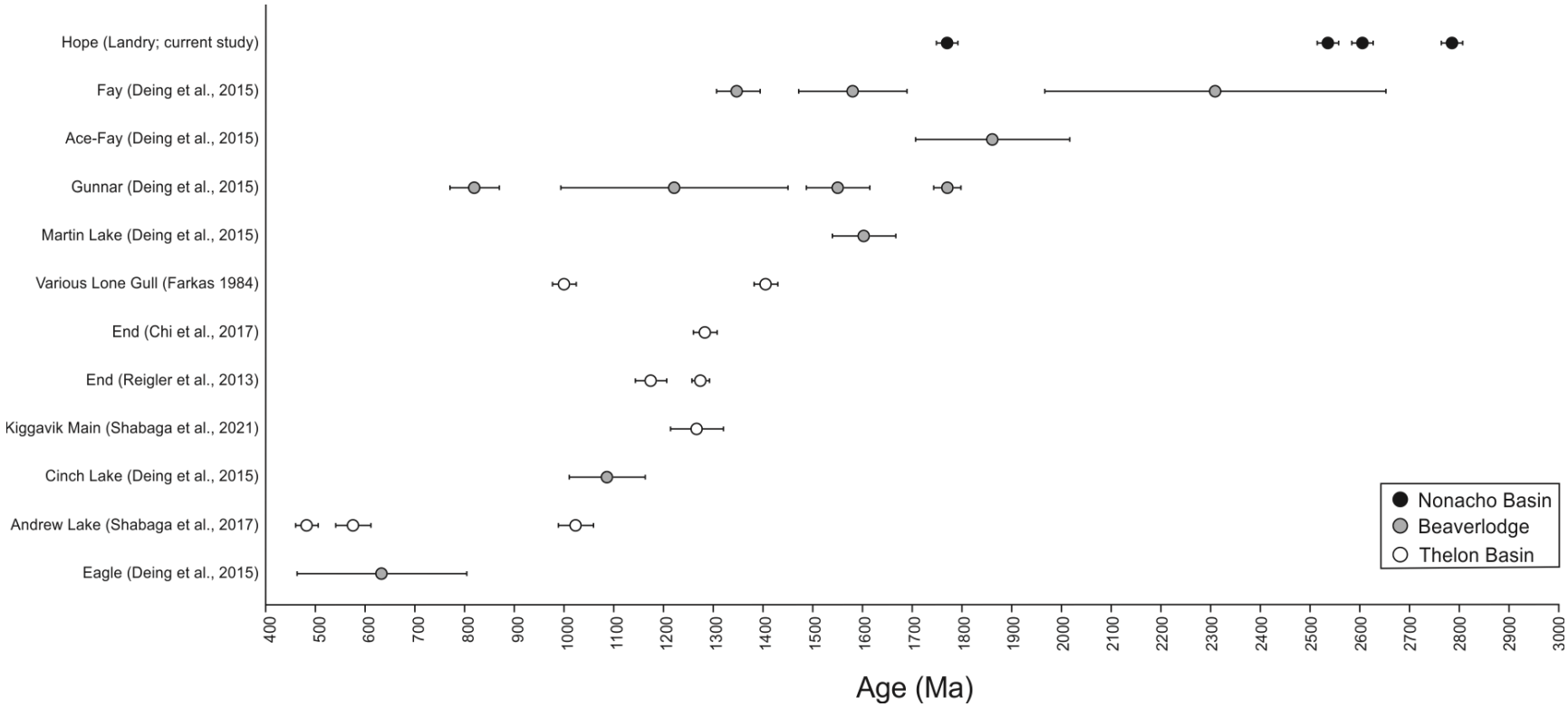

Figure A2-10: U-Pb ages of uraninite from various deposits in the Rae craton in millions of years (Ma) from various deposits in the Nonacho Basin, Beaverlodge district and Thelon Basin (Farkas 1984, Riegler, T. 2013, Dieng et al. 2015, Chi et al. 2016, Shabaga et al. 2017)

Table A2-6: Abundance of major oxides in chlorite (wt.%) and their atomic proportions from the thorite-sericite breccia sample (H-09) used to determine temperature (T in °C)

		H-09 1	**H-09 2**	**H-09 3**	**H-09 4**	**H-09 5**
O14	SiO_2	28.88	26.15	28.76	27.88	27.26
	TiO_2	0.11	0.10	0.15	0.12	0.11
	Al_2O_3	19.93	19.77	19.99	19.14	19.86
	Cr_2O_3	0.02	0.05	0.00	0.00	0.01
	NiO	0.02	0.00	0.01	0.04	0.01
	FeO	31.60	33.52	31.51	30.25	33.23
	MnO	0.24	0.16	0.16	0.16	0.14
	MgO	8.09	9.07	8.38	8.00	8.51
	CaO	0.17	0.04	0.12	0.19	0.10
	Na_2O	0.02	0.00	0.10	0.05	0.04
	K_2O	0.13	0.04	0.13	0.13	0.09
	SrO	0.00	0.04	0.00	0.00	0.00
	F	0.41	0.20	0.00	0.00	0.00
	Cl	0.02	0.02	0.01	0.04	0.00
apfu[a]						
T	Si	3.03	2.82	3.04	3.06	2.92
	Al	0.97	1.18	0.96	0.94	1.08
	sum	4.00	4.00	4.00	4.00	4.00
O	Al	1.49	1.33	1.53	1.53	1.43
	Fe	2.77	3.02	2.79	2.78	2.98
	Mg	1.27	1.46	1.32	1.31	1.36
	Mn	0.02	0.01	0.01	0.01	0.01
	sum	5.55	5.82	5.65	5.63	5.78
	vac	0.45	0.18	0.35	0.37	0.22
OH	F	0.14	0.07	0.00	0.00	0.00
	Cl	0.00	0.00	0.00	0.01	0.00
	OH*	7.58	7.78	7.99	7.98	8.00
Fe#*		**0.69**	**0.67**	**0.68**	**0.68**	**0.69**
T (°C) [§]		**250.85**	**318.50**	**246.67**	**240.95**	**285.03**

[a] Atom per formula unit (apfu) representing the atomic proportions of elements in each crystallographic site (T= tetrahedral, O = octahedral, OH = OH site)

* Fe# = Fe/(Fe+Mg)

[§] (Cathelineau 1988)

A2.1 References

Ashton, K.E., Hartlaub, R.P., Heaman, L.M., Morelli, R.M., Card, C.D., Bethune, K., and Hunter, R.C. 2009. Post-Taltson sedimentary and intrusive history of the southern Rae Province along the northern margin of the Athabasca Basin, Western Canadian Shield. Precambrian Research, **175**: 16–34. doi:10.1016/j.precamres.2009.09.004.

Berman, R.G., Sanborn-Barrie, M., Stern, R.A., and Carson, C.J. 2005. Tectonometamorphism at ca. 2.35 and 1.85 Ga in the rae domain, western Churchill Province, Nunavut, Canada: Insights from structural, metamorphic and in situ geochronological analysis of the southwestern Committee Bay Belt. Canadian Mineralogist, **43**: 409–442. Mineralogical Association of Canada. doi:10.2113/GSCANMIN.43.1.409.

Berman, R.G., Sandeman, H.A., and Camacho, A. 2010. Diachronous Palaeoproterozoic deformation and metamorphism in the Committee Bay belt, Rae Province, Nunavut: insights from 40Ar-39Ar cooling ages and thermal modelling. Journal of Metamorphic Geology, **28**: 439–457. doi:10.1111/J.1525-1314.2010.00873.X.

Bostock, H.H., van Breemen, O. 1992. Thetiming ofemplacement,and distribution of the Sparrow diabase dyke swarm, District of Mackenzie, Northwest Territories. In: Radiogenic Age and Isotopic Studies: Report 6, Geological Survey of Canada. *In* Paper 92-2. Geological Survey of Canada.

Bostock, H.H., van Breeman, O., and Loveridge, W.D. 1991. Further geochronology of plutonic rocks in the northern Taltson Magmatic Zone, District Mackenzie, N.W.T. Geological Survey Canada, **90**: 67–78.

Cathelineau, M. 1988. Cation site occupancy in chlorites and illites as a function of temperature.

Clay Minerals, **23**: 471–485. doi:https://doi.org/10.1180/claymin.1988.023.4.13.

Chi, G., Haid, T., Quirt, D., Fayek, M., Blamey, N., and Chu, H. 2016. Petrography, fluid inclusion analysis and geochronology of the End uranium deposit, Kiggavik, Nunavut, Canada [online]. Mineralium Deposita, **52**: 211–232. doi:10.1007/s00126-016-0657-9.

Dieng, S., Kyser, K., and Godin, L. 2015. Genesis of multifarious uranium mineralization in the Beaverlodge area, Northern Saskatchewan, Canada. Economic Geology, **110**: 209–240. doi:10.2113/econgeo.110.1.209.

Farkas, A. 1984. Mineralogy and host rock alteration of the Lone Gull deposit: Urangesellschaft Internal Report.

Hartlaub, A.R.P., Heaman, L.M., Chacko, T., Ashton, K.E., The, S., March, N., Hartlaub, R.P., Heaman, L.M., Chacko, T., and Ashton, K.E. 2007. Circa 2 . 3 - Ga Magmatism of the Arrowsmith Orogeny , Uranium City Region , Western Published by : The University of Chicago Press Circa 2 . 3-Ga Magmatism of the Arrowsmith Orogeny , Uranium City Region , Western Churchill Craton , Canada. University of Chicago Press, **115**: 181–195.

Hoffman, P.F. 1988. United plates of America, the birth of a craton: Early Proterozoic assembly and growth of Laurentia. doi:10.1146/annurev.ea.16.050188.002551.

LeCheminant, A.N., and Heaman, L.M. 1989. Mackenzie igneous events, Canada: Middle Proterozoic hotspot magmatism associated with ocean opening. Earth and Planetary Science Letters, **96**: 38–48. doi:10.1016/0012-821X(89)90122-2.

LeCheminant, A.N., Tella, S., Sanborn-Barrie, M., and Venance, K.. 1997. Geology, Parker Lake South, District of Keewatin, North- west Territories. Geological Survey of Canada, Open File

Map 3405, scale 1:50,000.

Mcglynn, J.C., Irving, E., and Park, J.K. 1974. Paleomagnetism and Age of Nonacho Group Sandstone and Associated Sparrow Dikes , District of Mackenzie. Canadian Journal of Earth Sciences, **11**: 30–42.

Pehrsson, S.J., Berman, R.G., and Davis, W.J. 2013. Paleoproterozoic orogenesis during Nuna aggregation: A case study of reworking of the Rae craton, Woodburn Lake, Nunavut. Precambrian Research, **232**: 167–188. Elsevier. doi:10.1016/J.PRECAMRES.2013.02.010.

Peterson, T.D., Van Breemen, O., Sandeman, H., and Cousens, B. 2002. Proterozoic (1.85-1.75 Ga) igneous suites of the Western Churchill Province: Granitoid and ultrapotassic magmatism in a reworked Archean hinterland. Precambrian Research, **119**: 73–100. doi:10.1016/S0301-9268(02)00118-3.

Riegler, T. 2013. , Système d'altération et minéralisation en uranium le long du faisceau structural Kiggavik-Andrew Lake (Nunavut, Canada): Modèle génétique et guides d'éxploration: Ph.D. thesis, Poitiers, France, Université de Poitiers.

Shabaga, B.M., Fayek, M., Quirt, D., Jefferson, C.W., and Camacho, A. 2017. Mineralogy, geochronology, and genesis of the Andrew lake ranium deposit, Thelon basin, Nunavut, Canada. Canadian Journal of Earth Sciences, **54**: 850–868. doi:10.1139/cjes-2017-0024.

Sun, S.S., and McDonough, W.F. 1989. Chemical and isotopic systematics of oceanic basalts: Implications for mantle composition and processes. Geological Society Special Publication, **42**: 313–345. doi:10.1144/GSL.SP.1989.042.01.19.

Appendix 3

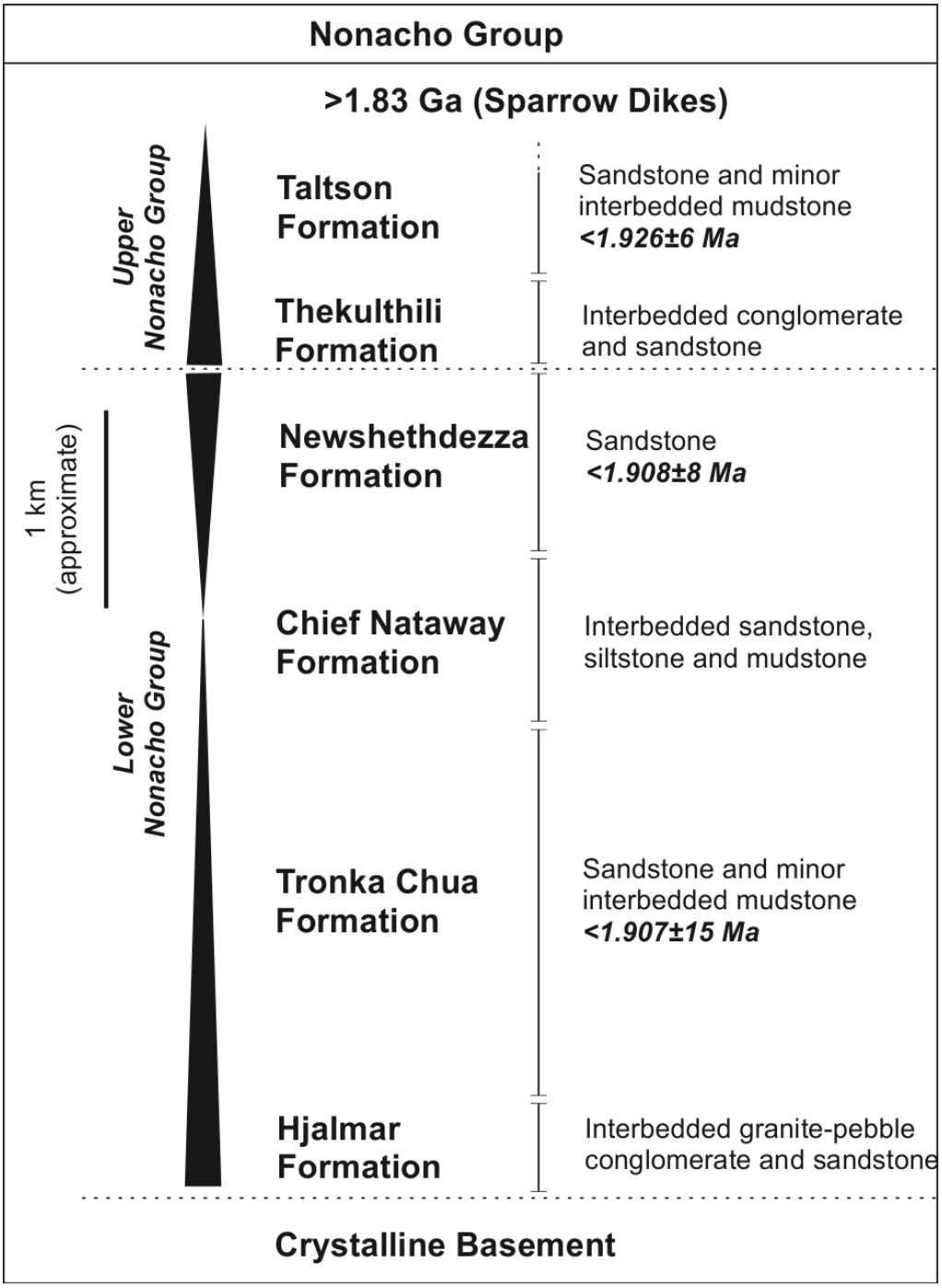

Figure A3-1: Generalized stratigraphic sequence of the Nonacho Group sediments after Aspler (1985) and Aspler and Donaldson (1985). Vertical black bars reflect relative grain size variation (fining and coarsening upward sequences) with divisions into lower and upper Nonacho Group. Dashed lines indicate the stratigraphic location of unconformities. Minimum ages for select units are measured from youngest detrital zircons (Ielpi et al. 2021). Absolute maximum age for Nonacho Group sediments constricted by 1.83 Ga Sparrow Dikes (Bostock and van Breemen 1992). Figure modified after Aspler and Donaldson (1985) and Ielpi et al. (2021).

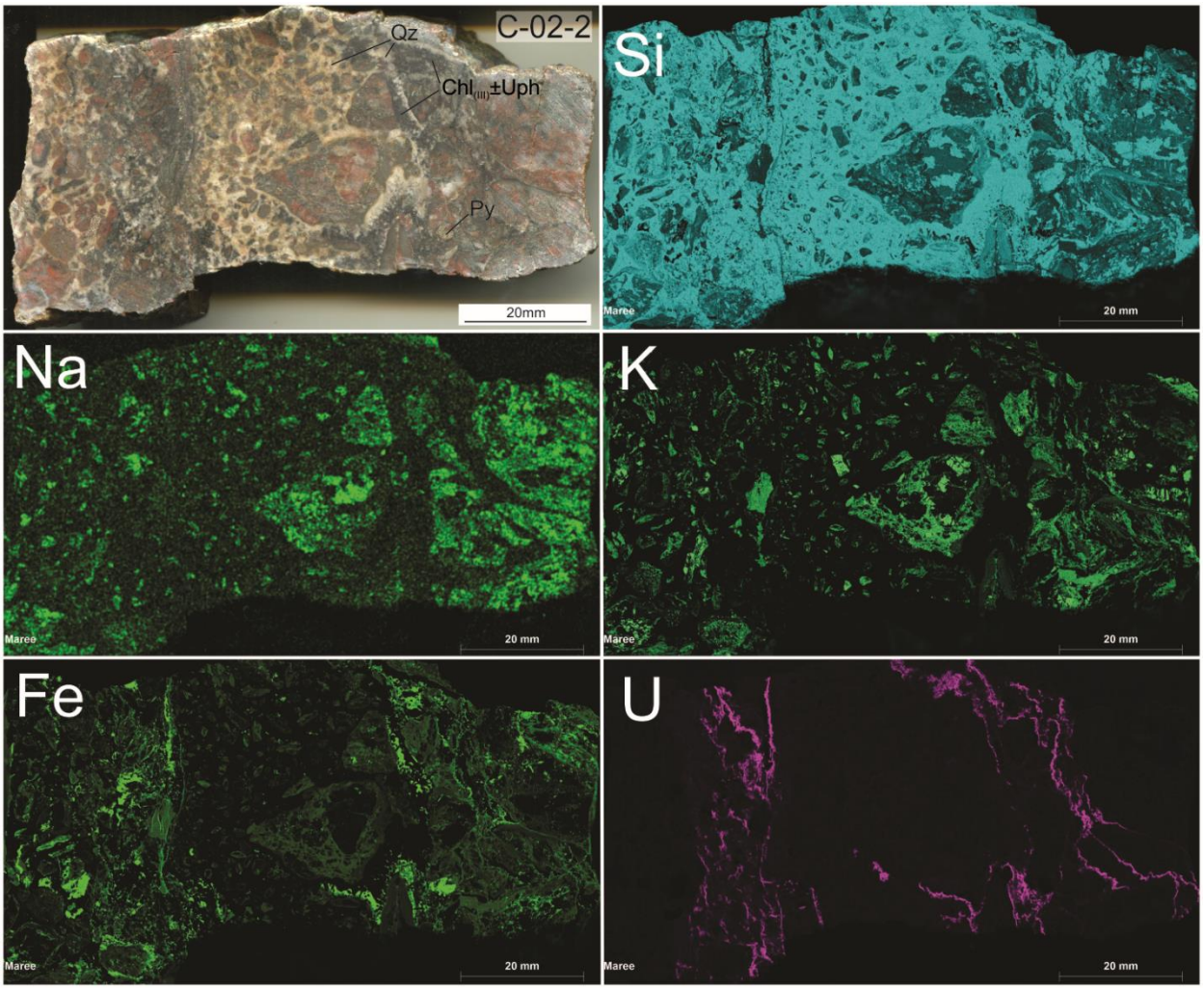

Figure A3-2: XRF false-colour elemental maps from sample C-02-2, a uranophane (Uph) mineralized quartz (Qz) breccia at the Cole occurrence. Abbreviations: chlorite (Chl), pyrite (Py)

Table A3-1: EPMA data in wt.% for MacInnis Lake uranium minerals from Kult-82, Island, Cole and Welch

	UO_2	PbO	ThO_2	SiO_2	TiO_2	Al_2O_3	MgO	FeO	CaO	K_2O	P_2O_5	SO_3	BaO	Zr_2O_3	Cl	La_2O_3	Ce_2O_3	Pr_2O_3	Nd_2O_3	Sm_2O_3	Eu_2O_3	Gd_2O_3	Tb_2O_3	Dy_2O_3	Ho_2O_3	Y_2O_3	Er_2O_3	Tm_2O_3	Yb_2O_3	Lu_2O_3	OH	Total
Kult-82																																
K82-C1-1	69.82	0.41	1.85	2.12	*nd*	0.02	*nd*	2.25	0.96	<0.09	*nd*	*nd*	1.76	*nd*	0.02	*nd*	1.29	*nd*	*nd*	*nd*	*nd*	*nd*	*nd*	0.27	*nd*	1.11	*nd*	*nd*	*nd*	*nd*	18.13	81.88
K82-C1-2	71.03	0.52	<0.04	2.70	*nd*	0.83	*nd*	3.65	1.26	0.16	*nd*	*nd*	1.66	*nd*	<0.01	*nd*	1.61	*nd*	*nd*	*nd*	*nd*	*nd*	*nd*	0.44	*nd*	1.21	*nd*	*nd*	*nd*	*nd*	14.93	85.07
K82-C1-3	70.69	0.87	<0.12	3.06	0.58	0.19	0.06	3.61	1.69	0.02	1.07	1.56	0.94	0.54	<0.02	0.40	1.81	0.31	1.25	0.47	0.06	0.36	<0.13	0.66	0.102	3.87	0.116	0.10	<0.16	<0.01	5.65	94.35
K82-C1-4	63.27	0.80	<0.12	1.04	1.16	<0.03	0.04	6.35	1.96	0.03	0.19	12.95	0.49	0.23	0.02	0.35	1.68	0.23	1.25	0.28	0.09	0.26	<0.13	0.51	0.116	1.60	0.115	0.09	0.02	<0.01	4.90	95.10
K82-C1-5	76.37	0.48	<0.12	2.16	1.11	0.02	0.03	3.37	1.87	0.02	0.14	1.44	0.78	0.48	<0.02	0.41	1.88	0.29	1.27	0.33	0.01	0.35	<0.13	0.61	0.207	2.08	0.052	0.08	<0.16	<0.01	4.15	95.85
K82-C1-6	76.99	2.37	<0.12	0.83	1.55	<0.03	0.02	3.58	2.46	0.01	0.09	1.4	0.46	0.20	<0.02	0.55	2.02	0.23	1.14	0.32	<0.16	0.43	<0.13	0.60	0.12	2.15	0.017	<0.15	<0.16	<0.01	2.49	97.52
K82-C1-7	78.52	1.22	<0.12	0.85	1.55	<0.03	0.03	3.12	2.57	0.02	0.12	0.59	0.62	0.16	0.01	0.47	2.24	0.28	1.38	0.22	<0.16	0.33	<0.13	0.59	0.155	2.10	0.025	0.04	0.07	<0.01	2.74	97.26
K82-C1-8	74.66	1.07	<0.12	4.37	0.62	0.27	0.12	3.37	1.33	0.03	0.15	1.30	1.12	<0.08	0.01	0.41	2.29	0.21	1.41	0.39	<0.16	0.19	<0.13	0.60	0.16	1.72	<0.14	0.05	0.11	<0.01	4.05	95.95
K82-C2-1	65.68	0.17	<0.04	4.14	*nd*	<0.03	*nd*	0.50	1.70	0.24	*nd*	*nd*	1.31	*nd*	0.01	*nd*	1.36	*nd*	*nd*	*nd*	*nd*	*nd*	*nd*	0.15	*nd*	1.15	*nd*	*nd*	*nd*	*nd*	23.59	76.41
K82-C2-2	80.23	0.05	<0.04	2.31	*nd*	<0.03	*nd*	0.98	2.18	0.14	*nd*	*nd*	0.96	*nd*	<0.01	*nd*	1.47	*nd*	*nd*	*nd*	*nd*	*nd*	*nd*	0.05	*nd*	0.04	*nd*	*nd*	*nd*	*nd*	11.61	88.39
K82-C2-3	66.73	0.36	<0.04	4.27	*nd*	<0.03	*nd*	0.53	1.64	0.22	*nd*	*nd*	1.36	*nd*	0.01	*nd*	1.55	*nd*	*nd*	*nd*	*nd*	*nd*	*nd*	0.26	*nd*	1.32	*nd*	*nd*	*nd*	*nd*	21.76	78.24
K82-C2-4	78.37	<0.06	<0.04	2.37	*nd*	<0.03	*nd*	0.96	2.18	0.14	*nd*	*nd*	1.35	*nd*	<0.01	*nd*	1.33	*nd*	*nd*	*nd*	*nd*	*nd*	*nd*	0.07	*nd*	0.09	*nd*	*nd*	*nd*	*nd*	13.15	86.85
K82-C2-5	71.05	<0.06	<0.04	3.52	*nd*	<0.03	*nd*	0.68	1.82	0.17	*nd*	*nd*	1.51	*nd*	<0.01	*nd*	1.47	*nd*	*nd*	*nd*	*nd*	*nd*	*nd*	0.15	*nd*	0.73	*nd*	*nd*	*nd*	*nd*	18.90	81.11
K82-C2-6	73.84	0.02	<0.04	2.93	*nd*	<0.03	*nd*	0.73	1.89	0.15	*nd*	*nd*	1.13	*nd*	<0.01	*nd*	1.51	*nd*	*nd*	*nd*	*nd*	*nd*	*nd*	0.04	*nd*	0.53	*nd*	*nd*	*nd*	*nd*	17.22	82.78
K82-C2-7	78.03	<0.06	<0.04	2.36	*nd*	<0.03	*nd*	0.83	1.89	0.17	*nd*	*nd*	2.44	*nd*	<0.01	*nd*	1.41	*nd*	*nd*	*nd*	*nd*	*nd*	*nd*	0.10	*nd*	0.17	*nd*	*nd*	*nd*	*nd*	12.61	87.39
K82-C2-8	82.28	0.10	<0.04	1.75	*nd*	<0.03	*nd*	1.18	1.97	0.17	*nd*	*nd*	1.72	*nd*	<0.01	*nd*	1.19	*nd*	*nd*	*nd*	*nd*	*nd*	*nd*	0.05	*nd*	0.06	*nd*	*nd*	*nd*	*nd*	9.52	90.48
K82-C2-9	80.15	0.21	<0.04	1.99	*nd*	<0.03	*nd*	0.90	2.01	0.10	*nd*	*nd*	2.31	*nd*	<0.01	*nd*	1.23	*nd*	*nd*	*nd*	*nd*	*nd*	*nd*	0.09	*nd*	0.03	*nd*	*nd*	*nd*	*nd*	10.90	89.10
K82-C2-10	69.91	<0.06	<0.04	3.52	*nd*	<0.03	*nd*	0.64	1.76	0.20	*nd*	*nd*	1.51	*nd*	<0.01	*nd*	1.42	*nd*	*nd*	*nd*	*nd*	*nd*	*nd*	0.12	*nd*	0.66	*nd*	*nd*	*nd*	*nd*	20.25	79.75
K82-C2-11	76.32	<0.09	<0.12	6.41	0.25	0.17	0.07	1.43	2.12	0.01	0.57	<0.03	2.85	0.01	<0.02	0.06	1.90	0.41	3.23	0.21	0.07	0.02	<0.13	0.03	<0.13	0.13	<0.14	<0.15	0.09	<0.01	3.66	96.34
K82-C2-12	79.84	0.07	<0.12	5.52	0.18	0.26	0.03	2.05	1.81	<0.04	0.21	0.01	1.85	<0.08	<0.02	0.12	1.65	0.41	2.76	0.26	<0.15	<0.11	<0.13	0.11	<0.13	0.06	<0.14	<0.15	<0.16	<0.01	2.80	97.20
K82-C2-13	81.09	<0.09	<0.12	4.47	0.25	0.20	0.05	2.13	2.31	0.01	0.21	<0.03	1.89	<0.08	<0.02	0.21	1.60	0.29	2.38	0.04	<0.14	0.01	<0.13	0.13	<0.13	0.04	<0.14	<0.15	<0.16	<0.01	2.72	97.28
K82-C2-14	75.53	2.35	<0.12	5.75	0.31	0.29	0.06	1.87	2.03	0.04	0.34	1.29	2.20	<0.08	<0.02	0.16	1.63	0.48	2.67	0.07	<0.14	0.05	<0.13	0.11	<0.13	0.04	<0.14	<0.15	<0.16	<0.01	2.74	97.26
K82-C2-15	77.51	<0.09	<0.12	5.77	0.25	0.19	0.05	1.47	2.36	0.02	0.34	<0.03	2.74	<0.08	0.01	0.15	1.80	0.62	2.86	0.13	0.03	<0.11	<0.13	0.05	0.027	0.08	<0.14	<0.15	<0.16	<0.01	3.56	96.44
K82-10-1	66.07	7.60	<0.04	2.79	*nd*	0.07	*nd*	1.16	6.40	0.18	*nd*	*nd*	2.20	*nd*	0.01	*nd*	0.21	*nd*	*nd*	*nd*	*nd*	*nd*	*nd*	0.07	*nd*	0.06	*nd*	*nd*	*nd*	*nd*	13.19	86.81
K82-10-2	75.96	4.02	<0.04	1.66	*nd*	<0.03	*nd*	1.08	5.65	0.17	*nd*	*nd*	1.45	*nd*	<0.01	*nd*	0.36	*nd*	*nd*	*nd*	*nd*	*nd*	*nd*	0.23	*nd*	0.01	*nd*	*nd*	*nd*	*nd*	9.42	90.58
K82-10-3	69.88	6.33	<0.04	3.60	*nd*	0.35	*nd*	0.77	3.17	0.39	*nd*	*nd*	2.48	*nd*	0.01	*nd*	0.33	*nd*	*nd*	*nd*	*nd*	*nd*	*nd*	0.20	*nd*	0.00	*nd*	*nd*	*nd*	*nd*	12.50	87.50
K82-10-4	56.64	6.26	<0.04	4.98	*nd*	1.21	*nd*	2.22	8.14	0.31	*nd*	*nd*	2.28	*nd*	0.01	*nd*	0.13	*nd*	*nd*	*nd*	*nd*	*nd*	*nd*	0.11	*nd*	0.01	*nd*	*nd*	*nd*	*nd*	17.72	82.28

	UO_2	PbO	ThO_2	SiO_2	TiO_2	Al_2O_3	MgO	FeO	CaO	K_2O	P_2O_5	SO_3	BaO	Zr_2O_3	Cl	La_2O_3	Ce_2O_3	Pr_2O_3	Nd_2O_3	Sm_2O_3	Eu_2O_3	Gd_2O_3	Tb_2O_3	Dy_2O_3	Ho_2O_3	Y_2O_3	Er_2O_3	Tm_2O_3	Yb_2O_3	Lu_2O_3	OH	Total
K82-10-5	66.04	3.46	<0.04	2.92	*nd*	0.36	*nd*	0.10	8.20	0.27	*nd*	*nd*	1.88	*nd*	0.02	*nd*	0.11	*nd*	*nd*	*nd*	*nd*	*nd*	*nd*	0.02	*nd*	0.01	*nd*	*nd*	*nd*	*nd*	15.71	84.30
K82-10-6	44.46	1.12	<0.04	7.15	*nd*	2.27	*nd*	4.42	1.45	2.36	*nd*	*nd*	3.06	*nd*	0.01	*nd*	0.43	*nd*	*nd*	*nd*	*nd*	*nd*	*nd*	0.16	*nd*	<0.03	*nd*	*nd*	*nd*	*nd*	33.13	66.88
K82-10-7	55.10	8.10	<0.04	3.63	*nd*	0.88	*nd*	7.65	1.89	0.82	*nd*	*nd*	3.39	*nd*	0.01	*nd*	0.43	*nd*	*nd*	*nd*	*nd*	*nd*	*nd*	0.06	*nd*	<0.04	*nd*	*nd*	*nd*	*nd*	18.03	81.97
K82-10-8	71.45	2.06	<0.04	2.67	*nd*	0.40	*nd*	2.50	2.46	0.33	*nd*	*nd*	3.41	*nd*	<0.01	*nd*	0.41	*nd*	*nd*	*nd*	*nd*	*nd*	*nd*	0.12	*nd*	0.01	*nd*	*nd*	*nd*	*nd*	14.20	85.80
K82-10-9	74.18	2.58	<0.04	2.90	*nd*	0.43	*nd*	3.43	3.08	0.26	*nd*	*nd*	3.50	*nd*	<0.01	*nd*	0.32	*nd*	*nd*	*nd*	*nd*	*nd*	*nd*	0.10	*nd*	0.01	*nd*	*nd*	*nd*	*nd*	9.23	90.77
K82-10-10	73.90	8.19	<0.12	3.72	0.29	0.19	0.08	3.18	3.90	0.09	0.21	2.25	2.43	0.19	<0.02	0.14	0.52	0.03	0.12	0.03	0.03	<0.11	<0.13	0.16	<0.13	<0.07	<0.14	<0.15	<0.16	<0.01	0.38	99.63
K82-10-11	61.55	7.84	<0.12	11.88	0.18	1.85	0.09	1.21	4.16	0.21	0.09	2.26	2.44	<0.08	0.02	<0.21	0.53	<0.16	0.12	<0.14	<0.14	<0.11	<0.13	0.03	<0.13	<0.07	<0.14	0.03	0.06	<0.01	5.46	94.54
K82-10-12	75.30	4.45	<0.12	6.61	0.14	0.25	0.05	1.23	3.78	0.06	0.11	0.55	2.03	<0.08	<0.02	<0.21	0.35	0.04	0.18	0.09	<0.14	<0.11	<0.13	0.09	<0.13	<0.07	<0.14	<0.15	0.01	<0.01	4.71	95.29
K82-10-13	71.87	5.49	<0.12	4.05	0.22	0.3	0.04	1.26	4.39	0.35	0.09	0.83	2.99	0.12	0.01	0.16	0.31	<0.16	0.13	<0.15	<0.14	<0.11	<0.13	0.09	<0.13	<0.07	<0.14	<0.15	<0.16	<0.01	7.31	92.69
K82-10-14	56.69	12.88	<0.12	11.83	0.17	2.18	0.18	1.98	4.11	0.16	0.09	2.23	2.64	0.04	0.04	0.06	0.28	<0.15	0.03	<0.13	<0.14	0.01	0.03	0.08	0.02	<0.07	<0.14	<0.15	<0.16	<0.01	4.27	95.73
K82-10-15	64.44	3.30	<0.12	12.08	0.19	2.02	0.35	2.65	3.27	0.09	0.13	0.04	2.89	<0.08	<0.02	0.11	0.38	0.08	0.08	0.01	0.04	<0.11	<0.13	0.23	<0.13	<0.07	0.012	0.09	<0.16	0.02	7.49	92.51
Island																																
I-12-1	2.12	0.11	<0.03	0.69	*nd*	0.07	*nd*	1.09	0.15	0.01	*nd*	*nd*	5.08	*nd*	<0.01	*nd*	<0.14	*nd*	*nd*	*nd*	*nd*	*nd*	*nd*	0.05	*nd*	<0.03	*nd*	*nd*	*nd*	*nd*	90.62	9.38
I-12-2	11.90	10.80	<0.03	4.04	*nd*	0.40	*nd*	4.86	0.57	0.02	*nd*	*nd*	4.56	*nd*	0.04	*nd*	0.44	*nd*	*nd*	*nd*	*nd*	*nd*	*nd*	0.04	*nd*	<0.03	*nd*	*nd*	*nd*	*nd*	62.34	37.66
I-12-3	9.87	0.18	<0.03	59.10	*nd*	2.70	*nd*	6.57	1.05	0.21	*nd*	*nd*	0.93	*nd*	0.06	*nd*	0.85	*nd*	*nd*	*nd*	*nd*	*nd*	*nd*	0.08	*nd*	0.08	*nd*	*nd*	*nd*	*nd*	18.32	81.68
I-12-4	17.23	5.03	<0.03	11.50	*nd*	2.62	*nd*	8.48	1.28	0.09	*nd*	*nd*	3.38	*nd*	0.03	*nd*	0.58	*nd*	*nd*	*nd*	*nd*	*nd*	*nd*	0.10	*nd*	0.04	*nd*	*nd*	*nd*	*nd*	49.64	50.37
I-12-5	29.71	2.07	<0.03	8.97	*nd*	0.63	*nd*	3.91	0.68	0.03	*nd*	*nd*	3.88	*nd*	0.02	*nd*	0.81	*nd*	*nd*	*nd*	*nd*	*nd*	*nd*	0.10	*nd*	0.10	*nd*	*nd*	*nd*	*nd*	49.10	50.90
Cole																																
C-02-2-1	7.06	0.76	<0.03	69.65	*nd*	5.87	*nd*	4.11	0.36	1.20	*nd*	*nd*	0.34	*nd*	0.09	*nd*	0.22	*nd*	*nd*	*nd*	*nd*	*nd*	*nd*	0.02	*nd*	0.03	*nd*	*nd*	*nd*	*nd*	10.30	89.70
C-02-2-2	4.21	0.27	<0.03	85.32	*nd*	0.82	*nd*	2.12	0.13	0.18	*nd*	*nd*	0.02	*nd*	0.03	*nd*	0.14	*nd*	*nd*	*nd*	*nd*	*nd*	*nd*	< 0.08	*nd*	<0.03	*nd*	*nd*	*nd*	*nd*	6.77	93.23
C-02-2-3	27.23	3.23	<0.03	28.83	*nd*	15.88	*nd*	8.38	1.77	2.54	*nd*	*nd*	0.47	*nd*	0.14	*nd*	0.53	*nd*	*nd*	*nd*	*nd*	*nd*	*nd*	0.17	*nd*	0.24	*nd*	*nd*	*nd*	*nd*	10.61	89.40
C-02-2-4	67.00	6.14	<0.03	6.95	*nd*	2.66	*nd*	2.57	3.52	0.44	*nd*	*nd*	0.22	*nd*	0.05	*nd*	1.03	*nd*	*nd*	*nd*	*nd*	*nd*	*nd*	0.30	*nd*	0.46	*nd*	*nd*	*nd*	*nd*	8.68	91.32
C-02-2-5	<0.1	0.16	0.01	51.95	*nd*	20.27	*nd*	9.43	0.19	3.83	*nd*	*nd*	0.53	*nd*	0.18	*nd*	0.08	*nd*	*nd*	*nd*	*nd*	*nd*	*nd*	0.06	*nd*	<0.03	*nd*	*nd*	*nd*	*nd*	13.32	86.69
Welch																																
W-01-1	0.59	0.02	<0.03	40.16	*nd*	25.23	*nd*	13.42	0.12	3.88	*nd*	*nd*	0.16	*nd*	<0.01	*nd*	< 0.11	*nd*	*nd*	*nd*	*nd*	*nd*	*nd*	0.03	*nd*	<0.03	*nd*	*nd*	*nd*	*nd*	16.39	83.61
W-01-2	16.32	0.14	<0.03	23.04	*nd*	11.52	*nd*	27.28	1.88	0.58	*nd*	*nd*	0.33	*nd*	0.02	*nd*	0.21	*nd*	*nd*	*nd*	*nd*	*nd*	*nd*	0.07	*nd*	<0.03	*nd*	*nd*	*nd*	*nd*	18.62	81.38
W-01-3	<0.1	0.02	0.01	43.49	*nd*	28.97	*nd*	9.27	0.11	3.90	*nd*	*nd*	0.26	*nd*	0.01	*nd*	0.05	*nd*	*nd*	*nd*	*nd*	*nd*	*nd*	0.01	*nd*	<0.03	*nd*	*nd*	*nd*	*nd*	13.91	86.10

Table A3-2: U-Pb ages determined using Bowles (2015) and EPMA data on MacInnis Lake uranium minerals

Sample	PbO (wt.%)	UO_2 (wt.%)	PbO (ppm)	UO_2 (ppm)	mol Pb	mol U	sum	at.% Pb	at.% U	Approximate age[a]	Calculated Age[b]	2σ
Kult-82 type-i												
K82-C1-6	2.37	76.99	23690.00	769870.00	0.01	0.14	0.15	6.93	93.07	509.23	509	20.36
K82-C1-7	1.22	78.52	12160.00	785150.00	0.01	0.15	0.15	3.56	96.39	257.42	280	11.2
K82-C1-5	0.48	76.37	4820.00	763650.00	0.00	0.14	0.14	1.41	98.50	101.08	138	5.52
K82-C1-1	0.41	69.82	4110.00	698210.00	0.00	0.13	0.13	1.20	98.60	86.20	125	5
K82-C1-2	0.52	71.03	5190.00	710340.00	0.00	0.13	0.13	1.52	98.26	109.03	146	5.84
K82-C1-3	0.87	70.69	8710.00	706870.00	0.00	0.13	0.13	2.55	97.10	184.07	213	8.52
K82-C1-8	1.07	74.66	10730.00	746560.00	0.00	0.14	0.14	3.14	96.64	227.09	253	10.12
Kult-82 type-i												
K82-C2-8	0.10	82.28	1010.00	822790.00	0.00	0.15	0.15	0.30	99.70	21.05	66	2.64
K82-C2-9	0.21	80.15	2050.00	801540.00	0.00	0.15	0.15	0.60	99.38	42.80	85	3.4
K82-C2-2	0.05	80.23	490.00	802320.00	0.00	0.15	0.15	0.14	99.85	10.21	56	2.24
K82-C2-6	0.02	73.84	220.00	738430.00	0.00	0.14	0.14	0.06	99.93	4.58	51	2.04
K82-C2-1	0.17	65.68	1670.00	656830.00	0.00	0.12	0.12	0.49	99.39	34.88	78	3.12
K82-C2-3	0.36	66.73	3600.00	667310.00	0.00	0.12	0.13	1.05	98.71	75.48	115	4.6
K82-C2-12	0.07	79.84	680.00	798440.00	0.00	0.15	0.15	0.20	99.79	14.17	60	2.4
K82-C2-14	2.35	75.53	23490.00	755320.00	0.01	0.14	0.15	6.87	93.00	505.46	508	20.32
Kult-82 type-ii												
K82-10-2	4.02	75.96	40180.00	759600.00	0.02	0.14	0.16	11.75	88.65	880.54	849	33.96
K82-10-8	2.06	71.45	20580.00	714450.00	0.01	0.13	0.14	6.02	93.48	442.73	449	17.96
K82-10-9	2.58	74.18	25750.00	741760.00	0.01	0.14	0.15	7.53	92.25	556.36	553	22.12
K82-10-1	7.60	66.07	76020.00	660660.00	0.03	0.12	0.16	22.24	78.22	1759.59	1659	66.36
K82-10-5	3.46	66.04	34610.00	660430.00	0.02	0.12	0.14	10.12	88.75	764.66	744	29.76
K82-10-7	8.19	73.90	81880.00	738970.00	0.04	0.14	0.17	23.95	78.86	1864.06	1757	70.28
K82-10-3	6.33	69.88	63340.00	698840.00	0.03	0.13	0.16	18.53	82.01	1435.40	1359	54.36
K82-10-13	5.49	71.87	54890.00	718660.00	0.02	0.13	0.16	16.06	84.40	1228.90	1170	46.8
K82-10-7	8.10	55.10	81020.00	550950.00	0.04	0.10	0.14	23.70	73.76	1957.18	1843	73.72
K82-10-12	4.45	75.30	44480.00	752970.00	0.02	0.14	0.16	13.01	87.49	979.92	941	37.64
K82-10-4	6.26	56.64	62590.00	566370.00	0.03	0.10	0.13	18.31	78.90	1470.22	1392	55.68
K82-10-6	1.12	44.46	11170.00	444610.00	0.01	0.08	0.09	3.27	94.27	242.07	267	10.68
K82-10-15	3.30	64.44	33010.00	644440.00	0.01	0.12	0.13	9.66	88.97	729.48	711	28.44
K82-10-11	7.84	61.55	78430.00	615520.00	0.04	0.11	0.15	22.94	76.43	1844.99	1739	69.56
Cole type-ii												
C-02-2-4	6.14	67.00	61400.00	669970.00	0.03	0.12	0.15	17.96	81.85	1398.38	1326	53.04

Notes: Assuming all U is ^{238}U and Th is negligible

[a]Calculated using Equation 2 from (Bowles 2015)

[b]Calculated using Equation 4 from (Bowles 2015)

Table A3-3: Abundance of major oxides in chlorite (wt.%) and their atomic proportions from Type-I chlorite at MacInnis Lake occurrences, used to determine temperature (T in °C)

Occurrence		**Kult-82**														**Island**					**Pyramid**				
Sample		**K82-C1**			**K82-05**						**K82-01**					**GFA-78-128**					**GFA-78-146A**				
Chlorite type		**I**			**I**						**I**					**I**					**I**				
O14	SiO_2	25.56	25.44	25.85	25.46	25.40	25.25	25.76	25.62	25.39	27.01	26.91	26.74	27.52	26.77	26.59	26.71	26.80	26.83	26.47	27.03	26.57	25.87	28.79	25.60
	TiO_2	0.02	0.08	0.07	0.08	0.09	0.11	0.15	0.10	0.10	0.13	0.08	0.10	0.07	0.12	0.11	0.12	0.16	0.15	0.13	0.20	0.13	0.31	0.15	0.11
	Al_2O_3	18.94	18.75	18.85	19.00	18.75	18.95	18.98	18.80	19.03	18.59	18.85	18.87	18.91	18.62	19.54	19.08	19.48	19.32	18.38	19.51	17.59	17.84	17.39	18.39
	Cr_2O_3	0.03	0.01	0.00	0.02	0.00	0.01	0.00	0.00	0.01	0.00	0.00	0.01	0.02	0.04	0.01	0.03	0.02	0.00	0.01	0.01	0.00	0.00	0.00	0.01
	NiO	0.01	0.00	0.00	0.00	0.00	0.03	0.02	0.01	0.00	0.01	0.02	0.00	0.01	0.03	0.00	0.00	0.02	0.03	0.04	0.00	0.00	0.06	0.01	0.02
	FeO	36.02	35.75	35.47	36.27	36.70	37.33	36.41	36.05	36.82	31.36	31.06	31.97	30.13	32.04	28.93	28.71	28.72	28.72	31.03	26.09	34.41	37.62	27.46	37.05
	MnO	0.57	0.63	0.59	0.62	0.57	0.57	0.58	0.60	0.60	0.91	0.90	0.84	0.85	0.91	0.31	0.33	0.29	0.29	1.19	0.26	0.44	0.73	0.38	0.70
	MgO	8.23	8.51	8.57	8.29	8.01	7.61	8.08	8.35	7.72	11.61	11.72	11.03	12.35	11.05	13.82	13.75	13.92	13.96	11.76	16.09	9.81	7.02	13.90	7.71
	CaO	0.02	0.03	0.04	0.02	0.03	0.03	0.02	0.04	0.01	0.04	0.02	0.02	0.04	0.03	0.01	0.03	0.01	0.00	0.03	0.00	0.04	0.03	0.08	0.04
	Na_2O	0.15	0.17	0.19	0.11	0.17	0.07	0.20	0.10	0.12	0.04	0.07	0.11	0.03	0.12	0.05	0.18	0.13	0.08	0.13	0.00	0.03	0.00	0.17	0.11
	K_2O	0.07	0.04	0.04	0.04	0.05	0.03	0.02	0.00	0.01	0.01	0.03	0.01	0.04	0.01	0.00	0.04	0.02	0.02	0.04	0.04	0.00	0.03	0.20	0.02
	SrO	0.00	0.00	0.00	0.00	0.05	0.00	0.00	0.00	0.00	0.00	0.00	0.00	0.00	0.00	0.00	0.00	0.00	0.00	0.00	0.00	0.00	0.00	0.02	0.00
	F	0.00	0.00	0.00	0.00	0.00	0.30	0.00	0.20	0.20	0.11	0.00	0.00	0.00	0.31	0.10	0.21	0.00	0.31	0.10	0.00	0.00	0.00	0.11	0.00
	Cl	0.02	0.01	0.00	0.03	0.01	0.00	0.02	0.01	0.01	0.03	0.01	0.02	0.03	0.01	0.01	0.02	0.01	0.01	0.02	0.04	0.02	0.03	0.09	0.04
apfu*																									
T	Si	2.80	2.79	2.82	2.78	2.79	2.77	2.81	2.80	2.78	2.87	2.86	2.86	2.90	2.85	2.80	2.82	2.81	2.80	2.84	2.80	2.90	2.86	3.02	2.82
	Al	1.20	1.21	1.18	1.22	1.21	1.23	1.19	1.20	1.22	1.13	1.14	1.14	1.10	1.15	1.20	1.18	1.19	1.20	1.16	1.20	1.10	1.14	0.98	1.18
	Sum	4.00	4.00	4.00	4.00	4.00	4.00	4.00	4.00	4.00	4.00	4.00	4.00	4.00	4.00	4.00	4.00	4.00	4.00	4.00	4.00	4.00	4.00	4.00	4.00
O	Al	1.25	1.22	1.24	1.23	1.22	1.21	1.24	1.22	1.24	1.20	1.23	1.23	1.24	1.19	1.22	1.19	1.22	1.17	1.16	1.19	1.16	1.19	1.17	1.20
	Fe	3.30	3.28	3.24	3.32	3.37	3.42	3.32	3.29	3.37	2.79	2.76	2.86	2.65	2.85	2.54	2.53	2.52	2.51	2.78	2.26	3.14	3.48	2.41	3.41
	Mg	1.34	1.39	1.39	1.35	1.31	1.24	1.31	1.36	1.26	1.84	1.86	1.76	1.94	1.76	2.17	2.16	2.18	2.17	1.88	2.49	1.60	1.16	2.17	1.27
	Mn	0.05	0.06	0.05	0.06	0.05	0.05	0.05	0.06	0.06	0.08	0.08	0.08	0.08	0.08	0.03	0.03	0.03	0.03	0.11	0.02	0.04	0.07	0.03	0.07
	sum	5.94	5.95	5.93	5.96	5.95	5.92	5.92	5.92	5.92	5.91	5.93	5.92	5.90	5.88	5.95	5.91	5.94	5.88	5.92	5.96	5.94	5.90	5.79	5.94
	vac	0.06	0.05	0.07	0.04	0.05	0.08	0.08	0.08	0.08	0.09	0.07	0.08	0.10	0.12	0.05	0.09	0.06	0.12	0.08	0.04	0.06	0.10	0.21	0.06
OH	F	0.00	0.00	0.00	0.00	0.00	0.05	0.00	0.04	0.04	0.02	0.00	0.00	0.00	0.05	0.02	0.03	0.00	0.10	0.03	0.00	0.00	0.00	0.03	0.00
	Cl	0.00	0.00	0.00	0.00	0.00	0.00	0.00	0.00	0.00	0.00	0.00	0.00	0.00	0.00	0.00	0.00	0.00	0.00	0.00	0.01	0.00	0.01	0.02	0.01
	OH*	7.99	8.00	8.00	7.99	8.00	7.84	8.00	7.89	7.89	7.94	8.00	7.99	7.99	7.84	7.95	7.89	8.00	7.69	7.88	7.98	7.99	7.98	7.85	7.98
Fe#**		0.71	0.70	0.70	0.71	0.72	0.73	0.72	0.71	0.73	0.60	0.60	0.62	0.58	0.62	0.54	0.54	0.54	0.54	0.60	0.48	0.66	0.75	0.53	0.73
T (°C)***		324.37	326.70	317.86	329.78	327.49	335.59	322.69	325.16	330.73	301.17	304.40	306.16	293.54	307.50	325.94	318.97	321.01	324.98	313.13	323.28	292.42	303.68	253.39	318.85

[a] Atom per formula unit (apfu) representing the atomic proportions of elements in each crystallographic site (T= tetrahedral, O = octahedral, OH = OH site)

* Fe# = Fe/(Fe+Mg)

[§] (Cathelineau 1988)

Table A3-4: Abundance of major oxides in chlorite (wt.%) and their atomic proportions from Type-II chlorite at MacInnis Lake occurrences, used to determine temperature (T in °C)

Occurrence		**Cole**									**Island**								**Pyramid**		
Sample		**C-04A**					**C-04B**		**C-02**		**GFA-78-132**								**GFA-78-146B**		
Chlorite type		**II**					**II**		**II**		**II**								**II**		
O14	SiO_2	27.52	27.25	27.48	27.01	27.61	28.27	27.78	27.00	28.78	27.93	27.98	28.09	28.16	27.87	27.88	27.87	27.81	27.03	26.90	27.03
	TiO_2	0.09	0.11	0.09	0.14	0.08	0.13	0.10	0.12	0.15	0.16	0.27	0.54	0.36	0.09	0.10	0.14	0.14	0.11	0.14	0.12
	Al_2O_3	19.94	20.20	19.99	20.33	20.15	19.62	19.19	19.81	20.61	18.35	18.45	18.38	18.16	18.62	18.53	18.66	18.63	19.38	19.01	19.35
	Cr_2O_3	0.00	0.04	0.00	0.04	0.03	0.00	0.00	0.01	0.00	0.06	0.00	0.00	0.02	0.03	0.00	0.00	0.03	0.02	0.08	0.00
	NiO	0.01	0.02	0.02	0.00	0.00	0.01	0.01	0.02	0.01	0.00	0.03	0.06	0.00	0.03	0.05	0.05	0.04	0.03	0.03	0.03
	FeO	23.03	23.35	23.31	24.40	23.13	26.08	25.52	23.70	22.79	25.05	25.21	24.13	24.08	24.12	24.36	24.18	23.89	26.07	26.51	26.32
	MnO	0.54	0.55	0.58	0.58	0.56	0.34	0.38	0.53	0.51	0.48	0.56	0.39	0.39	0.44	0.42	0.43	0.42	0.24	0.24	0.23
	MgO	17.82	17.37	17.59	16.62	17.38	14.82	15.99	16.73	15.55	16.09	16.11	16.89	17.13	17.11	17.01	17.09	17.26	15.89	15.52	15.85
	CaO	0.00	0.01	0.02	0.01	0.03	0.00	0.03	0.01	0.00	0.08	0.09	0.05	0.08	0.04	0.02	0.02	0.02	0.02	0.01	0.00
	Na_2O	0.07	0.04	0.06	0.18	0.20	0.04	0.18	0.15	0.07	0.18	0.14	0.07	0.04	0.12	0.06	0.31	0.17	0.28	0.24	0.20
	K_2O	0.00	0.06	0.02	0.01	0.15	0.32	0.02	0.05	0.80	0.11	0.08	0.03	0.04	0.06	0.07	0.09	0.02	0.08	0.06	0.04
	SrO	0.00	0.00	0.03	0.00	0.00	0.00	0.00	0.00	0.00	0.00	0.02	0.00	0.00	0.00	0.00	0.00	0.00	0.02	0.00	0.00
	F	0.21	0.00	0.32	0.32	0.11	0.00	0.32	0.21	0.00	0.00	0.21	0.00	0.00	0.00	0.00	0.00	0.21	0.00	0.00	0.21
	Cl	0.00	0.02	0.01	0.03	0.00	0.00	0.00	0.02	0.03	0.03	0.02	0.01	0.03	0.01	0.02	0.03	0.02	0.04	0.03	0.00
apfu*																					
T	Si	2.81	2.80	2.80	2.77	2.82	2.91	2.86	2.80	2.93	2.91	2.89	2.90	2.92	2.89	2.89	2.88	2.87	2.81	2.82	2.80
	Al	1.19	1.20	1.20	1.23	1.18	1.09	1.14	1.20	1.07	1.09	1.11	1.10	1.08	1.11	1.11	1.12	1.13	1.19	1.18	1.20
	Sum	4.00	4.00	4.00	4.00	4.00	4.00	4.00	4.00	4.00	4.00	4.00	4.00	4.00	4.00	4.00	4.00	4.00	4.00	4.00	4.00
O	Al	1.21	1.24	1.21	1.22	1.24	1.30	1.19	1.22	1.40	1.16	1.13	1.14	1.13	1.16	1.16	1.15	1.13	1.19	1.17	1.16
	Fe	1.97	2.00	1.99	2.09	1.97	2.25	2.20	2.06	1.94	2.18	2.18	2.09	2.09	2.09	2.11	2.09	2.06	2.27	2.32	2.28
	Mg	2.71	2.66	2.67	2.54	2.64	2.28	2.46	2.59	2.36	2.50	2.48	2.60	2.65	2.64	2.63	2.63	2.65	2.46	2.42	2.45
	Mn	0.05	0.05	0.05	0.05	0.05	0.03	0.03	0.05	0.04	0.04	0.05	0.03	0.03	0.04	0.04	0.04	0.04	0.02	0.02	0.02
	sum	5.94	5.95	5.92	5.90	5.91	5.85	5.88	5.91	5.75	5.89	5.84	5.87	5.90	5.93	5.94	5.91	5.88	5.94	5.94	5.91
	vac	0.06	0.05	0.08	0.10	0.09	0.15	0.12	0.09	0.25	0.11	0.16	0.13	0.10	0.07	0.06	0.09	0.12	0.06	0.06	0.09
OH	F	0.03	0.00	0.05	0.05	0.02	0.00	0.05	0.04	0.00	0.00	0.07	0.00	0.00	0.00	0.00	0.00	0.07	0.00	0.00	0.07
	Cl	0.00	0.00	0.00	0.00	0.00	0.00	0.00	0.00	0.00	0.01	0.00	0.00	0.01	0.00	0.00	0.01	0.00	0.01	0.00	0.00
	OH*	7.90	7.99	7.84	7.84	7.95	8.00	7.85	7.89	7.99	7.98	7.78	7.99	7.98	8.00	7.99	7.98	7.78	7.98	7.99	7.80
Fe#**		0.42	0.43	0.43	0.45	0.43	0.50	0.47	0.44	0.45	0.47	0.47	0.44	0.44	0.44	0.45	0.44	0.44	0.48	0.49	0.48
T (°C)***		321.47	325.70	323.53	334.68	318.92	287.94	304.20	324.21	282.50	288.76	295.79	290.68	287.13	296.16	294.78	298.50	303.04	320.87	318.11	324.64

[a] Atom per formula unit (apfu) representing the atomic proportions of elements in each crystallographic site (T= tetrahedral, O = octahedral, OH = OH site)

* Fe# = Fe/(Fe+Mg)

[§] (Cathelineau 1988)

Table A3-5: Abundance of major oxides in chlorite (wt.%) and their atomic proportions from Type-III and Type-IV chlorite at MacInnis Lake occurrences, used to determine temperature (T in °C)

Showing		**Cole**						**Welch**								**Cole**				
Sample		**C-02-2**						**W-01-1 1**								**C-09A 1**				
Chlorite type		**III**						**III**								**IV**				
O14	SiO_2	25.35	25.60	25.68	25.53	25.97	25.99	25.82	25.58	25.31	26.91	25.36	25.87	25.95	26.11	27.93	27.52	27.24	27.42	26.98
	TiO_2	0.06	0.09	0.09	0.12	0.12	0.08	0.08	0.18	0.11	0.12	0.10	0.08	0.34	0.15	0.13	0.07	0.10	0.11	0.07
	Al_2O_3	19.51	19.27	19.19	19.17	19.99	19.56	18.17	18.49	18.36	18.25	18.29	17.84	18.37	18.21	19.34	18.16	19.31	18.90	20.22
	Cr_2O_3	0.00	0.00	0.02	0.01	0.03	0.00	0.00	0.05	0.00	0.00	0.04	0.05	0.04	0.06	0.01	0.03	0.02	0.00	0.00
	NiO	0.00	0.00	0.00	0.00	0.00	0.02	0.00	0.02	0.00	0.03	0.00	0.01	0.01	0.01	0.01	0.00	0.00	0.00	0.02
	FeO	34.99	34.67	35.81	35.81	31.64	33.98	35.92	35.68	36.15	31.38	38.01	34.75	35.19	32.80	23.54	27.47	23.94	27.49	23.41
	MnO	0.57	0.63	0.61	0.59	0.70	0.64	1.66	1.72	1.64	2.19	1.15	1.65	1.71	2.39	0.55	0.57	0.57	0.65	0.58
	MgO	9.21	9.35	8.80	8.81	11.54	9.48	8.19	8.09	7.97	10.10	6.86	9.08	7.94	9.64	17.27	15.15	17.21	13.90	17.59
	CaO	0.01	0.02	0.00	0.01	0.01	0.00	0.01	0.04	0.00	0.03	0.00	0.00	0.03	0.00	0.03	0.02	0.00	0.02	0.02
	Na_2O	0.04	0.05	0.00	0.01	0.00	0.00	0.00	0.00	0.01	0.00	0.04	0.00	0.04	0.00	0.24	0.11	0.16	0.31	0.07
	K_2O	0.00	0.02	0.00	0.01	0.06	0.16	0.01	0.02	0.00	0.08	0.00	0.02	0.09	0.02	0.07	0.04	0.03	0.05	0.00
	SrO	0.00	0.00	0.00	0.00	0.03	0.00	0.00	0.15	0.00	0.00	0.00	0.00	0.00	0.00	0.00	0.02	0.03	0.00	0.08
	F	0.60	0.00	0.00	0.00	0.00	0.00	0.00	0.20	0.00	0.00	0.00	0.10	0.00	0.00	0.22	0.00	0.43	0.00	0.00
	Cl	0.00	0.01	0.01	0.00	0.00	0.01	0.00	0.01	0.01	0.01	0.00	0.00	0.01	0.01	0.02	0.00	0.01	0.04	0.02
apfu*																				
T	Si	2.74	2.78	2.79	2.78	2.76	2.80	2.83	2.79	2.80	2.91	2.81	2.83	2.84	2.84	2.86	2.89	2.81	2.89	2.77
	Al	1.26	1.22	1.21	1.22	1.24	1.20	1.17	1.21	1.20	1.09	1.19	1.17	1.16	1.16	1.14	1.11	1.19	1.11	1.23
	Sum	4.00	4.00	4.00	4.00	4.00	4.00	4.00	4.00	4.00	4.00	4.00	4.00	4.00	4.00	4.00	4.00	4.00	4.00	4.00
O	Al	1.22	1.24	1.24	1.23	1.26	1.29	1.18	1.17	1.18	1.23	1.20	1.14	1.21	1.18	1.19	1.13	1.15	1.23	1.22
	Fe	3.16	3.15	3.25	3.26	2.81	3.06	3.30	3.26	3.34	2.84	3.52	3.18	3.22	2.99	2.01	2.41	2.06	2.42	2.01
	Mg	1.48	1.51	1.42	1.43	1.83	1.52	1.34	1.32	1.31	1.63	1.13	1.48	1.30	1.57	2.63	2.37	2.65	2.18	2.69
	Mn	0.05	0.06	0.06	0.05	0.06	0.06	0.15	0.16	0.15	0.20	0.11	0.15	0.16	0.22	0.05	0.05	0.05	0.06	0.05
	sum	5.91	5.96	5.97	5.97	5.96	5.93	5.98	5.90	5.99	5.90	5.97	5.96	5.89	5.95	5.89	5.96	5.91	5.89	5.98
	vac	0.09	0.04	0.03	0.03	0.04	0.07	0.02	0.10	0.01	0.10	0.03	0.04	0.11	0.05	0.11	0.04	0.09	0.11	0.02
OH	F	0.10	0.00	0.00	0.00	0.00	0.00	0.00	0.07	0.00	0.00	0.00	0.03	0.00	0.00	0.03	0.00	0.07	0.00	0.00
	Cl	0.00	0.00	0.00	0.00	0.00	0.00	0.00	0.00	0.00	0.00	0.00	0.00	0.00	0.00	0.00	0.00	0.00	0.00	0.00
	OH*	7.69	8.00	8.00	8.00	8.00	8.00	8.00	7.78	8.00	7.99	8.00	7.90	7.99	8.00	7.89	8.00	7.79	7.99	7.99
Fe#**		0.68	0.68	0.70	0.70	0.61	0.67	0.71	0.71	0.72	0.64	0.76	0.68	0.71	0.66	0.43	0.50	0.44	0.53	0.43
T (°C)***		345.35	331.01	328.86	332.08	338.01	324.04	313.48	327.35	325.88	289.56	320.71	313.32	310.62	310.64	305.82	296.42	321.97	297.05	333.47

[a] Atom per formula unit (apfu) representing the atomic proportions of elements in each crystallographic site (T= tetrahedral, O = octahedral, OH = OH site)

* Fe# = Fe/(Fe+Mg)

[§] (Cathelineau 1988)

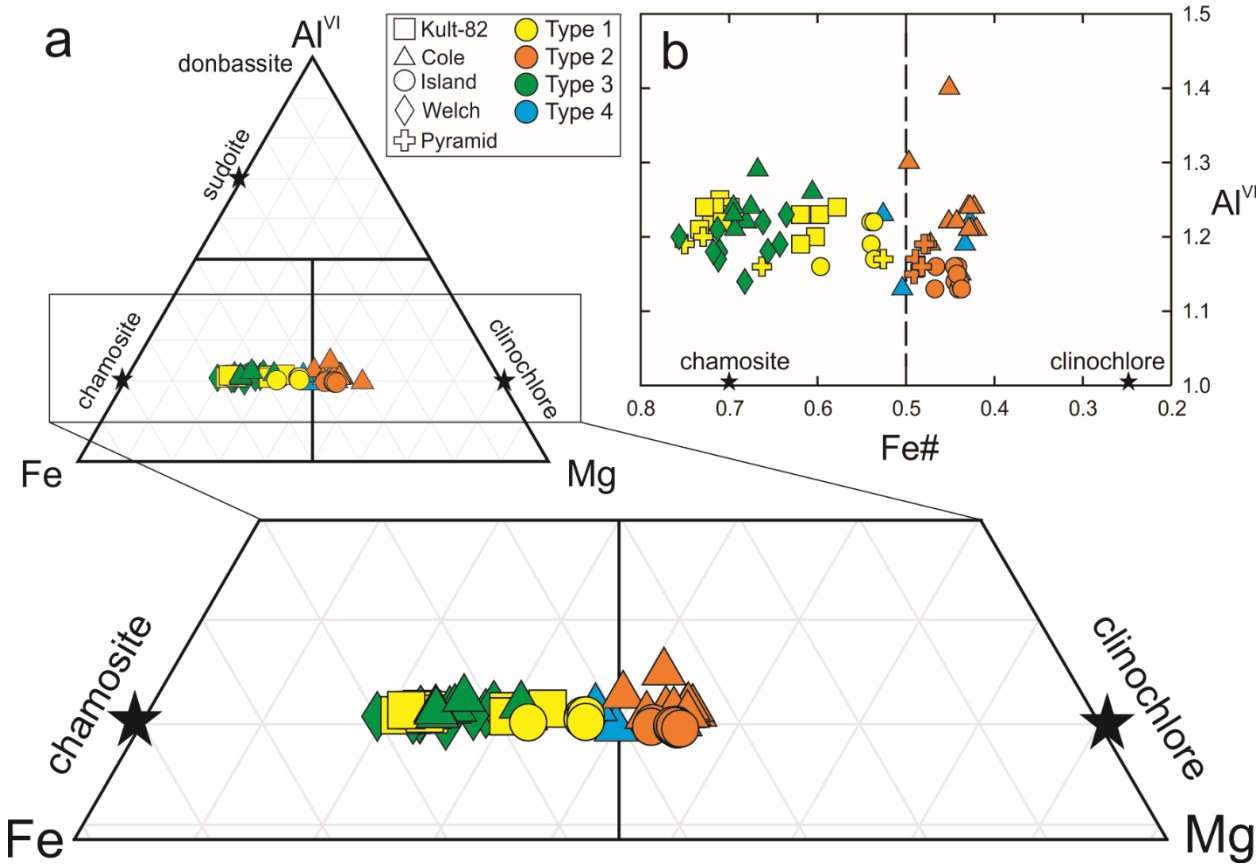

Figure A3-3: Chlorite classification for each showing and type of chlorite observed: (a) Al^{VI}-Fe-Mg ternary where ideal chlorite compositions for chamosite, clinochlore, sudoite and donbassite are plotted; (b) Al^{VI} vs. Fe# (Fe/[Fe+Mg]) biplot with ideal clinochlore and chamosite plotted.

Table A3-6: Whole rock geochemical data in weight % and ppm for the Cole, Welch and Dussault occurrences

Analyte Symbol	Unit Symbol	Detection Limit	Analysis Method	C- 01	C- 02	C- 03	C- 04	C- 05	C- 06	C- 09	C- 10	C- 11	W- 01	W- 03	W- 04	D- 03	D- 04	D- 05
Co_3O_4	%	0.005	FUS-XRF	< 0.005	< 0.005	< 0.005	< 0.005	< 0.005	< 0.005	< 0.005	< 0.005	< 0.005	< 0.005	< 0.005	< 0.005	< 0.005	< 0.005	< 0.005
CuO	%	0.005	FUS-XRF	< 0.005	< 0.005	< 0.005	< 0.005	< 0.005	< 0.005	< 0.005	< 0.005	< 0.005	< 0.005	< 0.005	< 0.005	0.017	< 0.005	0.177
NiO	%	0.003	FUS-XRF	0.005	0.004	< 0.003	< 0.003	< 0.003	0.006	< 0.003	< 0.003	< 0.003	0.007	< 0.003	0.003	0.004	< 0.003	0.005
SiO_2	%	0.01	FUS-XRF	60.53	68.64	71.12	65.08	65.42	63.72	66.67	71.37	69.01	62.09	88.03	88.52	86.43	70.2	65.96
Al_2O_3	%	0.01	FUS-XRF	16.44	14.39	14.37	15.4	13.05	16.33	13.43	13.83	14.43	18.05	5.48	5.25	6.3	14.1	14.16
Fe_2O_3(T)	%	0.01	FUS-XRF	4.75	3.93	2.24	6.49	3.71	5.55	3.13	2.13	3.98	5.66	2.42	2.85	1.97	5.13	6.51
MnO	%	0.001	FUS-XRF	0.062	0.035	0.016	0.022	0.07	0.056	0.062	0.021	0.046	0.07	0.033	0.047	0.032	0.059	0.056
MgO	%	0.01	FUS-XRF	2.02	1.23	0.71	1.28	1.85	2.02	1.23	0.59	1.74	1.81	0.61	0.71	0.41	1.28	1.49
CaO	%	0.01	FUS-XRF	2.27	0.41	0.44	0.47	3.83	1.82	3.16	0.63	0.95	0.22	0.06	0.1	0.16	0.26	0.13
Na_2O	%	0.01	FUS-XRF	3.42	2.53	2.97	1.75	2.87	3.19	2.6	3.11	3.35	1.92	0.42	0.61	1.82	2.12	0.52
K_2O	%	0.01	FUS-XRF	4.65	4.51	6.18	4.95	3.78	4.29	4.93	5.96	3.89	5.4	1.79	1.46	1.26	3.82	5.43
TiO_2	%	0.01	FUS-XRF	0.6	0.59	0.2	0.43	0.27	0.72	0.44	0.18	0.4	0.54	0.19	0.21	0.18	0.59	0.45
P_2O_5	%	0.01	FUS-XRF	0.2	0.2	0.21	0.15	0.1	0.22	0.14	0.05	0.15	0.14	0.04	0.05	0.1	0.17	0.1
Cr_2O_3	%	0.01	FUS-XRF	0.02	0.01	0.01	0.01	< 0.01	0.02	< 0.01	< 0.01	< 0.01	0.02	0.01	0.01	0.01	0.01	0.02
V_2O_5	%	0.003	FUS-XRF	0.014	0.012	0.011	0.011	0.008	0.013	0.008	0.01	0.008	0.019	0.005	0.008	0.003	0.01	0.021
LOI	%		GRAV	3.68	2.43	1.16	3.44	5.13	2.65	3.32	1.73	2.59	3.2	1.06	1.17	1.04	2.16	3.72
Total	%	0.01	FUS-XRF	98.66	98.93	99.64	99.5	100.1	100.6	99.13	99.62	100.5	99.16	100.2	101	99.76	99.91	98.74
B	ppm	20	TD-MS	< 20	< 20	< 20	< 20	< 20	< 20	< 20	< 20	< 20	< 20	< 20	< 20	< 20	< 20	< 20
Li	ppm	0.5	TD-MS	32.1	33.8	20.1	35.7	42.4	29.1	14.3	14.9	29.7	48.9	17.2	29.6	17.9	37.6	63.6
Na	%	0.01	TD-MS	> 3.00	2.5	> 3.00	1.75	2.94	2.89	1.98	2.43	2.61	1.48	0.33	0.49	1.41	1.6	0.42
Mg	%	0.01	TD-MS	1.37	0.88	0.38	0.93	1.37	1.5	0.72	0.27	0.98	1.07	0.3	0.39	0.19	0.76	0.86
Al	%	0.01	TD-MS	9.41	9.05	9.08	9.67	8.49	> 10.0	7.3	7.76	5.63	8.79	3.2	3.03	3.32	7.39	7.26
K	%	0.01	TD-MS	3.76	3.97	4.42	3.26	2.28	2.44	2.06	2.66	1.78	4.15	1.68	1.34	1.13	2.3	4.46
Ca	%	0.01	TD-MS	1.62	0.31	0.35	0.37	2.94	1.35	2.18	0.47	0.5	0.17	0.05	0.07	0.11	0.18	0.09
Cd	ppm	0.1	TD-MS	< 0.1	< 0.1	< 0.1	< 0.1	< 0.1	< 0.1	< 0.1	0.6	< 0.1	< 0.1	< 0.1	< 0.1	< 0.1	< 0.1	< 0.1
V	ppm	1	TD-MS	67	68	51	73	49	67	44	49	45	71	44	52	22	61	111
Cr	ppm	1	TD-MS	26	20	19	21	20	44	19	12	23	57	52	51	43	61	69
Mn	ppm	1	TD-MS	493	285	143	200	580	453	481	176	351	552	281	377	251	469	424
Fe	%	0.01	TD-MS	3.33	2.8	1.62	4.67	2.76	3.93	2.15	1.48	2.44	4	1.73	2	1.31	3.43	4.44
Hf	ppm	0.1	TD-MS	7.7	2.8	1	0.9	5.3	7	8.2	1	4.9	1.9	0.4	0.6	1.5	4.2	2.6
Ni	ppm	0.5	TD-MS	12.3	5	2.9	4	4.4	8.4	3.2	1.3	4.3	35.7	14	14.2	8.3	30.3	28.8
Er	ppm	0.1	TD-MS	1.6	1.6	1	4.9	1.5	2.8	1.2	0.6	1.1	1.4	0.9	1.1	1	2.4	1.9
Be	ppm	0.1	TD-MS	2.5	2.9	1.5	6	2.8	2.7	1.7	1.3	2.5	5	1.4	1.3	1.7	4.5	5.2
Ho	ppm	0.1	TD-MS	0.5	0.5	0.4	1.9	0.5	1	0.4	0.2	0.4	0.5	0.3	0.3	0.3	0.8	0.6
Hg	ppb	10	TD-MS	30	40	40	80	160	40	40	60	30	20	< 10	10	30	20	10
Ag	ppm	0.05	TD-MS	0.1	2.81	0.16	41.3	13.1	< 0.05	0.19	5.21	0.51	0.34	0.61	0.25	4.68	0.15	46.9
Au	ppb	0.02	BLEG-MS	2.2	6	9.9	92	78	0.7	0.3	167	4.1	0.7	0.9	6	2	0.4	3.8
Cs	ppm	0.05	TD-MS	2.1	2.25	1.13	4.72	2.23	1.75	0.96	1.06	1.97	14.3	3.59	2.82	4.46	13.4	12.6
Co	ppm	0.1	TD-MS	10.1	6.4	4.3	4.8	8.6	11.7	7	2.2	6.4	15.6	6	6.1	3.9	11.2	13.6
Eu	ppm	0.05	TD-MS	1.43	0.79	0.98	4.78	0.93	2.28	2.4	0.62	1.23	0.52	0.55	0.39	0.26	0.84	0.86
Bi	ppm	0.02	TD-MS	0.12	21.1	1.38	188	57.8	0.36	0.62	3.37	2.22	62.8	32.3	37.6	46.8	1.34	> 2000

Analyte Symbol	Unit Symbol	Detection Limit	Analysis Method	C- 01	C- 02	C- 03	C- 04	C- 05	C- 06	C- 09	C- 10	C- 11	W- 01	W- 03	W- 04	D- 03	D- 04	D- 05
Se	ppm	0.1	TD-MS	< 0.1	3.3	1	127	25.5	< 0.1	0.3	2.9	0.5	1	4.3	1.5	1.5	< 0.1	66.8
Zn	ppm	0.2	TD-MS	54.3	30.1	7	25.6	48.9	65.2	38.8	18.5	43.6	70.7	29.8	38.6	24	48.2	51.7
Ga	ppm	0.1	TD-MS	13.3	11.4	1.3	16.3	12.4	17	12.5	3.6	15.1	28.9	8.4	9.6	6.8	19.4	18.7
As	ppm	0.1	TD-MS	4.6	13.6	2.9	53.2	33.6	3.4	3.5	7	6.4	1.2	0.7	0.8	2.3	2	7.1
Rb	ppm	0.2	TD-MS	142	142	112	169	97.4	121	91.2	91.7	98.3	305	106	89.8	80.9	221	292
Y	ppm	0.1	TD-MS	12.6	20.5	9.2	66.4	19.2	24.1	13	5	13.6	12.5	10.6	10.3	10.8	20.4	21.8
Zr	ppm	1	TD-MS	312	143	32	97	178	291	351	117	199	66	16	21	58	214	91
Nb	ppm	0.1	TD-MS	5.6	6.2	4.3	2.8	5.7	1.2	5.7	0.3	8.8	0.2	2.9	4.6	4.8	2.9	10.4
Mo	ppm	0.05	TD-MS	0.88	0.7	0.91	1.05	0.75	0.61	0.77	0.87	0.81	0.13	1.17	1.5	2.24	0.46	0.68
In	ppm	0.1	TD-MS	< 0.1	< 0.1	< 0.1	0.1	< 0.1	< 0.1	< 0.1	< 0.1	< 0.1	< 0.1	< 0.1	< 0.1	< 0.1	< 0.1	< 0.1
Sn	ppm	1	TD-MS	1	1	2	< 1	< 1	2	1	< 1	1	4	2	2	3	9	5
Sb	ppm	0.1	TD-MS	1.7	4.5	2.5	8.6	9.5	0.2	1.5	5.2	5.6	< 0.1	0.2	0.3	0.8	0.1	1.9
Te	ppm	0.1	TD-MS	< 0.1	2.1	< 0.1	6.1	3.9	< 0.1	< 0.1	3	0.2	0.6	3.1	13.5	0.8	< 0.1	22.2
Ba	ppm	1	TD-MS	1610	1800	2970	1930	1440	1450	1860	3550	1250	1330	558	397	386	605	961
La	ppm	0.1	TD-MS	104	34.4	36.2	42.2	30.5	148	321	96.2	46.5	28.5	16.3	16.3	11.1	62.5	26.9
Ce	ppm	0.1	TD-MS	190	58.4	69.4	199	49.6	264	585	112	78.4	49.3	46.2	33.5	16.7	118	76.3
Pr	ppm	0.1	TD-MS	21.4	6.7	8.7	26.6	6.3	29.7	60.7	11.1	7.7	4.2	6.9	4.2	1.9	13.5	10.7
Nd	ppm	0.1	TD-MS	73.4	22.2	31.4	106	23.6	98	187	31	29	13.9	27.7	13.7	6.7	43.7	36.9
Sm	ppm	0.1	TD-MS	10	4.2	5.8	22.9	3.9	13	22.1	4.3	6.7	3.3	2.9	2.3	2	7.5	5.2
Gd	ppm	0.1	TD-MS	5.7	3.2	3.3	17.7	3.4	9.1	10.6	2.2	4.6	2.8	2.5	2	1.5	5.3	4.5
Tb	ppm	0.1	TD-MS	0.5	0.4	0.4	1.8	0.4	0.9	0.7	0.2	0.4	0.4	0.3	0.3	0.2	0.6	0.4
Dy	ppm	0.1	TD-MS	2.8	2.4	2	10.2	2.7	5.1	3.1	1.2	2.4	2.4	1.5	1.8	1.6	4.1	2.9
Cu	ppm	0.2	TD-MS	7.6	7.6	14.2	9.7	7.5	1.9	3.3	12.4	6.8	26.3	16.8	11.1	144	19.2	1380
Ge	ppm	0.1	TD-MS	< 0.1	0.2	< 0.1	0.4	0.2	< 0.1	< 0.1	< 0.1	0.1	0.5	0.1	0.2	0.1	0.1	0.3
Tm	ppm	0.1	TD-MS	0.2	0.2	0.1	0.5	0.2	0.3	0.1	< 0.1	0.1	0.2	0.1	0.1	0.1	0.3	0.2
Yb	ppm	0.1	TD-MS	1.2	1.4	0.8	2.9	1.3	2.3	0.8	0.6	0.8	1.5	0.7	1	1	2.2	1.6
Lu	ppm	0.1	TD-MS	0.2	0.3	0.1	0.5	0.2	0.4	0.1	0.1	0.1	0.2	0.1	0.1	0.2	0.3	0.3
Ta	ppm	0.1	TD-MS	0.1	0.3	0.1	< 0.1	0.3	< 0.1	0.1	< 0.1	0.4	< 0.1	0.2	0.4	0.6	0.3	0.9
Sr	ppm	0.2	TD-MS	257	218	414	139	233	418	570	431	194	52	14	21.7	45.6	46.2	22
W	ppm	0.1	TD-MS	0.5	1.3	0.8	1.1	0.7	< 0.1	1	0.4	1.5	< 0.1	0.5	0.4	1.5	0.7	2.3
Re	ppm	0.001	TD-MS	< 0.001	< 0.001	< 0.001	0.001	< 0.001	0.001	0.001	< 0.001	< 0.001	< 0.001	< 0.001	0.001	0.002	< 0.001	0.001
Tl	ppm	0.05	TD-MS	0.84	0.89	0.77	1.17	0.63	0.79	0.61	0.71	0.62	2.12	0.7	0.58	0.45	1.49	2.01
Pb	ppm	0.5	TD-MS	12.4	786	501	547	308	13.8	25.3	782	134	487	520	756	320	16.4	1590
Th	ppm	0.1	TD-MS	22.3	20.8	1.6	13.8	30.3	20.4	58.5	39.6	14	21.1	5.7	10.6	10.2	39.7	14.4
U	ppm	0.1	TD-MS	14.4	802	15.8	3480	1250	6.8	11.2	126	469	1510	711	1220	1530	15.7	2090

Table A3-7: Whole rock geochemical data in weight % and ppm for the Kult-82, Island and Pyramid occurrences

Analyte Symbol	Unit Symbol	Detection Limit	Analysis Method	K82-01	K82-05	K82-06	K82-07	K82-09	K82-10	I- 01	I- 02	I-03	I-04	I- 05	I- 06	I- 08	I- 09	I- 10	I-11	I- 12A	I- 12B	I-13	PY-02	PY-05
Co3O4	%	0.005	FUS-XRF	< 0.005	< 0.005	< 0.005	< 0.005	< 0.005	< 0.005	< 0.005	0.006	< 0.005	0.006	0.007	0.006	< 0.005	< 0.005	0.005	0.005	< 0.005	< 0.005	0.009	< 0.005	0.01
CuO	%	0.005	FUS-XRF	0.008	0.019	0.006	0.045	0.007	0.053	< 0.005	0.008	0.01	0.057	0.019	< 0.005	< 0.005	0.106	0.01	< 0.005	0.115	0.008	0.005	< 0.005	0.547
NiO	%	0.003	FUS-XRF	< 0.003	< 0.003	< 0.003	0.01	< 0.003	< 0.003	< 0.003	< 0.003	< 0.003	0.01	0.007	0.009	< 0.003	0.007	0.006	< 0.003	< 0.003	0.004	0.008	< 0.003	< 0.003
SiO2	%	0.01	FUS-XRF	74.28	56.82	48.66	50.13	75.37	46.15	66.04	57.78	72.09	52.43	54.48	54.13	73.24	57.55	48.8	53.95	65.62	73.35	57.73	74.4	82.98
Al2O3	%	0.01	FUS-XRF	12.58	18	19.12	12.13	12.93	16.49	15.49	13.81	10.09	14.99	13.69	13.72	13.07	14.31	13.98	13.4	13.1	10.65	12.53	13.05	4.6
Fe2O3(T)	%	0.01	FUS-XRF	1.72	4.06	5.87	5.25	1.2	7.91	4.12	14.09	6.56	15.23	14.85	14.25	1.39	10.85	13.24	14.89	5.89	4.07	15.15	1	3.96
MnO	%	0.001	FUS-XRF	0.017	0.058	0.109	0.233	0.012	0.144	0.027	0.223	0.141	0.261	0.346	0.242	0.021	0.186	0.22	0.242	0.104	0.09	0.226	0.009	0.044
MgO	%	0.01	FUS-XRF	0.37	0.8	2.5	3.84	0.26	1.4	0.76	3.54	2.57	5.07	6.01	6.72	0.36	3.44	5.98	7.04	2.03	1.81	3.77	0.15	0.92
CaO	%	0.01	FUS-XRF	0.1	5.01	7.16	11.31	0.13	7.49	0.83	0.28	0.28	0.56	0.47	0.37	0.64	0.29	9.28	0.32	0.55	0.52	0.21	0.36	1.14
Na2O	%	0.01	FUS-XRF	3.19	7.59	5	2.18	3.24	4.94	3.7	4.08	1.52	3.7	1.21	2.12	3.06	1.94	3.06	1.53	1.79	2.94	2.77	2.57	0.12
K2O	%	0.01	FUS-XRF	5.64	2.69	3.57	3.6	6.15	3.41	6.21	1.4	3.17	1.48	2.56	1.36	6.26	5.08	0.71	1.62	6.16	3	2.03	7.08	1.25
TiO2	%	0.01	FUS-XRF	0.12	0.52	0.73	0.47	0.16	0.59	0.74	1.13	0.81	1.53	1.58	1.41	0.04	1.32	1.24	1.46	0.86	0.66	1.18	0.06	0.43
P2O5	%	0.01	FUS-XRF	0.03	0.22	0.26	0.46	0.03	0.23	0.56	0.09	0.14	0.18	0.14	0.17	0.01	0.16	0.11	0.17	0.32	0.29	0.1	0.01	0.29
Cr2O3	%	0.01	FUS-XRF	0.01	< 0.01	< 0.01	0.02	< 0.01	< 0.01	< 0.01	0.01	< 0.01	0.03	0.03	0.02	0.01	0.03	0.03	0.02	< 0.01	0.01	0.02	0.01	< 0.01
V2O5	%	0.003	FUS-XRF	0.008	0.012	0.017	0.008	0.005	0.022	0.013	0.055	0.03	0.079	0.065	0.062	0.004	0.061	0.057	0.071	0.03	0.016	0.07	< 0.003	0.017
LOI	%		GRAV	0.87	4.42	7.57	10.66	0.55	7.93	1.45	3.52	2	3.68	4.77	4.77	1.3	3.47	2.62	4.53	1.82	1.65	3.22	0.69	2.2
Total	%	0.01	FUS-XRF	98.93	100.2	100.6	100.3	100	96.76	99.95	100	99.42	99.29	100.2	99.38	99.42	98.82	99.35	99.25	98.4	99.06	99.02	99.38	98.5
B	ppm	20	TD-MS	< 20	< 20	< 20	< 20	< 20	60	< 20	< 20	1.19	1.78	< 20	< 20	< 20	< 20	< 20	0.51	< 20	< 20	1.66	< 20	3910
Li	ppm	0.5	TD-MS	7.2	13.6	33.9	36.2	4.4	124	15.1	44.6	< 20	< 20	72.6	73.3	5.5	43.5	18.7	< 20	29.6	29.9	< 20	2.5	< 20
Na	%	0.01	TD-MS	2.46	> 3.00	> 3.00	1.47	2.33	> 3.00	2.55	> 3.00	45.2	53	0.83	1.42	2.27	1.34	1.99	75.1	1.3	2.17	42	2	46.3
Mg	%	0.01	TD-MS	0.14	0.35	1.32	2.01	0.08	0.66	0.28	2.05	1.14	2.97	3.04	3.35	0.14	1.75	2.92	1.3	1.06	0.99	2.15	0.05	0.12
Al	%	0.01	TD-MS	6.43	9.97	9.9	6.11	6.64	6.99	8.17	7.27	1.42	2.86	6.73	6.64	7.02	6.44	6.83	4.09	6.38	5.4	2.08	7.45	0.56
K	%	0.01	TD-MS	3.36	2.59	3.3	3.16	3.59	2.2	4.75	1.19	5.31	7.88	1.98	1.16	4.58	4.41	0.56	7.34	3.09	1.99	6.66	> 5.00	2.5
Ca	%	0.01	TD-MS	0.08	3.58	5.05	7.77	0.09	5.03	0.57	0.16	1.57	1.14	0.32	0.22	0.45	0.2	6.05	1.38	0.38	0.36	1.7	0.27	1.07
Cd	ppm	0.1	TD-MS	< 0.1	< 0.1	< 0.1	< 0.1	< 0.1	< 0.1	< 0.1	< 0.1	0.17	0.36	0.3	< 0.1	< 0.1	< 0.1	0.1	0.22	0.2	0.9	0.15	< 0.1	0.82
V	ppm	1	TD-MS	31	49	69	48	22	105	49	308	0.1	< 0.1	182	120	10	120	259	< 0.1	119	62	0.3	4	< 0.1
Cr	ppm	1	TD-MS	16	15	12	86	11	38	11	150	119	233	138	127	11	122	111	234	56	18	202	14	97
Mn	ppm	1	TD-MS	130	462	841	1830	94	1150	220	1750	64	129	2530	1820	165	1360	1630	117	820	675	114	92	28
Fe	%	0.01	TD-MS	1.22	2.88	4.04	3.61	0.75	5.58	2.79	9.77	1080	1990	9.68	9.47	0.94	7.09	8.63	1870	4.08	2.85	1680	0.7	343
Hf	ppm	0.1	TD-MS	4.8	6.5	5.1	3.5	2	5	0.4	2.2	4.47	10.4	3.4	1.5	4.7	2	1.8	10.7	3.2	0.9	10.2	2.3	2.88
Ni	ppm	0.5	TD-MS	1.6	6.7	6.7	94.6	1.6	32	4.4	39.7	3	3.2	61.8	54.9	2.1	30	52.9	3.1	17.4	7.2	1.5	0.9	0.2
Er	ppm	0.1	TD-MS	0.6	7.7	2.3	4	0.8	3.5	1.4	3.8	32.9	76.2	6.6	4.1	1.1	5.1	2.9	67.3	2.7	1.7	70.3	0.3	23.6
Be	ppm	0.1	TD-MS	0.6	5.5	2.8	1.5	0.5	3.7	2	2.8	4.2	3.4	5.4	2.5	1.1	2.4	0.5	5.1	2.6	1.6	3.9	0.8	2.7
Ho	ppm	0.1	TD-MS	0.2	2.8	0.8	1.4	0.3	1.3	0.5	1.3	2.8	2.9	2.3	1.4	0.3	1.7	1	2.2	1	0.6	2.5	< 0.1	1.9

Analyte Symbol	Unit Symbol	Detection Limit	Analysis Method	K82-01	K82-05	K82-06	K82-07	K82-09	K82-10	I-01	I-02	I-03	I-04	I-05	I-06	I-08	I-09	I-10	I-11	I-12A	I-12B	I-13	PY-02	PY-05
Hg	ppb	10	TD-MS	10	10	20	30	20	30	30	50	1.6	1.2	20	10	20	20	20	2	20	20	1.4	20	0.9
Ag	ppm	0.05	TD-MS	0.46	0.39	0.14	0.25	0.24	5.15	0.36	1.93	0.6	0.47	0.24	1.24	0.11	2.6	0.24	0.38	1.17	2.33	1.6	0.06	> 100
Au	ppb	0.02	BLEG-MS	63.8	7.7	3.7	1.5	2	67	0.2	25	nd	nd	0.4	0.7	0.1	nd	0.5	nd	4	3	nd	nd	nd
Cs	ppm	0.05	TD-MS	0.49	0.81	2.05	0.61	0.48	16.8	1.29	0.3	0.5	0.3	0.43	0.33	0.81	0.71	0.48	0.4	1.07	0.42	0.32	0.74	1.89
Co	ppm	0.1	TD-MS	4.2	7.2	12.2	13.8	1.5	18	5.4	42.1	19.6	43.4	44.6	48.5	3.2	38.6	43.1	32.4	23.3	16.6	56.9	0.9	80.8
Eu	ppm	0.05	TD-MS	1.28	2.12	1.83	2.66	1.06	1.93	4.34	3.68	3.17	1.75	2.97	1.28	0.21	1.92	1.23	1.8	3	2.79	2.29	0.44	2.01
Bi	ppm	0.02	TD-MS	2.13	0.98	0.38	0.37	1.75	34	1.82	32.1	10.3	11.7	10.2	27.5	0.42	16.2	0.13	15.7	18.2	21.7	40.9	0.05	522
Se	ppm	0.1	TD-MS	0.4	< 0.1	0.2	< 0.1	0.4	7	< 0.1	1.9	< 0.1	0.4	< 0.1	< 0.1	0.4	0.7	< 0.1	< 0.1	0.3	0.3	0.7	0.3	10.9
Zn	ppm	0.2	TD-MS	< 0.2	17.9	73.6	117	1.4	< 0.2	8.5	213	110	295	395	432	< 0.2	147	157	388	95.6	86.6	247	11	26.7
Ga	ppm	0.1	TD-MS	5.3	14	23.5	13	6.2	< 0.1	3.8	20.1	< 0.1	20.1	20.5	18.7	5.5	23.5	17	8.6	< 0.1	0.9	21.5	18.8	11.1
As	ppm	0.1	TD-MS	3.3	2	0.7	2	1.1	42.1	1.3	9.8	1.5	1.6	1	1.7	1.9	5.9	14.5	0.2	5.3	3	5.1	0.9	9.3
Rb	ppm	0.2	TD-MS	80.9	67.9	145	67.5	87.1	108	161	36.3	69.7	40.4	72	38.7	147	133	23.7	45.7	146	61.8	56.2	181	70.3
Y	ppm	0.1	TD-MS	8.1	55.6	20.2	35	7	31.5	14.9	42.9	41	34.2	55.2	38.3	8.4	51.2	22.7	48.6	28.7	20.2	40.9	1.9	42
Zr	ppm	1	TD-MS	168	249	219	153	117	204	57	82	97	103	128	59	122	70	65	99	171	63	41	67	10
Nb	ppm	0.1	TD-MS	1.3	11.5	3.9	8	0.6	6.7	0.7	3	0.5	0.2	0.1	0.2	1.7	1.4	1.1	0.2	2.1	1.2	0.4	2.8	0.7
Mo	ppm	0.05	TD-MS	1.53	0.34	0.09	0.81	1	0.18	2.68	0.93	0.42	< 0.05	0.11	0.09	1.17	0.19	0.56	< 0.05	1.01	1.01	0.07	1.73	0.69
In	ppm	0.1	TD-MS	< 0.1	< 0.1	< 0.1	< 0.1	< 0.1	< 0.1	< 0.1	< 0.1	< 0.1	< 0.1	0.1	< 0.1	< 0.1	< 0.1	< 0.1	< 0.1	< 0.1	< 0.1	< 0.1	< 0.1	< 0.1
Sn	ppm	1	TD-MS	< 1	3	< 1	1	< 1	1	< 1	< 1	< 1	< 1	< 1	< 1	< 1	1	< 1	< 1	< 1	< 1	< 1	< 1	< 1
Sb	ppm	0.1	TD-MS	5.6	1.3	1.3	1.7	4.5	6.3	0.1	0.7	< 0.1	< 0.1	< 0.1	< 0.1	0.6	0.2	0.2	< 0.1	2	0.8	0.4	1.5	15.6
Te	ppm	0.1	TD-MS	0.6	< 0.1	< 0.1	< 0.1	1	1	< 0.1	1.1	< 0.1	< 0.1	< 0.1	< 0.1	< 0.1	0.1	< 0.1	< 0.1	0.5	1.2	0.1	< 0.1	327
Ba	ppm	1	TD-MS	2900	1650	1310	2290	2300	4250	> 5000	297	> 5000	2230	> 5000	1970	> 5000	194	320	3050	4490	3860	451	558	585
La	ppm	0.1	TD-MS	84.5	50	64.6	60.2	93.7	48.3	252	98.6	72.7	15.8	52.2	20.5	3.3	13.8	9.7	12.4	104	132	32.7	5.6	57.8
Ce	ppm	0.1	TD-MS	156	111	122	124	156	106	485	208	142	39.9	90.8	34.1	6.7	37.8	18.7	32.6	207	251	67.2	9.1	114
Pr	ppm	0.1	TD-MS	19.3	16.3	15.4	17.3	15.9	13.5	56.7	24.2	17.1	5.2	11.5	4.4	0.9	5.7	2.7	5	24.5	29.8	8.2	1.1	13
Nd	ppm	0.1	TD-MS	65.7	72	53.5	68.4	47.2	50.8	200	85.6	61.3	21.8	41.6	19.1	3.7	25.8	12.1	22.3	87	102	31.8	3.9	52.4
Sm	ppm	0.1	TD-MS	8.9	18	9.5	13.7	5.8	9.6	22.4	13.2	11.7	4.7	9.7	5.5	1.2	7.4	3.3	5.4	15	11.8	5.8	0.8	7.1
Gd	ppm	0.1	TD-MS	5.4	14.6	6.7	10.5	3.9	7.5	11.1	10.6	9.8	5.8	10.1	5.8	1.2	8.1	3.8	7.9	10.4	8.4	7.2	0.5	6.5
Tb	ppm	0.1	TD-MS	0.4	2.1	0.7	1.3	0.3	1	0.8	1.3	1.4	1	1.5	0.9	0.2	1.1	0.6	1.4	1	0.7	1.1	< 0.1	0.7
Dy	ppm	0.1	TD-MS	1.7	13.5	4.2	7.4	1.5	6.3	3.5	7	7.7	5.9	10.8	6.4	1.4	7.8	4.2	9	5.5	3.4	7	0.3	4.1
Cu	ppm	0.2	TD-MS	70.1	128	39.7	331	44.7	400	16.8	57.9	91.4	446	153	35.2	5.8	773	73.9	20.7	886	62.4	36.6	6.3	5240
Ge	ppm	0.1	TD-MS	< 0.1	< 0.1	0.4	< 0.1	< 0.1	< 0.1	< 0.1	< 0.1	< 0.1	< 0.1	< 0.1	0.3	0.1	0.2	0.4	0.2	0.1	< 0.1	0.1	0.2	0.2
Tm	ppm	0.1	TD-MS	< 0.1	0.8	0.3	0.5	< 0.1	0.4	0.2	0.5	0.6	0.5	0.8	0.5	0.1	0.6	0.3	0.7	0.3	0.2	0.5	< 0.1	0.4
Yb	ppm	0.1	TD-MS	0.4	5.3	1.9	3	0.5	2.8	1	3.1	3.7	3.4	5.6	3.6	0.9	4.5	2.5	5.3	1.9	1.3	3.6	0.2	2.8
Lu	ppm	0.1	TD-MS	< 0.1	0.7	0.3	0.4	0.1	0.4	0.2	0.5	0.5	0.5	0.8	0.5	0.2	0.7	0.4	0.8	0.3	0.3	0.5	< 0.1	0.5
Ta	ppm	0.1	TD-MS	< 0.1	0.2	0.1	0.3	< 0.1	0.2	< 0.1	< 0.1	0.1	< 0.1	< 0.1	< 0.1	0.2	< 0.1	< 0.1	< 0.1	< 0.1	< 0.1	< 0.1	0.1	< 0.1
Sr	ppm	0.2	TD-MS	156	754	799	916	153	648	1320	175	132	154	107	144	200	150	607	129	165	182	154	178	77.1
W	ppm	0.1	TD-MS	1.1	0.1	0.2	0.3	0.5	0.1	0.6	0.3	0.2	< 0.1	< 0.1	< 0.1	< 0.1	< 0.1	< 0.1	< 0.1	0.6	0.3	0.1	0.2	1.3
Re	ppm	0.001	TD-MS	< 0.001	< 0.001	< 0.001	< 0.001	< 0.001	< 0.001	0.001	< 0.001	0.001	0.002	0.001	< 0.001	< 0.001	0.002	0.001	< 0.001	0.001	0.002	< 0.001	< 0.001	0.027
Tl	ppm	0.05	TD-MS	0.67	0.4	0.77	0.44	0.66	0.78	1.3	0.44	0.71	0.41	0.64	0.37	1.25	1.68	0.17	0.48	1.53	0.61	0.57	1.22	0.43
Pb	ppm	0.5	TD-MS	137	45.2	16.8	11.9	509	2960	174	1180	190	256	157	498	51.8	138	17.1	356	332	1370	1030	27	1490
Th	ppm	0.1	TD-MS	33	2.6	8.1	11.2	34	5.4	31.9	2.4	9.2	3.2	5	2.8	42.7	1.3	1.3	3	5.9	7.6	1.7	55.1	2.4

Analyte Symbol	Unit Symbol	Detection Limit	Analysis Method	K82-01	K82-05	K82-06	K82-07	K82-09	K82-10	I-01	I-02	I-03	I-04	I-05	I-06	I-08	I-09	I-10	I-11	I-12A	I-12B	I-13	PY-02	PY-05
U	ppm	0.1	TD-MS	197	18.4	13.5	2.2	78.1	> 10000	48.2	2400	401	356	206	975	17.4	834	4.1	669	788	741	2210	3.7	7220

A3.1 References

Aspler, L.B. 1985. GEOLOGY OF NONACHO BASIN (EARLY PROTEROZOIC) NWT, LAWRENCE B,. ASPlER.

Aspler, L.B., and Donaldson, J.A. 1985. The Nonacho Basin (Early Proterozoic), Northwest Territories, Canada: sedimentation and deformation in a strike-slip setting. Strike-slip deformation, basin formation, and sedimentation,: 193–209. SEPM, Tulsa; Special Publication 37. doi:10.2110/pec.85.37.0193.

Bostock, H.H., van Breemen, O. 1992. Thetiming ofemplacement,and distribution of the Sparrow diabase dyke swarm, District of Mackenzie, Northwest Territories. In: Radiogenic Age and Isotopic Studies: Report 6, Geological Survey of Canada. *In* Paper 92-2. Geological Survey of Canada.

Bowles, J.F.W. 2015. Age Dating from Electron Microprobe Analyses of U, Th, and Pb: Geological Advantages and Analytical Difficulties. Microscopy and Microanalysis, **21**: 1114–1122. doi:10.1017/S1431927615000446.

Cathelineau, M. 1988. Cation site occupancy in chlorites and illites as a function of temperature. Clay Minerals, **23**: 471–485. doi:https://doi.org/10.1180/claymin.1988.023.4.13.

Ielpi, A., Martel, E., Fischer, B., Pehrsson, S.J., Tullio, M., and Neil, B.J.C. 2021. A reappraisal of the Nonacho Basin (Northwest Territories, Canada): Record of post-orogenic collapse and marine flooding in the Palaeoproterozoic of the Rae Craton. Precambrian Research, **358**: 106140. Elsevier. doi:10.1016/J.PRECAMRES.2021.106140.